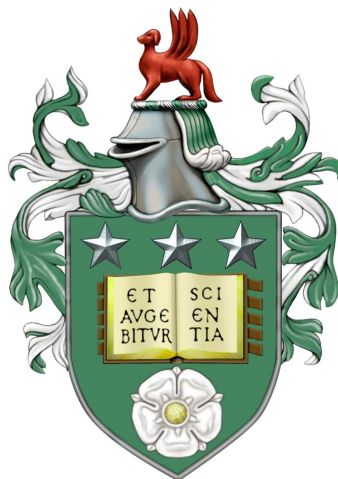


The neuromechanical control of *Caenorhabditis elegans* head
motor behaviour in 3D environments

Omer Yuval

Submitted in accordance with the requirements for the degree of

Doctor of Philosophy



School of Computing

University of Leeds

January 2022

The candidate confirms that the work submitted is his own and that appropriate credit has been given where reference has been made to the work of others.

Acknowledgements

I would like to thank Netta Cohen, my supervisor, for pushing me to expand my knowledge and skills and at the same time giving me the academic freedom to pursue my own interests. Equally important, I feel that Netta has been constantly and truly sensitive, aware and supportive of my personal struggles along the way.

This project required an exceptional combination of expertise and skills from multiple scientific fields, and the results and achievements obtained here would not have been possible were it not for exceptional team work, selfless support and great interpersonal skills. I would like to specifically thank Ian Hope for giving me the opportunity to effectively join his lab and group, participate in group meetings and for his support in general along the way. I feel very lucky to have had the opportunity to have a second scientific home during my PhD.

I would also like to thank our collaborators, Jerry Mellem and Andres Villu Maricq (University of Utah, US) for sharing their data and for the useful discussions, and the Haspel lab (NJIT, US) for sharing their *C. elegans* strains and for their warm welcome and hospitality during my visit to their lab.

Finally, I would like to express my deep appreciation for my family and friends who supported me along the way consistently and unconditionally. I feel grateful and very lucky to have you in my life, and I truly believe that each and every one of you contributed a significant part to the completion and success of this work.

Abstract

Individual neurons are capable of complex information processing and show great diversity both within nervous systems and across the animal kingdom. Their intrinsic neural dynamics give rise to network dynamics, and at the highest level to animal behaviour. Despite extensive research to bridge the gap between single-cell neural dynamics and whole-animal behaviour, many questions remain open. Biological systems are highly interconnected, operate at multiple scales, and evolved to function in specific environments. In particular, feedback loops have evolved to allow for robust and smooth animal behaviour which continuously adjusts to changing internal and external conditions. Thus, to understand the fundamental control principles of animal behaviour, it must be studied at multiple temporal and spatial scales, and in the context of a physical body and environment.

The 1mm long *C. elegans* nematode offers a unique model system for multi-scale investigation, and serves as a powerful tool for genetic manipulations and behavioural assays. In its natural habitat, *C. elegans* manoeuvres through complex 3D environments with changing physical and chemical properties. However, until recently, the worm's locomotion has been studied almost exclusively in quasi-planar settings, such as on an agar surface, while 3D locomotion remains almost completely unexplored. This has limited the scope of our investigation of the neuro-body-environment loop. *C. elegans*' mapped anatomy and sequenced genome allow to target individual cells and study their part in the whole. Given its compact anatomy (a cylindrical body with only 302 neurons and 95 body wall muscle cells), observing *C. elegans*' locomotion in a volume raises interesting questions regarding 3D motor behaviours and their underlying neuromuscular control mechanisms, which may have not been manifested in 2D settings.

I recorded freely-moving *C. elegans* worms in a range of gel viscoelasticity corresponding to gelatin concentrations. A 3D reconstruction tool combining deep learning, computer vision and optimisation techniques was developed to calibrate the volume and extract 3D worm shapes over time in lab coordinates, as well as their location and orientation in the volume. As a complementary method, I used 2D fluorescence imaging of a volume containing worms that express GFP in body wall muscles, in order to visualise the animal's intrinsic coordinate system. This allowed me to estimate the internal twist and the rolling of the worm's body during different patterns of locomotion.

Using quantitative analysis and various visualisations of the extracted 3D data, I identified multiple patterns of locomotion in a volume, some of which have not been reported in *C. elegans* to date. First, in high viscoelasticity environments, the worm crawls forward by propagating a wave of dorsoventral body bends from head to tail. This motion resembles forward locomotion in 2D, however in 3D the worm is highly non-planar, with the head bending outside the plane of undulations frequently, but not periodically. In low viscoelasticity environments, I found that the worm uses chiral motions. In the first, Coiling, the worm forms clockwise (CW) or counterclockwise (CCW) trajectories that emerge from postures with opposite chirality. Furthermore, during this motion, the worm rotates around its longitudinal axis with the same chirality as the trajectory, but at half the rate. In the second motion, Infinity, the worm forms 8-figure trajectories, and rotates around its longitudinal axis CW and CCW back and forth. Interestingly, I found that individual worms are capable of both CW and CCW Coiling, as well as Infinity. In these motions, undulation frequency is high and forward speed is low, compared to crawling.

While these chiral patterns originated at the head and propagated posteriorly throughout the entire body, maximum curvature posterior to the neck was still most correlated with the dorsoventral direction. This suggests that these chiral motions are an extension of planar gaits, rather than being completely separate gaits. I also found that for each of the four modes of forward locomotion (crawling, CW Coiling, CCW Coiling and Infinity), there is a corresponding reversal. This was unexpected, as the neuroanatomy in the tail is much simpler compared to the head, suggesting that passive, mechanical effects play a significant role in the generation of those patterns. Non-planar turning manoeuvres were also observed in which the worm changes its direction of motion and sometimes also its plane of undulations.

After characterising *C. elegans*' locomotion in a volume, I used mathematical modelling to link locomotion patterns to neural dynamics, specifically focusing on the neuromuscular head control of the Coiling behaviour. While the motor circuit posterior to the neck is left-right symmetrical, suggesting that feedforward control is only responsible for body bends in the dorsoventral direction, the head is not restricted in the same way. Rather, it contains more complex circuitry which potentially allows it to bend in all directions. I selected head motor neurons as candidates for the neural control of 3D locomotion. This includes the six RMD and the four SMD neurons. The RMD neurons were found to be intrinsically bistable with a graded response to input current. This is in contrast to most studied motor neurons in other animals, which fire action

potentials in an all-or-none manner. While RMD are not necessary for normal planar forward locomotion, SMD were shown to control the amplitude of head bending. They were also found to be proprioceptive, as their activity is modulated by the shape of the body through stretch receptors that they express.

To study the neural control of 3D locomotion, I first developed a single-cell neuron model based on current-clamp recordings from individual RMD neurons, available in the literature. The model accurately captures RMD's current-voltage relationship, in both normal and abnormal extracellular fluids. The importance of accurately capturing intrinsic neuron dynamics in this context is two-fold. First, predictions of single-cell dynamics can be tested in-vivo, creating a feedback loop in which models direct experiments, and experiments are then used to update the model. Second, constraining single-cell dynamics also constrains network dynamics. This is crucial for identifying biologically-relevant pattern generation mechanisms. Finally, models for chemical and electrical synapses were developed. These are also biologically-grounded as they are based on available data on the synapses that specifically couple RMD and SMD, in order to further constrain network dynamics.

Once the single-neuron and synapse models have been developed, their parameters were fixed and they were used to explore pattern generation in ensembles of bistable neurons. First, I found that a pair of bistable neurons connected via reciprocal inhibition can give rise to sustained rhythmic activity spontaneously. Asymmetry in synaptic weights was crucial to obtain spontaneous oscillations from an in-phase initial state. In ensembles of four of these neurons connected pairwise via reciprocal inhibition and/or electrical coupling, I found regimes that promote stable and unstable synchrony, as well as regimes that support spontaneous pattern switching. Finally, I show that a system of six bistable neurons in which two of them are entrained by mechanosensory feedback, is capable of generating both clockwise and counterclockwise muscle activation, and that chirality is selected spontaneously, based solely on initial membrane potentials.

Overall, in this work I acquired 3D locomotion data in unprecedented quality, and developed novel algorithms for the extraction of meaningful information. This led to the discovery of 3D locomotion patterns that have not been reported in *C. elegans* to date, including chiral gaits. Their analysis links postures and trajectories to the intrinsic coordinate system of the worm. The neural models developed here capture fundamental single-cell and network-level mechanisms for the control of 3D locomotion, which demonstrates the computational power of biological neural networks, and extend beyond the scope *C. elegans*.

Contents

1	Introduction	1
1.1	<i>C. elegans</i>	2
1.2	The case for biologically-grounded computational models	6
1.3	Significance	7
1.4	Thesis outline	9
2	Background	10
2.1	Fluid dynamics and the biomechanics of undulatory motion	10
2.2	Pattern generation, rhythmicity and feedback loops underlying motor behaviour	15
2.2.1	Rhythmic motor behaviour in animals	16
2.2.2	Neural activity underlying motor pattern generation	18
2.2.3	Models of rhythmic neural activity	23
2.3	<i>C. elegans</i>	29
2.4	Summary and conclusions	43
3	3D recording, calibration and reconstruction of <i>C. elegans</i> locomotion in a volume	48
3.1	Introduction	48
3.2	3D imaging of <i>C. elegans</i>	49
3.3	Camera calibration	55
3.3.1	Detection and indexing of calibration grids	56
3.3.2	Camera model refinement	59

3.4	3D midline reconstruction	61
3.4.1	A compact deep learning method for 3D point detection successfully tracks <i>C. elegans</i> head and tail	61
3.4.2	3D midline tracking	66
3.5	Imaging of worms expressing a fluorescent marker in body wall muscles	69
3.6	Collected and analysed 3D data	69
3.7	3D worm tracker (3DWT): A tool for annotation, calibration, reconstruction and analysis of 3D locomotion	70
3.8	Discussion	71
4	Characterisation of <i>C. elegans</i> motor behaviour in 3D environments	75
4.1	Introduction	75
4.2	Results	77
4.3	Four modes of forward locomotion in 3D environments	77
4.4	Chiral trajectories emerge from postures with opposite chirality	83
4.5	The material frame of the worm during Coiling and Infinity	91
4.6	Linking 3D postures and trajectories to the worm's internal coordinate system	94
4.7	Methods	98
4.8	Discussion	101
5	Neural modelling of 3D locomotion	104
5.1	Introduction	105
5.2	Results	108

5.2.1	A biologically-grounded single-neuron model accurately captures RMD intrinsic dynamics	108
5.2.2	An intrinsic mechanism for sequential RMD activations may underlie clockwise and counterclockwise muscle activation	112
5.2.3	Mechanisms for synchronisation and switching in plateau potential neurons connected via gap junctions and graded inhibitory synapses	117
5.3	Methods	123
5.4	Discussion	123
6	Concluding remarks and future outlook	130
7	References	138

List of Tables

1	Parameters for setting up and training a convolutional neural network for labelling calibration images.	58
2	Parameters for setting up and training a convolutional neural network for 3D point tracking.	64
3	Parameters for 3D midline tracking.	69
4	The duration of recorded and analysed 3D data per gelatin concentration and the elastic modulus.	70
5	Single-cell RMD model parameters	110
6	Parameters for the RMD circuit model	113

List of Figures

1	The anatomy of <i>C. elegans</i>	5
2	Description of the flow of a material in terms of shear stress and shear strain	11
3	3D imaging of <i>C. elegans</i> locomotion in a volume	52
4	Camera calibration and imaging of <i>C. elegans</i> in a volume	53
5	3D midline reconstruction and feature extraction	54
6	Grid detection and indexing, camera calibration and annotation-based camera model refinement	60
7	A compact method for 3D point tracking using convolutional neural networks (CNN)	63
8	3D head and tail tracking	65
9	3D midline reconstruction	68
10	Crawling	79
11	Clockwise coiling	80
12	Counterclockwise coiling	81
13	Infinity	82
14	Crawling - chirality of postures and trajectories	84
15	Clockwise coiling - chirality of postures and trajectories	85
16	Counterclockwise coiling - chirality of postures and trajectories	86
17	Infinity - chirality of postures and trajectories	87
18	Statistical analysis of gait chirality and gait classification	89
19	Statistical analysis of speed and curvature	90

20	Clockwise (CW) Coiling of a worm expressing GFP in muscles	92
21	Infinity of a worm expressing GFP in muscles	93
22	Linking 3D postures and trajectories to the worm's internal coordinate system	97
23	Neuromuscular synaptic connectivity in candidate 3D locomotion head circuits	107
24	A biologically-grounded single-neuron model accurately captures RMD intrinsic dynamics for different current inputs and ECF conditions	111
25	Simulations of the RMD motor circuit predict a gait switching mechanism	116
26	Stable and unstable in-phase synchrony in a system of four plateau potential neurons	120
27	An extrinsic mechanism for sequential RMD activations and a spontaneous chirality switch	122

List of abbreviations

	Abbreviation	Meaning
General	<i>C. elegans</i>	<i>Caenorhabditis elegans</i>
	WT	Wild Type
	NGM	Nematode Growth Medium
	ECF	Extracellular Fluid
Molecular biology	GFP	Green Fluorescent Protein
	RFP	Red Fluorescent Protein
	ACh	Acetylcholine
	GABA	Gamma-aminobutyric acid
	ACC	Acetylcholine-gated Chloride Channel
Anatomy	BWM	Body Wall Muscle
	GJ	Gap Junction
	NMJ	Neuromuscular Junction
	D	Dorsal
	V	Ventral
	L	Left
	R	Right
	VNC	Ventral Nerve Cord
Motor behaviour	CW	Clockwise
	CCW	Counterclockwise
	CoM	Centre of Mass
Hardware and software	CNN	Convolutional Neural Network
	FPS	Frames Per Second

1 Introduction

Understanding how behaviour arises from the nervous system is one of the greatest challenges facing neuroscience. Behaviour is a high-level description of the neural dynamics in our nervous system and its manifestation through a physical body. It can be externalised (such as speaking or walking) or internal only (such as thinking or retrieving visual memory), but either way all behaviours evolved to accomplish specific tasks in specific conditions and cannot be fully understood when isolated from their natural environment and physical body through which they are manifested. Sensory information from both the body and the environment continuously modulates the organism's behaviour. How human and animal behaviours arise from a complex network of cellular and molecular interactions is largely unknown. It requires a system-level view involving a multidisciplinary investigation at multiple spatial and temporal scales, and in particular associating neural dynamics with specific behaviours subjected to various perturbations and environmental conditions. Bridging this gap and closing the neuro-body-environment loop is crucial for understanding human and animal behaviour, as well as for preventing and curing neurodegenerative diseases.

Animal behaviour has been studied using modern science for centuries, with early major contributions by the physiologist, physicist, and mathematician Giovanni Alfonso Borelli and the philosopher and writer Charles-Georges Le Roy in the 17th and 18th centuries, respectively, and later by the naturalist Alfred Russel Wallace and the biologist Charles Darwin in the 19th century [1–4]. Borelli studied the biomechanics of animal locomotion and the connection between muscle contraction and body movement, while Le Roy associated the behaviour of different mammals with their environment and established a program for “animal biography” of all “higher species” [1, 2]. He particularly argued that sensory information plays a crucial role in guiding an animal's actions, rather than solely innate instincts. Wallace and Darwin are best known as the co-founders of the theory of natural selection. Both independently found compelling evidence for the correlation between animal anatomy and its surroundings, and for the acquirement of new traits through transgenerational, environment-dependent mutagenesis. However, both also had great interest in the plasticity of the mind in a single life-time, and pondered the importance of an individual's experience versus its instincts. [3–5].

Those people and many others helped develop the idea that animal behaviour is not a fixed nor an exclusively intrinsic phenomenon but rather adaptive, with sensory information from the environment playing

a significant role in both behaviour selection and modulation. Later, with advances in genetics and neuroscience, those concepts have taken a more mechanistic form, leading to the discovery of specific behavioural adaptation mechanisms that act on different time scales, either across generations (e.g., epigenetics), over days-years (e.g., associative learning and memory) or on the scale of milliseconds-seconds (e.g., sensory-motor feedback) [6–8].

Motor behaviour, describing actuated motion of living organisms, and its neural substrates, have been studied in depth in humans and other animals [9–11], and span many fields of research, including molecular and cellular biology, biomechanics, robotics and mathematical modelling [12–18].

Advances in genetic engineering, imaging and computing during the last few decades allow us to study motor behaviour in much finer detail. Genetic manipulation techniques allow us to target specific genes and cells and correlate their function with the behaviour of freely moving animals [19–22]. Improvements in optics and imaging techniques allow us to record whole-animal behaviour at high temporal and spatial resolutions [23–26]. This produces large databases of experimental data that can be stored, processed and shared. Finally, biologically-grounded and hypothesis-driven mathematical models can then be simulated computationally and used to make testable predictions in order to gain new insights into the underlying mechanisms of motor behaviour [27–32].

1.1 *C. elegans*

C. elegans is a 1mm long, transparent nematode that naturally lives in the soil and rotten vegetation, and feeds primarily on bacteria [33, 34]. It has gained its popularity as a powerful model organism for studying the genetic and molecular basis of embryonic development and neuro-development in particular [33, 35–37]. Many genes and molecular pathways are conserved from *C. elegans* to humans [34, 38]. This, together with its short generation time (3-4 days) and large brood size (~ 300) [33, 34], makes it a great model system for high throughput studies of the genetic and cellular basis of normal animal behaviour, and the failures that lead to disease [38, 39].

C. elegans is the first multicellular organism to have its genome fully sequenced [40, 41], and its anatomy fully mapped, including the cell lineage and connectome, both believed to be consistent across individuals [33,

35, 37, 42]. Its population consists mostly of self-fertilising hermaphrodites, and a much smaller number of males ($\leq 0.1\%$) that are different from the hermaphrodite both anatomically and behaviourally [43–45]. With the relative ease of genetically targeting specific cells, together with its anatomical and behavioural simplicity, *C. elegans* has been proven useful for uncovering fundamental principles shared by most living organisms including humans. This includes mechanisms that control gene expression and molecular pathways such as RNAi, epigenetics, cell fate specification, and the insulin pathway, all crucial for understanding normal human development and physiology, as well as disease [46–53].

The body of *C. elegans* is unsegmented, bilaterally symmetrical and has a cylindrical shape with a $\sim 40\mu\text{m}$ radius, and tapered at the head and tail (Fig. 1A-B) [33, 45]. The body of the adult, hermaphrodite worm consists of 959 cells, of which 302 are neurons and 95 are body wall muscle (BWM) cells [54]. It has three body axes: anterior-posterior (AP), dorsoventral (DV) and left-right (LR) (Fig. 1A-B) [45]. A tough and flexible cuticle separates its inside from the environment and maintains internal pressure [55]. Four bands of BWM extend longitudinally (Fig. 1A-B, green stripes), allowing the worm to bend through their attachment to the cuticle [56, 57]. Mutations in BWM and cuticle-related genes can lead to distorted morphology and abnormal locomotion [55, 58, 59].

When placed on a surface of a stiff gel (typically 2% agar), *C. elegans* lies on its side (either left or right) and moves forward by propagating a planar wave of antiphase dorsal and ventral muscle contractions from head to tail (Fig. 1C) [60]. Similarly the worm can move backward by propagating a wave from tail to head, and it exhibits a few more quasi-planar manoeuvres on multiple time-scales, such as omega turns and steering [61–63]. Its relatively simple undulatory behaviour, together with its transparency, makes it an attractive model organism for studying the underlying neuromechanical mechanisms of motor behaviour. In particular, *C. elegans* allows to genetically target and tag specific molecules in specific cells and observe them in freely-moving animals, which has been instrumental for understanding the control mechanisms of specific behaviours and for characterising the role of individual neurons and neural circuits [22, 62, 64–66]. Due to the high genetic conservation of basic molecular and neural pathways from nematodes to humans [46, 53, 67], the hope is that *C. elegans* will provide us with a minimal system for studying fundamental principles that are shared by more complex organisms.

Despite its simplicity and the accumulation of vast amounts of knowledge about *C. elegans* neuroanatomy

and motor behaviour, many things remain unknown. This includes the intrinsic dynamics of most neurons and synapses which determines circuit-level dynamics that underlies locomotion [14, 68–71]. In addition, the pattern generation mechanism for forward locomotion, the most studied behaviour in the worm, is not yet fully understood [72]. It was shown that gradually changing the worm’s environment from a stiff gel to a water-like environment causes the worm to gradually modulate its frequency, wavelength and amplitude of body undulations during forward locomotion (Fig. 1C) [73, 74]. Furthermore, the motor neurons and interneurons that control forward locomotion have been identified [75, 76], however, it is not yet known whether the generation and modulation of the posteriorly travelling wave rely on a central pattern generator (CPG) in the head, on intrinsically oscillating neurons distributed along the body, or on local mechanosensory feedback from the shape of the body [27, 72–74, 77, 78]. The answer might turn out to be a combination of all of these mechanisms which provides robustness, and both experiments and modellings works suggest that *C. elegans* heavily relies on mechanosensory feedback and that pattern generation can be initiated anywhere along the body [27, 30, 31, 37, 79].

Until recently *C. elegans* has been studied almost exclusively in planar settings that mechanically constrain its body to planar motion in the dorsoventral plane, with the exception of head lifting [80, 81], roll manoeuvres [82] and roller mutants [83, 84]. This has limited the study of its locomotion to 2D motor pattern generation and its underlying neural control, since in its natural habitat, *C. elegans* manoeuvres through complex, non-planar environments with changing chemical and mechanical properties [85]. This suggests that *C. elegans* anatomy and neuromuscular control have evolved to allow for 3D motion in a wide range of environmental parameters, some of which might not be manifested in 2D settings.

The neural anatomy throughout most of *C. elegans* body suggests that feedforward pattern generation is limited to the dorsoventral plane, as the ventral cord motor neurons that underlie forward and backward locomotion form neuromuscular junctions onto BWM in a left-right symmetrical pattern [37, 75, 86–88]. However, the head of the worm is not restricted in the same way and contains multiple neural circuits in which individual motor neurons dominantly form neuromuscular junctions onto a single muscle quadrant [37, 86]. Some of these circuits, including RMD, SMD and SMB form mutual inhibition connectivity which suggests that they play a role in rhythmic 3D motor activity [37, 68, 86].

Figure 1: The anatomy of *C. elegans*

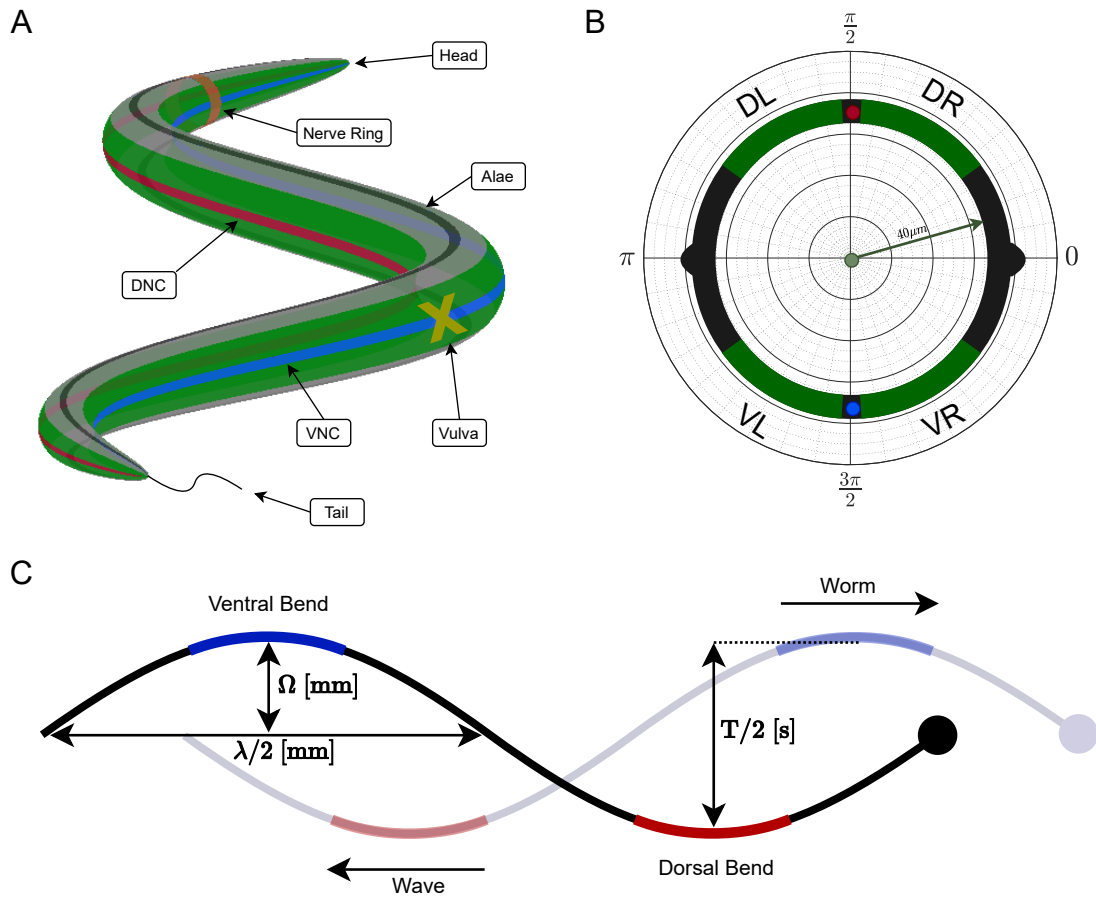


Figure 1. A. A schematic of the body of an adult hermaphrodite worm lying on its left side (with the dorsal side to the left), showing the four body wall muscle quadrants (green), vulval muscles (yellow), dorsal and ventral nerve cords (DNC in red and VNC in blue, respectively), the nerve ring (brown) and the alae (grey). B. A schematic of a cross section of the worm showing the four muscle quadrants (D=dorsal, V=ventral, L=left, R=right), the dorsal (red) and ventral (blue) nerve cords, and the alae (grey). The body radius of an adult worm is $\sim 40\mu\text{m}$. C. When placed on a planar surface, the worm lies on its side and crawls forward by propagating a wave of antiphase dorsal-ventral muscle contractions from head to tail. The black line represents the midline of the worm at time t_0 and the grey line at time t_0+dt . The circles mark the head. Ω , λ and T are the body amplitude, body wavelength and undulation period, respectively. $T = 1/f$, where f [Hz] is undulation frequency. The peaks in curvature of dorsal and ventral body bends are shown as red and blue stripes, respectively.

1.2 The case for biologically-grounded computational models

One of science's key meta-goals is to gradually refine our set of assumptions about the world through an unbiased thinking process leading to the formulation of testable hypotheses, carrying out experiments to test them, and using the results to update our set of assumptions (or their probability distribution, as in Bayesian reasoning [89]).

While biological experiments can teach us a lot about living systems, a formal representation of the assumptions, conclusions and predictions is often missing. This leads to misinterpretation of the experimental results and lowers their predictive power, since an unbiased and reproducible system for hypothesis evaluation is missing.

Because the purpose of a biologically-grounded model is to gain insight about a natural system, the choice of parameter values in the model should be constrained by existing knowledge about that system (or similar systems if data is unavailable). However, it is important to note that the aim of biologically-grounded computational models is not to reproduce (or make a virtual copy of) living systems, but rather to provide hypothesis-driven explanatory and predictive power. This means that model design should be driven by simplicity, intelligibility and interpretability, rather than to capture the full complexity of the system and/or make the model behave like the natural system without being able to understand how it does that. This should be distinguished from bio-inspired task-driven models (e.g., human vision-inspired pattern recognition models) where the output is the main focus, rather than mechanisms and implementation details. However, even in this case interpretability is important in order for us to be able to understand the decision making process of the model and avoid biases in its output (e.g., gender and race biases in face recognition models [90]).

An important objective of measurements from biological systems is the characterisation of their activity pattern in certain conditions, and generalisation to other conditions. Due to finite spatial and temporal sampling resolutions, interpolation of data points is often required. This can be done by modelling the data using a continuous (or quasi-continuous) function which allows sampling at an arbitrarily finer resolution. It can also be used to extrapolate data for conditions not tested in the experiment. Both interpolation and extrapolation are assumptions about the system and can be used to make predictions about its behaviour.

While it is theoretically possible to fit a model function to any data up to an arbitrarily small error by increasing its parameter space, the cost is the loss of both interpretability and generality, as the more complex a model is the harder it is to distill mechanistic principles about the modelled system, and the less likely it is to make accurate predictions about the behaviour of the system in different conditions. For similar reasons, the choice of aspects of the natural system to capture by the model should be hypothesis-driven to ensure that the model is only as complex as it must be.

The scientific effort to link low-level neural dynamics to the behaviour of an animal is effectively limited by the organism's complexity. This includes anatomical and functional complexities and redundancies that may be spatially distributed across the nervous system. This makes it harder to isolate and study the role of low-level components in the whole, such as the neural control of behaviour at the level of individual neurons. Despite the vast diversity in behaviour and complexity across the animal kingdom, the building blocks are often evolutionarily conserved and thus simple animals can be used to study mechanistic principles that are shared by more complex ones. This includes conserved genes and molecular pathways, and the nervous system which consists of neuronal cells and synapses that link them to one another. In particular, fundamental neuronal mechanisms for pattern generation that are required for any periodic behaviour (e.g., swimming, walking, eating and speaking) are likely to be conserved at the cellular level across animals and across behaviours. In this sense, *C. elegans* provides a unique model system for linking low-level cellular dynamics with the behaviour of the animal as a whole [18].

1.3 Significance

This work is on *C. elegans* motor behaviour in 3D environments. The neuromechanical control of *C. elegans* locomotion in a volume is addressed through computational modelling with a focus on head control and the RMD motor circuit.

Until recently, locomotion assays in *C. elegans* have been mostly limited to planar settings due to both the difficulty to image in 3D and the lack of tools for extraction of meaningful data from volumetric recordings. Since *C. elegans* evolved to manoeuvre through complex 3D environments, this has limited our investigation into *C. elegans* motor behaviour and its underlying neuromechanical mechanisms.

Using our novel 3D imaging system together with computer vision tools developed for feature extraction from noisy 3D video data, new locomotion patterns have been discovered and are discussed in depth. These are used to extend the existing corpus of *C. elegans* behaviour, and may be associated with neuronal functions that have not been manifested in 2D settings. These motor behaviours are likely to be shared by other swimmers, and their underlying feedforward and feedback neural mechanisms for 3D pattern generation may be shared by higher organisms throughout the animal kingdom.

The quantitative analysis of the reported behaviours is complemented by biologically-grounded mathematical modelling of head circuitry. The bistable RMD head motor neurons are considered as candidates for 3D pattern generation. First, a minimal single-neuron model is developed to capture RMD intrinsic dynamics based on electrophysiological recordings. This is followed by the development of a circuit model that consists of multiple RMD neurons connected via chemical and electrical synapses, based on neuroanatomy and neurophysiology data available in the literature. The model is used to propose hypotheses for pattern generation mechanisms in the RMD circuit that underlie the observed behaviours. The model is further used to explore mechanisms for synchronisation and switching of neural patterns in an ensemble of bistable neurons connected via reciprocal inhibition and electrical coupling.

Our 3D imaging setup is suited for assays that have been done in 2D (e.g., chemotaxis and optogenetics), and can be used to record other microswimmers. The computational tools developed for 3D calibration and feature extraction can be applied to other imaging systems with any number of cameras, as well as to other swimmers and behaviours on different spatial and temporal scales. Finally, the mathematical modelling and simulation framework developed in this work is well-suited for iterating prediction-experiment loops, and for studying neural dynamics in other neuron types and in larger ensembles of neurons. It can also be combined with biomechanical models in order to test locomotion predictions in the context of the material properties of the animal's body and its environment.

The main purpose of this work is to advance our understanding of the fundamental principles of pattern generation in biological neural networks. This may take us a step closer to understanding more complex phenomena in larger nervous systems that rely on pattern generation such as motor-related neurodegenerative pathologies (e.g., Parkinson's disease) and human language and speech. The control mechanisms demonstrated in this work may be implicated in robotic systems that require navigation in complex and

unpredictable environments such as micro-surgeries and exploration missions on earth and in space.

1.4 Thesis outline

In this thesis I describe an integrated approach for quantitative analysis of *C. elegans* locomotion in 3D environments. 3D imaging of freely-moving animals is combined with state-of-the-art computer vision, deep learning and signal processing techniques to collect and analyse 3D locomotion data. The results of this analysis extend the existing corpus of *C. elegans* motor behaviours that is largely biased towards 2D locomotion. My analysis is complemented by biologically-grounded mathematical modelling of specific motor neurons in the head of the worm that may underlie 3D locomotion. Together, the combination of experimental data and models lead to new insights into the underlying neuromechanical basis of 3D locomotion in *C. elegans*.

In chapter 2 I provide a literature review covering experimental and modelling work on the biomechanics and neural pattern generation underlying motor behaviour. In chapters 3-5 I describe the main results and novel contributions of this work, and discuss future directions.

Chapter 3 describes the methods used for 3D imaging and calibration, and the development of computational tools for the extraction of 3D worm shapes and trajectories from noisy data in a range of environmental viscoelasticity corresponding to gelatin concentrations. This is followed by the definition, classification and quantitative characterisation of the observed locomotion patterns in chapter 4. In particular, I introduce multiple novel motor gaits that have not been reported in *C. elegans* to date. In chapter 5 I describe the development and simulation of a mathematical model that captures neural activity in the head of the worm that underlies the behaviours introduced in chapter 4. The model focuses on the RMD head motor neurons, and it builds on available neurophysiology data and neuro-anatomical maps [37, 68, 70, 86]. The model is further used to explore pattern generation in an ensemble of those neurons, and reveals mechanisms for synchronisation and switching of neural patterns.

2 Background

In this chapter I provide a literature review by introducing key concepts and results in motor behaviour and related topics (including biophysics, fluid dynamics and electrophysiology), and by summarising recent relevant findings. This chapter is built top-down, from the biomechanics of motor behaviour down to cellular and molecular mechanisms for neuromuscular pattern generation. This is first given as a broad review across the animal kingdom, and then specifically for *C. elegans*. The latter ends with a short review of the specific topics discussed in the results chapters (3-5) to allow the reader for a smooth transition and to appreciate the novelty of this work in the context of what is known and what is still missing.

2.1 Fluid dynamics and the biomechanics of undulatory motion

The position of a small, passive particle (typically up to $1\mu\text{m}$ in diameter) over time in an isotropic Newtonian fluid is described by Brownian motion [91]. Microscopic swimmers exhibit active and more complex motion patterns, combining directed and undirected motion. The latter refers to any motion that its direction is independent on factors external to the organism (i.e., its environment). Both unicellular and multi-cellular organisms commonly use directed motion or biased random walk to get closer to attractants and away from repellents, while undirected motion is commonly used for exploration [92, 93].

Unicellular organisms use molecular motors to generate thrust, such as the flagella in *E. coli* used for swimming and tumbling [92, 94–96], and the pseudopodia of the amoeba [97]. Multi-cellular organisms have evolved muscles, cells specialised in movement which contain actin and myosin filaments that can induce contraction of the cell in response to changes in electric membrane potential [98, 99].

The material properties of animals in all scales, as well as their environment, play a significant role in their ability to generate thrust through sequential changes in the shape of their body that pushes against an external material [13]. Organisms across the animal kingdom and across a wide range of size and mass scales have evolved different strategies for propulsion such as fins, wings, legs, or undulatory motion by propagating a bending wave along their body. The geometry and material properties of the body have evolved with respect to the properties of the environments in which they need to operate. In particular, locomotion on land and in fluids such as air and water impose different mechanical and energetic constraints

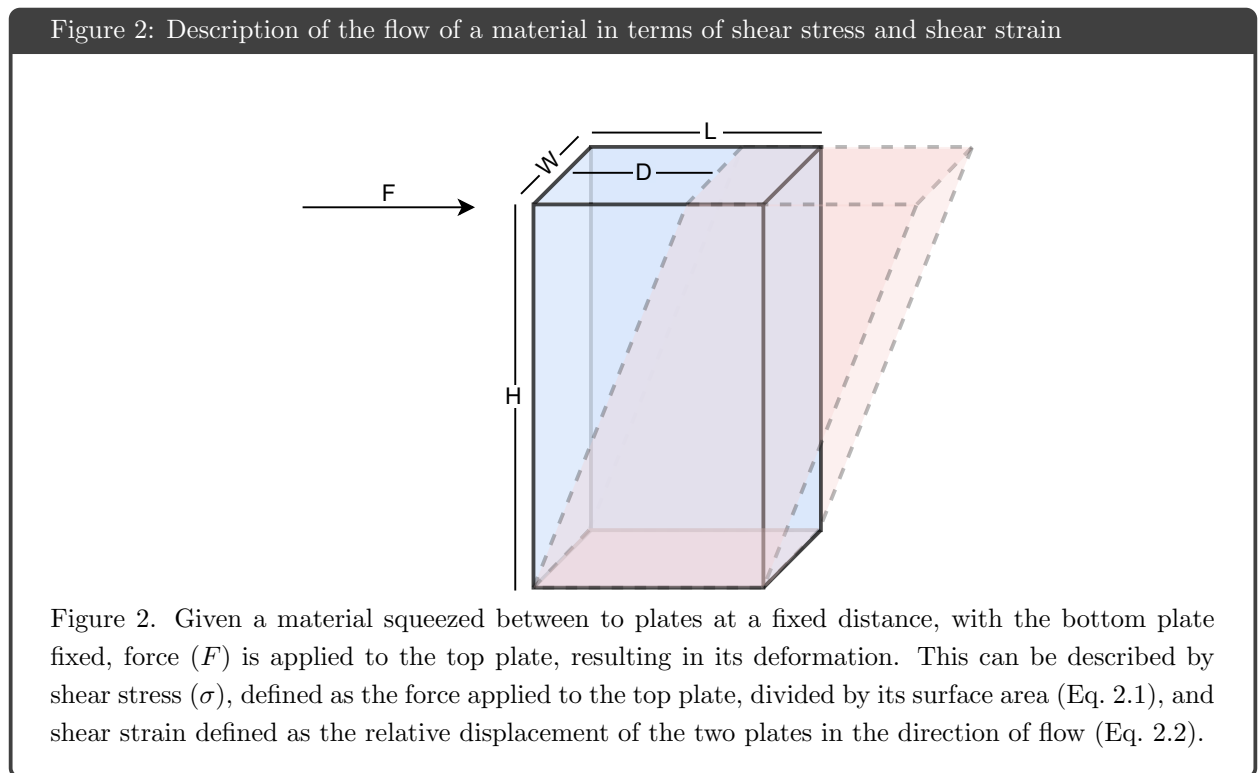
on locomotion, both directly through biomechanics and hydrodynamics, and indirectly through the metabolic pathways that provide muscles with their energy to generate force [13].

The flow of a material is often described in terms of shear flow. Given a material that is squeezed between two plates at a fixed distance, with the bottom one being fixed, force is applied to the top plate (Fig. 2). The flow of the material is induced by shear stress (σ), defined as the force applied to the top plate, divided by its surface area (Eq. 2.1 and Fig. 2). The resulting deformation is described by shear strain (γ), defined as the relative displacement of the two plates in the direction of flow, resulting in a dimensionless quantity (Eq. 2.2 and Fig. 2) [100].

$$\sigma = \frac{F}{A} \quad (2.1)$$

$$\gamma = \frac{D}{H} \quad (2.2)$$

where σ [Pa] is stress, F [N] is force applied applied to the top plate and $A = W \cdot L$ [m²] is the area of the top plate (see Fig. 2). γ is strain (dimensionless), D [m] is the relative displacement of the two plates in the direction of the flow, and H [m] is the distance between the plates (see Fig. 2).



For fluids, strain rate corresponds to flow rate. The viscosity of a fluid is defined as the ratio between its stress and strain rate, describing its resistance to deformations at a given flow rate [17, 100]. This can be thought of as the friction between fluid layers that move against each other. For Newtonian fluids, this ratio is constant at a given temperature/pressure, meaning that the shear stress arising from the fluid's flow is proportional to its rate of deformation (Eq. 2.3) [17, 100]. In other words, the resistance of the fluid to deformation increases linearly with the increase in the force applied to it. Examples of fluids that are conventionally approximated as Newtonian (with their respective viscosity at 20°C) include air (10^{-5} Pa · s), water (10^{-3} Pa · s), oil (10^0 Pa · s) and honey (10^4 Pa · s).

$$\sigma = \mu \frac{d\gamma(t)}{dt} \quad (2.3)$$

where σ [Pa] is stress, $\frac{d\gamma(t)}{dt}$ [s^{-1}] is strain rate, and μ [Pa · s] is the time-independent viscosity of the fluid.

In non-Newtonian fluids this relationship is not linear (i.e., viscosity is not constant). In particular, gels are often described in terms of viscoelasticity, as they exhibit both viscous and elastic properties in response to deformation [17, 100]. Non-Newtonian fluids can be shear thinning or shear thickening, meaning that their resistance to deformation either decreases or increases (respectively) when increasing the force applied to the fluid. Popular examples include ketchup as a shear thinning fluid, and oobleck (corn starch in water) for a shear-thickening fluid.

A body immersed in a fluid experiences both viscous and inertial forces. Viscous forces can be thought of as the friction at the body-fluid interface, whereas inertial forces are proportional to the body's mass and speed (and thus to its momentum), and they also depend on the properties of the fluid. When inertial forces dominate, turbulence may occur, associated with chaotic flows with secondary/indirect effects on fluid motion. When viscous forces dominate, fluid flow is mostly smooth and responds directly (and instantly) to external forces without indirect effects [17]. The Reynolds number (Re) is a dimensionless quantity often used to describe different flow regimes in Newtonian fluids. It is proportional to the ratio between inertial and viscous forces (Eq. 2.4) and can be derived from the governing equations of fluid dynamics (i.e., the Navier–Stokes equations) [17]. In particular, in $Re \gg 1$ inertial forces dominate and turbulence may occur.

$Re \ll 1$ indicates that viscous forces dominate and that inertial forces can be neglected [17].

$$Re = \frac{uL}{\nu} = \frac{\rho uL}{\mu} \quad (2.4)$$

where u [$\frac{m}{s}$] is flow speed, L [m] is the characteristic scale of the problem, ν [$\frac{m^2}{s}$] is kinematic viscosity, ρ [$\frac{Kg}{m^3}$] is fluid density and μ [$\frac{Kg}{m \cdot s}$] is dynamics viscosity.

The flow speed and characteristic length (u and L in Eq. 2.4) are affected by the external body interacting with the fluid. Example Re estimations of swimming in water at different scales include: bacteria (10^{-5}), nematodes (0.05-0.5), small fish (1), Lamprey and eel (10^4 - 10^5), human (10^4) and blue whale (10^7) [73, 101–104].

For micro-swimmers moving at low speeds (i.e., $uL \ll \nu$ in Eq. 2.4), viscous forces dominate and inertial forces can be neglected. Thus, their environment can be modelled using low Re (i.e., associated with laminar flows, $Re \ll 1$), characterised by time-reversible flows [95]. Under these conditions, the scallop theorem states that in order for a swimmer to generate non-zero net displacement it must move asymmetrically in time [95]. For example, a scallop moves by reciprocal motion in which it opens slowly and closes quickly. This motion is time-symmetric, as the opening and closing trajectories are identical, and thus according to the theorem the scallop will make zero net progress in low Re environments, because the displacements resulting from the opening and closing will cancel out (i.e., $Re \ll 1$). In high Re environments however, the scallop will make nonzero net displacement due to inertial forces which allow it to take advantage of different closing and opening speeds [105].

To generate thrust in low Re environments, swimmers have developed different strategies for time-symmetry breaking. Another requirement for propulsion (in any Re) is that the interaction with the environment must be anisotropic, resulting in uneven environmental resistance experienced by the body [106–108]. Most undulatory swimmers propagate waves of curvature along their primary body axis (from head to tail or from tail to head) in order to generate thrust. The directionality of wave propagation provides the necessary time-reversal symmetry-breaking, whereas its uneven drag profile along the body provides the geometric symmetry-breaking [96, 106–108].

Resistive force theory (RFT) was originally developed to analyse flagellar hydrodynamics, and has since

been used to describe the motion of many other organisms in low Re environments, that have long and thin bodies for which the radius of curvature is large compared to body radius, [109–111]. RFT approximates hydrodynamic forces as local and proportional to body velocity. The proportionality constant is defined as a drag coefficient that is decomposed to the normal and tangential directions relative to the local body surface. This allows to compute the forces acting on the body as a result of its deformation and local interaction with the fluid, and the resulting thrust. Slender body theory was developed to describe the motion of such long and thin swimmers in Newtonian fluids at the low Re regime, and is also derived from the Navier–Stokes equations [112]. It approximates the fluid forces acting on the body as local to the swimmer-fluid interface, thus reducing the fluid forces to local drag forces. These drag forces can be decomposed into their tangential and normal components (Eq. 2.5-2.6). Lighthill obtained formulas to approximate the tangential and normal drag coefficients for slender bodies based on experimental measurements. Their values depend on body geometry and fluid viscosity (Eq. 2.7-2.8) [113].

$$F_{\parallel} = -C_{\parallel}V_{\parallel} \quad (2.5)$$

$$F_{\perp} = -C_{\perp}V_{\perp} \quad (2.6)$$

where F_{\parallel} , C_{\parallel} and V_{\parallel} are the force, drag coefficient and velocity in the direction tangential to the body (\parallel), and F_{\perp} , C_{\perp} and V_{\perp} are the force, drag coefficient and velocity in the direction normal to the body (\perp).

$$C_{\parallel} = L \frac{2\pi\mu}{\ln\left(\frac{0.18\lambda}{r}\right)} \quad (2.7)$$

$$C_{\perp} = L \frac{4\pi\mu}{\ln\left(\frac{0.18\lambda}{r}\right) + 0.5} \quad (2.8)$$

where L is body length, r is local body radius, λ is body wavelength, and μ is the viscosity of the fluid.

The ratio of the drag coefficients, $K = \frac{C_{\perp}}{C_{\parallel}}$, must be different from 1 in order for the body to generate thrust, thus imposing the environmental anisotropy condition [113]. This ratio is independent of fluid viscosity (as μ cancels out). Intuitively, a posteriorly travelling wave of body bending will result in the environment pushing the body forward. However, somewhat counterintuitively, this holds only for $K > 1$. For $K < 1$ the motion will result in net backward movement. For worm-like body geometries, K is typically ~ 1.5 in Newtonian fluids and cannot exceed 2. This is because for infinitely thin bodies, $r \rightarrow 0$, and thus $\frac{\lambda}{r} \rightarrow \infty$

and $\ln(\frac{0.18\lambda}{r}) \gg 0.5$. Thus the denominators of Eq. 2.7-2.8 become equal, and cancel out in $\frac{C_{\perp}}{C_{\parallel}}$. Finally, $K_{r \rightarrow 0} = \frac{4\pi\mu L}{2\pi\mu L} = 2$ [107, 109, 110, 112].

Micro-swimmers do not always move in water-like fluids and often their environment cannot be approximated as Newtonian (e.g., wet soil, sand at the bottom of the ocean or the human body). Rather, their environment might have significant elastic, plastic or complex granular properties. Resistive force theory (RFT) is an approximation to slender body theory that discretises the body and considers the forcing on it as local interactions of points along the cylindrical shape. An important advantage of RFT is that it allows to solve the forces acting on swimmers in both Newtonian and non-Newtonian fluids by allowing the normal drag coefficient to increase such that K exceeds 2. This allows to approximate the resistance experienced by swimmers in environments with non-negligible elastic properties such as viscoelastic fluids and solids [73, 107, 109–111, 114].

2.2 Pattern generation, rhythmicity and feedback loops underlying motor behaviour

Contraction and relaxation of body wall muscles induce changes in body shape which result in force applied on an external material that mechanically constrains the body. Coordinated contraction and relaxation of muscles induce sequential changes in body shape that can be used to generate thrust or achieve other behavioural goals. The set of possible postures and motion patterns largely depends on the geometry and mechanical properties of the body, which vary significantly across species [13]. Motor pattern generation is controlled by the nervous system via neuromuscular junctions [99, 115, 116]. However, feedback mechanisms play a significant role in the entrainment of neuromuscular pattern generation (e.g., walking speed), as well as in motor program selection (e.g., walking or swimming), making the system more robust and allowing animals to modulate their behaviour in changing and unpredictable environments [117]. Altogether, feedforward neural control generates muscle activation patterns that induce sequential changes in body posture, while the environment mechanically constrains the body, and mechanosensory information from the shape of the body is used to modulate neuromuscular activity, thus closing the neuro-body-environment loop (see section 2.3 for more details about feedforward and feedback mechanisms in *C. elegans*).

Biological rhythms are present in all living systems, from unicellular organisms, to plants and humans, and underlie many fundamental biological processes [118]. The cell cycle, the mechanism for cell division that lies at the heart of the emergence, development, variation and survival of all living organisms, is a controlled process consisting of well-defined steps and checkpoints. During this process the cell grows in size, replicates its DNA and finally divides into two daughter cells through a chain of biochemical reactions. These reactions generate coordinated temporal and spatial rhythms that regulate gene expression and molecules in the cell [119]. This is achieved through positive and negative feedback loops that allow downstream components to regulate upstream components [119]. In particular, positive feedback is often used in biological systems to initiate or enhance a response, whereas negative feedback is used to balance or terminate it. Positive and negative feedback loops can be coupled to make reversible and irreversible switches, and provide a mechanism for hysteresis, in which a system has multiple steady states, and its dynamics depends on its history [120].

Many motor behaviours are rhythmic as well, and require a mechanism for pattern generation [121]. They include locomotion, respiration, digestion, heartbeat and speech, and are achieved via coordinated contraction and relaxation of muscle cells that are attached to other tissues and induce their bending [122].

2.2.1 Rhythmic motor behaviour in animals

Undulatory swimming in anguilliform (e.g., eel and lamprey) and carangiform (finned fish) is achieved by a backward-travelling wave pushing against the water to generate thrust [123, 124]. The wave reaches its maximum amplitude at the tail, meaning that most of the thrust is generated by the posterior half of the body [124]. Electromyography (EMG) recordings revealed that in many of these species, muscle activation propagates posteriorly faster than body curvature [124, 125]. This neuromechanical phase lag between EMG and muscle strain varies along the body and across species, and determines the pattern of work generated by the muscles, and the force applied to the water. A muscle cell is performing positive work if it is generating force while shortening, and negative work if it is generating force while lengthening (this is called a lengthening contraction). In most species, EMG begins before the muscle begins to shorten and ends before shortening is over. This ensures that the overall muscle activity produces positive work [124, 125]. However, the varying correlation between muscle activity and strain along the body and negative muscle work have their own purpose. Despite not resulting in force applied directly to the water, a lengthening

contraction makes the muscle stiffer (and the body region it is attached to), and is used to transmit force to other body regions (posteriorly in forward locomotion) [123, 125]. In addition, muscle relaxation is generally slower than activation, but the ratio between the rates also depends on activation level, as higher activation leads to faster relaxation. This ratio also depends on intrinsic properties of the cell that can vary throughout the body [123]. For example, it was shown that in the scup, anterior muscles have an intrinsically faster relaxation rate compared with posterior muscles. This partially compensates for the lower strain in the anterior region and allows anterior muscles to generate significant power [123].

The lamprey is one of most extensively studied animals in terms of rhythmic motor behaviour and its underlying neuromuscular control [126, 127]. The lamprey's body is segmented, and like all anguilliform fish, it swims by propagating a wave of left-right undulations from head to tail (or from tail to head in backward swimming) [128]. Undulation frequency in forward locomotion ranges between 1-8Hz, while backward frequency is significantly lower (approximately four-fold) [129]. In brain and spinal cord preparations, rhythmic motoneuron activity was recorded both with and in the absence of rhythmic motion, showing that oscillatory activity can arise in the absence of mechanosensory input [130]. However, for coordinated locomotion, the lamprey relies on sensory feedback, which entrains both cycle period and intersegmental phase lags [131, 132]. Similar results were obtained for the leech [133, 134]. Furthermore, intersegmental coordination was shown to persist in intact animals in body regions disconnected from the CNS, showing that sensory feedback is sufficient for intersegmental coordination [132, 134].

Cangiano and Grillner investigated the ability of ventral hemicords in the lamprey to generate motor rhythms. They found that each hemicord is capable of generating oscillatory activity, independent of ipsilateral nor contralateral inhibition. They also showed that each hemisegment is capable of generating both high and low frequency bursts, but only high frequency bursts are correlated with fictive swimming. This was shown by gradually reducing cross axonal connections between the two hemicords uniformly along the midline, which caused a gradual increase in burst frequency, along with a gradual dissociation of the originally bilaterally alternating rhythms. This gradual frequency modulation happened for induced high frequencies but not for low frequencies [135].

There are two groups of stretch receptor neurons in the lamprey (also called edge cells). One group excites ipsilateral neurons and the other inhibits contralateral neurons. These cells entrain the swimming circuit

by processing mechanosensory information [136, 137]. In the leech, sensory feedback is mediated by stretch receptors embedded in longitudinal muscles [138]. These stretch receptors were found to be functionally and anatomically linked to the swimming circuit [139, 140]. Cang and Friesen artificially generated oscillations in these stretch receptors by directly injecting them with currents in a sinusoidal pattern. By adjusting the injected pattern, they were able to entrain intersegmental phase lags [139]. Taken together, while pattern-generating circuits may be sufficient to generate oscillatory motion for certain gaits and environmental conditions, it is clear that these animals rely heavily on sensory feedback for coordinated motion and for the adaptation of undulation frequency [126, 141].

Some insects, such as cockroaches, exhibit a high speed running gait ($100 - 300 \text{ cm} \cdot \text{s}^{-1}$) [142], while others, such as stick insects, use a slow walking gait ($10 - 50 \text{ cm} \cdot \text{s}^{-1}$) [143]. Either way, coordinated movement on land is more challenging than in water in the sense that it requires an interaction with highly non-uniform and unpredictable terrain, suggesting that mechanosensory feedback plays a significant role in insect locomotion. Indeed, sensory feedback was found to be essential for both interleg and intraleg (across joints) coordination through the entrainment of feedforward oscillatory control mechanisms [142, 144, 145]. Interestingly, it was also shown that each leg can entrain the undulation frequency of neighbouring legs, and that increasing their frequency increases their coupling by decreasing intersegmental phase lags [145].

2.2.2 Neural activity underlying motor pattern generation

The rhythms that underlie motor behaviour can arise from intrinsic cellular properties (such cells are called pacemakers), or at the network level from the interaction of an ensemble of neurons (e.g., reciprocal inhibition) [121]. Intrinsic oscillators can generate rhythmic activity even when isolated from the body, given an appropriate depolarising input current. Extrinsic oscillations are a property of a network and are the result of both intracellular properties and the interaction between cells in the network [121].

Interestingly, biological rhythms have evolved to function within certain ranges of environmental parameters, and their initiation, termination, amplitude and frequency are modulated within those ranges. This stresses the importance of studying neural activity in physiological conditions and in the context of a physical body and environment in order to understand the full scope of a motor control system [8, 146].

Neural pattern generation is facilitated by the opening and closing of ion channels that allow ions to cross the cell's membrane and change its electric potential [8]. Consequently, rhythmic activity may arise in isolated cells or as a result of the interaction between multiple cells [8]. The intrinsic properties of a neuron are largely determined by the ensemble of ion channels embedded in its plasma membrane, as well as other factors such as dendritic morphology and calcium storage [8, 147]. External factors can modulate the type and kinetics of ion channels, resulting in the modulation of the neuron's dynamics which can give rise to different patterns of activity [8].

Neuron-neuron interaction is achieved via chemical and electrical synapses (the latter are also known as gap junctions) [148]. While chemical synapses are uni-directional and selective, gap junctions are, by and large, bi-directional and non-selective [148]. Chemical synapses can be excitatory or inhibitory, depending both on the neurotransmitter released from the presynaptic neuron, and its receptor in the postsynaptic neuron [148].

Neurons have compartments specialised in signal transduction. Axonal processes transfer signals from the soma to other cells, while dendrites process information from other cells and propagate it to the soma [149]. Axons and dendrites contain microtubules and actin filaments that are required for their formation and maintenance. The orientation of microtubules, controlled mainly by plus-end tracking proteins, determines neuronal polarisation and specification of axonal and dendritic processes [149]. Axon and dendrite specification is not absolute nor fixed, and largely depends on microtubule stability. Microtubule polarisation has been shown to be plastic, mostly during development but also in mature neurons, adding to the computational complexity of the network [150–154].

In many neuron classes, dendritic trees develop highly arborised and organised structures that are thought to be tightly related to the function of the neuron [155, 156]. For example, a highly arborised neuron in *C. elegans*, called PVD, extends almost throughout its entire body, with an extensive dendritic tree, consisting of a repeating structural pattern called menorah (or candelabra) [157]. As most *C. elegans* neurons show much simpler morphologies, the PVD is often used as a model for studying the relationship between neuronal structure and function [157–159]. The PVD neuron mediates an escape behaviour in response to harsh touch and was also proposed to play a role in proprioception [158]. However, the PVD has only a single axon, which raises the question of how a single neuron can encode multiple responses while being able to send signals

down to other neurons through a single process. Tao et al. showed that harsh touch anywhere along the dendritic tree results in excitation of the PVD cell body, that then excites downstream neurons responsible for the escape response. They were able to identify the specific ion channels that are necessary for this response, but are not necessary for normal locomotion. They also found another set of channels necessary for normal locomotion but not for harsh touch. Furthermore, they showed that during normal locomotion, calcium transients oscillate locally within individual neurons in a frequency similar to the frequency of body undulations, and that these signals do not propagate to the cell body or other regions throughout the cell. They identified a neuro-peptide (NLP-12) that is secreted locally from PVD dendrites and is necessary for normal locomotion. This suggests that the PVD neuron mediates its proprioceptive response locally via the secretion of NLP-12 from individual dendritic sub-units [160]. Overall, this example shows that even individual neurons can carry out complex computations and encode multiple distinct responses independently and simultaneously, taking advantage of dendritic morphology, gene expression and time-scale separation.

In most animals, most neurons maintain a resting membrane potential of $-70 \pm 10 \text{mV}$, with higher extracellular concentrations of sodium (Na^+), chloride (Cl^-) and calcium (Ca^{2+}) ions, and a higher intracellular concentration of potassium (K^+) [161]. The equilibrium membrane potential is determined by the net charge of all ions, as well as their concentration gradient, the (passive) membrane permeability, and the active transport of each ionic species [161]. In most neurons, this equilibrium is determined by the neuron's permeability to Na^+ , Cl^- , Ca^{2+} and K^+ , as well as the high concentration of impermeant anions inside relative to outside the cell [161].

The electric potential of individual ionic species can be computed using the Nernst equation which considers their intracellular and extracellular concentrations (Eq. 2.9) [161]. The total membrane potential considering all permeable ions can be computed using the Goldman–Hodgkin–Katz equation (Eq. 2.10, showing for Na^+ , K^+ and Cl^-) [161–163]. For a single ion species, this equation reduces to the Nernst equation (Eq. 2.9). In addition, there is active (ATP-dependent) ion transport, with the sodium-potassium pump being the most important in determining the equilibrium membrane potential. This pump transports three Na^+ ions outside the cell for every two K^+ ions that are transported inside [164–166].

$$E_I = \frac{RT}{zF} \ln \left(\frac{[I_{\text{out}}]}{[I_{\text{in}}]} \right) \quad (2.9)$$

where R is the gas constant ($R=8.314 \text{ J}\cdot\text{mol}^{-1}\cdot\text{K}^{-1}$), F is the Faraday constant ($96485 \text{ C}\cdot\text{mol}^{-1}$), T is temperature [K], z is the valence of the transported ion (.e.g., $+1$ for Na^+ and $+2$ for Ca^{2+}), and $[I_{\text{in}}]$ and $[I_{\text{out}}]$ are the concentrations of the ion inside and outside the cell, respectively.

$$E = \frac{RT}{F} \ln \left(\frac{P_{\text{Na}}[\text{Na}^+]_{\text{out}} + P_{\text{K}}[\text{K}^+]_{\text{out}} + P_{\text{Cl}}[\text{Cl}^-]_{\text{in}}}{P_{\text{Na}}[\text{Na}^+]_{\text{in}} + P_{\text{K}}[\text{K}^+]_{\text{out}} + P_{\text{Cl}}[\text{Cl}^-]_{\text{out}}} \right) \quad (2.10)$$

where P is the permeability coefficient [$\text{cm}\cdot\text{s}^{-1}$] of each ion.

Neurons encode information through fluctuations in membrane potential facilitated by the ion channels embedded in their plasma membrane, and communicate this information to other cells via chemical and electrical synapses, as well as extra-synaptic transmission [160, 161, 167]. The action potential is a common intrinsic, transient response in excitable cells, described by the fast depolarisation and hyperpolarisation of the membrane potential, typically in the order of magnitude of milliseconds [168]. It was first described by Hodgkin and Huxley that recorded the membrane potential of the squid giant axon in the late 1930s [169]. Almost 40 years later, electrophysiological recordings were done from individual ion channels, shedding light on the contribution of the dynamics of ion channels and ionic currents to the membrane potential and to the propagation of signals along an axon [170].

Action potentials are facilitated by voltage-gated ion channels and characterised by fast depolarisation, followed by fast hyperpolarisation, followed by a refractory period during which an action potential cannot be evoked [168, 169]. In most studied cases, the fast depolarisation was found to be Na^+ -dependent, although cases where it is Ca^{2+} -dependent (and Na^+ -independent) were also identified [171, 172]. Once the voltage threshold of the Na^+ channel is crossed at some sub-region of the membrane, it opens and initiates a chain reaction that causes other Na^+ channels to open. This results in a fast influx of Na^+ ions and the depolarisation of the membrane potential. This then causes the Na^+ channels to close, and the K^+ channels to open, resulting in fast outward K^+ current, bringing the membrane potential back down. Then, both Na^+ and K^+ channels inactivate, and the sodium-potassium pump actively transports Na^+ ions outside and K^+ ion inside, in order to recover their concentrations. This transport, together with the inactivation of Na^+ and K^+ channels, is responsible for the refractory period during which the membrane potential is lower than its resting potential, and an action potential cannot be evoked [168, 169]. The distribution of voltage-gated

channels across the plasma membrane is not uniform, causing different regions of the plasma membrane to be more excitable than others [168, 169]. Interestingly, a much slower response involving gene expression, on the time-scale of minutes to hours, was found in excitable neurons and was suggested to play a role in long-term memory consolidation [173].

Another type of an intrinsic response is graded potentials, where subthreshold fluctuations in membrane potential result in a gradual, rather than all-or-none, response, with its magnitude depending on the magnitude of the depolarising or hyperpolarising input [121]. Graded synaptic transmission has been implicated in sensory systems [174], and was also found in pattern-generating circuits [121]. For example, retinal cells in several invertebrates and vertebrates were found to have a calcium-dependent graded response to light, allowing them to use their entire voltage range to encode subtle changes in light intensity [174]. In addition, oscillating contralateral pairs of interneurons in the leech heart were found to have calcium-dependent graded potentials [172].

Many other intrinsic neuronal dynamics exist, and they can be combined in the same neuron, either simultaneously or under different conditions [121]. Some neurons exhibit plateau potentials, having two stable membrane potentials. In response to sufficient depolarising input current, these neurons generate a sustained membrane potential that is higher than the resting potential and outlasts the duration of the stimulus [121]. Some plateau potential neurons fire bursts of action potentials in their ON state, or show a graded response to depolarising inputs. Plateau potential neurons have been implicated in oscillatory motor circuits [121]. For example, current-clamp recordings from the RMD head motor neurons in *C. elegans* showed that their response is graded and that they have two stable membrane potentials, one at -70mV (resting potential), and the other at -35mV (plateau potential) [69, 70].

Reciprocal inhibition is perhaps the simplest mechanism for pattern generation resulting from the connectivity between two cells. Reciprocal inhibition has been shown to underlie oscillatory neural activity and rhythmic motor activity in many species, including the leech (heartbeat and swimming) [175, 176], the lamprey (swimming) [177] and the lobster (gastric mill) [178]. In the simplest case, two inhibitory neurons are reciprocally connected via inhibitory chemical synapses, and a third neuron provides a depolarising current that does not carry time information. In addition, some sort of a habituation mechanism is required to allow the inhibited cell to “escape from inhibition”, and the depolarised cell to release itself from the

depolarising current [179]. Then, the inhibited cell becomes the inhibiting cell, and the cycle repeats. This can be achieved through a desensitisation mechanism that can be either synaptic or intrinsic to the cells [180, 181].

2.2.3 Models of rhythmic neural activity

Many neural models have been developed over the past century, with the objective of capturing neural dynamics and their underlying ionic currents observed in biological neurons. The level of abstraction varies across models and is chosen with respect to the driving hypothesis. Some models are more phenomenological and biologically-grounded and thus contain details about low-level properties such as ionic currents, channel conductances and dendritic morphology. Others aim to capture higher-level dynamics at the cellular or network level. Models can be used to analyse and predict intrinsic dynamics of neurons and neural networks across a wide range of parameters, corresponding to physiological conditions and synaptic inputs. These can be combined with biomechanical models in order to study neural activity in mechanical context that allows to test hypotheses regarding feedforward and feedback interaction with a body and an environment.

The harmonic oscillator is perhaps the simplest model used to captures rhythmic activity in excitable cells, and is derived from Newton’s second law of motion (Eq. 2.11) [182]. The Van der Pol relaxation oscillator, an extension of the harmonic oscillator, is a dissipative oscillator with nonlinear damping. Its mechanical representation is a mass-spring-damper system, where the damper is orthogonal the the spring Eq. 2.12 [183]. This model system can generate oscillations with dynamics that resemble that of biological neural oscillations with fast depolarisation, slow hyperpolarisation and a refractory period (Eq. 2.12-2.13). When the damping (μ) is set to zero, the model reduces to a simple harmonic oscillator (Eq. 2.11) [182, 183].

$$F = ma = m \frac{d^2x}{dt^2} = -kx \quad \implies \quad x(t) = A \cos(\omega t + \phi), \quad \omega = \sqrt{\frac{k}{m}} \quad (2.11)$$

where F [N] is force, m [kg] is mass, a [$\frac{m}{s^2}$] is acceleration, x [m] is position, t [s] is time, and k [$\frac{N}{m}$] is the spring constant. In the solution, A [m] is amplitude, ω is angular frequency [$\frac{rad}{s}$] and ϕ [rad] is the phase

angle.

$$m \frac{d^2x}{dt^2} = \left(c - c_h \frac{x^2}{a^2 + x^2} \right) \frac{dx}{dt} - kx \quad (2.12)$$

$$\frac{d^2y}{dt^2} = \mu(1 - y^2) \frac{dy}{dt} - y \quad (2.13)$$

where m, k, x, t are as in Eq. 2.11, c is a proportionality coefficient for the force applied to the system, c_h is the linear damping coefficient and a is the length of the damper, as described in [183]. This mechanical representation can be simplified and abstracted to obtain Eq. 2.13, where μ is the damping coefficient [183].

The leaky integrate-and-fire (LIF) model gained its popularity for its simplicity and ability to generate dynamics that resemble biological neurons. It models the plasma membrane as a capacitor with non-zero conductance (i.e., finite resistance) that allows for passive flow of ions. However, it does not consider specific ionic currents and their time- and voltage-dependent conductances. The model captures some aspects of the dynamics of spiking neurons, as well as some subthreshold dynamics. It is obtained by taking the time derivative of the law of capacitance (Eq. 2.14-2.15). The additional leakage term ($-GV(t)$ in Eq. 2.15) models the membrane conductance (G) that acts as a rate constant and allows the system to adapt to input current and relax in its absence [184].

$$q = CV \implies \frac{dq}{dt} = C \frac{dV(t)}{dt} \implies C \frac{dV(t)}{dt} = I(t) \quad (2.14)$$

where C [μF] is membrane capacitance, q [C] is the electric charge held in the capacitor, V [mV] is membrane potential, I [pA] is injected current and t [s] is time.

$$C \frac{dV(t)}{dt} = I(t) - GV(t) \quad (2.15)$$

where G [nS] is the membrane conductance and the rest is as in Eq. 2.14.

Hodgkin and Huxley (HH) used the voltage-clamp technique to record from the squid giant axon [169]. They were the first to suggest, based on their measurements, a model that captures action potentials in

excitable cells and explains the dynamics of the underlying ionic currents [185]. They were awarded the Nobel Prize in Physiology or Medicine in 1963 for their pioneering work. The formulation of the model specifically addresses voltage-gated sodium and potassium currents, and the passive leakage of ions through the membrane (Eq. 2.16-2.19). The model was later shown to be useful for describing the dynamics of many other excitable cells in other organisms [184, 185].

$$C \frac{dV(t)}{dt} = I(t) + g_K n^4 (V - V_K) + g_{Na} m^3 h (V - V_{Na}) + g_l (V - V_l) \quad (2.16)$$

$$\frac{dn}{dt} = \alpha_n(v)(1 - n) - \beta_n(V)n \quad (2.17)$$

$$\frac{dm}{dt} = \alpha_m(v)(1 - m) - \beta_m(V)m \quad (2.18)$$

$$\frac{dh}{dt} = \alpha_h(v)(1 - h) - \beta_h(V)h \quad (2.19)$$

where C [μF] is membrane capacitance, V [mV] is the membrane potential, I [pA] is injected current, g_K, g_{Na}, g_l [nS] are potassium, sodium and leak conductances (respectively), V_K, V_{Na}, V_l are potassium, sodium and leak potentials (respectively), and n, m, h are dimensionless variables that capture potassium channel activation, sodium channel activation and sodium channel inactivation (respectively). Activation/inactivation corresponds to the fraction of open/closed channels of each of the ionic species. α_i, β_i for $i = \{n, m, h\}$ are voltage-dependent channel activation and inactivation rate functions (respectively), formulated based on experimental measurements.

The FitzHugh-Nagumo (FHN) model is a simplification of the HH model, designed to capture the dynamics of excitable cells without details about the underlying electrophysiological mechanisms. The model consists of two first-order differential equations, one containing a cubic function to capture fast depolarisation, and the second contains a linear function to capture the slow recovery response of the neuron during repolarisation (Eq. 2.20-2.21). Simulations show that the model successfully captures different dynamics observed in biological neurons, including action potentials, bistability and tonic spiking. However the model cannot generate tonic bursting (repeated discrete groups of spikes separated by a quiescence period), also

observed in biological neurons [186–188].

$$\frac{dV}{dt} = V - \frac{V^3}{3} - W + I \quad (2.20)$$

$$\frac{dW}{dt} = a(bV - cW) \quad (2.21)$$

where I [pA] is injected current, V [mV] is membrane potential, W is a slow recovery variable, and a, b, c are constant scalars.

Later, the Morris-Lecar (ML) model was developed to account for a variety of oscillatory activities that have been observed in current-clamp experiments in muscle fibres of the giant barnacle, where voltage-gated calcium channels dominate (rather than sodium channels). It is also a simplification of the Hodgkin-Huxley model, formulated using a system of two nonlinear differential equations (Eq. 2.22-2.23). The ML model was shown to capture the complex relationship between membrane potential and the activation of ion channels embedded in the plasma membrane. In contrast to the FHN model, the second equation is non-linear (a sigmoid) which allows to capture more complex types of excitability such as tonic and phasic bursting [189].

$$C \frac{dV(t)}{dt} = I(t) - g_{Ca} M_{ss}(V - V_{Ca}) - g_K W(V - V_K) - g_l(V - V_l) \quad (2.22)$$

$$\frac{dW}{dt} = \frac{W_{ss} - W}{\tau_W} \quad (2.23)$$

where C [μ F] is membrane capacitance, I [pA] is injected current, V [mV] is membrane potential, W is a slow recovery variable, g_{Ca}, g_K, g_l [nS] are calcium, potassium and leak conductances (respectively), V_{Ca}, V_K, V_l are calcium, potassium and leak reversal potentials (respectively), τ_W is a firing time scale constant, and M_{ss} and W_{ss} are voltage-dependent hyperbolic functions.

Moving from individual neurons to small neural networks, Wang and Rinzel suggested a simple ionic model for an intrinsic mechanism of a non-oscillating cell that exhibits post-inhibitory rebound (PIR), a mechanism that has been observed in electrophysiological recordings [121]. Simulations show that the model successfully generates oscillations in a system of two identical, reciprocally inhibiting cells, and a third cell that provides a depolarising current that does not carry time information. Furthermore, the model is used to predict two mechanisms that underlie oscillatory behaviour in neurons - escape and release. The “escape” mechanism is an adaptation to hyperpolarising inputs, allowing the inhibited cell to escape from inhibition

and, once above threshold, inhibit the other cell. The “release” mechanism is an adaptation to excitation, allowing the excited cell to gradually depolarise and release itself from the depolarisation input current [179]. Skinner et al. extended this work by modelling the escape and release mechanisms as either intrinsic only or synaptic only. They demonstrated how the frequency of oscillation is dominantly controlled by either neuron or synapse parameters depending on whether the escape and release are modelled as part of the neuron or synapse (respectively) [28].

Inspired by the gastric mill central pattern generator of the lobster, Rowat and Selverston studied neural pattern generators focusing on oscillatory behaviour in pairs of cells coupled by reciprocal inhibition through graded transmission synapses. Their model consists of two first order differential equations modelling fast and slow currents (Eq. 2.24-2.25). An N-shaped function (using hyperbolic tangent) describes the fast current (Eq. 2.26), and a linear function describes the slow current (Eq. 2.25 and 2.27). The synaptic current depends on both the pre- and post-synaptic membrane potentials, and contains a sigmoid function of the pre-synaptic membrane potential (Eq. 2.28-2.29). In a simplified version of the model the hyperbolic function in the fast current model (Eq. 2.26) was replaced by a piecewise linear function (Eq. 2.30), and the synaptic conductance (Eq. 2.29) was changed to a binary function (Eq. 2.31). By changing single-neuron model parameters they obtained six different behaviours that correspond to intrinsic physiological dynamics observed in biological neurons: quiescence, almost-an-oscillator, endogenous-oscillation, permanent-depolarisation, permanent-hyperpolarisation, and plateau-potentials. They then examined the coupling of all possible pairs through reciprocal inhibition. By fixing all neuron parameters and only adjusting synaptic weights and thresholds they were able to generate oscillations in all pairs [190, 191].

$$\tau_m \frac{dV}{dt} = -F_{\text{fast}}(V, \sigma_f) - q + I_{\text{inj}} - I_{\text{syn}} \quad (2.24)$$

$$\tau_s \frac{dq}{dt} = -q + q_{\infty}(V) \quad (2.25)$$

$$F_{\text{fast}}(V, \sigma_f) = V - A_f \cdot \tanh\left(\frac{\sigma_f}{A_f} V\right) \quad (2.26)$$

where V [mV] is membrane potential, q [mV] models slow current, I_{inj} [pA] is injected current, I_{syn} [pA] is synaptic current (see Eq. 2.28), σ_f and A_f are dimensionless constants controlling the slope and width of the fast nullcline, and τ_m [μ F] and τ_s [μ F] are fast and slow activation time constants (respectively), such that

$\tau_m < \tau_s$.

$$q_\infty(V) = \begin{cases} \sigma_{in}(V - E_s), & \text{for } V < E_s \\ \sigma_{out}(V - E_s), & \text{for } V \geq E_s \end{cases} \quad (2.27)$$

σ_{in} and σ_{out} are the inward and outward conductances (respectively), and $\sigma_{in} < \sigma_{out}$.

$$I_{syn} = W \cdot F_{syn}(V_{pre})(V - E_{post}) \quad (2.28)$$

$$F_{syn}(V) = \frac{1}{e^{-\gamma(V-\theta)}} \quad (2.29)$$

where V is post-synaptic potential, V_{pre} is pre-synaptic membrane potential, W is the maximum postsynaptic conductance and E_{post} is synaptic reversal potential. θ is the synaptic threshold and θ is a rate constant.

$$F_{fast}(V, \sigma_f) = \begin{cases} V + A_f, & \text{for } V < -\frac{A_f}{\sigma_f} \\ V - A_f, & \text{for } V > \frac{A_f}{\sigma_f} \\ (1 - \sigma_f)V, & \text{otherwise} \end{cases} \quad (2.30)$$

$$F_{syn}(V, \sigma_f) = \begin{cases} 1, & \text{for } \theta \geq \theta_{ij} \\ 0, & \text{for } \theta < \theta_{ij} \end{cases} \quad (2.31)$$

where θ_{ij} is the synaptic threshold between the presynaptic neuron i and post-synaptic neuron j .

2.3 *C. elegans*

C. elegans is a 1mm nematode that naturally lives in moist environments such as soil and rotten vegetation and feeds primarily on bacteria. It was first studied in the 1940s and later in the 1960 it was selected as a model organism by Sydney Brenner. Since then it has been the subject of research into the genetics and molecular basis of embryonic development and ageing, and in particular neurodevelopment and its connection to the behaviour of the animal [34]. *C. elegans* is one of the smallest multicellular model organisms, making it a powerful research tool that is anatomically and functionally compact with little redundancy. This makes it easier to understand the role of specific molecular and cellular components in the context of the whole animal. Its large brood size (~ 300) and short generation time (3-4 days) make it suitable for high throughput studies [33, 34].

The cell lineage and anatomy of the adult, wild-type *C. elegans* have been fully mapped, including its connectome [35, 37, 42], although synaptic identity is not yet fully mapped, and intrinsic single-cell neural dynamics are still largely missing. This makes it possible to target individual cells and study their role at a whole system level. This includes genetic and laser ablation of specific cells, fluorescent tagging of cells and calcium imaging of specific neurons and muscles used to associate their function with the behaviour of freely-moving animals [34, 192, 193].

Locomotion is one of most studied behaviours in the worm, as its undulatory motion provides a clearly visible behavioural output and a direct link to neuromuscular activity. The locomotion of the worm consists of forward and backward locomotion and various manoeuvres. These are often used to study neuronal mechanisms for pattern generation that are likely to be implicated in the nervous system of other organisms. While the role and connectivity of many cells have been identified, the intrinsic dynamics of individual neurons is still largely missing, partly due to the difficulty to record from small cells. Despite the vast accumulation of knowledge regarding *C. elegans* locomotion, some basic questions regarding the mechanisms for pattern generation remain open. In particular, the mechanisms that underlie pattern generation during forward locomotion are still unclear. This includes the contribution of central pattern generators (CPG) located in specific body regions, intrinsically oscillating neurons, and the molecular and cellular mechanisms that mediate mechanosensory feedback that leads to gait modulation [72].

Biomechanics and fluid dynamics

The ability of *C. elegans* to generate thrust largely depends on the geometry and mechanical properties of its body, as well the properties of the external material it is pushing against [60, 73, 74, 194–199]. Given its small size and speed, *C. elegans* locomotion can be modelled using low Reynolds numbers physics (laminar regime), where viscous forces dominate and inertial forces can be neglected [73, 74, 195, 199]. In this regime, we can define the environmental forces that resist the worm’s motion for both Newtonian and viscoelastic fluids [73, 74, 196, 199]. For motion in the dorsoventral plane, two drag coefficients are defined, C_t and C_n , that describe the resistance of the environment to the worm’s motion in the tangential and normal directions, both in the dorsoventral plane (Eq. 2.5-2.8) [73, 74, 113, 196, 199].

The mechanical properties of undulatory swimmers are often described in terms of the elastic and viscous properties of their body. The Young’s modulus (also called tensile modulus) describes the resistance of a material to deformation along its long axis, and is defined as the ratio between stress and strain. For a cylinder, often used as an approximation for the worm’s body geometry, the Young’s modulus describes its resistance to compression and stretching along the cylinder’s main axis. The bending modulus is defined as the product between the Young’s modulus and the moment of inertia of the cross section of the cylinder. Different methods and models have been used to estimate *C. elegans* material properties, resulting in values ranging from 3kPa to 380MPa for the Young’s modulus [194, 196, 198], and $4.2 \cdot 10^{16}$ - $9.5 \cdot 10^{14}$ Nm² for the bending modulus [74, 195]. Tissue viscosity on the other hand describes the damping of the body in response to bending, and was estimated at -860Ps·s [195]. Note that most of these estimations are based on the assumption that *C. elegans* body is homogeneous. However, the stiffness of the worm varies along its body, and may also vary across behaviours due to differences in muscle tone. In particular, the body region anterior to the vulva was found to be significantly stiffer compared the region posterior to it, while stiffness within each region was approximately uniform [198].

C. elegans moves forward by propagating a wave of curvature from head to tail. This is achieved via the contraction and relaxation of body wall muscles (BWM) that allow *C. elegans* to change the shape of its cylindrical body through their attachment to the cuticle [56, 57]. 95 BWM cells are arranged in four longitudinal quadrants, where three quadrants (DL,DR,VR) consist of 24 BWM cells and one (VL) consists of 23 BWM cells [57]. Neighbouring BWM are electrically coupled via gap junctions, both within each

quadrant, and across neighbouring left-right quadrants on the dorsal and ventral sides (but never between dorsal and ventral quadrants) [57]. Each BWM cell consists of a contractile filament, a non-contractile body that contains the nucleus and cytoplasm, and muscle arms that extend from the soma to form neuromuscular junctions (NMJ) with motor neurons in the nerve ring or in the dorsal/ventral cords [54, 200]. BWM cells in *C. elegans* are obliquely striated, with their filaments aligned with the longitudinal axis of the cell with a slight offset ($\sim 1\mu\text{m}$) between neighbouring filaments [201]. The oblique organisation is thought to allow the force generated by the muscles to be more evenly distributed and thus allow for smoother motion [202]. Finally, each BWM cell is basally attached to the hypodermis and cuticle, and laterally to neighbouring muscle cells [54].

The excitation-contraction coupling (ECC) is the process through which depolarisation leads to cell deformation [57]. In *C. elegans*, excitation at the NMJ by cholinergic motor neurons triggers an action potential in the soma in a graded manner, meaning that depolarisation amplitude correlates with input intensity, as opposed to an all-or-none response [57, 203, 204]. This results from the opening of nicotinic acetylcholine receptors in the muscle arm, that trigger a response which propagates to the contractile unit of the muscle [57]. This response is thought to be mediated by voltage-gated Ca^{2+} channels, as there are no voltage-gated Na^+ channels in *C. elegans* [205–207]. Evidence from electron microscopy (EM) indicate that excitatory cholinergic motoneurons form dyadic synapses onto BWM cells and GABAergic motoneurons, while inhibitory GABAergic motoneurons form monadic synapses onto BWM cells [208].

Forward locomotion

When placed on a planar surface of 2% agar, the worm spends most of its time crawling forward through sinusoidal-like body undulations in the dorsoventral plane that propagate from head to tail [75, 80]. Two modes of undulation frequency are associated with forward crawling ($\sim 0.2\text{Hz}$ and $\sim 0.5\text{Hz}$), and frequency is positively correlated with forward speed ($\sim 0.1\text{mm} \cdot \text{s}^{-1}$ and $\sim 0.3\text{mm} \cdot \text{s}^{-1}$) [209]. During forward crawling the nose undulates much faster (at 4.5Hz ; this is called foraging) [21, 80, 210, 211]. The worm also reverses through dorsoventral sinusoidal undulations that propagate from tail to head [62, 75, 80], during which foraging is inhibited [212]. Similar to forward crawling, two modes of undulation frequency are observed in backward crawling, and frequency is positively correlated with backward speed [209]. Post-reversal, the worm either moves forward again or performs a turning manoeuvre to reorient its direction of motion (the most

common ones are pirouettes and omega turns) [61, 62]. The worm can also reorient itself on a larger time-scale in order to improve its conditions, for example while following a chemical, thermal or aerial gradient. It does that by gradually changing its direction of motion through small and consistent adjustments to its sinusoidal undulations, a navigation strategy called klinotaxis [62, 213].

When placed in a water-like environment, the worm swims forward and backward through sinusoidal-like dorsoventral undulations at a higher frequency and wavelength compared to crawling on 2% agar [73, 74, 80, 212, 214]. While two modes of undulation frequency were also observed in backward swimming, during forward swimming only the higher frequency mode is observed ($\sim 1.8\text{Hz}$) [209].

The differences between crawling and swimming raise questions regarding the role of the environment in locomotion. In particular, whether crawling and swimming are two distinct motor programs that the worm switches between depending on external conditions and internal state, or whether they are opposite extremes of a single motor program. The answer to this question has consequences regarding the underlying neural control of these behaviours, as the switch hypothesis implies two distinct neural programs (analogous to forward and backward locomotion), while the single gait hypothesis suggests modulation of a single neural program. To test this, forward locomotion was recorded within a range of viscoelasticity from water-like environments to stiff agar. These experiments showed clearly that gradually increasing medium viscoelasticity (and thus increasing the mechanical load on the body) results in gradual modulation of the frequency, wavelength and amplitude of body undulations, with swimming and crawling at the extremes [73, 74]. This suggests that the swimming and crawling are part of the same motor gait that is modulated by the environment. It was also shown that during both crawling and swimming the frequency of muscle activation matches the frequency of body bending, confirming that modulation is achieved at the level of muscle activity, rather than only in body shape [214]. This means that in addition to the mechanical constraints of the external material on the body, mechanosensory information is fed back to modulate muscular activity. In addition, stretch receptors were suggested to be expressed along undifferentiated dendrites of ventral cord motor neurons implicated in the forward and backward locomotion neural circuits [37], adding to the evidence that sensory feedback plays a role in the adaptation of locomotion through the modulation of neuromuscular activity.

Of the 302 neurons in the nervous system of the hermaphrodite, 113 are motor neurons that form neuromuscular junctions (NMJ) onto body wall muscles. Of these, 38 innervate head muscles, whereas the

other 75 are organised along the ventral nerve cord (VNC) and form NMJs onto muscles posterior to the head. VNC motor neurons are conventionally divided into 8 classes, DA, VA, DB, VB, DD, VD, VC and AS (where D or V in the first letter indicate that they innervate dorsal or ventral muscles, respectively). A-type (DA and VA) and B-type (DB and VB) are cholinergic and depolarise muscles, causing them to contract, whereas D-type neurons (DD and VD) are GABAergic and inhibitory to muscles, as well as to the A-type and B-type neurons. [37, 215]. Interestingly, the pattern of muscle innervation of all 75 VNC motor neurons is left-right symmetrical, which suggests that feedforward pattern generation posterior to the head is restricted to the dorsoventral plane [37, 86]

Genetic and laser ablation of VNC motor neurons led to the association of specific motor neuron classes with specific motor behaviours. The B-type neurons were shown to be necessary for forward locomotion, whereas the A-type are necessary for backward locomotion [37, 75, 87]. The D-type neurons are necessary for coordinated locomotion in both the forward and backward directions [75, 216]. The forward and backward locomotion motor circuits are associated with command interneurons that control gait selection and activation, mostly via gap junctions that couple them to their respective motor neurons. The AVB and PVC command neurons activate the B-type neurons and control forward locomotion, while AVA, AVD and AVE activate A-type neurons and control backward locomotion [62, 75, 87, 88, 217, 218]. Gap junctions also couple neighbouring B-type and A-type neurons within each class, and were shown to be necessary for coordinated forward and backward locomotion [79, 88, 219]. Specifically, the innexins UNC-7 and UNC-9 are expressed by forward and backward motor neurons and interneurons in the locomotion circuits, and were shown to underlie gait selection by establishing dominance of forward over backward, as well as the overall bias for forward locomotion [88]. Interestingly, specifically the electrical coupling in the backward locomotion circuit (AVA-A) was found to be necessary for forward locomotion gait selection, through the reduction of AVA activity [88].

Evidence from electron microscopy show that B-type neurons send dendritic processes posteriorly that do not form any synapses. The same was observed for A-type neurons, but with opposite directionality [37]. Thus, these processes were suggested to be proprioceptive [37]. While a direct evidence of a proprioceptive function in these neurons has not been reported yet, ventral B-type and A-type motor neurons were found to express UNC-8 and DEL-1, members of the DEG/ENaC family and candidate subunits of a mechanically-

gated Na⁺ ion channel, and are also expressed in sensory neurons (with DEL-1 exclusively expressed in VB, VA and the mechanosensory neuron FLP) [220]. Many of the members of the DEG/ENaC family were shown to play a role in mechanotransduction [221], and *unc-8* mutants show uncoordinated locomotion [220]. In addition, evidence from optogenetic activation and inhibition of muscles or B-type motor neurons at different location along the worm's body, show that all body regions are capable of pattern generation even without propagation of undulations from other body regions, and that their undulation frequency can be entrained by changing the frequency of other body regions [222]. This further supports the hypothesis that pattern generation is distributed and adaptive.

The role of inhibition in locomotion

Inhibition plays many important roles in human and animal behaviour including gait selection and antisynchrony required for pattern generation in many motor systems [223, 224]. Inhibition is dominantly mediated by the GABA (gamma-Aminobutyric acid) neurotransmitter, although GABA can also be excitatory [225]. In particular, inhibition has an important role in *C. elegans* locomotion [72, 216, 226].

The GABAergic D-type motor neurons have been implicated in the forward and backward locomotion circuit. Ventral and dorsal D-type counterparts (DD and VD, respectively) form reciprocal inhibition and send inhibitory synapses to body wall muscles on the opposite dorsoventral side. VD are different from DD in that they send inhibitory synapses to their neighbouring VB neurons, a connection that is absent on the dorsal side (Fig. 23A) [37]. Overall, D-type neurons act to promote antiphase muscle contractions [209, 216]. GABA mutants move at lower speed and frequency during both forward and backward crawling. A similar result was obtained in animals in which GABA was inactivated optogenetically, during both crawling and swimming. Inhibition specifically from D-type neurons was shown to be more important during high-frequency undulations (such as in swimming). The inhibition of muscles helps promote antiphase muscle activation, and the neural inhibition from VD to VB was suggested to act as a reset mechanism during high-frequency undulations, where B-type neurons must activate and deactivate faster [209].

Inhibition is also dominant in the head motor circuit. Extensive reciprocal inhibitory connections are formed within the SMD and RMD motor circuits, mediated by acetylcholine (ACh) [37, 68, 227]. The GABAergic RME motor neurons were shown to modulate head bending amplitude during forward locomotion

through the inhibition of SMD and body wall muscles [167, 226]. Finally, the SMB head motor neurons control the amplitude of head bending, and their ablation results in a “loopy” forward locomotion phenotype [62, 64, 228].

Single-cell and circuit-level neural dynamics

So far there has been no evidence for all-or-none action potentials in *C. elegans* neurons. Instead, many neurons were found to have a graded response [70, 205, 229]. This may be partly due to the relative small cell size of *C. elegans* neurons that limits the number of ion channels responsible for depolarising currents, resulting in high electrical resistivity of the membrane [205]. Other responses and dynamics have also been observed in *C. elegans* neurons. The RMD head motor neurons were found to have plateau potentials, with two stable membrane potentials and a non-linear, graded response [70]. The AWA chemosensory neurons were found to fire Ca^{2+} -dependent action potentials in their depolarised state, also in a graded manner [230].

The neurons in the nervous system of *C. elegans* are conventionally categorised hierarchically, and information flow is often described as a feedforward sequential process, from sensory neurons to interneurons to motor neurons to muscles that generate the behavioural output. However, this hierarchy is often violated, as neurons in *C. elegans* play multiple roles and information flows in all directions [37, 86, 231]. Examples include proprioceptive motor neurons (e.g., SMD) [232], sensory neurons that form NMJs (e.g., IL1) [37], and interneurons that feed information back to sensory neurons (e.g., RIM) [233].

For example, food deprivation increases the worm’s tolerance for threats, pushing it to take more risk while seeking food. The RIM neuron was shown to integrate multisensory information, determine a “threat-reward” state, and output a decision to the motor circuit. The “threat-reward” state depends on food availability and the presence of repellents (such as hyperosmolarity). In addition to this feedforward information processing, RIM was found to send positive feedback to the osmosensory neurons ASH extrasynaptically, through the secretion of tyramine, on a time scale of minutes. One hour of food deprivation results in the inhibition of RIM, and in particular the inhibition of the positive feedback to ASH. This decreases ASH activity and thus increases its sensitivity to hyperosmolarity, making the worm more sensitive to threats and pushing it to take less risk [233]. Overall, this example shows that information flow in *C. elegans* is not restricted to a certain feedforward hierarchy, and that biological systems use feedback mechanisms to modulate their

sensitivity to stimuli, internal states and motor behaviour.

Gap junctions

Most gap junctions appear early in *C. elegans* development, and are known to contribute to key developmental processes, and neurodevelopment in particular. One example is the functional specification of the two chemosensory AWC neurons. AWC do not form mutual gap junctions in the adult animal, but during development they form a transient network of gap junctions with each other and with neighbouring sensory neurons. This promotes an asymmetric specification, where one adopts the ON-function (depolarises in response to certain stimuli), and the other adopts the OFF-function (depolarises in response to the removal of certain stimuli) [234].

The formation of a gap junction is the result of a complex made of two hemichannels, each expressed by one of the paired cells. Each hemichannel is an hexameric complex of innexins (similar in structure, but not in sequence, to connexins in vertebrates). The types of innexins in each hemichannel largely determine the conductance of the junction [235]. The coupling coefficient (CC) is commonly used as a measure for the strength of electrical coupling, defined as the ratio between the membrane potentials of the two coupled cells following a hyperpolarising current injection to one of them (and thus can be calculated for each direction of the junction separately) [236]. The electrical properties of gap junctions are regulated in various ways. First, structural asymmetry between the two hemichannels can lead to asymmetry in conductance in opposite directions [235]. Intracellular pH and Ca^{2+} levels have also been shown to regulate gap junction conductance [236]. In addition, in some cases phosphorylation of the hemichannels regulates the conductance, open probability, assembly and trafficking of the junction [236]. Finally, asymmetry in gap junction conductance may also be the result of different conductances of the cells themselves, even in the case of a homomeric junction [236].

Voltage-clamp recordings from pairs of coupled cells were done to characterise gap junction dynamics in *C. elegans*. Specifically different combinations of UNC-7 and UNC-9 hemichannel isoforms were tested, as they are expressed in many motor neurons and body wall muscles [71, 237, 238]. First, the membrane potential of both cells was clamped to the same value. Then, a voltage step was applied to one of the cells while recording current from the other. This was done for different values within a wide range of

membrane potentials (typically within -100mV and +100mV). Gap junction dynamics was found to be most dominantly dependent on membrane potential difference between the coupled cells, rather than their absolute membrane potentials. Further, following a voltage step, the current flowing through the channel drops exponentially and plateaus after approximately 5 seconds, with higher drop rates for larger potentials. The drop rate also depends on the combination of hemichannels, and is sometimes asymmetric for negative and positive potentials. The initial current following a voltage step was found to be approximately proportional to gap junction potential (meaning that gap junction conductance is constant), and at steady state the current-voltage relationship is a bell-shaped function (that may be asymmetrical depending on hemichannel combination), meaning that channel conductance plateaus above/below some positive/negative potential threshold [71, 237, 238].

Neuromechanical modelling of locomotion

Hypothesis-driven computational models have been developed to address mechanistic questions regarding pattern generation underlying *C. elegans* locomotion. Such models can be simulated computationally and are used to make predictions that can then be tested in-vivo [27, 30, 31, 239]. Some models focus on the mechanics of the worm and its environment, and only contain biologically-grounded details about its geometry and material properties, using simplified control to drive the body. Other models focus on the neural control of muscle actuation, with different levels of abstraction of body anatomy and mechanics.

The level of abstraction of different model components is chosen with respect to the hypothesis. A model should be designed to be the simplest possible with respect to its driving hypothesis. Making the model redundantly more realistic and detailed, reduces its explanatory power and makes its predictions harder to test and interpret. On the other hand, oversimplification reduces the model's generality and its ability to capture phenomena across a range of parameters. Finally, regardless of the level of abstraction, in order to make biologically-relevant predictions, the model must be constrained by existing knowledge and experimental findings.

For example, including neuromechanical feedback in the model might be necessary to capture postural dynamics across a range of viscoelasticity of the external material. However, including details about the dynamics of the underlying mechanosensory ion channels will make the model more complicated and might

not improve its predictive power with regard to postural dynamics. Finally, the magnitude of the effect of neuromechanical feedback on neural activity, and whether it is inhibitory or excitatory, may be constrained by experimental measurements.

Niebur and Erdős published the first computational implementation of a model of forward locomotion in *C. elegans*. The model focuses on body mechanics, and uses a sine wave activation at the head to drive the body forward, meaning that the presence of a central pattern generator (CPG) in the head is assumed, but the propagation of this pattern posteriorly is mediated locally via depolarising stretch receptors, located at fifth body length posterior to the muscles they control. Simulations of the model were shown to generate head undulations that propagate along the body. To generate forward thrust, the model requires a minimal stiffness of the environment [27].

Bryden and Cohen developed a biologically-grounded neuromuscular model of forward locomotion with mechanosensory feedback. They modelled the worm body as a sequence of pseudo-segments, each made of two 2D massless rods connected by a frictionless joint. A pair of dorsal and ventral muscle cells associated with each joint directly determine its bending angle. The muscles are controlled by a pair of dorsal and ventral excitatory B-type motor neurons. The activity of B-type neurons in the model is modulated by the bending angle along a short region posterior to their position (approximately 1/11 body length), in line with the hypothesised stretch receptors along their undifferentiated dendrites [37]. Finally, the AVB command interneurons provide all B-type neurons with depolarising currents via gap junctions. Simulations of the model with one, two and 11 segments (full body model) generate sustained oscillations without any CPG, but rather as a chain of reflexes with intersegmental phase lags entrained by mechanosensory feedback. Furthermore, oscillations were shown to be stable even in the presence of random perturbations, demonstrating robustness to noisy and unpredictable environments due to sensory feedback. In an extended version of the model, the neuromuscular circuit in each segment also includes a pair of GABAergic, inhibitory D-type neurons, where ventral (dorsal) D-type neurons are activated by dorsal (ventral) B-type neurons, and inhibit ventral (dorsal) muscles. Simulations suggest that D-type neurons increase bending amplitude but are not necessary for stable forward locomotion [240].

Berri et al. showed that forward locomotion is continuously modulated by the mechanical load of the environment on *C. elegans* body, and in particular that undulation frequency and wavelength correlate

with the viscoelasticity of the external material [73, 74]. Based on these results, Boyle et al. developed a mechanical framework that includes an articulated worm body and its environment, and used it to study the role of sensory feedback in forward locomotion. Following current-clamp recordings from individual RMD head motor neurons by [70], B-type and D-type motor neurons were modelled as bistable with hysteresis (i.e., the threshold for switching between the ON and OFF states is state-dependent). In the model, B-type neurons receive sensory feedback from stretch receptors along a region that extends half body length posterior to their position (or until the tail). The sensory input to B-type neurons is depolarising in response to local body stretch, and polarising in response to local body compression. The model predicts that a single neural control mechanism accounts for forward locomotion across a wide range of viscoelasticity of the external material, and in particular crawling and swimming in its extremes. In the model, this is achieved via mechanosensory feedback that modulates the activity of B-type motor neurons. The bistability and non-linearity of these neurons, together with sensory feedback from the shape of the body, ensures that contralateral muscles contract and relax in antiphase. In this work, the role of inhibition from D-type motor neurons was revisited following experimental evidence for an inhibitory connection from D-type to B-type neurons, but only on the ventral side [241]. In line with [240], the model predicts that inhibition from D-type neurons contributes to, but is not necessary for stable forward crawling. However, their inclusion in the model was necessary to achieve normal swimming. At low viscoelasticity media, in the absence of sufficient mechanical load and where the worm undulates at higher frequencies, D-type neurons “reset” neurons and muscles to their hyperpolarised state to maintain antiphasic contractions required for coordinated locomotion [30].

Izquierdo and Beer used the biomechanical framework developed in [30] and integrated a neural model of the head, in addition the neural circuit along the body that consists of B-type and D-type motor neurons. Their head model includes simplified RMD and SMD circuits, with SMD activity modulated by mechanosensory feedback from a posterior body region. B-type motor neurons also receive sensory feedback, but in contrast to [30], here their receptive field is an anterior, rather than posterior, body region relative to the muscles innervated by those neurons. In this work, rather than focus on a single mechanism for pattern generation, a systematic analysis was performed over a population of models using an evolutionary search algorithm to map the space of unknown parameters, under some experimentally-informed constraints. In particular, their neuron model can generate different intrinsic dynamics, and while RMD neurons were

constrained to the bistability regime, all other neurons were not. The analysis focused on forward crawling in a fixed, agar-like environment and the parameter space was narrowed to biologically-relevant models by matching worm speed and body bending to values obtained experimentally. The contribution of different model components to successful locomotion was then quantified, including sensory feedback, gap junctions and each of the neuron classes. They found that dorsoventral undulations can propagate from head to tail solely via sensory feedback, even in the absence of synaptic coupling of the head and body and electrical coupling between neighbouring VNC neurons. They also showed the extent to which undulations would propagate from the head posteriorly in the absence of all VNC motor neurons, demonstrating the contribution of body mechanics to locomotion [239].

Wen et al. used a microfluidic device to immobilise different regions of different lengths along the worm's body in order to test the role of proprioceptive coupling during forward locomotion. They found evidence that pattern generation during forward locomotion requires at least a $200\mu\text{m}$ neighbouring anterior body region that is free to bend. Furthermore, they showed that B-type motor neurons, and specifically their posteriorly oriented axons, are necessary for this proprioceptive coupling of neighbouring body regions, while the inhibitory D-type motor neurons are not. Based on their findings, they modelled body wavelength, taking into account the mechanical load on the body as a result of fluid viscosity. Simulations of their model produce a body wavelength that closely matches experimental measurements across a range of fluid viscosity [242].

Motor behaviour in 3D environments

Despite living in complex, non-planar environments, the study into *C. elegans* locomotion has been mostly limited to 2D, as worms are conventionally both cultivated and assayed on a planar agar surface [33]. Nevertheless, even in 2D environments, the worm exhibits some non-planar behaviours, including lifting of its head and burrowing into the gel, as well as body twisting in roller mutants in which the cuticle is deformed, resulting in the worm rolling around its long axis and crawling on the surface in circles.

The study of locomotion in 2D settings was a crucial simplification and has contributed immensely to our understanding of *C. elegans* locomotion and its underlying biomechanics and neural control. However, observing the worm in a volume might introduce new locomotion patterns, which may lead to the discovery of

new neuronal functions and control principles that are not manifested in 2D, as well as advance our knowledge of the material properties of *C. elegans* body and its interaction with the external material. Studying 3D locomotion introduces new challenges, including the hardware required for 3D recording, the computational tools needed to extract meaningful features from noisy volumetric data, and the mathematical framework needed to model and characterise the biomechanics of locomotion in three dimensions.

The motor circuit posterior to the neck that underlies forward and backward locomotion, including B-type, A-type and D-type neurons, forms left-right symmetrical neuromuscular junctions (NMJ) onto body wall muscles, suggesting that feedforward pattern generation along the body is limited to the dorsoventral plane [37, 86]. However, the head is not restricted in the same way. In particular, three classes of head motor neurons, RMD, SMD and SMB, each consists of four or six neurons connected via reciprocal inhibition, where each neuron forms NMJ dominantly onto a different muscle quadrant [37, 86]. Thus, these neurons provide the symmetry-breaking required for feedforward 3D pattern generation. SMD and SMB were shown to play a significant role in 2D forward locomotion, while the contribution of RMD neurons was minor [62, 64, 228, 232]. Interestingly, the SMD neurons express stretch receptors that are necessary for normal head bending during forward locomotion [232], whereas SMB is necessary for normal head bending angle [64, 228]. The synaptic connectivity within the RMD circuit suggests that it is biased towards left-right neural and muscular pattern generation, which may explain its minor contribution to 2D dorsoventral body bending [37, 86]. In addition, recordings from single-RMD cells showed that they are plateau potential neurons, with two stable membrane potentials and a graded response to input currents [70].

In recent years studies are beginning to address the locomotion of *C. elegans* in a volume. This includes the development of imaging systems suitable for capturing volumetric data [243–245], as well as the development of mathematical frameworks for describing and modelling the biomechanics of 3D locomotion [82, 246].

Kwon et al. developed a 3D imaging setup that records the worm from three orthogonal directions using two cameras. A set of mirrors is used to project two views onto one camera, and the third view onto the other camera. The recorded volume is made of a 1.5x1.5x1.25cm quartz cuvette, filled with 3% (w/v) gelatin and attached to a motorised stage used to track the worm in real-time. They recorded young-adult worms at 18°C, each for 3 minutes following a 30 minutes delay to let the animals settle. These recordings were used to compare locomotion parameters such as speed, undulation frequency and non-planarity, between

worms moving in a volume versus worms moving on a planar surface (between two glass slides filled with 3% (w/v) gelatin and separated by $100\mu\text{m}$). They found that worm postures in 3D are less planar compared to 2D, while speed and frequency were unchanged. They further tested mutants with head-related and mechanosensory-related defects, and found differences between mutants and wild-type, some of which were selective to locomotion in a volume (see more details in chapter 4) [244].

Shaw et al. developed a custom light-field microscope (LFM) to record *C. elegans* locomotion in a volume. By mounting an array of microlens on a camera connected to a wide field microscope, they were able to record a tiled array of circular microlens sub-images that contains both spatial and angular information. They used this system to record a 1.3mm^2 scene (maximum depth not specified) made of 0.25% w/v agarose gel in M9 on a microscope coverslip. They recorded wild-type and mutant young-adult worms for 30 seconds each, at 100 frames per seconds (although in their analysis they down-sampled this data to 20 frames per second). Using depth estimation methods, they were able to reconstruct 3D worm shape sequences and extract locomotion parameters such as speed, undulation frequency and non-planarity. They note that their method currently cannot be used to resolve and reconstruct self-occluding postures. First, they found that wild-type animals in a 3D environment of agarose gel are mostly planar. In a representative example, they showed that a posture sequence from a 30 seconds recording fits into a minimal bounding box with a depth of $110\mu\text{m}$ (which is only slightly more than the $80\mu\text{m}$ typical diameter of a young-adult worm [33]). They also compared locomotion in 3D of two mutants with cuticle defects and found that undulation frequency and non-planarity are significantly lower in *dpy-10* compared to *dpy-13*. Finally, they constructed a 3D shape-space of fundamental postures (also called eigenworms) using data from both wild-type and mutants, and used it to analyse postural dynamics in 3D. They showed that only four components from this shape-space are sufficient to account for 95% of the variance in their data [245]. They note that this result is similar to a previous analysis of 2D postures [247].

Bilbao et al. identified a 3D reorientation manoeuvre in data from [244], in which the worm rotates its plane of undulation by 90° , as well as its direction of forward motion. They used mathematical modelling and mechanical reasoning to suggest a mechanism for this behaviour. According to their model, this manoeuvre is accompanied by an internal twist that propagates from head to tail, and is necessary for achieving reorientation [82].

Ranner developed a biomechanical framework for modelling *C. elegans* in 3D environments [246]. In this model, which extends a 2D biomechanical model of *C. elegans* [31], the worm's body is represented as a continuous incompressible viscoelastic shell, and the parameterisation of the model allows to control the properties of the body and its interaction with the environment. Its formulation is based on resistive force theory (RFT) approximations (see section 2.1) and is thus suitable for studying undulatory motion in the low-Reynolds regime, in both Newtonian and viscoelastic fluids. It is also suited for integrating neural control in the animal's natural coordinate system, thus providing a framework for testing neuromuscular activation patterns in mechanical context in order to close the neuro-body-environment loop.

2.4 Summary and conclusions

Organisms manoeuvre through complex, non-homogeneous environments with changing geometrical and mechanical properties in order to sample their surrounding and move towards more favourable conditions. Thus, they must be able to adapt their behaviour for efficient locomotion which is crucial for their growth and survival. The evolution of form and function often converges across distant species. Organisms at different scales may evolve similar body shapes and motion patterns to locomote in similar environments, while their material properties and control mechanisms may be different. For example, locomotion in fluids is shared by organisms from the scale of micrometers to tons, and varies from Newtonian fluids such as water, to viscoelastic and granular fluids such as the bloodstream in the human body. While animal locomotion has been studied in depth across species, scales and environments, it has been mostly limited to planar settings or 2D projections. This may have limited our understanding of animal locomotion, as swimmers typically move in volumes rather than on surfaces in their natural habitats. Only in recent years 3D locomotion is beginning to be addressed, revealing new motion patterns used by organisms that move in a volume. This is crucial for uncovering both universal and organism-specific control principles of animal locomotion, under biomechanical constraints of the organism's body and its environment.

Unicellular organisms use molecular motors to generate directed motion within fluids, including biological tissues. *E. coli* is a $1\mu\text{m}$ long bacterium that produces approximately 10 flagella that are uniformly-distributed across the surface of the cell. *E. coli* has two main modes of locomotion - run and tumble. A run is achieved by counterclockwise (CCW) rotation of all flagella, which causes them to bundle and point

in the same direction, resulting in motion in a consistent direction. Tumbling on the other hand is achieved by clockwise (CW) rotation and sparse directionality of the flagella, resulting in rotation of the whole cell around its centre of mass [94, 248–250]. Sperm cells develop a single flagellum and use it to propel themselves towards the egg using chemical gradients. Receptors expressed on the surface of the flagellum are used to sense those chemical cues in order to modulate sperm locomotion [251, 252]. While the majority of sperm form planar head trajectories, some form helical trajectories. Both CW and CCW helices have been observed. Furthermore, during this motion the cell also rolls around its longitudinal axis (i.e., head-tail axis) [251]. For example, in human sperm suspended in human tubal fluid, only 5% of the cells form helical head trajectories, of which 90% are right-handed (CW). The radius of these trajectories range between $0.5\text{--}3\mu\text{m}$, with 3–20 rotations per seconds. While it is not yet clear whether helical trajectories are advantageous and whether all sperm cells are capable of generating them, they have been shown to be suppressed by higher concentrations of seminal plasma, higher viscosity, as well as by surface boundaries such as glass [253–255]. It was also found that even if head trajectories are planar within each period, they can form helical ribbons on a larger time-scale, while the sperm gradually reorients itself based on chemical cues [256, 257].

Multi-cellular organisms have more complex body geometries and evolved muscles, cells specialised in generating mechanical force, and motor neurons to control them. Spatial and temporal coordination of muscular contraction and relaxation can lead to periodic changes in the shape of the body, which pushes against an external material, and may result in the generation of thrust. Muscle cells are controlled by neurons via neuromuscular junctions (NMJ). The neural rhythms that arise from ensembles of neurons coupled via chemical and electrical synapses, give rise to muscular rhythms, which then give rise to periodic body bending. Bending is constrained by the body’s geometry and mechanics, as well the external material, and in many systems mechanosensory information is fed back to modulate muscular and/or neuronal dynamics [126, 136–141]. Feedback mechanisms provide animals with further control and allows them to adapt their locomotion across a range of environmental parameters.

In the context of the control of motor behaviour, one of the greatest challenges facing neuroscience has been to bridge the gap from neural dynamics to whole-animal behaviour. How do animals generate rhythmic motor patterns? How do they coordinate motion throughout their bodies under geometrical and mechanical constraints? What feedback and adaptation mechanisms are used to modulate, select and switch between

motor patterns? Answering these questions requires to study biological systems at multiple spatial and temporal scales, and in different mechanical contexts.

C. elegans is a 1mm long nematode that naturally lives in moist environments such as soil and rotten vegetation. Its anatomical simplicity with little redundancy, makes it a great model organism for multi-scale investigation which allows to study low-level components in the context of the whole animal. The body of *C. elegans* is cylindrical and tapered at the head and tail. 95 body wall muscle cells are arranged in four longitudinal quadrants and allow *C. elegans* to bend its body through their attachment to the cuticle (Fig. 1A-B) [56, 57]. On surfaces, *C. elegans* lies on its left or right side and moves forward by propagating a planar wave of antiphase dorsoventral muscle contractions from head to tail (Fig. 1C) [60]. Given its small size and speed, *C. elegans* locomotion can be described using low Re physics (laminar regime). This allows to model the worm's locomotion in both Newtonian and viscoelastic fluids using resistive force theory (RFT) [73, 74, 195, 199].

Neurons show great variation in intrinsic cell dynamics, both within nervous systems and across species. This includes phenomena such as action potentials, multi-stability, all-or-none activity, graded responses, frequency doubling, desensitisation and post-inhibitory rebound [65, 70, 121, 191, 258]. The characterisation of single-neuron dynamics is typically done using electrophysiological measurements where the cell is perturbed by various current injection patterns, while its membrane potential is recorded [69]. The intrinsic dynamics of individual neurons is largely missing in most species, and has only been characterised for a handful of neuronal classes. This is particularly true for *C. elegans* neurons, despite the accumulation of knowledge about other neuronal aspects such as neurotransmitter profiles and synaptic connectivity and polarity [37, 68, 226]. This limits our understanding of network dynamics and our ability to bridge the gap from neural activity to whole-animal behaviour.

One set of six interconnected motor neurons in the head of the worm, called RMD, has been characterised using current-clamp recordings. RMD were shown to have plateau potentials, with two stable membrane potentials, and a graded response to input current [70]. This is in sharp contrast to neurons that fire action potentials and respond to input current in an all-or-none manner, which are more common in other species and have been studied in much more depth [121, 169].

Mathematical models have been developed to capture single-cell neural dynamics observed in biological systems. Such models provide a formal framework for hypothesis testing and for directing experiments by generating predictions that can be tested in-vivo. While some models capture details about the underlying ionic species and currents [185], some only capture neural dynamics at the whole-cell level [188, 189]. Such models have been used to capture the dynamics of *C. elegans* neurons, and RMD in particular [30, 239, 259]. In the context of motor behaviour, constraining single-cell neural dynamics using experimental measurements, also constrains network dynamics and the patterns of muscle activation that they generate. Thus, it is crucial to narrow down the parameter space of the model to biologically-relevant rhythms.

To model circuit dynamics, individual neurons are coupled via chemical and electrical synapses, which also have their own complex dynamics [68, 71, 203, 227, 237, 238]. One of the simplest cases is a system of two reciprocally inhibiting neurons that give rise to rhythmic activity [121, 179, 191]. More complex cases include the modelling of whole motor circuits that underlie a specific function, such as swimming, heartbeat and gastric mill [30, 121, 190, 239]. Neural synchronisation mechanisms are used by animals to orchestrate pattern generating circuits throughout their bodies in order to generate coordinated locomotion [30, 130, 131, 179, 222, 260]. Some studies tested synchronisation in such systems by measuring the cross-correlation between circuit components in different regimes [179, 260–264]. In particular, some focused on the combined role of inhibition and electrical coupling in promoting synchronised neural activity, as this motif was observed in biological neural networks [265–269]. However, such studies mostly focused on neurons with all-or-none activity that fire action potentials. In *C. elegans*, the RMD motor neurons, which may underlie 3D head motions based on neuromuscular anatomy, have been shown to have plateau potentials and respond to input current in a graded manner [37, 70, 86]. In addition, the RMD circuit is coupled with another head motor circuit, SMD, via both inhibitory and electrical synapses, suggesting a role in neural synchronisation.

The locomotion of living organisms has been studied in depth across environments and scales, from single-cell organisms [94, 251], to microscopic nematodes [73, 209], to fish [123, 124, 134] and cockroaches [142, 143]. However, only recently studies have begun to address 3D locomotion in a volume [82, 244, 245, 255–257]. Studying locomotion in 3D is a difficult task compared to planar settings, due to both the hardware needed to record a volume in high spatial and temporal resolutions, as well as the computer vision software needed to extract meaningful information from volumetric data. Since swimmers usually

manoeuvre in 3D environments in their natural habitat, they must have evolved motor gaits for locomotion in such environments. Studying swimmers in 3D environments may lead to the discovery of such motor gaits, as well as their underlying neuromechanical control mechanisms, some of which might not have been manifested in planar settings. This in turn, may lead to the discovery of universal mechanisms for the control of animal locomotion under geometrical and mechanical constraints.

3 3D recording, calibration and reconstruction of *C. elegans* locomotion in a volume

In this chapter I introduce a novel system for 3D imaging of freely-moving *C. elegans* worms, and describe the computer vision and signal processing techniques developed for feature extraction and 3D locomotion analysis, respectively. The imaging setup consists of three approximately orthogonal cameras attached to telecentric lens, that record simultaneously at high spatial and temporal resolution with large depth of focus, required to capture the high-frequency, non-planar locomotion dynamics of microscopic worms. Prior to recording, the volume is calibrated using photogrammetry in order to map points in the 3D lab coordinate system to camera pixel space. Following recording, video files are processed through the computer vision pipeline that consists of deep learning and optimisation modules, which results in the extraction of worm shape sequences over time and their location and orientation in the volume. Finally, this data is processed through the signal processing pipeline to extract key features of postures and trajectories and obtain a quantitative characterisation of the worm's locomotion in a volume across a range to gelatin concentrations. An open-source, interactive tool was developed in MATLAB (MathWorks Inc.) to make the full pipeline accessible, and it can be used for different assays, other worm-like animals and imaging setups with a different number of cameras.

3.1 Introduction

Imaging of locomotion is widely used for studying animal behaviour across scales and environmental conditions, including in air, water, and on land [270–273], and is often combined with imaging of neuronal activity to study the neural control of locomotion [193, 274, 275]. While the temporal and spatial resolutions of image acquisition continue to improve, the combination of both remains a challenge and is crucial for capturing the precise shapes and behavioural dynamics of small and/or fast animals. Despite the fact that animals naturally move in non-homogeneous and non-planar environments, imaging of animal motor behaviour is often limited to 2D due to limitations of the optics and the difficulty to process and analyse volumetric data. This clearly biases our understanding of animal behaviour, which in turn limits our understanding of the underlying neuromechanical control mechanisms.

New technologies have emerged in recent years that allow us to capture high-resolution volumetric data with minimal damage to living samples, including spinning disk confocal microscopy (SDCM), light sheet microscopy (LSM), light field microscopy (LFM) and Wide-field multiphoton microscopy [25, 276–279]. For example, SDCM is an improvement of conventional confocal microscopy, often used to record neuronal morphology and dynamics by capturing sequential 2D sections. It allows to record $1\mu\text{m}$ -thick sections at up to 1000Hz [276]. LFM captures a whole 3D volume in a single shot, with temporal and spatial resolution up to 10Hz and $1\mu\text{m}$, respectively. It has been used to measure whole-brain activity in *C. elegans*, fruit fly, zebrafish and mice [25, 278].

Following imaging, there remains the challenge of extracting meaningful features from noisy image data and interpreting them. This includes the separation of signal from background noise and disambiguating features using spatial and temporal information. In recent years, deep convolutional neural networks (CNN) have gained popularity in computer vision for their multi-scale feature detection and their ability to generalise from a relatively low number of examples. Although they often require manual or semi-manual annotation of data, they remove the need for hand-crafted rules and can find complex correlations in data that humans often cannot [280, 281]. Such algorithms are particularly widely used for analysing 2D and 3D time series image data of animal behaviour [282, 283].

3.2 3D imaging of *C. elegans*

Despite *C. elegans* naturally living in complex 3D environments, to date it has mostly been observed in 2D settings while focusing on planar dorsoventral undulations. Nevertheless, even in 2D *C. elegans* exhibits complex motor behaviours and their study has significantly advanced our understanding of its underlying biomechanics and neural control mechanisms [18, 72].

In recent years, whole-brain imaging of freely-moving *C. elegans* worms has become possible, mostly due to advances in fluorescence SDCM, as well as two-photon and LFM [193, 245]. SDCM allows thin sectioning with acquisition rates up to 10 volumes per second, suitable for capturing both locomotion and neural dynamics of the typical 0.5-1Hz forward crawling gait of *C. elegans* [73, 214]. This allows to correlate single-neuron activity and whole-brain states to locomotion patterns in freely-moving animals [22, 24, 284].

Such techniques however are not yet suitable for studying higher frequency and/or non-planar gaits (e.g., swimming at 2Hz). This is due to the limitation in acquisition rate and because the z-sectioning requires worms to remain planar during imaging [73, 214].

C. elegans exhibits some non-planar behaviours even in planar settings, such as burrowing and head-lifting [80, 285–287], as well as body twisting in roller mutants in which the cuticle is deformed due to developmental defects, which results in rolling and crawling in circles on planar surfaces [83, 84]. Such phenotypes have been characterised using 2D imaging and by z-sectioning using electron microscopy (EM) and fluorescence confocal microscopy.

3D imaging of *C. elegans* in a volume introduces more behavioural complexity and requires more complex hardware, as well as computational tools for image analysis and feature extraction from volumetric data.

Kwon et al. developed an imaging system for recording *C. elegans* in a volume using two orthogonal cameras coupled to 3X telecentric lens, and a motorised stage for tracking individual worms [243]. They later upgraded this system to record from three orthogonal directions in order to be able to better resolve self-occluded postures [244]. To do this, they used an array of mirrors such that two orthogonal views are projected onto one camera, and the third view onto the second camera. This system was used to record freely-moving, wild-type, young-adult worms in 2.5-3% (w/v) gelatin in M9 within a quartz cuvette at 18°C. Each worm was recorded for 3 minutes following a 30 minutes delay to let it settle in the medium. For kinematic analysis they recorded a 5mm³ volume at 13Hz while tracking the worm in real-time, whereas for trajectory analysis they used lower magnification and acquisition rate (25mm³ at 0.5Hz) while the stage remained fixed.

Shaw et al. developed a custom light-field microscope (LFM) by mounting an array of microlens on a camera connected to a wide field microscope. This allowed them to capture a tiled array of circular microlens sub-images that contains both spatial and angular information. They used this system to record young-adult worms in 0.25% w/v agarose gel in M9 on a microscope coverslip. Each worm was recorded for 30 seconds at 100 frames per second with a field of view of 1.3mm² (maximum depth not specified). By combining this with depth estimation methods, they were able to reconstruct worm shapes over time and extract locomotion parameters such as speed and undulation frequency. However, they note that using their

current depth estimation method is not yet possible to resolve postures that are self-occluded in the camera’s focus plane [245].

In order to study *C. elegans* 3D locomotion and to accurately reconstruct its shape and position in a volume, I used a multi-camera imaging setup, designed and built by Robert Holbrook and Netta Cohen from our group (Fig. 3). In order to study the role of the environment in 3D locomotion, I recorded the worm within a range of gel viscoelasticity (1% – 4%, corresponding to $4 \leq G' \leq 600$ Pa [73]).

To accurately capture the worm’s shape over time, the space must be calibrated to account for camera distortion and to capture the relative position and orientation of the cameras. Thus, the space is calibrated at the beginning of each experiment, and the setup remains fixed during the experiment. We chose an orthogonal camera configuration, but since the space is calibrated, cameras do not have to be precisely orthogonal, and non-orthogonal camera configurations are also possible. The camera and lens specifications were chosen to maximise the field of view and depth of focus (1mm^2 and 1mm, respectively) as well as magnification (7X) and image resolution (see below), and are thus suitable for capturing long motion sequences and exploration behaviours. The volume is made of a 2x2x2cm coverslip container filled with gelatin. Importantly, the dimensions of the container are significantly larger than the worm (1mm) and the volume of view (1cm^3) in order to avoid wall effects.

The setup consists of three approximately orthogonal cameras (Ximea xIQ MQ042RG-CM), each connected to a 7X telecentric lens (Navitar Inc.). Each camera has a pixel size of $5\mu\text{m}$ and produces a 2048x2048 pixels image converted to a 4.2MB file. The telecentricity of the lens means that the trajectories of the photons are made close to parallel (here within a $\pm 0.4^\circ$ error), thus reducing the error in the perception of size and orientation, and increasing the depth of focus.

Recording was done using the StreamPix software (Norpix Inc.) in sequence format (.seq) that assigns a time stamp to each recorded frame. The cameras are connected to a computer through a trigger device that synchronises their acquisitions. The maximum acquisition rate of the cameras is 90Hz, but here it is limited to 40Hz, as at higher rates the synchrony of the cameras cannot be guaranteed. During the experiment the only source of light in the room is infrared backlight required for the cameras. I recorded hermaphrodite *C. elegans* worms in a range of gelatin concentrations (1% – 4%, corresponding to $4 \leq G' \leq 600$ Pa [73]).

The recorded volume is made of a 2x2x2cm coverslip container filled with molten gelatin in M9 (Fig. 3). Recordings were done at 25Hz, using 5X-7X magnification, a field of view of $\sim 1\text{cm}^3$, and a depth of focus of $\sim 1\text{cm}$. Here, the depth of focus refers to the maximum distance range from the lens within which the worm's shape appears sufficiently sharp to be resolved.

Figure 3: 3D imaging of *C. elegans* locomotion in a volume

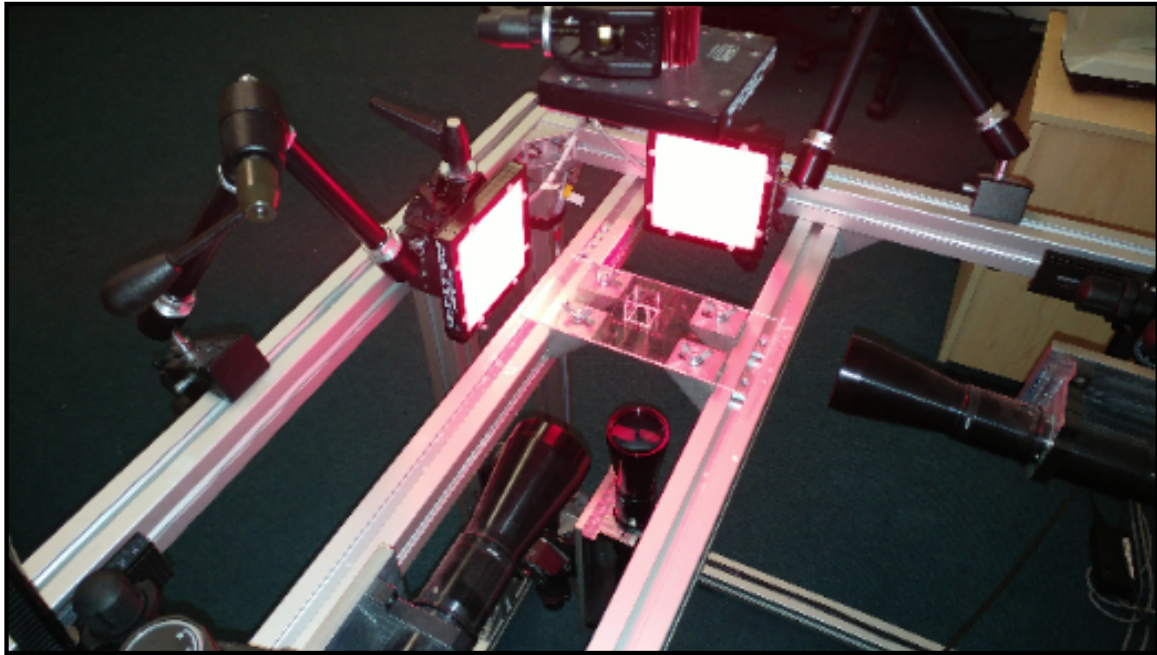


Figure 3. The imaging setup is made of three approximately orthogonal cameras, each attached to a telecentric lens with infrared lighting. A glass container is attached to the stage and filled with molten gelatin in M9 solution at the desired concentration. Once the gel sets, individual worms are placed within the gel and recorded while they are in the field of view and in focus in all cameras.

N2 *C. elegans* worms were grown at 20°C and maintained under standard conditions [33]. Worms were age-synchronised by placing 3-10 young-adult worms on a fresh NGM plate with $150\mu\text{l}$ OP50, and removing them after 24 hours, leaving only the eggs. The recording of worms started 48 hours later and lasted up to 8 hours. Thus, worms were within the young-adult to adult age range. A total of 8 hours of locomotion data was recorded. The total duration per gel concentration is summarised in Table 4. Prior to recording, the volume is calibrated using photogrammetry to solve for the lens distortion and camera geometry (Fig. 4A) [288]. To calibrate the volume, at the beginning of each experiment I took snapshots of a calibration slide in the molten gel, captured from all cameras simultaneously (Fig. 4B-C). This was used to obtain camera models that describe intrinsic and extrinsic camera properties (see section 3.3).

Figure 4: Camera calibration and imaging of *C. elegans* in a volume

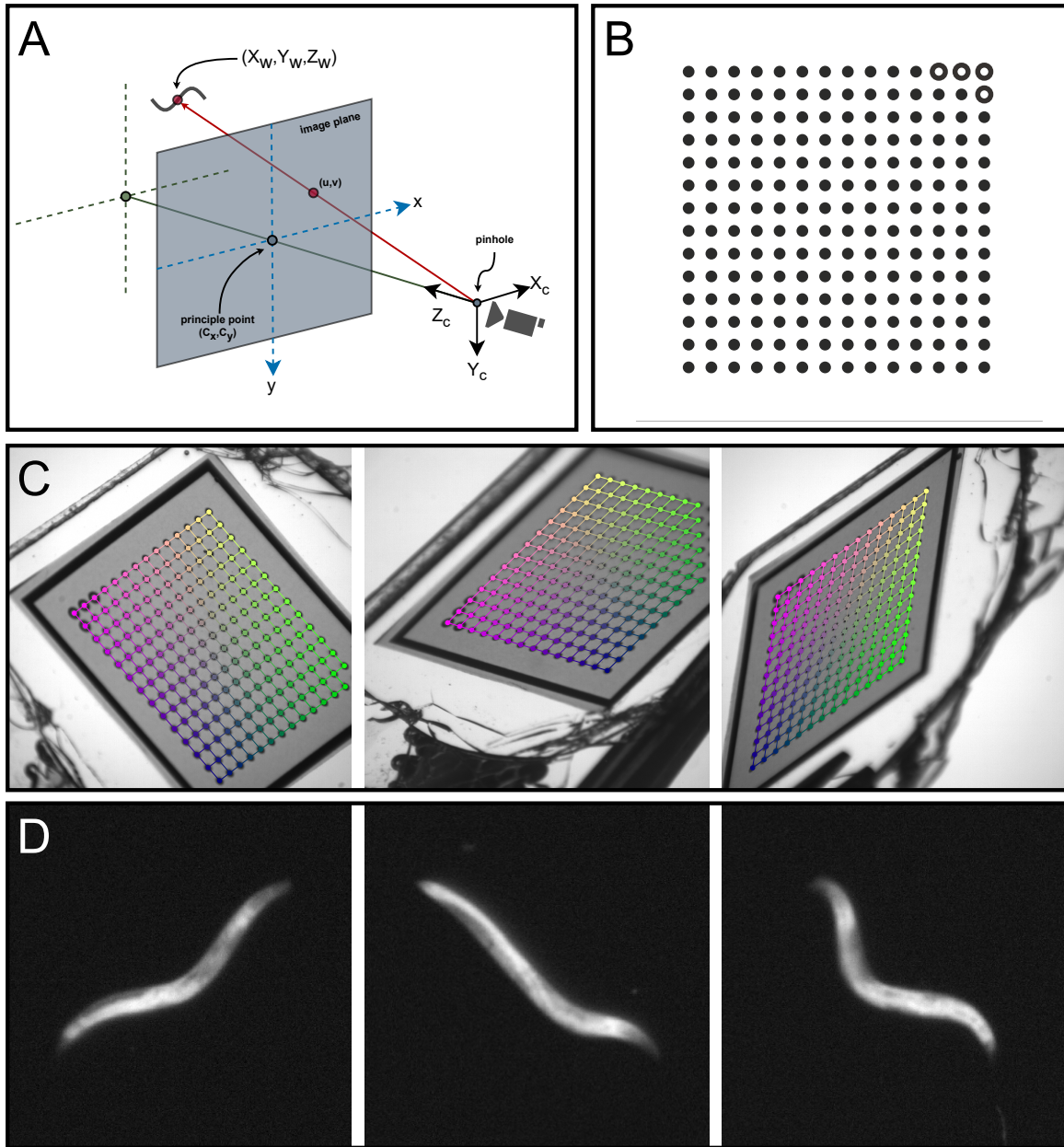
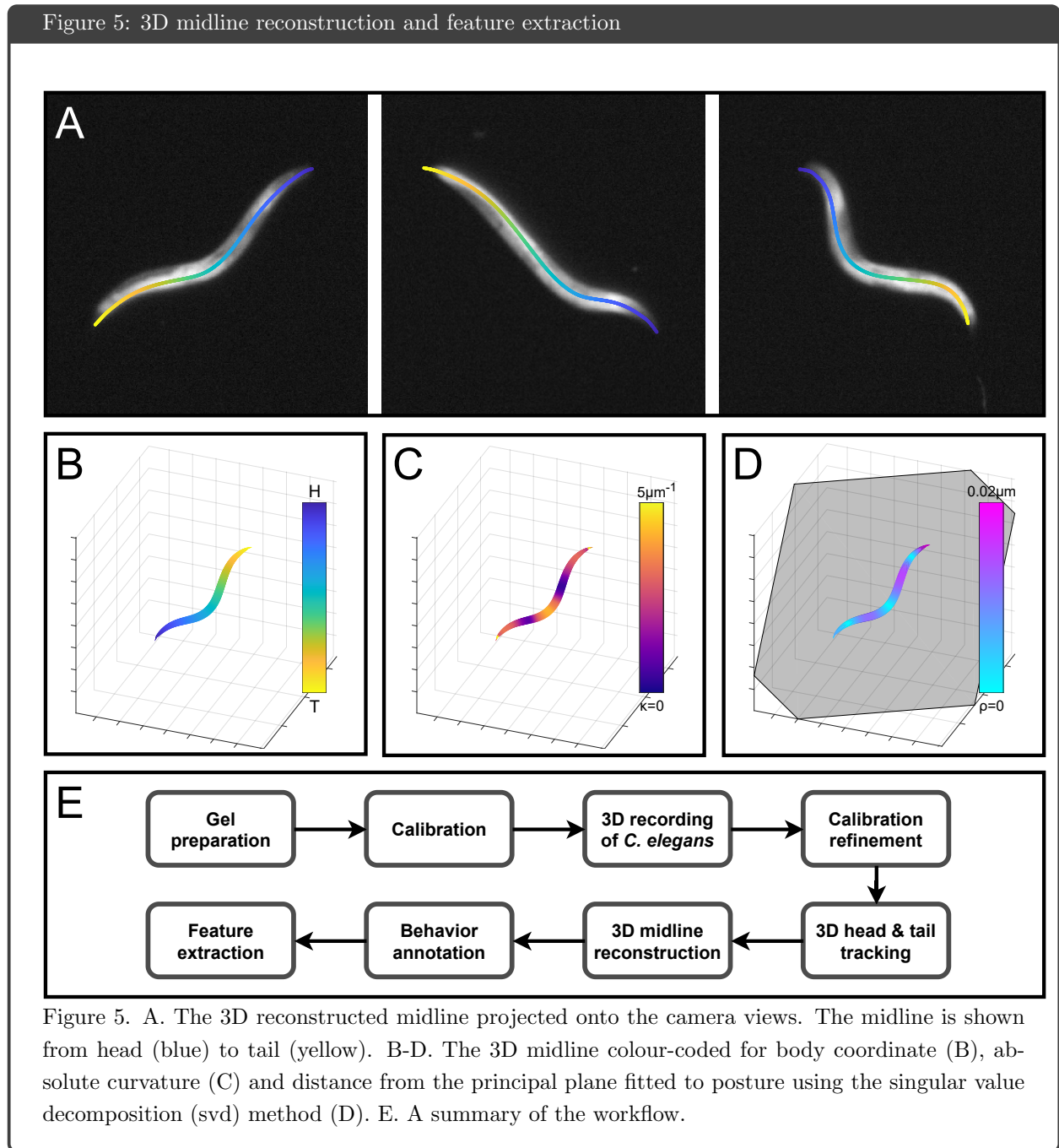


Figure 4. A. The pinhole camera model, describing the projection of a point in lab coordinates (X_w, Y_w, Z_w) onto the image plane (u, v) of a camera positioned at the origin of the lab coordinate system (X_c, Y_c, Z_c) with principal point (C_x, C_y) . B. An asymmetric grid pattern is used to calibrate the volume. C. Calibration is done by mapping corresponding grid points across cameras to 3D lab points. D. An example frame of a worm imaged by three cameras simultaneously.

After a standby period of three hours to let the gel set and reach room temperature, individual worms were picked using a platinum wire and placed inside the gel (Fig. 4D). The recording of a worm started after at least 30 seconds to let it settle, and continued as long as the worm was in the field of view and in focus

in all three cameras. Video duration ranged from 10 seconds to 20 minutes. Importantly, the setup must remain fixed throughout the experiment, as any change to the position of the cameras or the scene would require changes to the camera models. The complete imaging protocol is attached as supporting information. Once a recording of the worm is obtained, it is processed through the reconstruction and analysis pipeline. This includes the reconstruction of the worm's 3D posture in all frames, behavioural annotation and feature extraction (Fig. 5).



3.3 Camera calibration

In order to reconstruct the precise shape of the worm in the 3D lab coordinate system, the cameras must be calibrated. This means that for each camera we construct a model that describes its intrinsic and extrinsic properties, which contains information about the position and relative orientation of the cameras, as well as different types of distortion. This step is crucial for matching 3D points in lab space to their projection onto the cameras.

Here I used the pinhole camera model which describes the relationship between 3D points in the lab coordinate system and points projected onto the image plane [288]. The model approximates real pinhole camera models by assuming that their aperture is infinitely small, meaning that each point in the 3D scene is mapped to exactly one point in the image plane. In real cameras, the aperture has a finite size, and thus multiple light rays from a single 3D point are mapped to multiple points in the image plane, resulting in some blur.

The first step for obtaining the camera models is to sample the volume using a pattern of known shape and size. We use an asymmetric grid pattern that allows us to identify individual grid points uniquely from both sides of the grid (Fig. 4B). This is necessary to match projected points that correspond to the same point in 3D space. The grid pattern is printed on a thin photographic film (0.18mm thick) and glued between two coverslips (18x18x0.15mm) used to flatten the film. To sample the volume, we take approximately 250 snapshots of the calibration grid in different orientations from all cameras simultaneously (Fig. 4C). The large number of images is to ensure a large enough sample size, considering that the detection of the pattern in some images might fail due to poor image quality (e.g., out-of-focus, noise and sharp tilting angle).

Following the acquisition of the calibration images, the grid points are detected and indexed. Then, an indexed list of 3D coordinates from all calibration images is fed into an OpenCV 3D calibration toolbox, which was adjusted for our custom calibration pattern by Tom Ranner from our group [289]. This results in a model that describes the intrinsic and extrinsic (Eq. 3.1- 3.5) properties of each camera, and that can be

used to project 3D points in lab coordinates onto the camera views, and vice versa.

$$\mathbf{I} = \begin{pmatrix} f_x & 0 & C_x \\ 0 & f_y & C_y \\ 0 & 0 & 1 \end{pmatrix} \quad (3.1)$$

where f_x and f_y are focal length in x and y, and C_x and C_y are the x and y coordinates of the principle point.

$$\mathbf{E} = \begin{pmatrix} r_{1,1} & r_{1,2} & r_{1,3} & t_x \\ r_{1,1} & r_{1,2} & r_{1,3} & t_y \\ r_{1,1} & r_{1,2} & r_{1,3} & t_z \end{pmatrix} \quad (3.2)$$

where $r_{i,j}$ form the rotation matrix that projects 3D points onto the camera view, and t_i form the translation vector.

$$\mathbf{D} = (k_1, k_2, p_1, p_2, k_3) \quad (3.3)$$

$$x_{\text{distorted}} = x(1 + k_1r^2 + k_2r^4 + k_3r^6) + 2p_1xy + p_2(r^2 + 2x^2) \quad (3.4)$$

$$y_{\text{distorted}} = y(1 + k_1r^2 + k_2r^4 + k_3r^6) + p_1(r^2 + 2y^2) + 2p_2xy \quad (3.5)$$

where k_i and p_i are radial and tangential distortion coefficients, respectively. $x_{\text{distorted}}$ and $y_{\text{distorted}}$ are the distorted coordinate in the camera's coordinate system. The indices of the coefficients correspond the order of approximation. Higher-order approximations and other types of distortion exist, but are not considered in this work.

3.3.1 Detection and indexing of calibration grids

To obtain camera models using the calibration images, grid points must first be detected and indexed. This involves separating the grid points from the background of the image and finding their centre coordinates, followed by the the assignment of a unique index to each point consistently across all images and cameras. The high variability in contrast and focus across images, as well as noise and non-grid features, make it harder to formulate a general and robust set of rules for the detection of grid points. Moreover, since the

images contain a pattern projected from 3D, grid points appear elliptic rather circular and vary in their radii due to both tilting angle and distance from the camera. Examples of non-grid features include glue, glass cracks, dirt, the boundary of the film, and the tweezers used to hold the slide during image acquisition (Fig. 6A, yellow arrows in the top row).

Here, I used a convolutional neural network (CNN) to label grid pixels in noisy calibration images using a combination of synthetic and experimental examples (Fig. 6A, top row). This allows to capture and generalise complex relationships between image features without the need for hand-crafted rules. The architecture of the CNN is based on SegNet that was designed for semantic segmentation problems with a small number of examples [281]. The last layer of the network is a pixel classification layer that uses the cross-entropy loss function to classify pixels into the pre-defined classes (Table 1). For our specific grid pattern, I defined three feature classes: solid grid points, hollow grid points, and background (Figs. 4B and 6A, middle row).

Synthetic training samples were generated by augmenting a model grid image (Fig. 4B). Augmentation included 3D rotations, size scaling, translation, blurring and random image enhancement (Table 1 and Fig. 6A, top row, leftmost panel). Experimental samples were generated using a custom binarisation and labelling algorithm, and were augmented using 2D rotation, translation, mirroring and size scaling (Table 1 and Fig. 6A, top row, column 2-6). Importantly, the parameters in this custom labelling algorithm had to be manually adjusted for different images. This stresses the need for a more general and robust solution that does not require manual parameterisation.

While the synthetic dataset is useful for generalising for grid size, position, orientation and blurriness, the experimental dataset is necessary to calibrate the CNN model for setup-specific features that are difficult to generate synthetically (Fig. 6A, top row). Here, a total of 1085 samples was used to train the CNN. Of these, 500 were synthetic samples generated by augmenting the model grid, and 585 are experimental images, generated by augmenting 39 labelled images. 20% of the dataset was used as a validation set and the rest was used for training.

The CNN was trained to label pixels of grayscale images as solid grid points, hollow grid points, or background (Fig. 6A, middle row). Importantly, classes were weighed unevenly to account for the imbalance in pixel frequency across classes, as the full pattern contains 192 solid points, only 4 hollow points, and a

significantly higher number of background pixels (Fig. 6A, middle row and Table 1).

The CNN successfully labelled synthetic and experimental images from the validation set, as well as experimental images taken from experiments that were not included in the training and validation sets. Importantly, the CNN labelled pixels such that points are more likely to be separable, and deals well with high blurriness, sharp angles and non-grid objects in the image (Fig. 6A, middle row).

	Parameter name	Value
Dataset	Original image size	2048x2048px
	Size of input images	1024x1024px
	Number of synthetic samples	500
	Number of labelled experimental images	39
	Number of experimental samples (augmented)	585
	Random translation upper bound	600px
	Random 3D rotation upper bound	70°
	Random size scaling upper bound	10%
	Blur length and angle upper bounds	[10px,360°]
	Random background enhancement range (8-bit)	[50,150]
Standard deviation of random Gaussian noise	0.01±0.001	
Network	Number of filters	64
	Filter size	3
	Encoder depth	3
	Number of convolution layers (per encoder)	2
	Loss function	cross-entropy
Training	Solver	adam
	Class weights (solid, hollow, background)	[14,340,1]
	Number of epochs	100
	Mini batch size	256
	Initial learning rate	0.001
	Learning drop rate	0.5
	Learning rate drop period	10 iterations
	Dropout probability	0.8
	L2 regularisation	0.0001
Test set ratio	0.2	

Table 1. Parameters for setting up and training a convolutional neural network for labelling calibration images. Image blurring was applied using the MATLAB function “fspecial” with the parameter “motion”. Noise was added using the MATLAB function “imnoise” with the parameter “gaussian”.

Following the detection and classification of grid points, they are indexed using a custom algorithm that I developed, based on our grid model and guided by the hollow grid points (Fig. 6A, bottom row). Only images in which exactly four hollow points were detected are indexed, otherwise, the image is excluded from further analysis. In cases where some grid points are missing, the indexing algorithm skips them without affecting the indexing of other points (Fig. 6A, see yellow arrows in the bottom row).

Finally, the indexed list of grid point coordinates is used to obtain camera model parameters using an external OpenCV library, adjusted to our custom model grid by Tom Ranner from our group (the source code is available as supporting information) [289].

3.3.2 Camera model refinement

Since calibration images are taken in the molten gel, but worms are recorded only once it has set, changes in the structure of the material might cause a discrepancy between the camera models and the actual scene, resulting in a larger error when mapping 3D points to 2D points across cameras. Optical changes to the properties of gelatin may be due to changes in the refractive index of the material during cooling and polymerisation [290]. Indeed I found that for a given set of camera models, the error for worm points is often larger compared to the error of the calibration grids (Fig. 6B). Bundle adjustment methods are commonly used to refine camera model parameters by using features in the image to minimise the calibration error [288, 291, 292].

Given the unique features of our problem, I developed a custom bundle adjustment algorithm that uses worm points to refine extrinsic camera model parameters. The algorithm uses points from 2D midline annotations from multiple frames to refine the camera position and orientation by minimising the distance between the projection of 3D triangulated midlines and their corresponding annotations. Importantly, although all worm points from all midlines are used simultaneously to refine the camera model, each 3D midline is paired with its corresponding annotation. This is in contrast to common bundle adjustment algorithms that typically search for a global match without indexing features or partitioning them into sub-groups. Furthermore, in our recordings the head and tail are the only identifiable features that can be localised to a single point, thus they are optimised in a one-to-one manner. Since the head and tail are at the endpoints of the worm’s midline, they are particularly important for obtaining the correct scale, and are thus given a higher weight in the optimisation.

The method requires midline annotations from a few selected frames (3-10) and typically results in an error ≤ 1 pixel (Fig. 6C-D). The frames are selected such that the shape of the worm, and its end-points in particular, are clearly visible in all cameras. 2D midline annotations are first obtained automatically using a pre-trained CNN (not shown) and can then be manually corrected using a custom annotation tool (see section

3.7). The optimisation is based on a hill climbing approach [293] (see section 3.4.2 for more details on hill climbing methods), such that extrinsic model parameters are perturbed using uniformly-distributed random noise, and the distance between 3D projected points and their corresponding annotations are minimised (Fig. 6C-D). During this process, the coordinates of the 3D points are optimised too, to ensure that the error stems from model parameters only, and not from shifts in the position of 3D points.

Figure 6: Grid detection and indexing, camera calibration and camera model refinement

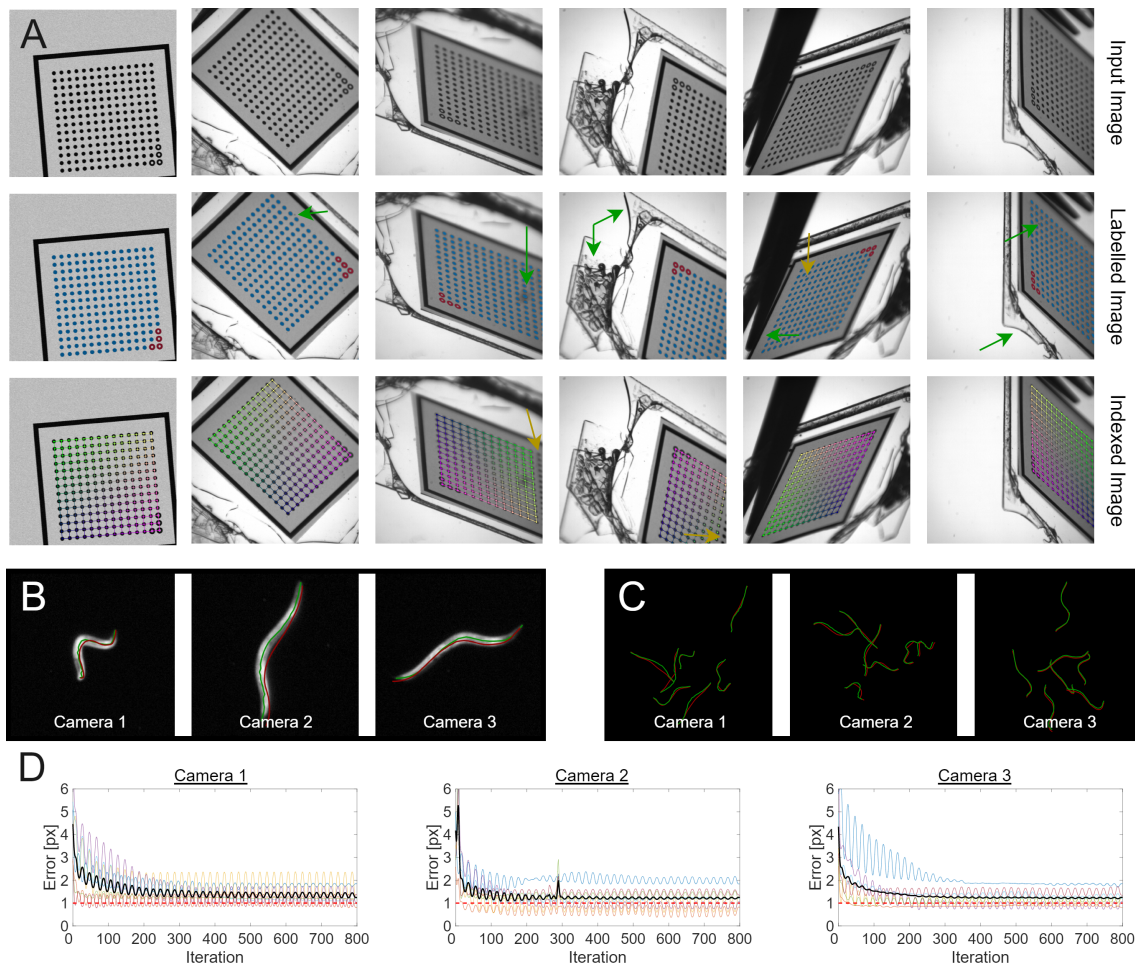


Figure 6. A. Examples of input calibration grid images (top row), CNN-based grid-labelling (middle row) and grid indexing (bottom row). In the middle row, pixels that belong to solid grid points are marked in blue and to hollow grid points in red. The leftmost column shows a synthetically generated image, and the rest of the columns show images taken from an experiment from which no images were included in the training set. The indexing of the pattern (shown as a colour map in the bottom row) is consistent across images and cameras. The green arrows in the middle row show examples of successful CNN classification, and the yellow arrows show false positives or missed points. The yellow arrows in the bottom row show unindexed grid points. B-C. Projections of 3D midlines onto the cameras views before (red) and after (green) camera model refinement. D. The mean reprojection error (in pixels) during the optimisation process for each of the midlines in C. The black line shows the average error across all midlines.

3.4 3D midline reconstruction

To study the dynamics of motor behaviour in 3D environments, I reduced the shape of the worm to its midline, represented as a set of 3D coordinates, ordered from head to tail. Tracing and tracking the midline in clips recorded in a range of environmental viscoelasticity can be used to perform postural analysis and study locomotion dynamics in a volume under different mechanical constraints.

The precise position of the head and tail points is often hard to detect in image data due to the higher transparency of the worm itself in those regions, resulting in low signal-to-noise ratio. The precise shape of the head of the worm is particularly important in this work which focuses on head control that underlies 3D pattern generation. Accurate detection of the shape and dynamics of the head will enable a better characterisation of 3D gaits and their underlying neuromechanical control mechanisms.

Thus, the 3D midline reconstruction problem was broken down into two parts. First, the head and tail points are detected and tracked in 3D throughout the entire clip, and only then the full 3D midline is traced while constrained at the end-points. Not only that this approach provides precise detection of the head and tail, it also simplifies the midline finding problem and ensures its convergence.

While other methods exist for 3D midline finding in multi-camera recordings [294], I chose to develop this method for two main reasons. First, the separate detection of the end-points provides a custom solution that focuses on accurate head detection that is particularly important for this work. It also constrains the midline finding algorithm and ensures its convergence. Second, both end-point and midline finding are based on a tracking approach that uses time information to track worm features from one frame to the next. Using the shape, position and orientation of the worm in each frame as a template for finding the midline in the next frame is particularly important for resolving shape ambiguities, such as 2D loops and head/tail directionality.

3.4.1 A compact deep learning method for 3D point detection successfully tracks *C. elegans* head and tail

To detect the precise position of the head and tail points in 3D space, I trained a convolutional neural network (CNN) and applied it to 3D recordings of *C. elegans* locomotion. Head points were annotated in

lab coordinates using a custom 3D annotation tool (Fig. 7A and Section 3.7). Frames for annotation were selected from different recordings and gelatin concentrations to generalise for signal-to-noise ratio and worm size and speed. The network predicts the $\{dx,dy,dz\}$ translation of head position from one frame to the next, given a multi-channel image where each channel corresponds to a different camera (Fig. 7F).

Here, the 3D scene is represented as a compact 3D grid space that corresponds to a small neighbourhood of the head (or tail) point. The grid space is defined using three orthogonal 2D grids oriented in parallel to the idealised camera orientations (Fig. 7B). The position of the head in the previous frame is implicitly encoded as the centre point of the grid space, and the CNN is designed to predict the $\{dx,dy,dz\}$ translation from its centre to the head point in the current frame. To generate input samples for training, an annotated head point is first positioned at the origin of the grid space (Fig. 7C). Then, uniformly-distributed random noise is added to shift the centre point from the origin of the grid space (dashed square in Fig. 7C and Table 2). This is done to simulate the head position in the previous/next frame. Next, each 2D grid is projected onto its camera view to extract pixel values (Fig. 7D-E). This results in an RGB image that contains pixel information in lab coordinates from a small neighbourhood of the head point in all cameras, and its centre point encodes the head point in the previous frame (Fig. 7F and Table 2).

Note that the RGB image does not contain pixel information from other frames. Instead, it implicitly encodes time information by being centred at the head point of the next/previous frame. The CNN uses the RGB image as an input sample, and the output is a vector of three real numbers that encodes the $\{dx,dy,dz\}$ translation (in mm) from the centre of the 3D grid space to the position of the head point. This provides a tracking tool in lab coordinates that is independent of the global position of the worm in the volume. The purpose of using uniformly-distributed random noise to simulate the head point from a neighbouring frame is to avoid any bias for the direction or speed of head motion (Fig. 7C, dashed squares). Importantly, the upper limit for the maximum random noise must be smaller than the size of the grid space (Fig. 7B-C, dashed and solid squares) to ensure that the sample contains context for prediction (for example, if the head point is on the boundary and the rest of the worm’s body is outside). The lower limit (of the maximum random noise size, dashed squares in Fig. 7C) is the maximum possible distance travelled by the head point from one frame to the next. Thus, it depends both on worm speed (that varies across gaits and environments) and on the frame rate of the recording.

Figure 7: A compact method for 3D point tracking using convolutional neural networks (CNN)

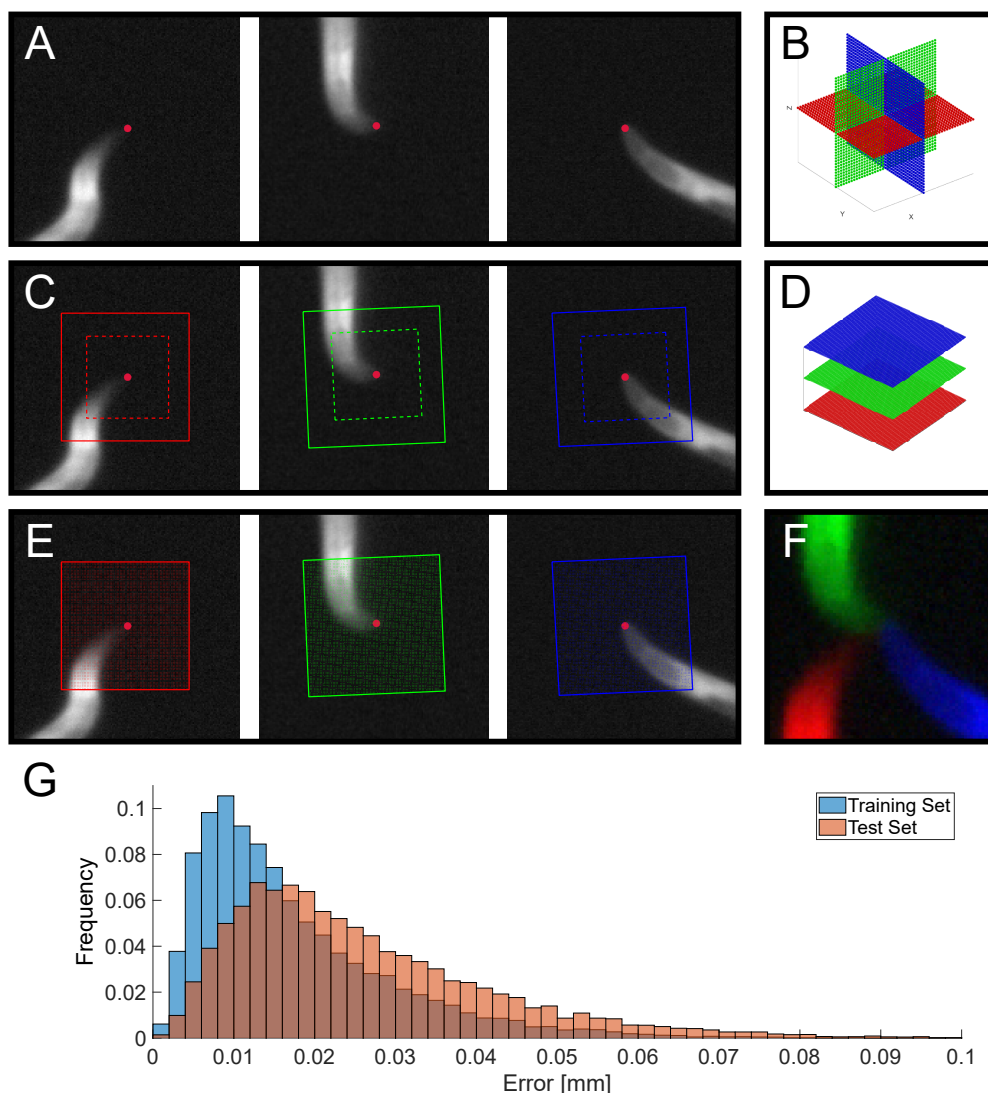


Figure 7. A. An example of a 3D head point annotation projected onto the camera views. B. A 3D grid space made of three orthogonal planar grids is used to represent the compact 3D space in lab coordinates. Each planar grid corresponds to a different camera view. C. Training samples are generated by randomising the position of the target (annotated) point in all directions (x,y,z) independently and uniformly, and centring the 3D mesh (B) around that point. The solid squares show the boundary of the projected grids, and the dashed squares show the boundary of the uniformly-distributed random noise. D-F. Once the 3D grid (B) is centred around the randomised point, each planar grid (D) is projected onto its corresponding camera view (E), and each projected point is rounded to the nearest integer for pixel value extraction (dots). Finally, the extracted matrices of pixels values are stacked to form a multi-channel image, with each channel corresponding to a different camera (F). The resulting multi-channel image is used as an input sample to the network, with its centre point corresponding to the reference (randomised) point in 3D. The output (response) is a vector of three real numbers, corresponding to the $\{dx,dy,dz\}$ translation (in mm) from the 3D reference point to the target head point. Each sample is further augmented by applying camera permutation, reflection and random image enhancement (not shown). G. Error distributions with mean of 0.025 ± 0.016 mm for the test set (orange, 272 samples augmented 50 times each), and 0.017 ± 0.012 mm for the training set (blue, 618 samples augmented 50 times each). The frames used for the test set were taken from clips from which no frames were used for training.

The CNN is based on a standard architecture of stacked convolution and ReLU layers [280]. Its last layer is a regression layer used for predicting real numbers (as opposed to classification problems) and its loss is defined as the mean-squared-error function (Table 2) [280].

The CNN was trained using head annotations from 618 frames taken from different recordings and gelatin concentrations. In addition to the randomisation of the annotated head points, the dataset was augmented by axes permutation and reversing to generalise for the orientation of the worm relative to the cameras, as well as by applying random image enhancement. Overall, each head annotation was augmented 100 times. 20% of the dataset was used for validation during training. 272 annotated frames from clips from which no training frames were taken, were used as a test set (Fig. 7G). The network was then used to track the head point in full clips containing thousands of frames each (Fig. 8A-G). This includes frames where the the head region is blurry or occluded by other body regions (Fig. 8C-G). Though trained using head annotations only, the network successfully tracks both head and tail (Fig. 8H-M). Importantly, head and tail were tracked simultaneously without confusing them, apart from rare unresolvable cases where they were in the same neighbourhood in all three views (Fig. 8J,L,M).

	Parameter name	Value
Dataset	Grid size in mm	$(1/3.5) \times (1/3.5) \times 3$ mm
	Grid size in pixels	79x79x3 px
	Random noise size	± 0.09 mm
	Random enhancement range	[0.5,0.6]
	Augmentation (per frame)	x100
Network	Number of filters	128
	Filter size (first convolution layer)	7
	Filter size (hidden layers)	3
	Number of hidden layers	5
	Loss function	mean-squared-error
Training	Solver	adam
	Number of epochs	10
	Mini batch size	256
	Initial learning rate	0.001
	Learning drop rate	0.9
	Learning rate drop period	50 iterations
	Dropout probability	0.8
	Test set ratio	0.2

Table 2. Parameters for setting up and training a convolutional neural network for 3D point tracking.

Figure 8: 3D head and tail tracking

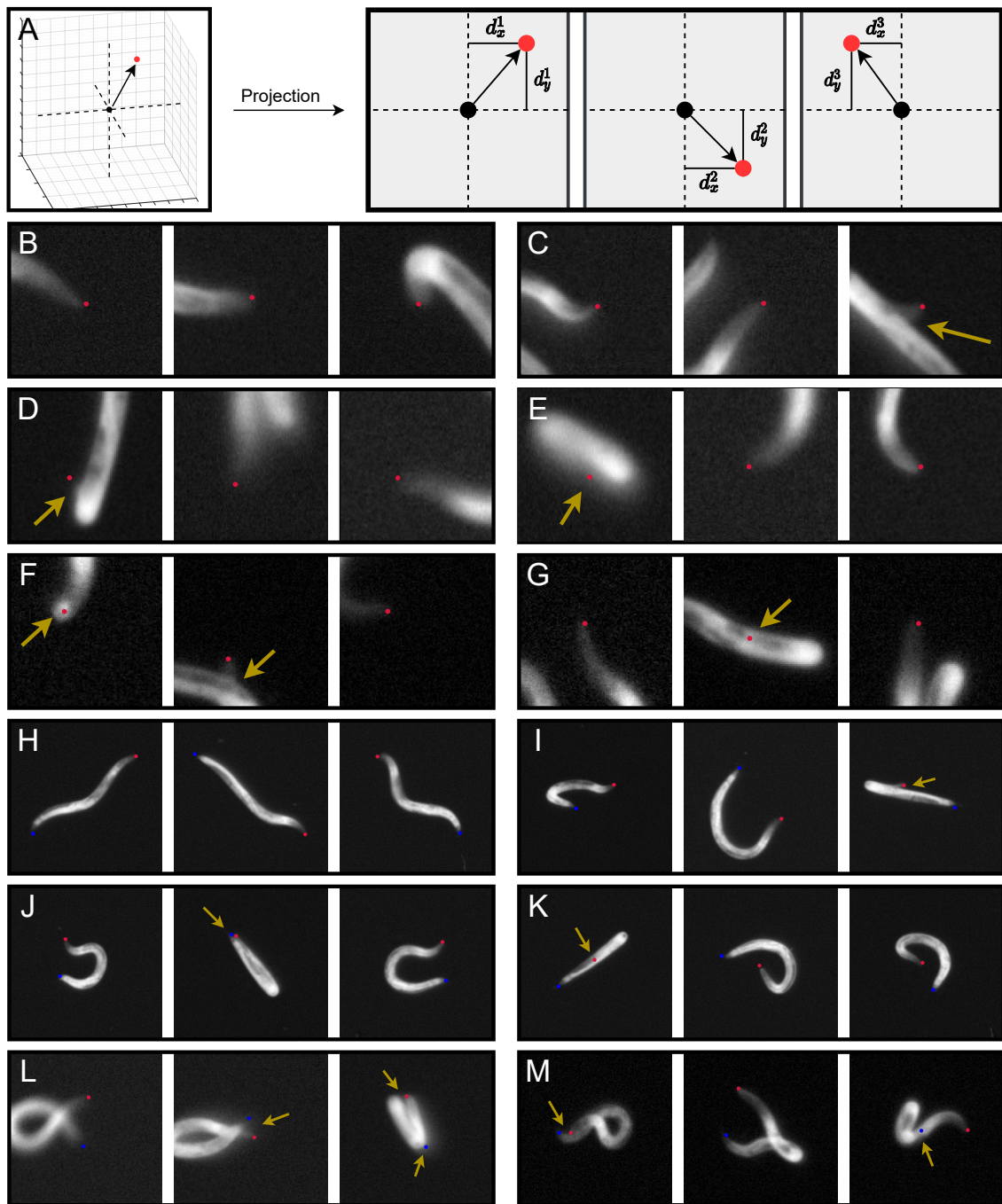


Figure 8. A. A pre-trained convolutional neural network (CNN) predicts the 3D translation from a reference point from a neighbouring frame (black) to the target point (red). B-G. Examples of projected 3D head points (red dot) predicted by the CNN. The yellow arrows show cases where the target point is close to another body region (C-D), where the signal is blurry (E), and where the target point is occluded by another body region (F-G). H-M. The CNN is used to track both head (red) and tail (blue) points simultaneously and independently. The yellow arrows show cases where the head/tail point is close to the body (I), where head and tail are close to each other in one view (J,L,M) and where the head/tail point is occluded by another body region (K).

3.4.2 3D midline tracking

To reconstruct the shape of the worm over time in 3D recordings of its locomotion, I developed a hill climbing algorithm for 3D midline tracking. Hill climbing is an optimisation method that uses small perturbations to a system's state repetitively, starting from an initial state and using local information to find a global maximum (or minimum) [293]. The optimisation policy is a loss function used to compute the error of random solutions. The error is minimised by repetitively selecting the best solutions and using them as an initial state for the next iteration.

Here, I used this technique to track the shape of the worm using the 3D midline in each frame as the initial state for the optimisation in the next frame. Importantly, the midline was discretised to a set of points ordered from head to tail, and the worm's body geometry was approximated as a cylinder. This allowed to apply perturbations to midline points in the worm's (rather than the image) coordinate system, using the tangential and radial directions with respect to its midline (corresponding to the centreline of the cylinder). The optimisation policy includes the mean pixel value of the neighbourhood of each point, the overlap of those neighbourhoods, as well as the total arc-length of the worm. This method was used in combination with head and tail tracking (see section 3.4.1), such that head and tail were first detected in all frames, and then the midline was tracked while fixed at the end points.

Given an initial 3D midline, a pool of random midlines is generated by adding uniformly-distributed random noise to the position of the points in the tangential and radial directions (Table 3). A pixel score is then computed for each midline by projecting it onto the camera views and extracting pixel values using a square mask centred at each projected midline point. The total pixel score is obtained by averaging mask pixel values across midline points and cameras. In each iteration, the midline assigned with the highest score is used as a template for the next iteration and the process repeats until either a predefined score threshold or a maximum iteration number is reached (Table 3). The upper limit for the random noise decreases and its resolution increases with iteration number to allow for finer optimisation as the midline gradually converges to the shape of the worm (Fig. 9A-F). Finally, the resulting midline is used as a template for the next frame, and the process repeats until the last frame is reached.

Using only the mean pixel value for the optimisation policy often results in midline points concentrating

at regions of higher pixel values. To avoid that, overlapping mask pixels of different midline points are only counted once. This adds an implicit penalty to the optimisation policy that makes it preferable for the midline to spread and cover more pixels, rather than to only maximise the mean pixel value (Fig. 9B,E,F). In addition, to control the length of the midline, the ratio between the total arc-length of a random midline (L_i) and a reference value (L_0) is constrained by including it in the optimisation policy $(1 - |(1 - \frac{L_i}{L_0})|)$. Constraining the smoothness of the midline and the order of its points is necessary to maintain a worm-like shape during the optimisation process. These were not included in the optimisation policy, but were instead enforced by smoothing and equidistantly-distributing the midline in each iteration.

Apart from the head and tail, our recordings do not contain identifiable worm features that can be localised to a single point (such as the vulva and body wall muscles). This stresses the importance of using a tracking approach that preserves postural information from one frame to the next, and constrains the optimisation process to small deformations of the template midline (Table 3). In particular, optimising the midline using the worm’s coordinate system (approximated as a cylinder) allows to perturb midline points in the tangential and radial directions independently. The maximum tangential shift to each point must be smaller than half the 3D euclidean distance from its neighbours to maintain their order across iterations, and is dependent on the worm length and the discretisation of the midline (i.e., the number of midline points). In contrast, perturbations in the radial direction only depend on the motion of the worm. Altogether, tracking the worm’s shape in lab coordinates and optimising its midline in its own coordinate system using integrated information from all cameras simultaneously, ensures that matching 2D points across cameras correspond to the same position in 3D. This was crucial for resolving postural ambiguities, such as loops and overlaps between different body regions (Fig. 9C and 9E).

This method was combined with head and tail tracking (see Section 3.4.1). First, the head and tail were detected in all frames, and then the midline was found while fixed at the end-points. This combination makes the optimisation process significantly more robust and faster, as it reduces the degrees of freedom for the midline’s shape and position, and keeps its arc-length stable. This two-step approach also significantly simplifies validation, because once the end-points have been validated and fixed, the midline is highly constrained and rarely requires correction. This approach was used to track the worm’s midline in clips recorded in a range of gelatin concentrations, each including thousands of frames (Fig. 9A-F and Table 4).

Figure 9: 3D midline reconstruction

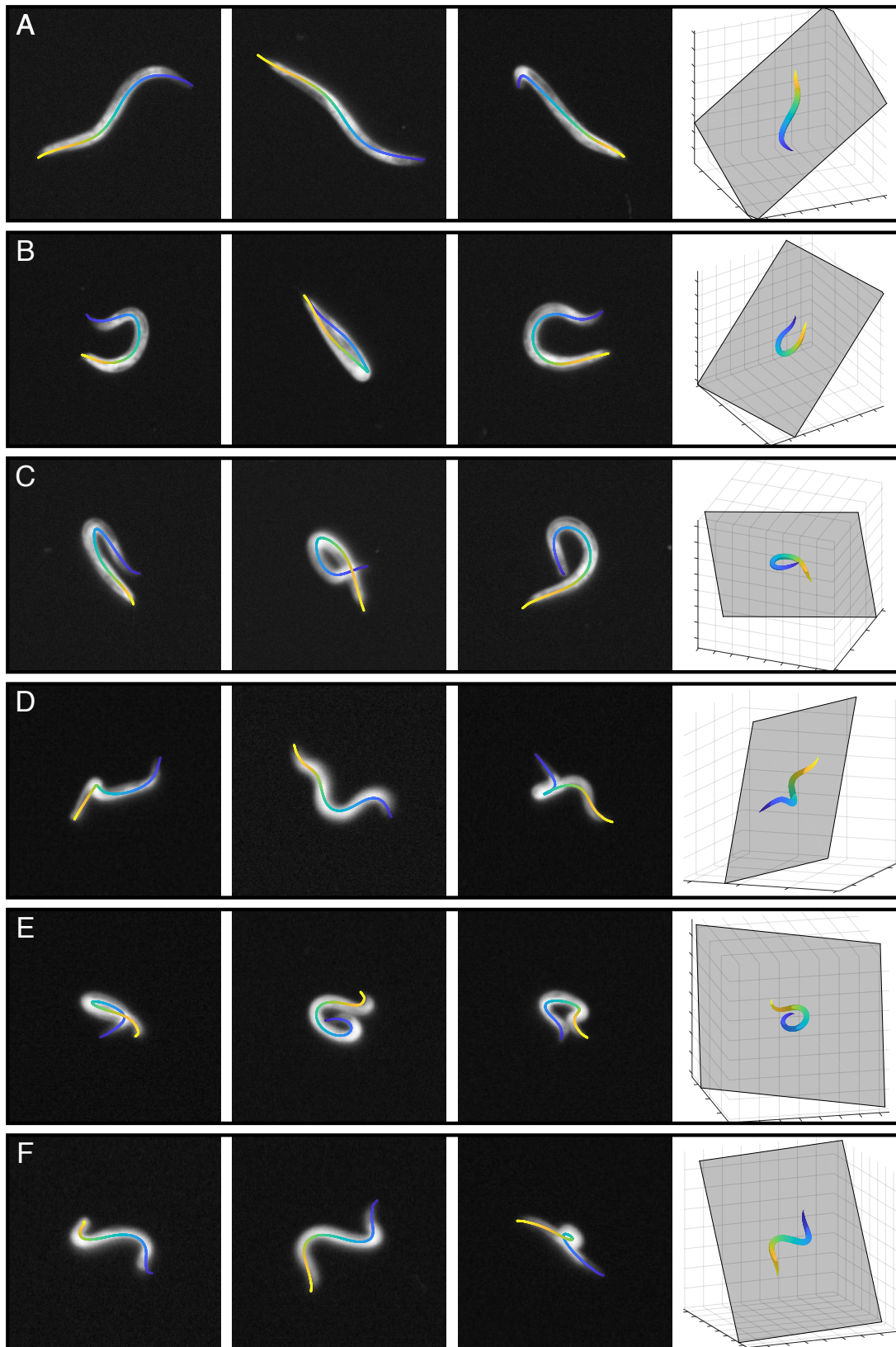


Figure 9. A-F. Examples of reconstructed 3D midlines (rightmost column), from head (blue) to tail (yellow), and their projection onto the camera views (column 1-3). For the 3D midline, a fitted PCA plane is shown (see Methods section). The midline finding algorithm is able to resolve the shape of the worm including cases of convoluted postures and 2D self-occlusions. The algorithm uses the CNN-derived end-points as a constraint for the midline optimisation (see Figs. 7 and 8).

Parameter name	Value
Maximum number of iterations	200
Number of random midlines	100
Number of midline points	36
Smoothing parameter	0.05
Midline point mask size	5x5 px
Maximum noise size (tangential)	0.002mm
Maximum noise size (radial)	0.002mm

Table 3. Parameters for 3D midline tracking.

3.5 Imaging of worms expressing a fluorescent marker in body wall muscles

As a complementary approach to 3D imaging, I used 2D imaging of a volume containing wild-type worms that express GFP and RFP in body wall muscles, in order to observe the worm’s internal coordinate system during different motor behaviours. This was done using a 35mm microscopy dish with a #1.5 coverslip bottom. First, molten gelatin was poured into the dish, then 10-20 young-adult worms were placed inside the gel and a coverslip was placed on top. I used the strain TOL43 (aatEx25 [myo-3p::nls::RCaMP2; myo-3p::nls::eGFP; pha-1(+); pha-1(lf)e2123 III]) that expresses GFP in the cytoplasm and RCaMP in the nucleus of body wall muscles. The strain was provided by the Haspel lab (NJIT). Note that this strain is genetically, but not phenotypically, distinct from the N2 strain. These recordings were used for a qualitative characterisation of the worm’s internal twist and rolling during different behaviours (see Figs. 20 and 21).

3.6 Collected and analysed 3D data

I recorded a total of 8 hours of 3D locomotion data and obtained midline reconstruction for a total of 1.7 hours (Table 4). Some of the analysed data for concentrations 2% and 4% were obtained by Robert Holbrook. The choice of clips to analyse was based on the quality of the recordings (mainly the focus of the worm) and the calibration error.

Gelatin Conc. (%)	Recorded [h] (# of clips)	Analysed [min] (# of clips)	Elastic Modulus (G') [Pa]
1	1.66 (51)	22 (15)	4
1.25	1.97 (33)	7 (9)	11
1.5	1.42 (31)	13 (6)	13
2	1.53 (27)	2 (1)	100
3	1.25 (27)	4 (2)	300
4	0.37 (6)	4 (2)	600

Table 4. The table shows the total duration of recorded and analysed data (in hours). The numbers in parentheses indicate the number of clips recorded, that roughly corresponds to the number of different worms recorded. The data for 2% and 4% includes recordings by Robert Holbrook. The values for the elastic modulus (G') corresponding to gelatin concentration are taken from [73].

3.7 3D worm tracker (3DWT): A tool for annotation, calibration, reconstruction and analysis of 3D locomotion

I developed an interactive tool with a user-interface for the analysis of multi-camera recordings of *C. elegans* locomotion. The tool contains all the functionalities described in this chapter including image enhancement, 3D calibration, and 3D point and midline annotation and tracking. In addition, the tool contains different post-processing options for the analysis of posture and trajectory dynamics (for example see Figs. 10-17). The tool was tested using three-camera recordings, but can be used with any number of cameras and other worm-like animals.

For each analysed recording, a single project file (.mat) is generated that stores its data (e.g., camera models, annotations and midline reconstructions) and meta data (e.g., experimental details, software version and user information). Since video files are typically large, only their path is saved into the project file in order to keep its file size small (typically up to 10MB). The format of the project file supports storing data for multiple recordings and can be loaded into the software. This is useful for performing statistical comparisons across data sets (e.g., gelatin concentrations, age or worm strains).

The source code of the tool and a user manual, as well example project files are available as supporting information.

3.8 Discussion

3D imaging

In this chapter I presented a novel multi-camera system for 3D imaging of *C. elegans* locomotion. We have used this setup to record young-adult hermaphrodite worms across a range of gel viscoelasticity at 25Hz. The setup is well-suited to extend locomotion data from assays that are conventionally done in planar settings, such as navigation (e.g., chemotaxis), optogenetics and testing mutant strains. These can be used to study the nature of *C. elegans* locomotion in a volume and its underlying neuromuscular mechanisms and biomechanics.

As with any other imaging system, this system too has limitations. Using three cameras helps resolve shape ambiguities that cannot be resolved using two cameras only. However, some cases cannot be resolved by adding more cameras. This includes cases in which the worm loops on itself, and the identification of the worm's intrinsic coordinate system. As a complementary approach, I used 2D fluorescence imaging of a volume containing worms that express GFP in body wall muscles. While this can be used for a qualitative analysis of the worm's intrinsic coordinate system during different behaviours, future work may attempt to combine 3D imaging with fluorescence imaging in order to quantify the correlation between worm shapes its intrinsic coordinate system.

The maximum magnification in this setup is 7x, bounded by the specifications of the lens. This gives a field of view and depth of focus of approximately 1cm^3 and 1cm, respectively. Lower magnifications may be used to capture longer trajectories in larger volumes, although resolving the posture might become harder due to the lower resolution. The maximum acquisition rate is 40Hz, as at higher rates the synchrony across cameras cannot be guaranteed. While I recorded all videos at 25Hz, higher acquisitions rates may be used for faster gaits that are more common in low gelatin concentrations (typically $\leq 2\%$, corresponding to $G' \leq 100$ Pa, see Table 4).

Calibration

The calibration of the volume is used to obtain camera models that describe intrinsic and extrinsic camera and lens properties. This allows to map points in camera pixel space to points in 3D lab coordinates, and to accounts for different types of optical distortion resulting from intrinsic camera and lens properties. In

particular, the camera models were used for head/tail and midline tracking, in order to match corresponding points across cameras (see section 3.4).

I used a square calibration slide with an asymmetric grid pattern that includes both filled and hollow circles (Fig. 4B). The method that I developed for the detection and indexing of the grid pattern is scale-free and can be used to analyse other grid patterns with different number of points, point classes, and even different shapes (e.g., triangles). The use of a mixed set of synthetic and experimental training examples makes it easier to adjust the method to different patterns and imaging setups as it requires a small number of annotations (see section 3.3.1).

Here, camera models are based on calibration images taken in the molten gel, while worms are recorded only after the gel has set. This causes a small, but significant difference to the optical properties of the scene that increases the calibration error and may result in the failure to map corresponding points in the image projections to 3D points in lab space. This discrepancy may be due to changes in the refractive index of the material during solidification [290]. To account for these optical changes during gel solidification, I developed a custom bundle adjustment algorithm for refining camera model parameters. While I only used it to refine extrinsic model parameters, it can also be used to refine intrinsic model parameters. The method uses 2D midline annotations that were obtained semi-automatically (using a CNN and manual correction of its result) in order to refine the camera models (typically 3-10 midlines are required to obtain a calibration error ≤ 1 pixel). Future work may attempt to fully automate this step, and test whether obtaining a higher number of midline annotations of lower quality can be used to achieve a similar calibration error.

3D point and midline tracking

The problem of finding the worm’s 3D midline was broken into two parts. First, the head and tail points were detected throughout an entire clip using a pre-trained convolutional neural network (CNN), and then the midline was found using a hill climbing optimisation method while constrained at the end-points. This two-step approach provides a method for precise detection of the head and tail regions, and significantly simplifies the midline finding problem and guarantees its convergence. Importantly, both methods use time information and track points in 3D lab coordinates. The 3D point-tracking algorithm uses a small neighbourhood of the target point (head/tail in the current frame) centred around a reference point (corresponding to the

head/tail point in the previous/next frame). The midline-tracking algorithm uses the midline in each frame as a template for its optimisation in the next frame. Time information is implicitly used by constraining the change to the position of points from one frame to the next (Table 3). This was important for resolving shape ambiguities such as head-tail directionality and loops (see Fig. 9B-F).

Both point- and midline-tracking fail when there is no sufficient information in all views to resolve a shape ambiguity, for example, when the neighbourhoods of the head and tail overlap in at least two views, or when a region of the projected worm is occluded by another region in at least two views. Such cases were rare and were corrected manually using a custom 3D annotation tool (see section 3.7).

The CNN used for 3D point-tracking is not *C. elegans*-specific and can be applied to other features in other animals and scales, and can also be used with any number of cameras. Its definition of the input and output is suitable for time-lapse tracking as it implicitly encodes time information and uses the relative, rather than absolute positions of the reference and target points. The method is compact in the sense that it reduces the 3D space ($N \times N \times N$, where N is the number of points in each dimension of the discretised volume) to a set of planar grids, stacked to form a multi-channel image where each channel corresponds to a different camera ($N \times N \times C$, where C is the number of channels, which equals to the number of cameras). This significantly reduces the size of the input, as well as training and prediction time. Furthermore, using only a small neighbourhood of the target point, rather than the entire recorded volume, also reduces the size of the input and excludes irrelevant and misleading information in other image regions, resulting in a more stable and reliable tracking. In particular, it allows tracking of multiple target points (e.g., head and tail) independently without confusing them (Fig. 7).

For midline tracking, the initial 3D midline for each clip was obtained by triangulating a 2D annotation of a single frame (one midline annotation per camera), and then tracked in 3D for all other frames. Using the midline in each frame as a template for the next was important for the finding the correct shape of the worm, as optimisation algorithms, and hill climbing methods in particular, are sensitive to the initial state. In addition, perturbing the midline using the worm's, rather than the image coordinate system allows to control the movement of points in the tangential and radial directions independently. This was important since worm points move at different speeds in the tangential and radial directions. Moreover, the movement in the tangential direction must be restricted to maintain the order of the points and depends on the total

arc-length of the worm and the choice of the number of points to represent the midline (Fig. 9).

There are a few factors that may cause the detected 3D midline to deviate from the worm's actual centreline or from the 2D centreline in the projections. First, since the worm's anatomy is not uniform in the radial direction, pixel values in the projections are not uniformly distributed and may bias the midline towards higher pixel values (for example see Fig. 9A). Second, errors in the camera model may result in 3D points projected onto slightly different locations on the worm's body in different cameras. In addition, the smoothness and total-arc length constrains are used to maintain a worm-like shape with a stable length. However, these constrains may cause local over-smoothing of the midline (for example see Fig. 9B). One possible reason for this is that the length of the actual worm is not fixed and may change as the worm bends and unbends. While the optimisation policy does allow the total arc-length to vary, it does not explicitly define the relationship between length and local curvature. Thus, in some cases, local over-smoothing (and thus shortening) may be favourable over a longer and more curved midline (for example see Fig. 9E). This may be addressed in future work by modifying the policy to explicitly constrain local curvature along the midline, for example by defining a curvature threshold above which a penalty is given, while below the threshold all curvature values are equally scored.

4 Characterisation of *C. elegans* motor behaviour in 3D environments

In this chapter I use the data acquired in chapter 3 to characterise *C. elegans* locomotion in a volume. Key features are extracted to quantitatively describe postures and trajectories. By observing those features using custom 3D visualisation tools I identified and classified 3D locomotion patterns that have not been reported in *C. elegans* to date. As a complementary method, fluorescent imaging of body wall muscles of worms in a volume is used to resolve the orientation of the worm within its own intrinsic coordinate system (i.e., internal twist) and with respect to the lab coordinate system for each of the identified behaviours. This analysis helps to link postures and trajectories to the neuromuscular control of those behaviours, which will be discussed in chapter 5.

4.1 Introduction

While 2D locomotion has been studied extensively, typically on a 2% agar surface, 3D locomotion of *C. elegans* received much less attention. While *C. elegans* exhibits some non-planar behaviours in planar settings, such as head lifting [80, 81] and rolling in roller mutants [83, 84], its locomotion in a volume has only started to be addressed in recent years. Since the worm naturally lives in non-planar environments, this has limited our investigation of the worm's locomotion and its underlying neuromechanical mechanisms.

Shaw et al. provided a proof-of-concept for the application of their custom light-field microscope (LFM) for capturing the motion of young-adult *C. elegans* worms in a volume in 30 seconds clips. In addition to worm shapes, they extracted locomotion parameters such as speed, planarity and undulation frequency. Their analysis showed that both individual postures and posture sequences do not show significant non-planarity. A representative posture sequence from a 30 seconds recording was shown to fit into a minimal bounding box with a depth of $110\mu\text{m}$, which is only slightly larger than the $80\mu\text{m}$ typical diameter of a young-adult worm [33]. In order to characterise postural dynamics, they constructed a 3D shape space of fundamental postures (also called eigenworms) using principle component analysis (PCA). This was used to show that four components from this PCA space are sufficient to account for 95% of the variance in their

posture database [245]. This result was similar to a previous analysis of 2D locomotion [247].

In another study, Kwon et al. used a 3D imaging system to extract locomotion parameters, and compared forward speed and frequency of undulations (referred to as curving rate in the paper) of worms in 2D and 3D environments. First, they found that the undulation frequency of worms in 3D is significantly higher compared to 2D, while speed was unchanged. They suggest that the difference in frequency is due to the additional degrees of freedom of postures in 3D. They next tested the contribution of the head to 3D locomotion by looking at mutants with head-related defects. They found that *vab-10* mutants, that are defected in head muscles, show higher undulation frequency compared to wild-type, in both 2D and 3D environments. They also tested *eat-4* mutants that have defects in glutamatergic transmission and show excessive head-lifting. However, the undulation frequency of those mutants was indistinguishable from wild-type worms in both 2D and 3D. Finally, they examined mutants with defects in mechanotransduction to assess the importance of sensory feedback in 3D locomotion. They found one DEG/ENaC mutant (*mec-4*) that showed higher undulation frequency in 3D, but not in 2D environments, compared to wild-type. They also found a TRP mutant (*trp-4*) which showed higher forward speed in 3D compared to 2D (while there was no difference in wild-type). These results suggest that mechanosensation plays a role in 3D locomotion that is at least quantitatively different from 2D [244].

Finally, Bilbao et al. discovered a reorientation manoeuvre during burrowing and swimming in a volume in data from [243]. In this manoeuvre, worms rotate their plane of undulations by approximately 90° within a single undulation period. Their mathematical model and mechanical analysis predict that this rotation is accompanied by a non-zero internal twist that propagates from head to tail. The authors suggest that this 3D manoeuvre is crucial for the nematode to explore large 3D environments [82].

While microscopy and computer vision techniques continue to improve, the characterisation of 3D locomotion also requires the development of methods, metrics and models for the extraction and unbiased description of meaningful features of 3D reconstructed worm shapes and trajectories. In addition, since 3D data is often non-intuitive and difficult to interpret compared to 2D data, 3D interactive visualisation tools play an important role in the analysis of such data, and help gain insights that can assist the identification and characterisation of locomotion dynamics in 3D.

4.2 Results

As a preliminary visual inspection of the data (see Chapter 3), I looked at worm shapes, as well as postural and trajectorial dynamics. This included raw recordings and videos showing the 3D reconstructed midlines over time and the corresponding kymogram of absolute curvature. I also looked at the trajectory of individual midline points in short time intervals (typically 1-4 seconds), which I found to contain valuable information, as it can be used to identify and distinguish different locomotion patterns. I use the term “microtrajectories” to refer to short interval trajectories of a single point along the worm, to avoid confusion with centre-of-mass (CoM) and long-term point trajectories. Microtrajectories were also colour-coded for different features such as body curvature in order to link them to postural dynamics.

4.3 Four modes of forward locomotion in 3D environments

In recordings from high gelatin concentrations (typically 2% – 4%, corresponding to $100 \leq G' \leq 600$ Pa, see Table 4) the worm spends most of its time moving forward by propagating a dorsoventral body curvature wave from head to tail with mean CoM speeds of 0.085 ± 0.051 mm·s⁻¹ (Fig. 19A). While speed is similar to planar crawling, as shown by our lab in [209], in 3D, worm postures seem mostly non-planar and the worm frequently (but not periodically) goes out of the plane by gradually reorienting its anterior part of the body (Fig. 10A). In low gelatin concentrations (typically 1% – 1.5%, corresponding to $4 \leq G' \leq 13$ Pa, see Table 4), I found that the worm exhibits high frequency undulations with non-planar postures and low CoM speed. In particular, I identified two forward locomotion patterns that account for most of the worm’s locomotion in low concentration recordings. The first, Coiling, is best characterised by a circle-like microtrajectory, most pronounced in the anteriormost third of the body, and low CoM speed. I observed this behaviour in both clockwise (CW) and counterclockwise (CCW) modes (Fig. 11 and 12, respectively) which showed a slight difference in mean CoM speed (0.0703 ± 0.026 mm·s⁻¹ and 0.056 ± 0.028 mm·s⁻¹, respectively; see Fig. 19A). The second, Infinity, is best characterised by an eight-shaped microtrajectory, also most pronounced in the anteriormost third of the body, with higher frequency undulations and lower CoM speed compared to Coiling (0.038 ± 0.024 mm·s⁻¹, Figs. 13 and 19A). In comparison, planar swimming speed in similar environments is approximately 0.4 ± 0.1 mm·s⁻¹, as shown by our lab in [209].

In crawling behaviour, body and microtrajectory curvature are similar (Fig. 10B, see curvature scales). However, in Coiling and Infinity, trajectory curvature is significantly higher compared to body curvature (Figs. 11B, 12B and 13B). While the kymograms of absolute body curvature of crawling in 3D resemble those of 2D crawling (Fig. 10C), the kymograms of Coiling and Infinity seem different with a less uniform wave propagation (Figs. 11C, 12C and 13C). This may be the result of the combination of two curvature waves that propagate posteriorly, in the dorsoventral and left-right directions. In addition, the frequency of body curvature in Coiling and Infinity is significantly higher compared to crawling (Figs. 10D, 11D, 12D and 13D).

Finally, Individual worms can do both CW and CCW Coiling, as well as Infinity and sometimes switch between them abruptly. Turning manoeuvres and reversals were also observed, including Coiling and Infinity reversals with wave propagation from tail to head. Turning manoeuvres and reversals are beyond the scope of this current analysis and are not described further (see Discussion).

Figure 10: Crawling

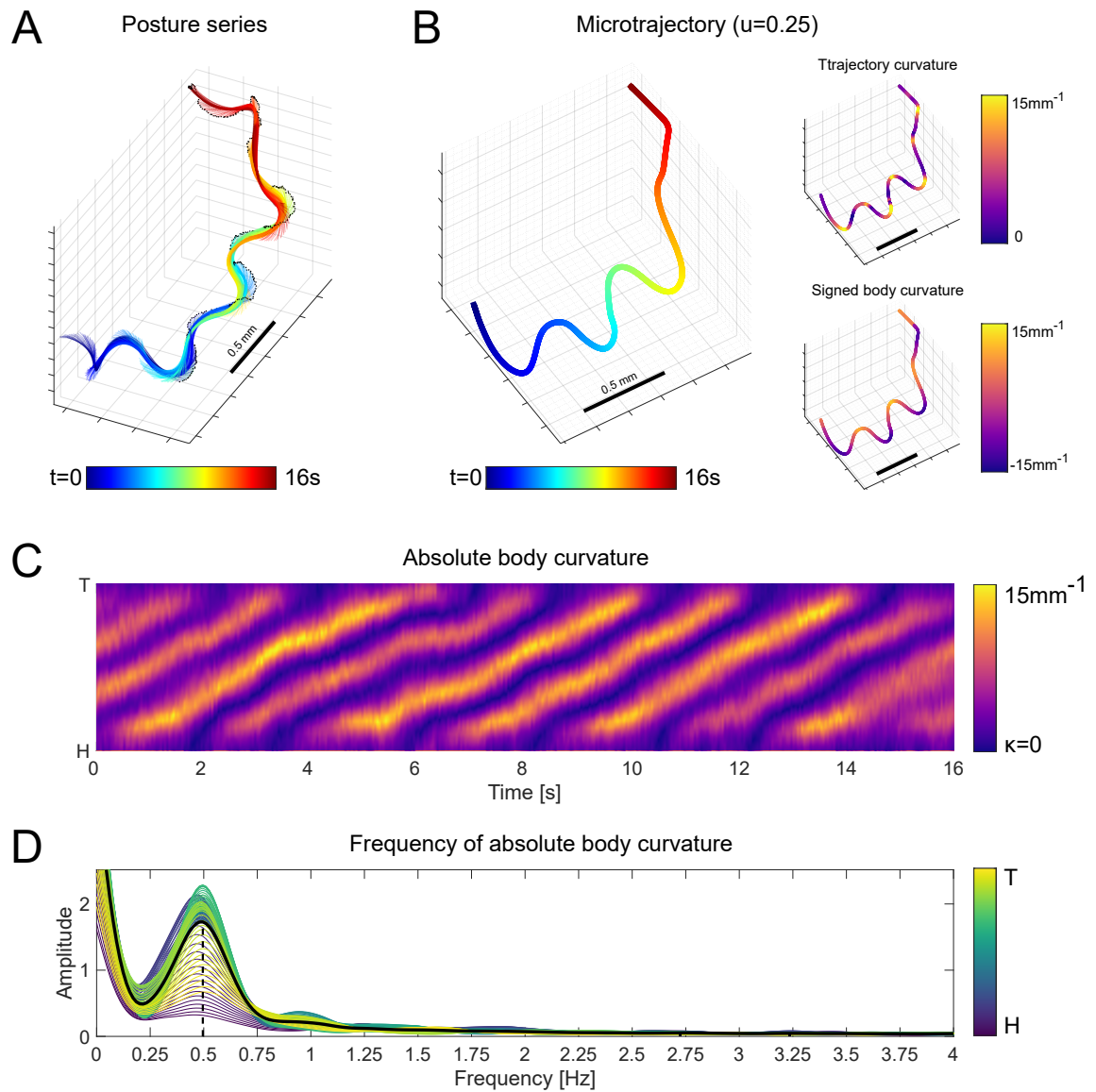


Figure 10. A. Posture time-series. B. Microtrajectory at 25% body arc-length from the head, colour-coded for time (left), trajectory absolute curvature (top-right) and posture signed curvature (bottom-right). C-D. Kymogram (C) and frequency domain (D) of absolute body curvature.

Figure 11: Clockwise coiling

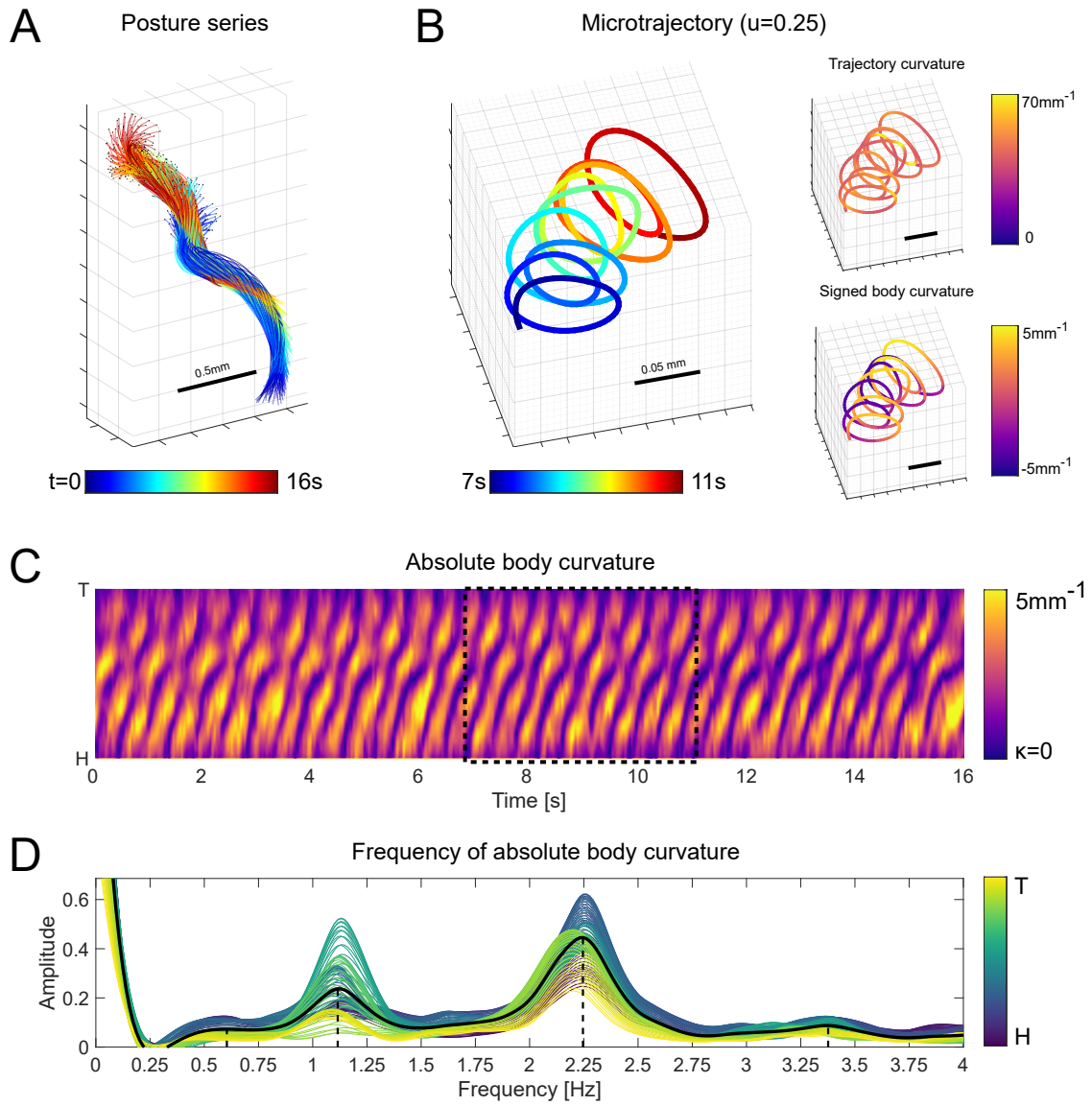


Figure 11. A. Posture time-series. B. Microtrajectory at 25% body arc-length from the head, colour-coded for time (left), trajectory absolute curvature (top-right) and posture signed curvature (bottom-right). C-D. Kymogram (C) and frequency domain (D) of absolute body curvature.

Figure 12: Counterclockwise coiling

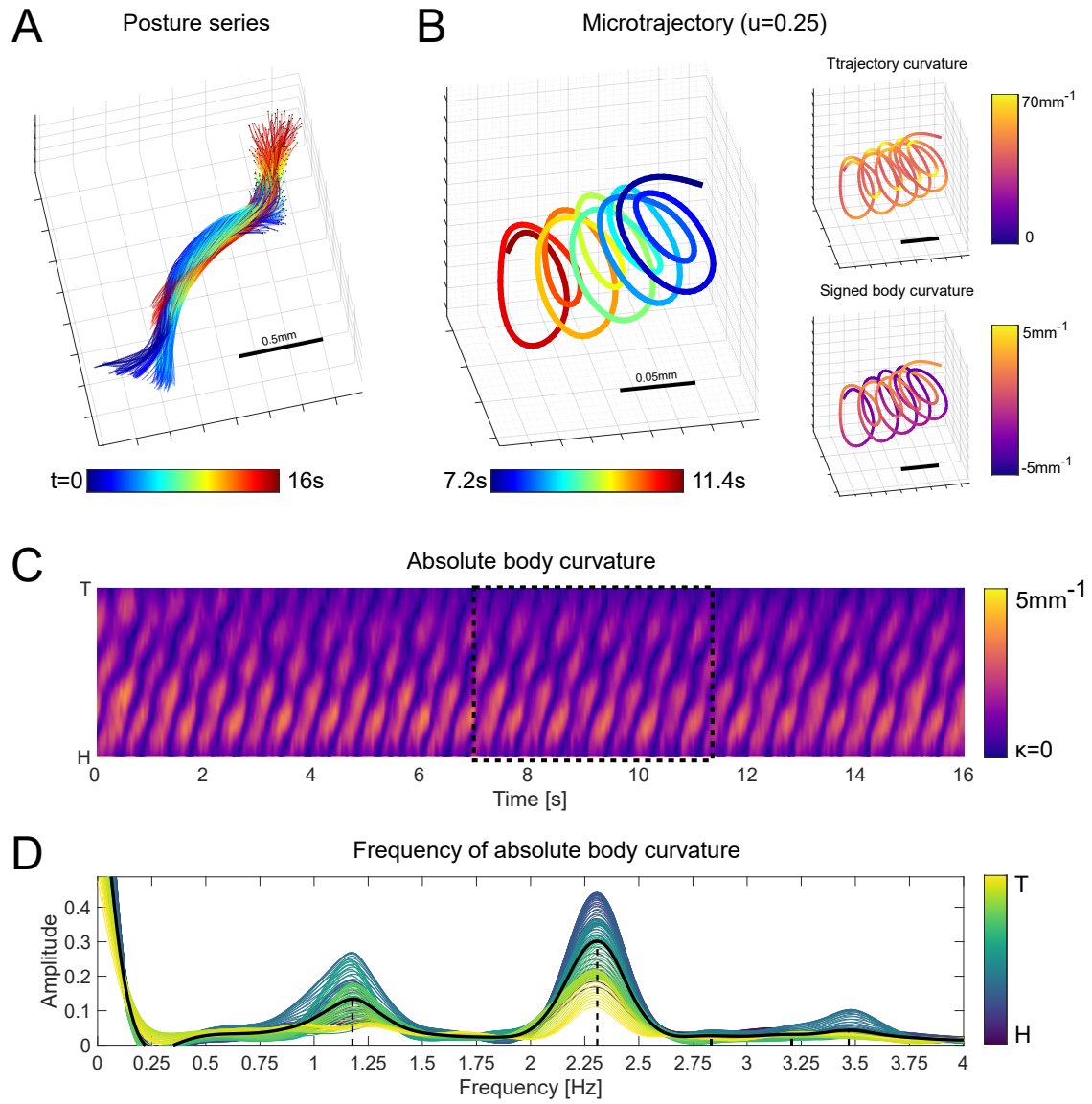


Figure 12. A. Posture time-series. B. Microtrajectory at 25% body arc-length from the head, colour-coded for time (left), trajectory absolute curvature (top-right) and posture signed curvature (bottom-right). C-D. Kymogram (C) and frequency domain (D) of absolute body curvature.

Figure 13: Infinity

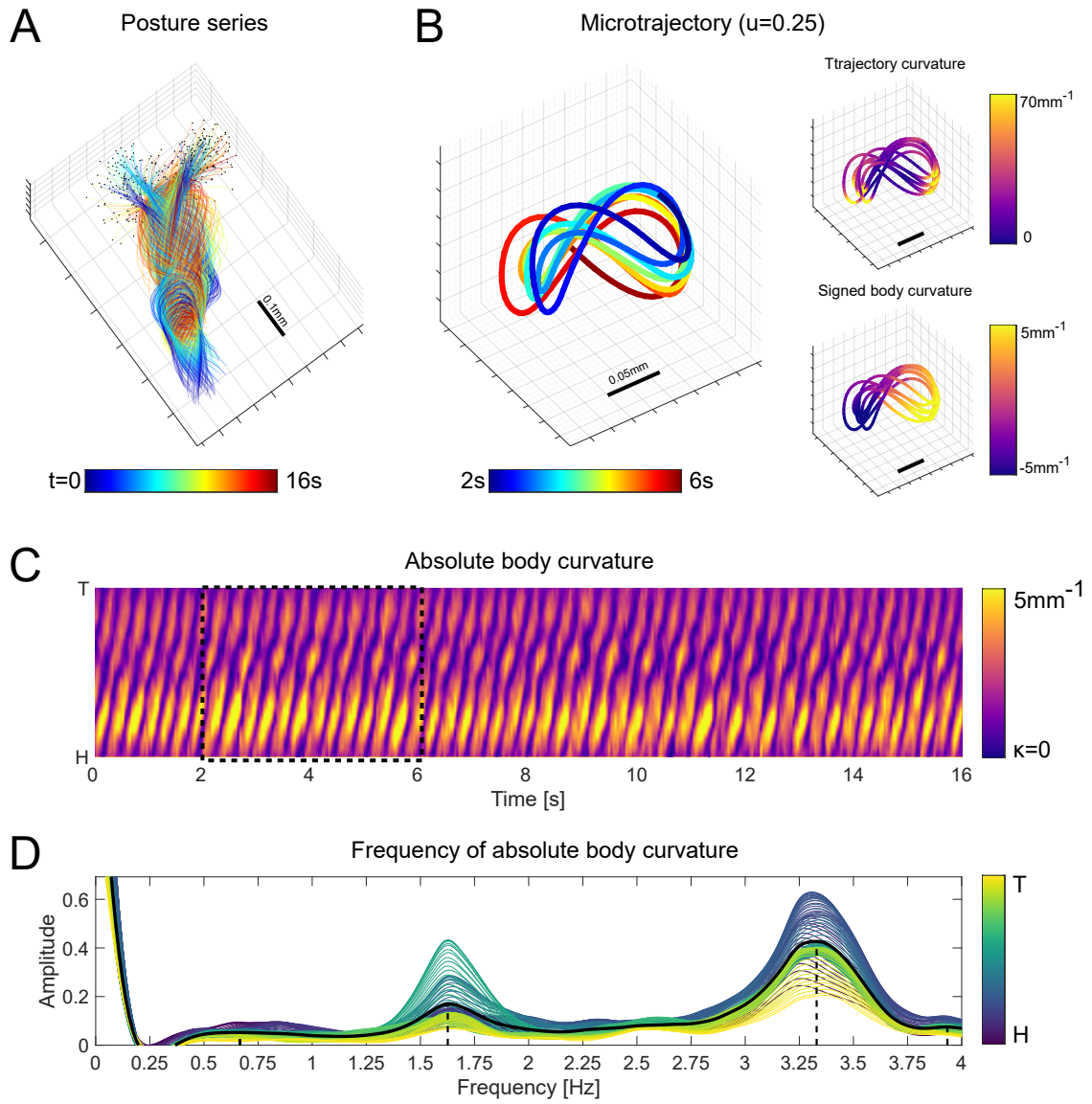


Figure 13. A. Posture time-series. B. Microtrajectory at 25% body arc-length from the head, colour-coded for time (left), trajectory absolute curvature (top-right) and posture signed curvature (bottom-right). C-D. Kymogram (C) and frequency domain (D) of absolute body curvature.

4.4 Chiral trajectories emerge from postures with opposite chirality

Following the qualitative characterisation of the forward locomotion behaviours in a volume (Figs. 10-13), I created an ontology dictionary with tags corresponding to different behaviours (see Methods section). I used this ontology to annotate the entire reconstructed dataset and used it to extract behaviour-specific features. To further characterise the data and to quantitatively describe each of the identified locomotion pattern, I extracted key features from postures and microtrajectories. These include speed, curvature and chirality.

To describe the chirality of postures I projected each midline onto the plane perpendicular to the line connecting the tail to the head (panel C in Figs. 14-17). Note that all projected head and tail points are at the origin $([0,0])$ of the projection coordinate system. For each posture I then computed the angle of each projected midline point in polar coordinates (ϕ) . The change in this angle from tail to head was defined as posture chirality at each midline point $(d\phi)$. Panel E in Figs. 14-17 shows the change in this angle in polar coordinates for the same posture time-series as in panel C. I next defined chirality for microtrajectories. This was done by finding the centreline of each microtrajectory and projecting each of its points onto the plane perpendicular to the local tangent of the centreline (panel D in Figs 14-17). The centreline was defined as the average of body coordinates over time (see Methods). Similar to postures, the angle of each projected microtrajectory point in polar coordinates was computed (θ) , and the change in this angle was defined as the chirality of the trajectory $(d\theta)$, panel F in Figs. 14-17).

To quantify the chirality of postures and microtrajectories over the entire dataset, I plotted the distributions of posture and trajectory chirality (Fig. 18A-B). Each data point for posture chirality was computed using a sliding window of half body length, and microtrajectory chirality using a sliding time window of 0.25s only along a short neck region ($u=0.25\pm 0.03$, where u is body coordinate from head to tail, and the total body arc-length is normalised to 1). Expectedly, crawling behaviours did not show any preferred chirality for both postures and microtrajectories (Fig. 14E-F, 18A and 18B). Surprisingly, I found that in Coiling, chiral postures generate microtrajectories with opposite chirality (Fig. 15E-F, 16E-F, 18A and 18B). Note the smaller peaks for CW and CCW Coiling in posture chirality (Fig. 18A, orange and purple) that suggest a small subset of postures and/or body regions with opposite chirality within each cycle (see Discussion). For Infinity the matching between posture and trajectory chirality was less clear as the sample size of both

sub-populations were similar (see Discussion).

Figure 14: Crawling - chirality of postures and trajectories

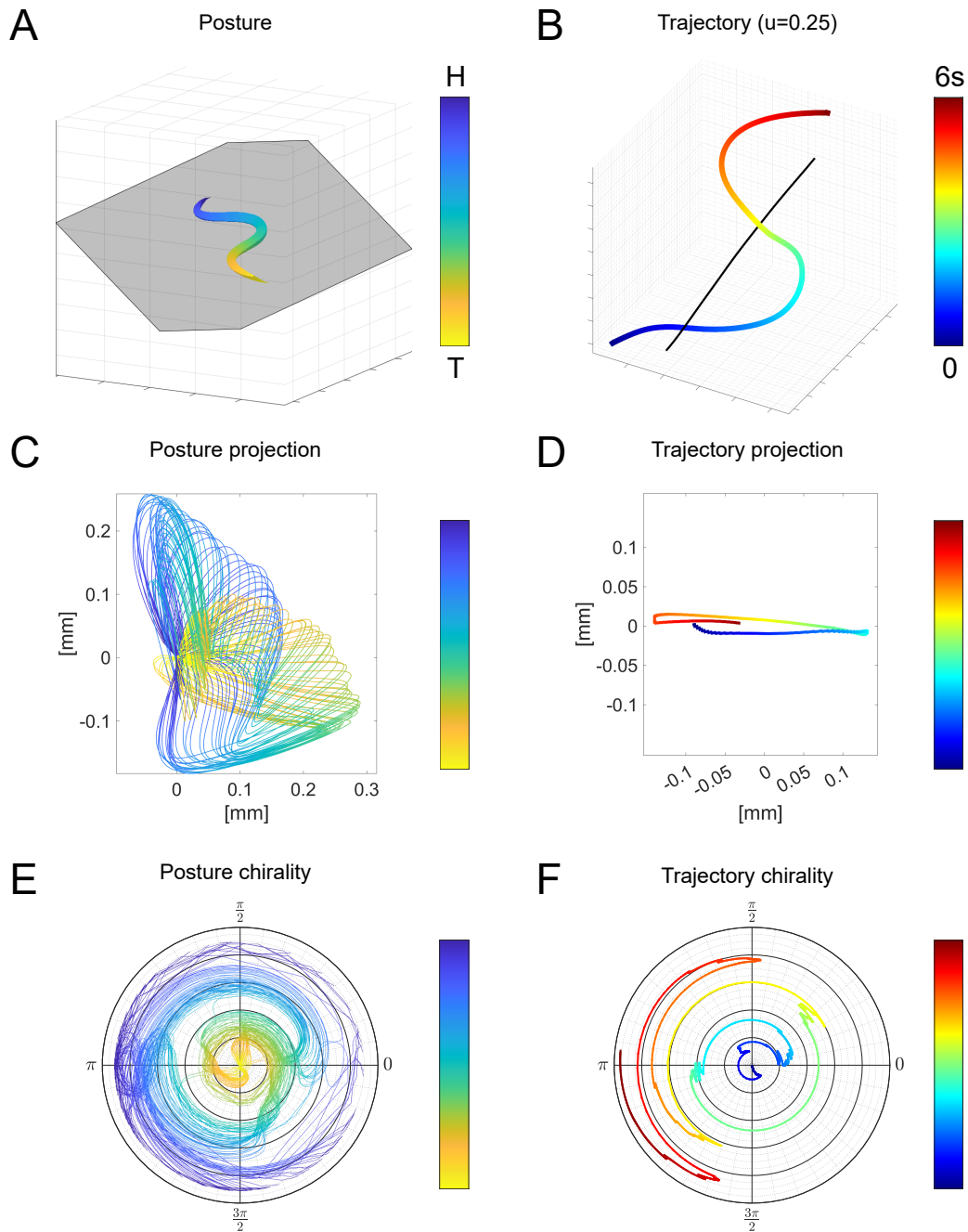


Figure 14. A. a representative 3D posture and a plane fitted to it (grey). B. representative microtrajectory ($u=0.25$) and its centreline (black, see Methods section). C. Projection of posture sequence onto the plane perpendicular to the line connecting the head and tail. D. Projection of each microtrajectory point onto the plane perpendicular the local tangent of the centreline. E. Phase plane of projected postures showing angles between body segments from tail (yellow) to head (blue). F. Phase plane of projected trajectories. G-H. Body curvature (at $u=0.25$, G) and microtrajectory curvature (at $u=0.25$, H) over time.

Figure 15: Clockwise coiling

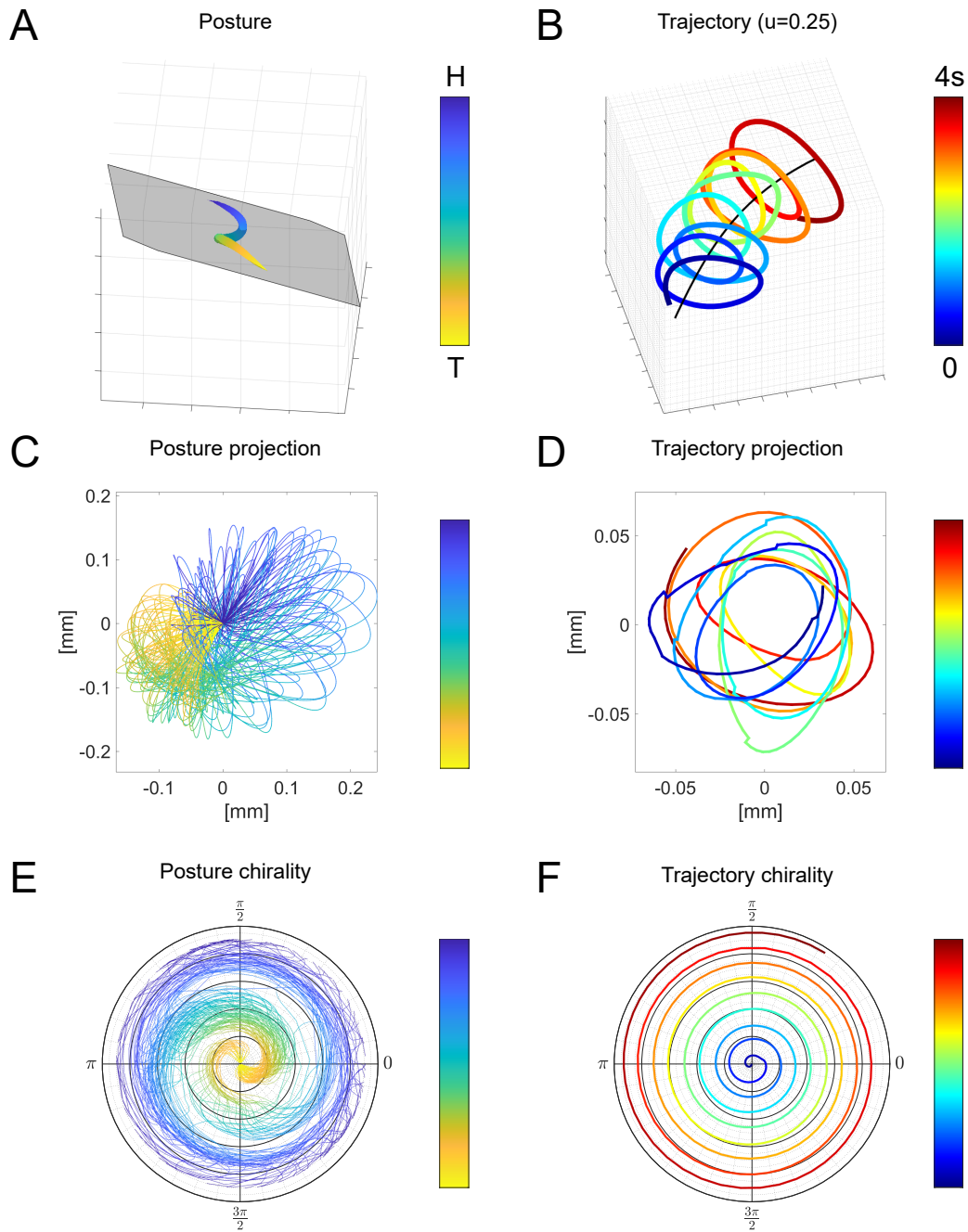


Figure 15. A. a representative 3D posture and a plane fitted to it (grey). B. representative microtrajectory ($u=0.25$) and its centreline (black, see Methods section). C. Projection of posture sequence onto the plane perpendicular to the line connecting the head and tail. D. Projection of each microtrajectory point onto the plane perpendicular to the local tangent of the centreline. E. Phase plane of projected postures showing angles between body segments from tail (yellow) to head (blue). F. Phase plane of projected trajectories. G-H. Body curvature (at $u=0.25$, G) and microtrajectory curvature (at $u=0.25$, H) over time.

Figure 16: Counterclockwise coiling

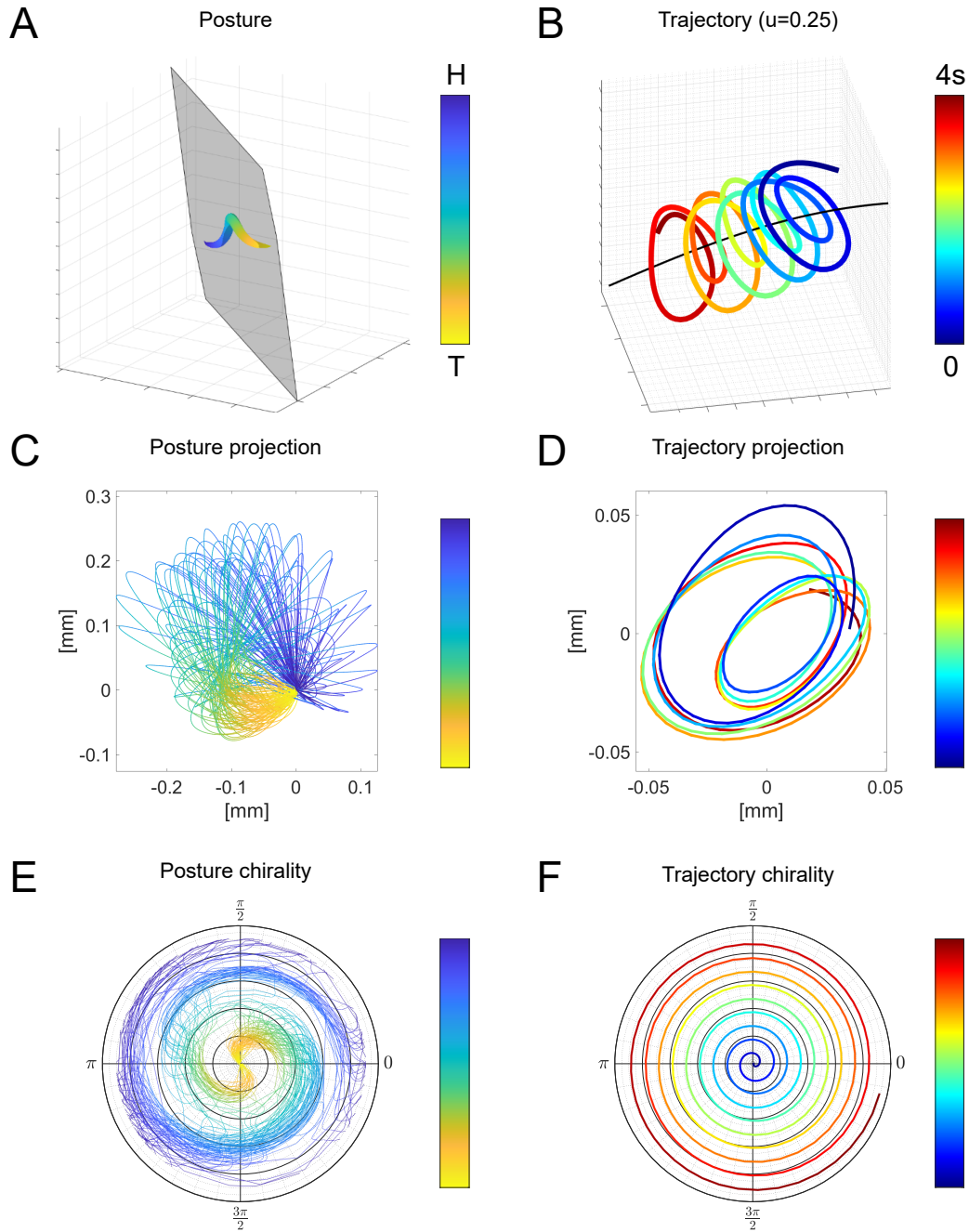


Figure 16. A. a representative 3D posture and a plane fitted to it (grey). B. representative microtrajectory ($u=0.25$) and its centreline (black, see Methods section). C. Projection of posture sequence onto the plane perpendicular to the line connecting the head and tail. D. Projection of each microtrajectory point onto the plane perpendicular to the local tangent of the centreline. E. Phase plane of projected postures showing angles between body segments from tail (yellow) to head (blue). F. Phase plane of projected trajectories. G-H. Body curvature (at $u=0.25$, G) and microtrajectory curvature (at $u=0.25$, H) over time.

Figure 17: Infinity

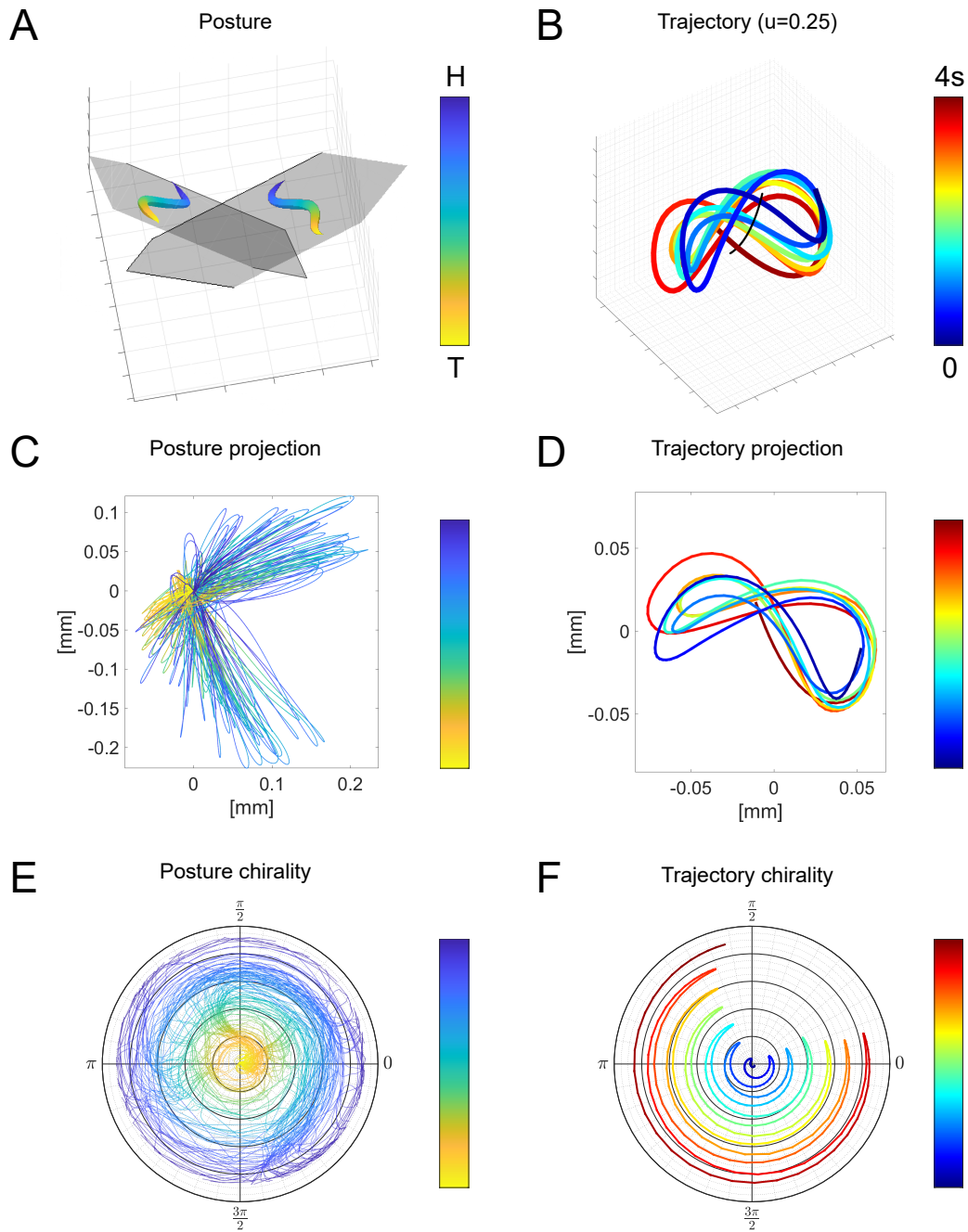


Figure 17. A. a representative 3D posture and a plane fitted to it (grey). B. representative microtrajectory ($u=0.25$) and its centreline (black, see Methods section). C. Projection of posture sequence onto the plane perpendicular to the line connecting the head and tail. D. Projection of each microtrajectory point onto the plane perpendicular the local tangent of the centreline. E. Phase plane of projected postures showing angles between body segments from tail (yellow) to head (blue). F. Phase plane of projected trajectories. G-H. Body curvature (at $u=0.25$, G) and microtrajectory curvature (at $u=0.25$, H) over time.

In addition to posture and trajectory chirality, I computed extrinsic posture rotation and signed body curvature in order to further characterise postural dynamics for each of the identified locomotion patterns. Extrinsic body rotation was measured by fitting a plane to individual postures (using the SVD method, see Methods section), and computing the signed change in angle between planes in consecutive time points. This metric may be indicative of the rotation of the worm's intrinsic coordinate system relative to the lab (Fig. 18C). Signed body curvature was computed by changing the sign of each second peak in the graph of absolute body curvature (Fig. 18D, see Methods section). This sign of the curvature may indicate the separation between dorsal and ventral body bends (see Section 4.6).

The distribution of extrinsic rotation rate indicates that in Coiling, postures rotate at the same chirality, but at half the rate, compared to trajectories (Fig. 18C). In addition, the average of signed body curvature is highest for Infinity and lowest for Crawling, while CW and CCW have similar values in between (Fig. 18D).

Finally, to test whether the four identified locomotion patterns are indeed separate motor gaits, all four metrics (Fig. 18A-D) were used to perform a cluster analysis that is unbiased and in particular independent of manual annotation of behaviour. This was done using a PCA analysis, in which the input data points are the mean and standard deviation of each annotated sub-clip, for each of the four metrics in Fig. 18A-D. Plotting the data points in PCA space using the first two component (PC-1 and PC-2 in Fig. 18E) shows that indeed data points for clips annotated for the same behaviour cluster together. To verify this, a Gaussian mixture model was fitted to this 2D PCA space. This resulted in four distinct clusters that match the classification by manual annotation (Fig. 18E, where ellipses show the clusters detected automatically by the Gaussian mixture model, and the colours indicate manual annotation of behaviour).

Figure 18: Statistical analysis of gait chirality and gait classification

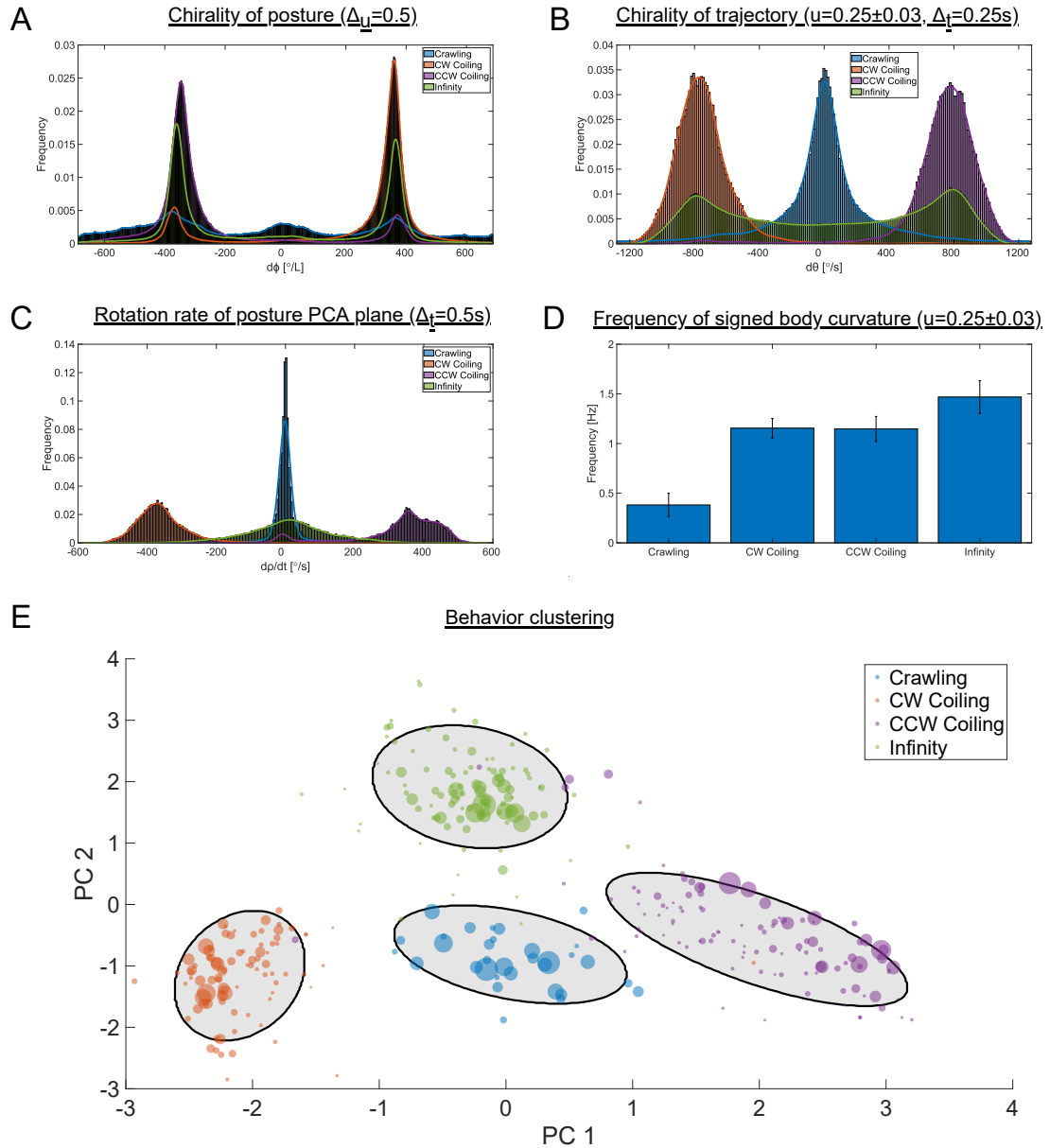
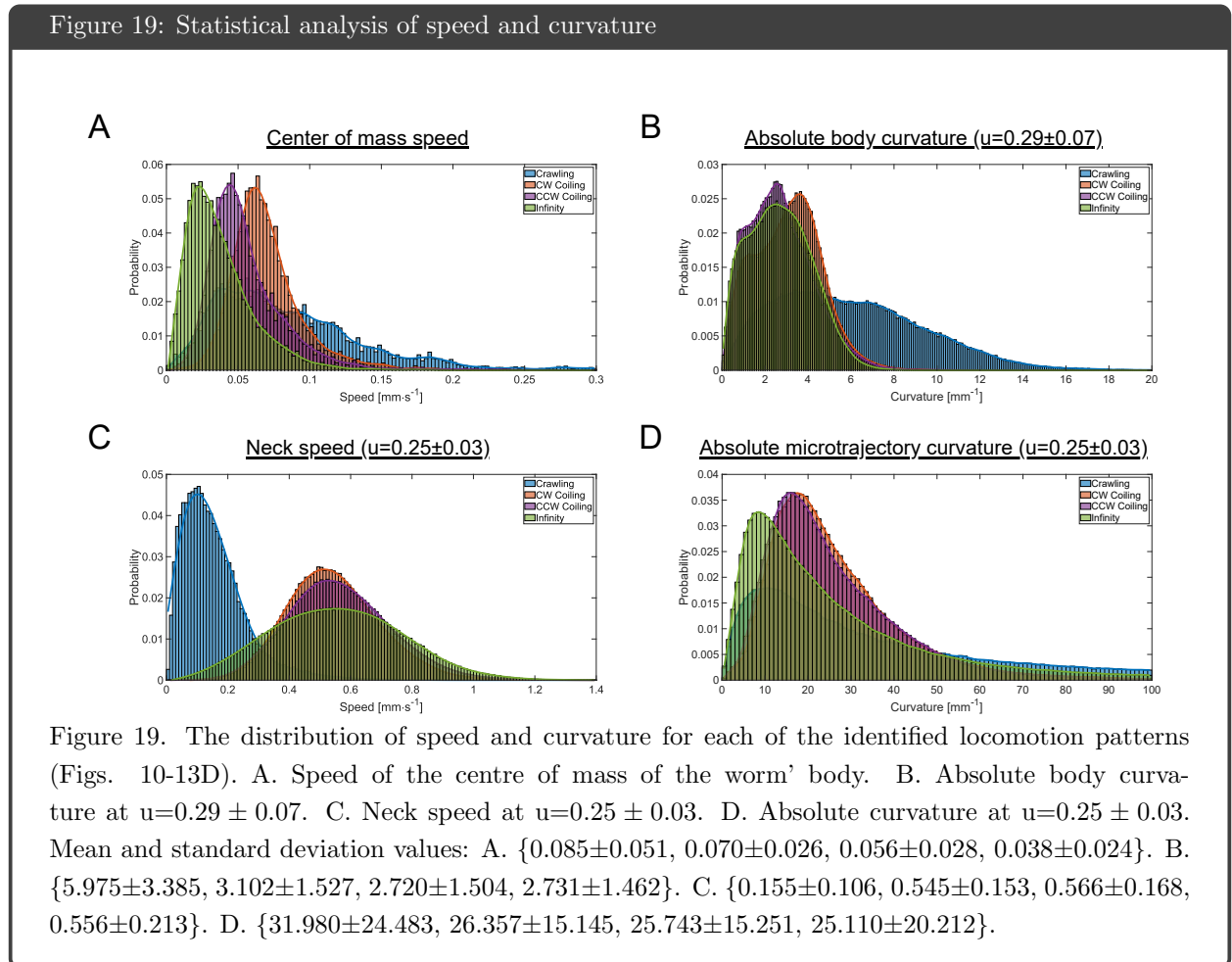


Figure 18. A. Distribution of rotation orientation (chirality) of projected postures. B. Distribution of rotation orientation of projected trajectories of the neck region ($u=0.25\pm 0.03$). C. Rotation rate of the PCA plane fitted to individual postures (see Methods section), using a time window of 0.5 seconds. D. Mean frequency of signed body curvature at $u=0.25\pm 0.03$. E. PCA analysis and clustering of the four identified locomotion patterns using the metrics in A-D (see Methods). The input to the PCA is the mean and standard deviation of each data point in A-D. Only the first two PCA components are used. A Gaussian mixture model is used to automatically detect clusters in PCA space. Mean and standard deviation values: A. $\{-60.5740\pm 372.5422, 228.1084\pm 269.7538, -247.7276\pm 253.0768, -34.2656\pm 348.0372\}$. B. $\{2.7800\pm 343.3444, -749.2396\pm 182.7728, 748.2776\pm 212.8384, 30.5424\pm 645.4128\}$ C. $\{-1.1886\pm 41.5712, -358.7306\pm 77.8086, 329.9468\pm 140.7246, 7.0352\pm 131.9584\}$.

In addition to chirality, I extracted CoM speed, neck speed, and absolute body and microtrajectory curvatures (Fig. 19). The average CoM speed was highest for crawling and lowest for Infinity, with CW and CCW in between (Fig. 19A). Also, the standard deviation of CoM speed for crawling was significantly higher compared to Coiling and Infinity. Mean body curvature was similar in CW/CCW Coiling and Infinity, and their distributions seem to consist of two sub-populations (Fig. 19B). Here too, the standard deviation of body curvature in crawling was significantly higher (Fig. 19B). The neck speed of Coiling and Infinity was significantly higher compared to crawling (Fig. 19C). Note that neck speed mostly reflects motion perpendicular to the direction of CoM motion (i.e., perpendicular to forward direction). Finally, CW and CCW showed similar distributions of absolute microtrajectory curvature, with mean values higher compared to both crawling and Infinity.



4.5 The material frame of the worm during Coiling and Infinity

The 3D recordings obtained by our setup can be used to extract the worm's 3D shape, but they do not contain sufficient information to extract its material frame, that is, its anatomical coordinate system. As a complementary approach, I used 2D fluorescence imaging of a volume containing worms that express GFP in body wall muscles (BWM) in order to obtain a qualitative estimation of the relative orientation of the material frame along the body (i.e., internal twist) and over time with respect the lab coordinate system (i.e., rolling). This was only done for low gelatin concentrations in order to induce Coiling and Infinity behaviours.

First, I noticed that in both Coiling and Infinity, non-planar body bending is most dominant in the head and this pattern decays posteriorly as the body becomes more planar. This is in line with absolute curvature extracted from 3D reconstructions that show maximum curvature at the head region (Fig. 11C, 12C and 13C). Second, along most of the body the direction of maximum curvature was associated with dorsal/ventral body bending (Figs. 20 and 21). Given that the neuromuscular circuit underlying 2D forward locomotion shows left-right symmetry [37, 86], this suggests that active non-planar undulations are generated at the head only and propagate passively towards the tail due to the mechanics, while active dorsoventral pattern generation dominates along most of the body.

Further, I observed that during both Coiling and Infinity the worm rolls, meaning that its internal coordinate system (i.e., material frame) rotates with respect to the lab coordinate system. Because the peaks of dorsoventral body bends were clearly identifiable along the body, I was able to correlate rolling with dorsoventral undulations, which were used as a reference cycle. In Coiling, the worm rolled with a preferred chirality by approximately 2π within each dorsal or ventral body bend (Fig. 20), whereas in Infinity it rolled by approximately $\frac{\pi}{2}$ within each dorsal or ventral bend, with alternating chirality (e.g., CW for a dorsal bend and CCW for a ventral bend, Fig. 21).

Figure 20: Clockwise (CW) Coiling of a worm expressing GFP in muscles

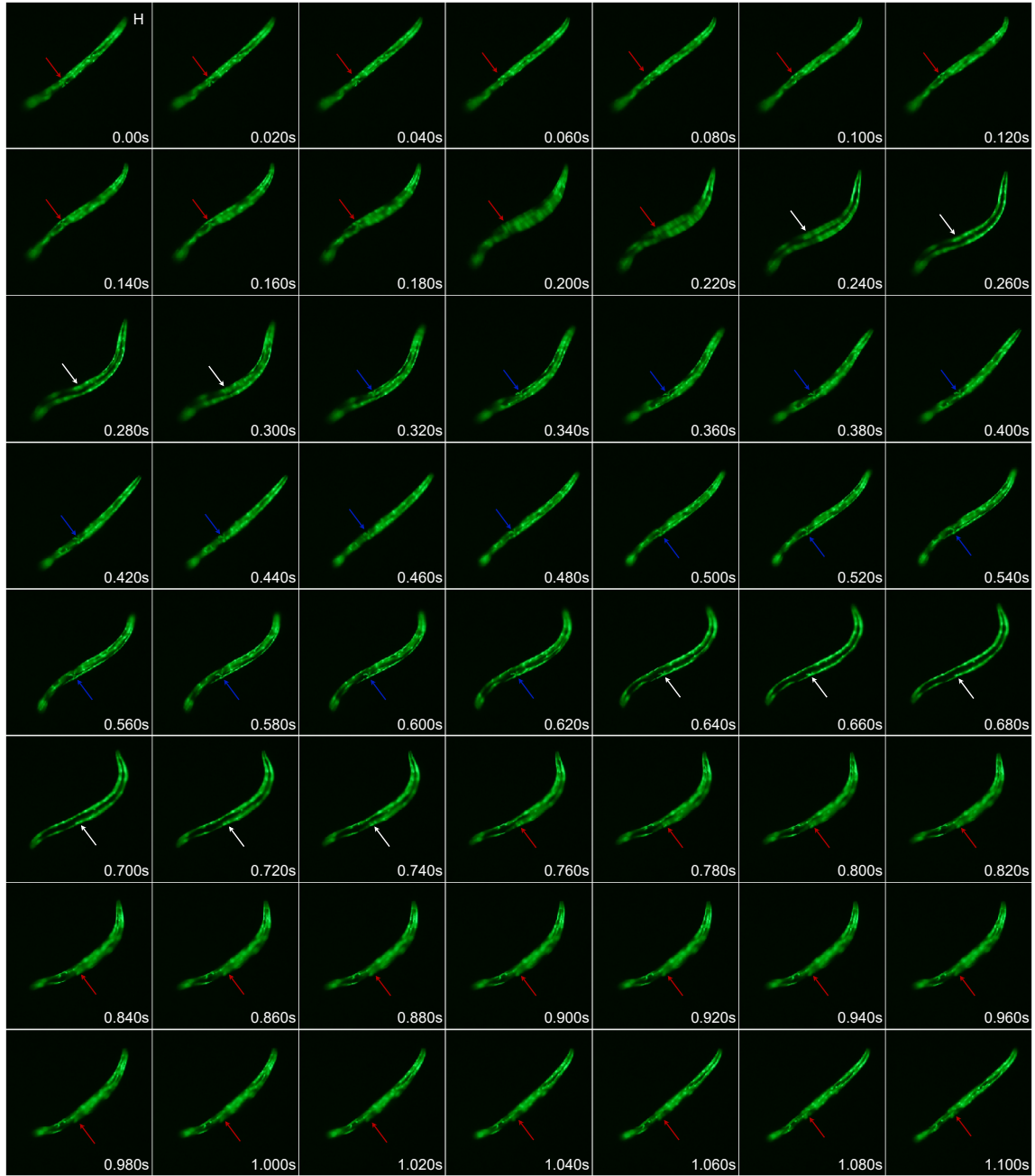


Figure 20. The arrows show the location of the vulva, and the colour indicates whether it is pointing inside (red) or outside (blue) the image, and the white arrow is used when it points parallel to the image plane. At $t=0$, the curvature at the anterior half of the body is zero ($\{\theta_{dv} = 0, \theta_f = 0, \theta_{\mu t} = 0\}$), and the vulva is behind the worm (inside the screen). A ventral bend begins with CW rotation of the frame and reaches its maximum at 0.26s ($\{\theta_{dv} = \frac{\pi}{2}, \theta_f = \frac{\pi}{2}, \theta_{\mu t} = \frac{\pi}{2}\}$), and then relaxes back to zero curvature at 0.46s. The frame has rotated by 180° and the vulva is now at the front ($\{\theta_{dv} = \pi, \theta_f = \pi, \theta_{\mu t} = \pi\}$). This sequence is then repeated for a dorsal bend, also with CW rotation of the frame, returning to the starting posture and orientation at 1.04s ($\{\theta_{dv} = 2\pi, \theta_f = 2\pi, \theta_{\mu t} = 2\pi\}$).

Figure 21: Infinity of a worm expressing GFP in muscles

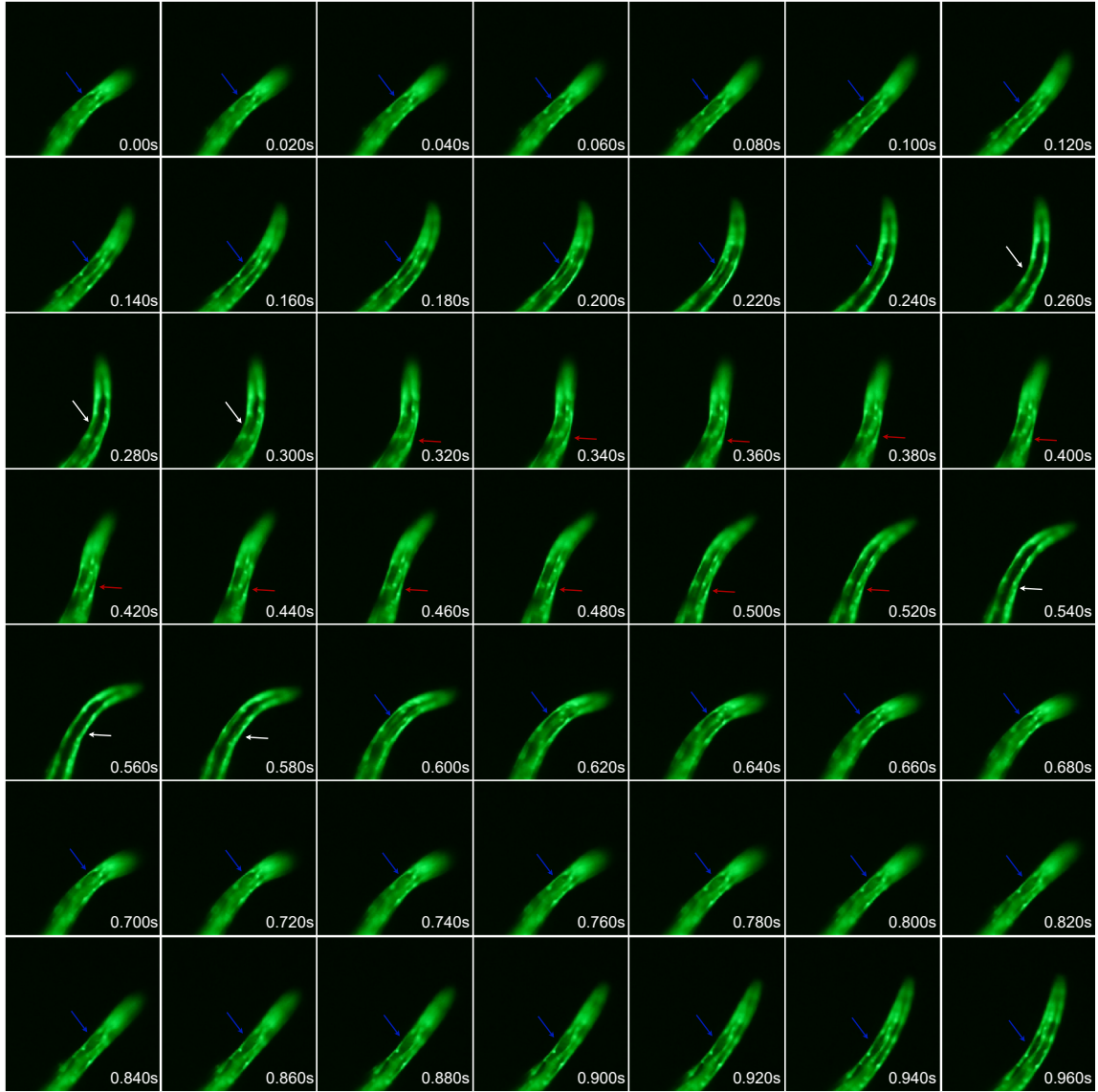


Figure 21. The arrows indicate the dorsal or ventral side of the worm (red or blue) that points outside the image in the neck region, and white when both dorsal and ventral are oriented parallel to the image plane. At $t=0.10\text{s}$, the curvature at the anterior half of the body is zero ($\{\theta_{dv} = 0, \theta_f = 0, \theta_{\mu t} = 0\}$), and the ventral side points up. A ventral bend begins with counterclockwise rotation of the frame, reaches its maximum at 0.20s ($\{\theta_{dv} = \frac{\pi}{2}, \theta_f = \frac{\pi}{4}, \theta_{\mu t} = \frac{\pi}{2}\}$), and then relaxes back to zero curvature at 0.40s . The frame has rotated by 90° , the ventral side is inside the screen and the dorsal side is partially visible at the front ($\{\theta_{dv} = \pi, \theta_f = \frac{\pi}{2}, \theta_{\mu t} = \pi\}$). This sequence is then repeated for a dorsal bend, with clockwise rotation of the frame and microtrajectory, returning to the starting posture and orientation at 0.90s ($\{\theta_{dv} = 2\pi, \theta_f = 0, \theta_{\mu t} = 0\}$). Note that the difference in duration of the visibility of the dorsal and ventral sides is mostly due to the orientation of the worm relative to the camera, and might also be affected by asymmetry in the duration of the dorsal and ventral bends.

Rolling was associated with an internal twist that was highest at the head and lowest at the tail. The internal twist was harder to identify from this data, and I estimate the maximum twist to be $\leq 45^\circ$. Both rolling speed and twist magnitude did not seem uniform, but rather correlated with local dorsoventral body bending. Rolling speed and twist magnitude were highest at the peaks of absolute body curvature (i.e., maximum bending), and lowest when local body curvature was zero.

4.6 Linking 3D postures and trajectories to the worm's internal coordinate system

While microtrajectories contain valuable information that can be used to classify motor gaits, they do not contain information about body postures, with respect to which motor behaviour is defined. To link microtrajectories to the dynamics of body shape and orientation, I characterised the relationship between trajectorial cycles and the cycles of body undulations and the rotation of the worm's material frame with respect to the lab coordinate system. Since the direction of maximum curvature along most of the body was correlated with dorsal and ventral body bends, and since their cycle has a clear beginning and a clear end, I used the cycle of dorsoventral undulations as a reference, to which the other cycles were linked. To do this, I defined three time-dependent variables:

- θ_{dv} describes the cycle of dorsoventral body bending at a single point along the body. Curvature is zero for $\theta_{dv} = \{0, \pi\}$, maximum positive for $\theta_{dv} = \frac{\pi}{2}$ (corresponding to a dorsal bend), and maximum negative for $\theta_{dv} = \frac{3\pi}{2}$ (corresponding to a ventral bend). $\theta_{dv} \in [0, 2\pi]$ corresponds to one period of dorsoventral body bending.
- θ_f describes the rotation angle of the material frame with respect to the lab coordinate system (i.e., rolling).
- $\theta_{\mu t}$ describes the rotation of the microtrajectory in lab coordinates in the plane perpendicular to its centreline (see panel F in Figs. 14-17).

The following is a detailed description of the mutual evolution of those three quantities in the neck region, also summarised in Fig. 22. Note that the chirality of Coiling and Infinity is defined with respect to

microtrajectories, not postures.

Forward clockwise Coiling

During one dorsoventral period, the material frame of the worm completes a 360° rotation with respect to the lab coordinate system (i.e., rolling), and a microtrajectory of two circle-like loops is formed, one associated with a dorsal bend, and the other with a ventral bend (Fig. 22A). Both rolling and microtrajectory progress in a CW direction while postures remain mostly CCW.

Starting from zero curvature $\{\theta_{dv} = 0, \theta_f = 0, \theta_{\mu t} = 0\}$, a dorsal bend begins, with a CW rotation of both the frame and the microtrajectory. Once the worm reaches its maximum dorsal bend (maximum positive curvature), it has rotated its frame by 90° , and formed half a circle-like microtrajectory $\{\theta_{dv} = \frac{\pi}{2}, \theta_f = \frac{\pi}{2}, \theta_{\mu t} = \pi\}$. Next, body curvature starts to decrease until it is zero again. By then, the worm has rotated its frame by another 90° , and formed a full circle-like microtrajectory $\{\theta_{dv} = \pi, \theta_f = \pi, \theta_{\mu t} = 2\pi\}$. Then, a ventral bend begins and reaches its maximum at $\{\theta_{dv} = \frac{3\pi}{2}, \theta_f = \frac{3\pi}{2}, \theta_{\mu t} = 3\pi\}$, and finally, the curvature goes back to zero and a single dorsoventral period is complete $\{\theta_{dv} = 2\pi, \theta_f = 2\pi, \theta_{\mu t} = 4\pi\}$.

The period of a dorsoventral cycle ($\theta_{dv} = [0, 2\pi]$) is ~ 0.8 seconds with a frequency of ~ 1.2 Hz, and this pattern can repeat for many seconds and even minutes. It stops once the worm switches to a different motion pattern, such as a turning manoeuvre or reversal. Microtrajectories often seem elliptic with two curvature peaks within each loop. In CCW Coiling, the reversed pattern is observed, with CCW rolling and microtrajectories and CW postures.

Infinity

In Infinity, during one dorsoventral period the worm rolls back-and-forth in opposite directions by approximately 90° and forms an 8-shaped microtrajectory. Each petal-like loop (“half” 8-shape) of the microtrajectory is associated with a dorsal/ventral bend, alternately. Here too, rolling and microtrajectories progress in the same orientation, however the matching of posture chirality is not yet known.

Starting from zero curvature $\{\theta_{dv} = 0, \theta_f = 0, \theta_{\mu t} = 0\}$, a dorsal bend begins with a CCW rotation of both the frame and the microtrajectory. Once the worm reaches its maximum dorsal bend (maximum positive curvature), it has rotated its frame by 45° , and formed half a petal-shaped microtrajectory

$\{\theta_{dv} = \frac{\pi}{2}, \theta_f = \frac{\pi}{4}, \theta_{\mu t} = \frac{\pi}{2}\}$. Next, body curvature starts to decrease until it is zero again. By then, the worm has rotated its frame by a total of 90° , and formed one petal-shaped microtrajectory $\{\theta_{dv} = \pi, \theta_f = \frac{\pi}{2}, \theta_{\mu t} = \pi\}$. Then, a ventral bend begins with a CW rotation of the frame and the microtrajectory. The ventral bend reaches its maximum at $\{\theta_{dv} = \frac{3\pi}{2}, \theta_f = \frac{\pi}{4}, \theta_{\mu t} = \frac{\pi}{2}\}$, the frame has rotated back by 45° , and another half a petal-shaped microtrajectory has formed. Finally, the curvature goes back to zero, one dorsoventral period is complete, the frame has rotated back to its original orientation, and an eight-shaped microtrajectory has formed $\{\theta_{dv} = 2\pi, \theta_f = 0, \theta_{\mu t} = 0\}$.

The period of a dorsoventral cycle ($\theta_{dv} = [0, 2\pi]$) is ~ 0.6 seconds with a frequency of ~ 1.65 Hz. Similar to Coiling, this pattern can repeat for minutes and it stops once the worm switches to a different motion pattern.

Figure 22: Linking 3D postures and trajectories to the worm's internal coordinate system

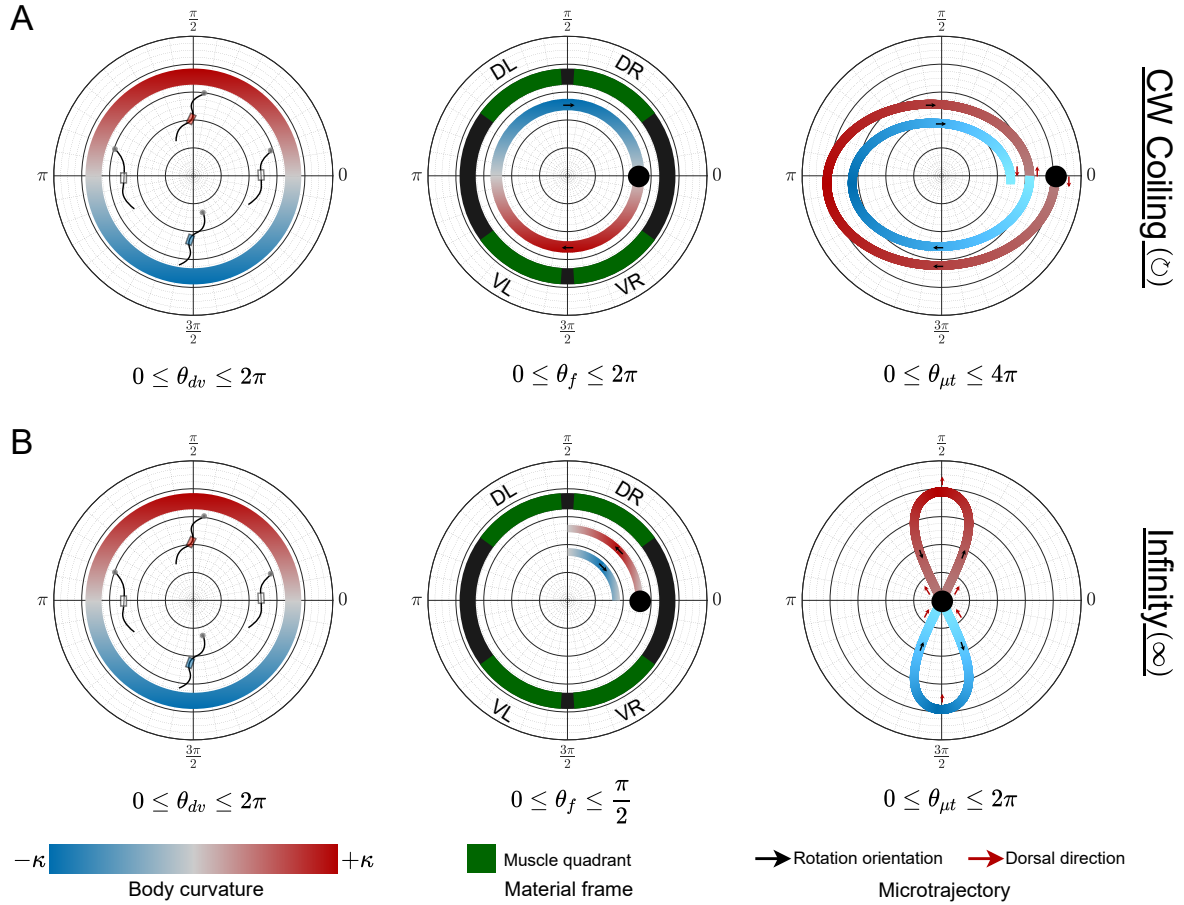


Figure 22. Schematics of the evolution of rolling and microtrajectories with respect to dorsoventral body bending in Coiling and Infinity. left column: curvature phase portrait of dorsoventral body undulations posterior to the head. A dorsal bend is defined as positive curvature (red, maximum at $\theta_{dv} = \frac{\pi}{2}$) and a ventral bend as negative curvature (blue, maximum at $\theta_{dv} = \frac{3\pi}{2}$). Middle column: Rotation of the worm around its long axis with respect to the lab coordinate system (i.e., rolling). Right column: the shape of microtrajectory projected onto the plane perpendicular to its centreline (see panels B,D and F in Figs. Fig. 15 and 17). The direction of motion of the worm's centre of mass is inside the page with increasing $\theta_{\mu t}$ values. A. Forward clockwise (CW) Coiling (see Figs. 11 and 15). Within a dorsoventral period ($\theta_{dv} = [0, 2\pi]$, left), the worm completes a 2π rotation around its long axis ($\theta_f = [0, 2\pi]$, middle), and the microtrajectory forms two circle-like loops, each corresponding to a dorsal or ventral body bend ($\theta_{\mu t} = [0, 4\pi]$). B. Forward Infinity (see Figs. 13 and 17). During a dorsoventral period ($\theta_{dv} = [0, 2\pi]$, left), the worm alternately rotates around its long axis by 90° CCW and then 90° CW ($\theta_f = [0, \frac{\pi}{2}]$, middle), and the microtrajectory forms an eight-shape. Here CCW rotation corresponds to a dorsal bend (red, $\theta_{\mu t} = [0, \pi]$), and CW rotation to a ventral bend (blue, $\theta_{\mu t} = [\pi, 2\pi]$). Note that the matching between CCW-dorsal and CW-ventral is arbitrary and does not imply that this combination is possible or that the opposite combination is not.

4.7 Methods

Data pre-processing

All worm midlines were smoothed using the “smoothn” algorithm [295] and up-sampled to have 128 equidistant points using cubic spline interpolation. The position of the end-points (i.e., head and tail) were fixed and were not affected by these operations. The final postures were validated by projecting them onto the camera views and checking that they match the projected worms.

A microtrajectory is defined as the trajectory of a single midline point over time. Each microtrajectory was smoothed (using the “smoothn” algorithm [295]) and up-sampled to have 4x the original number of time points using cubic spline interpolation. For all microtrajectories of the crawling behaviour (Fig. 10), a higher smoothing parameter was used compared to Coiling and Infinity (since in crawling the arc-length of the trajectory per unit time is significantly longer compared to Coiling and Infinity). The shape of the final trajectories was validated against the original trajectories.

Curvature

Absolute curvature (κ) was computed for each point along midlines and trajectories (Eq. 4.1). In some cases, signed curvature was computed for postures by detecting maxima in the graph of absolute curvature at individual body points over time, and changing the sign of the curvature to negative for even peaks.

$$\kappa = \left| \frac{d\vec{T}}{ds} \right| \quad (4.1)$$

where $d\vec{T}$ is the tangent vector at the point where curvature is calculated, and ds is the arc-length associated with that point.

Frequency

The frequency of body curvature was computed using one-sided Fourier transform, first for each midline point separately, and then averaged across midline points in the frequency domain.

Plane fitting, non-planarity and extrinsic posture rotation

Each worm posture was fitted with a plane by applying the singular value decomposition (SVD) method to the discretised midline. All midline points were used and were equally weighed. The method fits a plane to a point cloud by minimising the distance of all points from the plane. This plane was used to compute non-planarity and extrinsic posture rotation. Non-planarity of individual postures is defined as the average of the minimal Euclidean distance of all midline points from the fitted plane.

Extrinsic posture rotation was defined as the signed change in angle between planes in consecutive time points. For each midline, the mean tangent was first projected onto the fitted plane. The resulting vector, T_i , is perpendicular to the plane normal N_i (since T_i lies in the plane). To obtain the signed change in angle between planes, all vector pairs (T_i, N_i) were rotated such that T_i is aligned with T_1 (the mean tangent of the first midline in the sequence). This was done using the “vrrotvec” MATLAB function which finds the minimal 3D rotation needed to align one vector with another. This resulted in all normal vectors projected onto the same 2D coordinate system, while approximately preserving their relative orientation. Then, the angle of each projected normal vector was computed by conversion to polar coordinates (using the “atan2” MATLAB function). Finally, the minimal angle difference between projected normal vectors was computed, and its sign was defined according to the rotation needed to align each vector with the next in the direction of the minimal angle.

Chirality

To find posture chirality, each posture was projected onto the line connecting the tail to the head, resulting in a 2D closed loop with its endpoints at the origin. Then, the angle ($\phi=[0,2\pi]$) corresponding to each projected midline point was calculated using the arctan function (using the MATLAB function “atan2”; for example see panels A, C and E in Figs. 14-17). Chirality was then defined as the change in this angle along the midline ($d\phi$). For statistical analysis, $d\phi$ was averaged along the midline using a half body length sliding window (for example see Fig. 18A).

To find microtrajectory chirality, each point along the trajectory was projected onto the plane perpendicular to the local tangent of the trajectory centreline (for example see panels B, D and F in Figs. 14-17). The centreline of a trajectory is defined as the set average coordinates of each midline point over time from

tail to head. Then, the angle ($\theta=[0,2\pi]$) corresponding to each projected midline point was calculated using the arctan function. Chirality was then defined as the change in this angle over time ($d\theta$). For statistical analysis, $d\theta$ was considered only at the neck region ($u=0.25\pm 0.03$, where u is body coordinate from head to tail, and the total body arc-length is normalised to 1) and averaged over time using a sliding window of 0.25s (for example see Fig. 18B).

Analysed data

The total duration of analysed data for each behaviour was [6.8, 6.7, 7.3, 7.5] minutes, corresponding to crawling, CW Coiling, CCW Coiling and Infinity, respectively. All analysed recordings were annotated for behaviour as a qualitative description of motion patterns. This was done by assigning non-overlapping frame ranges with numerical indices corresponding to behavioural descriptors from a pre-defined ontology dictionary. This required looking at posture dynamics, microtrajectories at different points along the body, and the kymogram of absolute body curvature. The annotation was done using a custom tool included in the software described in section 3.7.

4.8 Discussion

In this chapter I performed quantitative analyses of the data extracted from 3D recordings of *C. elegans* locomotion (see chapter 3). Four main forward locomotion patterns have been identified and defined: crawling, clockwise (CW) and counterclockwise (CCW) Coiling and Infinity.

Crawling

Crawling through sinusoidal undulations in the dorsoventral plane is presented first as it resembles 2D crawling and provides an intuitive link to previous works in planar settings. Crawling was observed mostly in high gelatin concentrations (2%-4%, corresponding to $100 \leq G' \leq 600$ Pa, see Table 4) that resemble the stiffness of 2% agar typically used in planar settings. However, a closer examination revealed that crawling behaviour in 3D is highly non-planar. While 2D and 3D crawling might share the same neural control mechanisms, the difference in planarity demonstrates the importance of the environment and specifically here the lack of near-solid substrate.

Coiling and Infinity

Coiling behaviour is most easily identified by circle-like microtrajectories with a preferred chirality, whereas in Infinity microtrajectories alternate between clockwise (CW) and counterclockwise (CCW) (Figs. 11-13, and 15-17). In Coiling and Infinity undulation frequency is 2-3 times higher compared to crawling (see Figs. 19A and 18D). Since trajectories are not sufficient to define motor behaviours, they must be linked to postures. Note that CW and CCW were defined with respect to microtrajectories, not postures. Surprisingly, I found that in Coiling, chiral postures generate trajectories with opposite chirality (Fig. 18A and 18B). However, looking at the distributions of posture chirality, both CW and CCW Coiling show a smaller peak of opposite chirality (Fig. 18A). This suggests that within each Coiling cycle, chirality is significantly biased towards CW or CCW, but a sub-population of postures have the opposite chirality. This may offer a mechanistic link between Coiling and Infinity. For Infinity, matching posture and microtrajectory chirality was harder to resolve, and more work is needed to characterise their relationship.

Twisting and rolling

To characterise the internal twist and rolling of the worm during Coiling and Infinity, I recorded worms in a volume that express a fluorescent marker in body wall muscles. This was used to estimate the change in orientation of the worm’s material frame (i.e., the frame defined by its internal coordinate system) along the body (i.e., internal twist) and with respect to the lab coordinate system (i.e., rolling).

Despite the non-planar undulations in Coiling and Infinity, the direction of maximum curvature was associated with the dorsal and ventral directions along most of the body, suggesting that 3D gaits build on 2D pattern generation, rather than using a completely distinct motor program. I combined the material frame data with previous analyses to link the worm’s internal coordinate system to postures and trajectories. In particular, I describe the mutual evolution of rolling and microtrajectories with respect to dorsoventral body bends.

In Coiling, the worm rotates its material frame by π and completes one circle-like microtrajectory loop within each dorsal or ventral body bend (Fig. 22A). In Infinity, the trajectory forms an 8-shape within a dorsoventral period such that one petal-like loop (“half” 8-shape) corresponds to a dorsal bend and the other to a ventral bend. The worm rotates its internal frame only by $\frac{\pi}{2}$ within each loop with alternating chirality from one loop to the next (Fig. 22B). Note that Infinity may also have two modes, as CW loops may correspond to a dorsal or a ventral body bend. In addition, the kymograms of absolute curvature of Coiling and Infinity show an interesting pattern that deviates from the uniform wave propagation seen in 2D and 3D crawling (see Figs. 11-13). This pattern is likely to reflect the combination of curvature waves that propagate posteriorly in the dorsoventral and left-right direction. Biomechanical modelling work may use these unique patterns as signatures of Coiling and Infinity. Capturing these locomotion patterns in biomechanical frameworks can be used to decompose the curvature into its dorsoventral and left-right components, which can in turn be used to find the muscular control underlying those behaviours.

The internal twist during Coiling and Infinity was harder to estimate from this data and more work is needed to improve its estimation. Such work should focus both on improving the quality of the recordings and the computer vision methods used to estimate the twist. A better estimation of the internal twist may be used to update our knowledge about the material parameters of the worm in general and specifically during active motion.

Gait variations, 3D reversals and turning manoeuvres

High variation was observed in both Coiling and Infinity behaviours, both within and across sequences. Some variations show periodicity that may be associated with asymmetry in dorsoventral body bends, while others are more sparse and do not seem to follow a clear pattern. First, in Coiling sequences, the radius of microtrajectory loops sometimes seems to alternate between two sizes. In Infinity, the size of the two petal-like loops that make up a single 8-shape are often asymmetric. Furthermore, in both Coiling and Infinity loop size changes along the body. Other variations include periodic alternation between Coiling and Infinity within each dorsoventral period, and periodic alternation of the plane of undulation. While gait variations have not been explicitly addressed in this work, they may be highly important for gaining mechanistic insights into the neural and muscular control that underlie those behaviours. In particular, gait variation might offer clues as to whether Coiling and Infinity form a continuum or are separate motor gaits, possibly also driven by distinct neural programs.

All worms seem to be capable of both CW and CCW Coiling, as well as Infinity. This suggests that forward locomotion gait selection depends on internal state and external conditions and is not hard-wired. However, individual worms often seem to have a preferred Coiling chirality, and more work is needed to characterise chirality preference across individuals. Switches and transitions between forward locomotion gaits were also observed and may provide mechanistic insights. This includes switching between CW/CCW Coiling, between Coiling and Infinity, as well as short crawling or turning manoeuvres (typically up to 2s) that interrupt Coiling and Infinity sequences, and are characterised by a significant increase in forward speed.

In addition to forward locomotion, reversals were observed for each of the four behavioural classes (see Figs. 10-13). This was surprising considering that only the neuromuscular anatomy in the head has the left-right symmetry-breaking needed for feedforward 3D neural and muscular pattern generation [37, 86, 296]. Future work may test whether these patterns are actively generated by the tail or stem purely from passive mechanical effects. The correlation between the type of reversal and the type of forward locomotion that precedes it might offer some clues. Different turning manoeuvres were also observed, and they resembled crawling in some cases, while in other cases they were Coiling-like. Those may be investigated and properly defined in future works.

5 Neural modelling of 3D locomotion

In this chapter I model the neuromuscular control of the head of the worm that underlies the motor behaviours introduced in chapter 4. I start by presenting a biologically-grounded single-cell model that I developed to capture the intrinsic dynamics of the plateau potential RMD motor neurons, based on electrophysiological recordings (Fig. 24) [70]. I then explore the dynamics of ensembles of those model neurons connected via chemical and electrical synapses and find physiological regimes that give rise to spontaneous oscillatory activity. In *C. elegans*, four of the six RMD neurons form neuromuscular junctions (NMJ) onto body wall muscles (BWM) such that each RMD dominantly innervates a different muscle quadrant (Fig. 23). I show that the RMD circuit may be intrinsically capable of spontaneously generating sequential RMD oscillations that give rise sequential muscle activations of the four BWM quadrants with a preferred chirality (Fig. 25).

While mechanisms for synchrony have been explored in depth in spiking neurons, plateau potential and/or graded transmission regimes received much less attention. I next use the single-neuron model developed here to explore mechanisms for synchronisation and gait switching in a simple system of four neurons. I find regimes in which electrical coupling and inhibition work synergistically to generate stable or unstable synchrony that may underlie a spontaneous switch mechanism for motor gaits (Fig. 26).

I then take the insights gained from this simple system back to *C. elegans*, and test an alternative hypothesis for sequential RMD activations that requires them to be externally driven by the SMD neurons, assuming that the RMD circuit is intrinsically inclined to left-right pattern generation. In particular, I demonstrate how oscillatory activity in the proprioceptive SMD neurons may synchronise with that of RMD to destabilise left-right oscillations and enforce a dorsal-ventral phase, leading to sequential RMD activations that are associated with preferred chirality in muscle activation (Fig. 27).

5.1 Introduction

In its natural habitat, *C. elegans* manoeuvres through 3D complex environments with varying physical and chemical properties. However so far it has been studied almost exclusively in 2D settings (i.e., on a planar agar surface). Despite extensive characterisation of the worm’s locomotion in 2D and profound insights about its underlying biomechanics and neural control, this may have biased our investigation, as most characterised behaviours in *C. elegans* are planar, with the exception of head lifting [80, 81], roll manoeuvres [82] and roller mutants [83, 84]. As a result, locomotion and navigation models are largely restricted to planar dorsoventral undulations [27, 30, 31, 239].

While the neuromuscular anatomy in the ventral nerve cord indicates left-right symmetry (Fig. 23A) [37, 75, 86], suggesting that indeed feedforward pattern generation is restricted to undulations in the dorsoventral plane, the head is not restricted in the same way and contains more complex circuitry that breaks this symmetry [37, 86]. Several candidate head motoneurons, sensory neurons and interneurons have been identified and correlated with forward locomotion in 2D [37, 62, 75, 297, 298]. In particular, the head motor neuron classes RMD, SMD, SMB and RME, consists of four or six interconnected neurons, where each cell dominantly forms neuromuscular junctions (NMJ) onto body wall muscles (BWM) in a different quadrant and were implicated in the control of head and neck bending (Fig. 23B-C and 23E-F) [37, 62, 86].

The RMD circuit consists of six cholinergic motoneurons in the nerve ring of *C. elegans* that form neuromuscular junction with the anteriormost two rows of body wall muscles (BWM). They express the ACC-1 (acetylcholine-gated chloride channel 1) receptors which makes RMD-RMD chemical synapses inhibitory [37, 68, 227]. In contrast to the left-right symmetry in the ventral cord motor circuit along the body, four of the RMD neurons form excitatory neuromuscular junctions (NMJ), each dominantly onto muscles in a different quadrant (RMDDL \rightarrow DR, RMMDR \rightarrow DL, RMDVL \rightarrow VR, RMDVR \rightarrow VL, where D=dorsal, V=ventral, L=left and R=right), while the other two (RMDL and RMDR) form dorsal-ventral symmetric NMJs on opposite left-right sides (Fig. 23C). Three RMD pairs are connected via reciprocal inhibition, and gap junctions couple the neurons on each dorsal-ventral side (Fig. 23C). All this suggests that RMD play a role in non-planar head pattern generation [37, 68, 86].

The RMD neurons were found to be unnecessary for normal forward locomotion, although they are necessary for the aversive head-withdrawal reflex and for foraging (high frequency movements of the head) [62, 210, 297, 299], and RMD-ablated mutants show a higher reversal rate [62]. However, these results were obtained in 2D settings, and it is unclear whether they extend to 3D environments that lack a near-solid substrate. The RMD neurons receive glutamatergic, excitatory synaptic inputs from two classes of mechanosensory neurons: OLQ and IL1, that are also necessary for the aversive head-withdrawal reflex and for foraging [62, 210, 297, 299]. The IL1 neurons form NMJ onto head BWM, although their electrical coupling and the absence of chemical synapses suggest that they do not generate periodic patterns (Fig. 23D). The RMD neurons also receive significant synaptic inputs from RIA and SMD (Fig. 23H-I) [37, 68, 86]. RIA function mostly as interneurons, integrating inputs from multiple sensory neurons (thermal in particular) which leads to a behavioural response [62, 298]. They send extensive excitatory synaptic inputs to both RMD (Fig. 23I) and SMD, and were suggested to modulate their frequency and control forward runs and turns [37, 62, 68, 86, 298].

The SMD circuit consists of four cholinergic neurons that form excitatory NMJ onto head and neck muscles (most dominantly onto rows 3-8), and form reciprocal inhibition connectivity between one another (Fig. 23B), which suggests a role in pattern generation [37, 68, 86]. Indeed SMD activity was shown to be correlated with head bending during forward locomotion, and ablation of SMD neurons results in more reversals and no omega turns [62, 65, 232]. Furthermore, SMD were shown to be proprioceptive, meaning that their activity is modulated by the shape of the body through stretch-sensitive ion channels. Specifically their expression of the TRP-1 and TRP-2 mechanosensory channels is necessary for SMD-body bending synchrony, and genetic ablation of both channels specifically in SMD causes a ventral bias, resulting in worms moving in circles [232]. SMD also form gap junctions and send inhibitory chemical synapses to RMD (Fig. 23H) [37, 68, 86]. The mutual role of these two motor neuron classes in locomotion is not well understood. Since SMD were shown to be highly correlated with dorsoventral body bending during forward locomotion and entrained by them [62, 65, 232], and since RMD connectivity suggests a bias towards left-right oscillations, it is possible that SMD-RMD connectivity is used to synchronise RMD pattern generation with dorsal-ventral pattern generation in SMD and the rest of the body.

While the intrinsic dynamics and the role in 2D locomotion of both RMD and SMD have been studied

both experimentally and in modelling works, their role in 3D locomotion has not been addressed yet [30, 37, 62, 65, 68, 232, 239, 259]. Here, I model the neural control of the head in 3D locomotion, focusing specifically on the control of the motor behaviours introduced in chapter 4.

Figure 23: Neuromuscular synaptic connectivity in candidate 3D locomotion head circuits

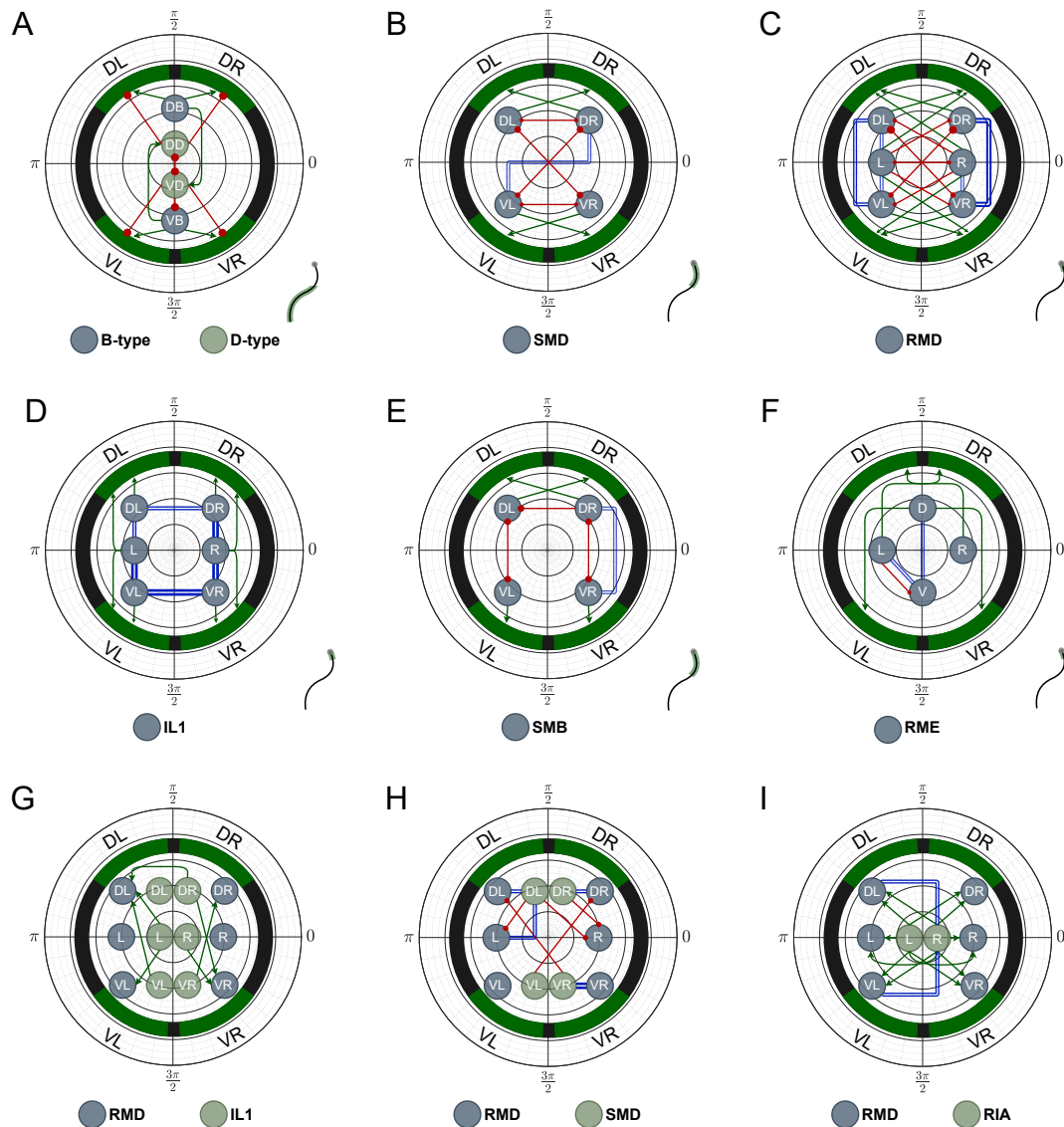


Figure 23. A-F. Simplified neuromuscular anatomy of the B-type and D-type neurons (A), SMD, (B) RMD (C), IL1 (D), SMB (E) and RME (F). G-I. Simplified synaptic connectivity to RMD from IL1 (G), SMD (H) and RIA (I). Muscles are shown as green arcs, excitatory chemical synapses are shown as green arrows, inhibitory chemical synapses are shown as red lines with a circle on the side of the inhibited neuron/muscle, and electrical synapses (gap junctions) are shown as blue double lines. In A-F, the worm diagram on the bottom-right shows the approximate body region of body wall muscles (in green) controlled by the neurons in the main diagram. B-type and D-type neurons (in A) are shown to demonstrate the difference in complexity and symmetry between the motor circuit along the body and in the head. The connectivity data is based on [37, 86].

5.2 Results

5.2.1 A biologically-grounded single-neuron model accurately captures RMD intrinsic dynamics

The 3D behaviours introduced in chapter 4 provide the first step in the investigation of *C. elegans* locomotion in a volume. Understanding how the worm generates 3D locomotion patterns and how it switches between them, requires a better understanding of the underlying neuromuscular control. Despite the vast knowledge about *C. elegans* genetics, development, anatomy and physiology, the intrinsic dynamics of individual neurons is largely unknown. Most *C. elegans* neurons do not fire action potentials, but rather show a graded response to excitatory and inhibitory inputs [70, 205, 229]. Mathematical modelling of biological neurons is often used to capture neural dynamics observed in living organisms. Such models provide a formal framework for testing assumptions and hypotheses, and they can be simulated computationally and be used to make testable predictions.

The unique characteristics of the RMD motor circuit make it a great candidate for the neural control underlying non-planar head pattern generation, that then passively propagates posteriorly and lead to 3D body postures and trajectories. The neuroanatomy and electrophysiology data available for the RMD neurons provide strong constraints that can be used to narrow down the parameter space of mathematical models that aim to capture specific aspects of its neural dynamics. Current-clamp recordings are widely used to characterise the dynamics of individual ion channels and cells [69]. In this technique current is injected into the cell through an electrode that is also used to record its membrane potential over time. Mellem et al. used this technique to inject different patterns of currents into single RMD neurons in extracellular fluid (ECF) conditions. They found that RMD are plateau potential neurons that can remain stable at both -70mV and -35mV, and that this bistability is $\text{Na}^+/\text{Ca}^{2+}$ -dependent [69, 70].

To further characterise the RMD neurons and their role in 3D motor pattern generation, I developed a single-cell model that captures their neural dynamics. The model addresses RMD current-voltage relationship at the whole-cell level and is constrained by electrophysiological recordings in RMD [70]. The model however does not consider sub-cellular components, such as ion channels or specific ionic currents, that are outside the prediction scope of the model. The importance of accurately capturing intrinsic RMD dynamics in a

computational model is motivated by the opportunity to learn about its dynamics in wider contexts, and to distill mechanistic principles that may be shared by other neurons and other organisms. The strong constraints on single-cell RMD dynamics also constrain pattern generation in an ensemble of RMD neurons, and in particular the parameters for the dynamics of chemical and electrical synapses. Such biologically-grounded models can be integrated into more complex models that contain other neurons, muscles, and mechanical context including the material properties of *C. elegans* body and its environment.

The development of this model builds on previous work by Boyle et al. that developed a model of the RMD based on the same electrophysiology data ([70]) and used to model *C. elegans*' forward locomotion motor circuit [30]. Both models show bistability and hysteresis (state-dependent threshold for depolarisation/hyperpolarisation, see the Discussion section for more details). Here, the model accurately captures RMD dynamics in response to different perturbations, as well as in different ECF conditions, as indicated by current-clamp recordings (see Methods).

The model consists of two ordinary differential equations. The first equation describes the cell's membrane potential, whereas the second describes a slower time-scale response (Eq. 5.1- 5.3). The neuron's fast response was defined as a piecewise function, and it consists of two linear and two quadratic parts (Eq. 5.4, Fig. 24A and Table 5). An additional parameter d_I is used to capture RMD dynamics in different ECF conditions. All model parameters were manually adjusted to fit the model to the experimental data in [70] (Table 5).

$$C \frac{dv}{dt} = g \cdot (f(v) - d_I) + I_{\text{syn}} - s \cdot s_{01} \quad (5.1)$$

where v is membrane potential, C is membrane capacitance, g is the membrane conductance, I_{syn} is synaptic input current (or injected current), $f(v)$ is the fast nullcline (Eq. 5.4) and d_I is a parameter for ECF condition (Table 5). The variable s models the slow response and s_{01} is a binary variable (Eq. 5.3-5.4).

$$\frac{ds}{dt} = \alpha \cdot s_{01} \quad (5.2)$$

$$s_{01} = \begin{cases} 1, & \text{for } (L \leq V < T) \\ 0, & \text{otherwise} \end{cases} \quad (5.3)$$

$$f(v) = \begin{cases} m_1(-v + L), & \text{for } (x < L) \\ m_2(v - L)(v - T), & \text{for } (L \leq V < T) \\ m_3(v - H)(v - T), & \text{for } (x < H) \ \& \ (x \geq T) \\ m_4(-v + H), & \text{for } (x \geq H) \end{cases} \quad (5.4)$$

where L is the resting potential, H is the plateau potential and T is the depolarisation threshold (Table 5).

The model successfully captures RMD dynamics as indicated by current-clamp experiments in [70], for multiple input current steps (Fig. 24B-C) and for different ECF conditions (Fig. 24D-G). A single parameter change, d_I , captures RMD dynamics in Na^+ -free ECF (Fig. 24D-E) and in normal ECF following Na^+ -free ECF (Fig. 24F-G). The values used for up/down steps are identical in all simulations (Fig. 24C, 24E and 24G). These values are similar but not identical to the values used in the experiment, and were adjusted to capture interesting model dynamics including those that are comparable to the current-clamp recordings.

The model is further used to make predictions for current-clamp experiments that have not yet been tested in-vivo (Fig. 24H-I). Model predictions (for normal ECF) include voltage responses to sine wave current inputs with either fixed frequency (Fig. 24H) or fixed amplitude (Fig. 24I). The model neuron shows a non-linear graded response to input current across a wide range of frequencies and amplitudes.

Symbol	Value	Description
C	7pF	Membrane capacitance
g	1nS	Membrane conductance
L	-70mV	Resting potential
T	-45mV	Depolarisation threshold
H	-35mV	Plateau potential
a	0.0011	Desensitisation rate constant
m_1	0.7	
m_2	1/81	
m_3	-1/30	
m_4	0.17	
d_I	0pA	Normal ECF
d_I	3pA	Na^+ -free
d_I	1pA	Normal ECF following Na^+ -free

Table 5. Single-cell RMD model parameters. ECF = extracellular fluid. The values for d_I are for different ECF conditions. The last condition is normal ECF after the it was normal, then replaced with Na^+ -free ECF, and then replaced back to normal ECF.

Figure 24: A biologically-grounded single-neuron model accurately captures RMD intrinsic dynamics for different current inputs and ECF conditions

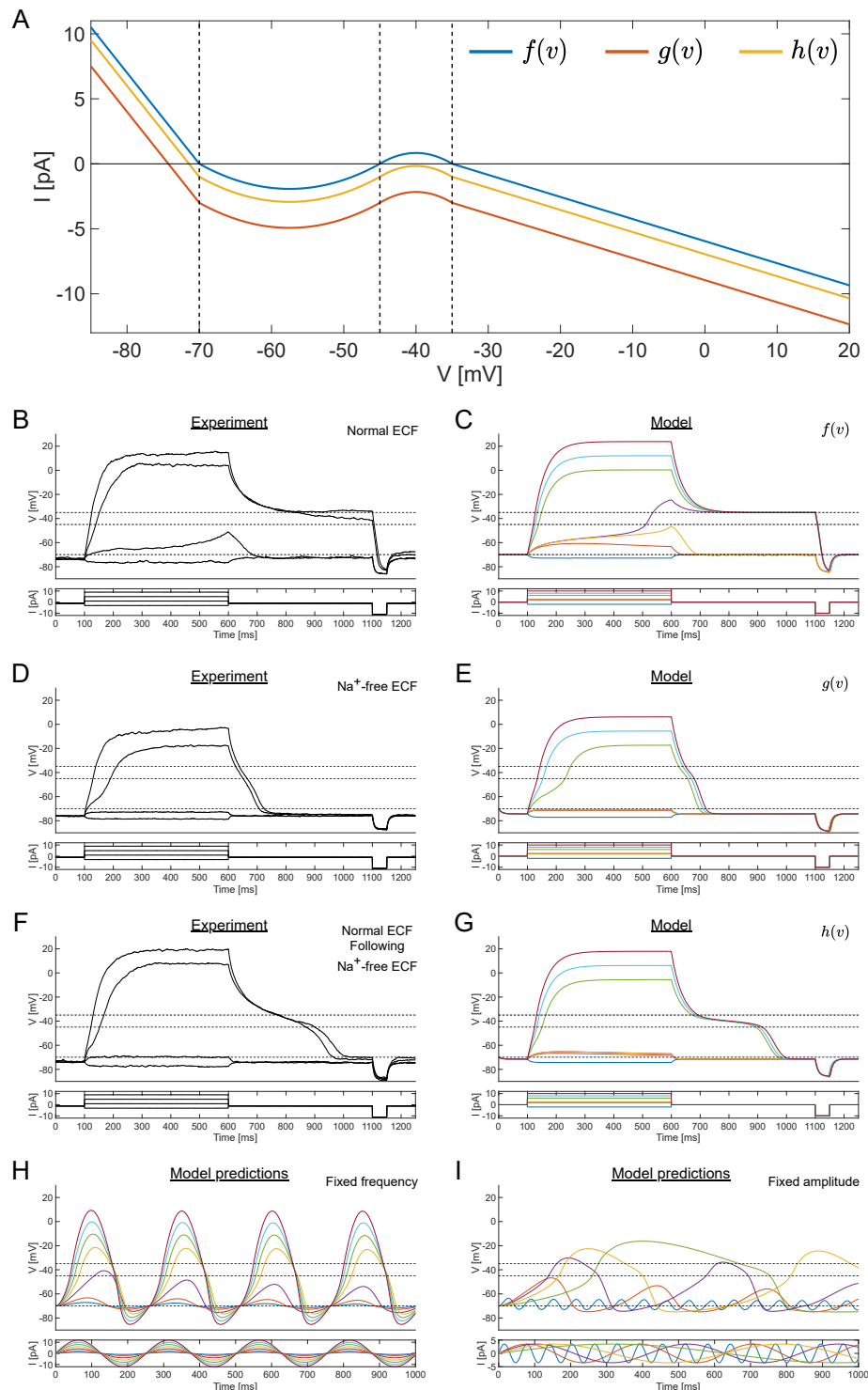


Figure 24. A. The fast nullcline and its variations. B-G. Current-clamp traces from [70] (B,D,F) and corresponding model simulations (C,E,G). Conditions: normal ECF (B-C), Na^+ -free ECF (D-E) and normal ECF following Na^+ -free ECF (F-G). H-I. Model predictions for current-clamp dynamics that have not been tested experimentally, with either fixed frequency (H) or fixed amplitude (I). In C,E,G the current steps are $[-2,2,2.295,2.282,2.8,6,8,10]$ pA. In H the input values are 0.025Hz and $[1,2,4,6,8,10,12]$ pA. In I the input values are 3.5pA and $[0.005,0.01,0.015,0.02,0.1]$ Hz. Note that the time-scale in B,E and F does not match that of Fig. 2a in [70] (J. Mellem, personal communication).

5.2.2 An intrinsic mechanism for sequential RMD activations may underlie clockwise and counterclockwise muscle activation

Considering the behaviours introduced in chapter 4 and the experimentally-informed constraints on single-RMD neural dynamics, I start by asking what muscle activation patterns could give rise to non-planar postures and trajectories with a preferred chirality?

To break the dorsoventral symmetry, a left-right asymmetry in muscle activation must be introduced. This can be achieved for example by sequential activation of the four muscle quadrants with a fixed phase between neighbouring quadrants. In the RMD circuit, each of the four dorsal-ventral neurons dominantly forms neuromuscular junctions (NMJ) onto a different muscle quadrant in the head, such that left RMDs synapse onto right muscles and vice versa (Fig. 23). Thus, a clockwise (CW) muscle activation pattern can be achieved by counterclockwise (CCW) activation of those four RMD neuron, and vice versa.

How may such activation patterns be achieved in the RMD circuit? A mechanism for sequential RMD activations with a preferred chirality may arise from the intrinsic properties of the RMD circuit, or may require inputs from other neurons external to the RMD circuit. Here I test the hypothesis that the mechanism for CW and CCW muscle activation in the head is intrinsic to the RMD circuit. In section 5.2.3 I test an alternative hypothesis that RMD is intrinsically inclined towards left-right oscillations and its sequential CW and CCW activation is externally-driven by the SMD neurons.

To test whether the RMD circuit may underlie CW and CCW muscle activation patterns in the head, I modelled the RMD circuit by connecting identical units of the single-cell RMD model (see Fig. 24) via chemical and electrical synapses. I start from the simple case of two neurons connected via symmetric reciprocal inhibition, and gradually increase the complexity by introducing more neurons and synapses, and by setting synaptic weights asymmetrically (Fig. 25A). In all simulations, all model parameters are fixed except for synaptic weights and the initial membrane potential of the neurons. Synaptic weights are symmetrical unless stated otherwise.

In this model, input synaptic currents into RMD neurons include graded inhibitory chemical synapses and gap junctions (Eq. 5.1 and 5.5). The current through the inhibitory chemical synapses was modelled as a sigmoid function of the presynaptic neuron (Eq. 5.6-5.7), multiplied by a sensitivity factor (s) that models

synaptic desensitisation (Eq. 5.8). Intuitively, this means that inhibition of the postsynaptic neuron occurs when the presynaptic neuron is above its resting potential. At the same time the synapse loses its sensitivity at a rate proportional to the depolarisation of the presynaptic neuron, which causes the inhibition on the postsynaptic neuron to decrease (Eq. 5.8). While the presynaptic neuron is below its resting potential, no inhibition is applied to the postsynaptic neuron and the synapse recovers its sensitivity at a constant rate (b in Eq. 5.8). The graded sigmoidal response and desensitisation are supported by experimental evidence showing that the response of cholinergic synapses in *C. elegans* motor neurons is input-dependent and its activation is followed by a fast synaptic depression [203]. In addition, the ACC-1 (an ACh-gated Chloride Channel) is a postsynaptic receptor that is expressed by the RMD neurons [68]. Voltage-clamp recordings of ACC-1 expressed in *Xenopus* oocytes showed a sigmoidal current response to different ACh concentrations while the membrane potential was held at -80mV [227].

Gap junctions were modelled as a sigmoid function of the difference in membrane potential between the postsynaptic and presynaptic neurons (Eq. 5.9). Intuitively, this means that the membrane potential of two cells coupled by a gap junction will get closer to each other at a rate that depends only on their difference and such that it plateaus above and below some threshold membrane potential difference. This is supported by voltage-clamp recordings from pairs of cells expressing different gap junctional channels from *C. elegans*, showing that gap junction current at steady-state can be approximated as a sigmoid function of the membrane potential difference between the two coupled cells (see Discussion) [71, 237, 238]. In particular this was shown for UNC-7b which is the specific innexin isoform expressed in RMD [71, 237].

In addition to inhibition and electrical coupling, all neurons receive a constant depolarising current required for their activation. This models inputs from RIA interneurons that do not carry time information (Fig. 23I). Since this current acts on a larger time-scale than RMD frequency, the response of RMD to it is assumed to be at steady-state and thus a mechanism for synaptic desensitisation is neglected. Synaptic parameters for data is unavailable were adjusted manually to allow for rhythmic activity (Table 6, see Discussion).

Symbol	Value	Description
V_{pre}^0	-70mV	Resting potential of presynaptic neuron
a	0.000035	Rate coefficient of synaptic fatigue
b	0.005	Rate coefficient of synaptic recovery

Table 6. Parameters for the RMD circuit model.

$$I_{\text{syn}} = I_{\text{Chem}} + I_{\text{GJ}} \quad (5.5)$$

where I_{Chem} is current through the inhibitory chemical synapse and I_{GJ} is current through the gap junction.

$$I_{\text{Chem}} = -W_{\text{Chem}} \cdot G_{\text{Chem}}(V_{\text{pre}}) \cdot s \quad (5.6)$$

where I_{Chem} is synaptic current, G_{Chem} is synaptic conductance, V_{pre} is the membrane potential of the presynaptic neuron, and s is synaptic fatigue (i.e., desensitisation).

$$G_{\text{Chem}}(V) = \frac{1}{1 + e^{0.125(V_{\text{pre}} + 52)}} \quad (5.7)$$

where G_{Chem} is synaptic conductance and V_{pre} is the membrane potential of the presynaptic neuron.

$$\frac{ds}{dt} = \begin{cases} -a(V_{\text{pre}} - V_{\text{pre}}^0), & \text{for } (V_{\text{pre}} > V_{\text{pre}}^0) \ \& \ s > 0 \\ b, & \text{for } (V_{\text{pre}} \leq V_{\text{pre}}^0) \ \& \ s < 1 \end{cases} \quad (5.8)$$

where s is synaptic fatigue, a and b are rate constant for synaptic desensitisation and recovery (respectively), V_{pre} and V_{pre}^0 are the membrane potential and resting potential of the presynaptic neuron (respectively).

$$I_{\text{GJ}} = W_{\text{GJ}} \cdot \frac{32}{1 + e^{0.2(V_{\text{post}} - V_{\text{pre}})}} - 16 \quad (5.9)$$

where I_{GJ} is gap junctional current from the presynaptic to the postsynaptic neuron, W_{GJ} gap junction conductance, and V_{pre} and V_{post} are the presynaptic and postsynaptic membrane potentials.

I first consider the simple case of two RMD neurons connected by symmetric reciprocal inhibition such that the initial membrane potentials are in anti-phase. Given sufficient excitatory input, this system generates sustained antiphase oscillations (Fig. 25A1 and 25B). Next, oscillatory activity is shown for a pair of neurons with asymmetric reciprocal inhibition (Fig. 25C, left and right panels show 2s and 10s long simula-

tions, respectively). The initial membrane potentials were set as in Fig. 25B. It is then shown that oscillatory activity can arise spontaneously when the initial membrane potentials of both neurons are in-phase for asymmetric, but not for symmetric inhibition (Fig. 25D, left for symmetric inhibition and right for asymmetric inhibition). Since the strength of the inhibition depends on the membrane potential of the pre-synaptic neuron, asymmetric inhibition allows one neuron to depolarise faster and inhibit the other neuron stronger, thus reaching its ON state and keeping the other neuron in its OFF state.

I then test whether sequential oscillatory activity can arise spontaneously in a system of four RMD neurons with asymmetric inhibition such that the two dorsal RMDs receive stronger inhibition than the two ventral RMDs (but left-right counterparts receive identical inhibition strength). Since left-right counterparts receive identical inputs, setting the initial membrane potential of all four neurons in-phase results in fully synchronised dorsoventral oscillations between the two pairs connected by reciprocal inhibition (as in Fig. 25D, left panel). To break this symmetry, I first set the initial membrane potential of a single RMD to the plateau potential. This is shown for either RMDVL (Fig. 25E, left panel) or RMDVR (Fig. 25E, right panel). Both cases generate sequential activation of RMD neighbours with a fixed phase and such that the order is maintained. However, the phase is only determined by the relative initial membrane potentials of the four neurons, which may be completely random in the animal, and is thus not a robust mechanism for enforcing sequential activations.

To find a more robust mechanism for spontaneous, sequential RMD activations that does not rely on initial conditions, I test whether adjusting synaptic weights can be used to induce a non-zero phase between all four RMD neurons. First, I set the activation of neurons on the left and right to be asymmetric, in addition to asymmetric inhibition. This results in phased activations with a fixed order, although the phase is unstable and uneven (Fig. 25F, left panel). I then show that adding gap junctions (symmetrically) between dorsal-ventral counterparts results in more stable and even phases between the four RMD neuron (Fig. 25F, right panel). This can be explained by the coupling of oscillatory activity between dorsal-ventral counterparts. Fig. 25H shows a schematics of RMD CCW activation and CW muscle activation (corresponding to the right panel in Fig. 25F).

Figure 25: An intrinsic mechanism for sequential RMD activations may underlie clockwise and counterclockwise muscle activation

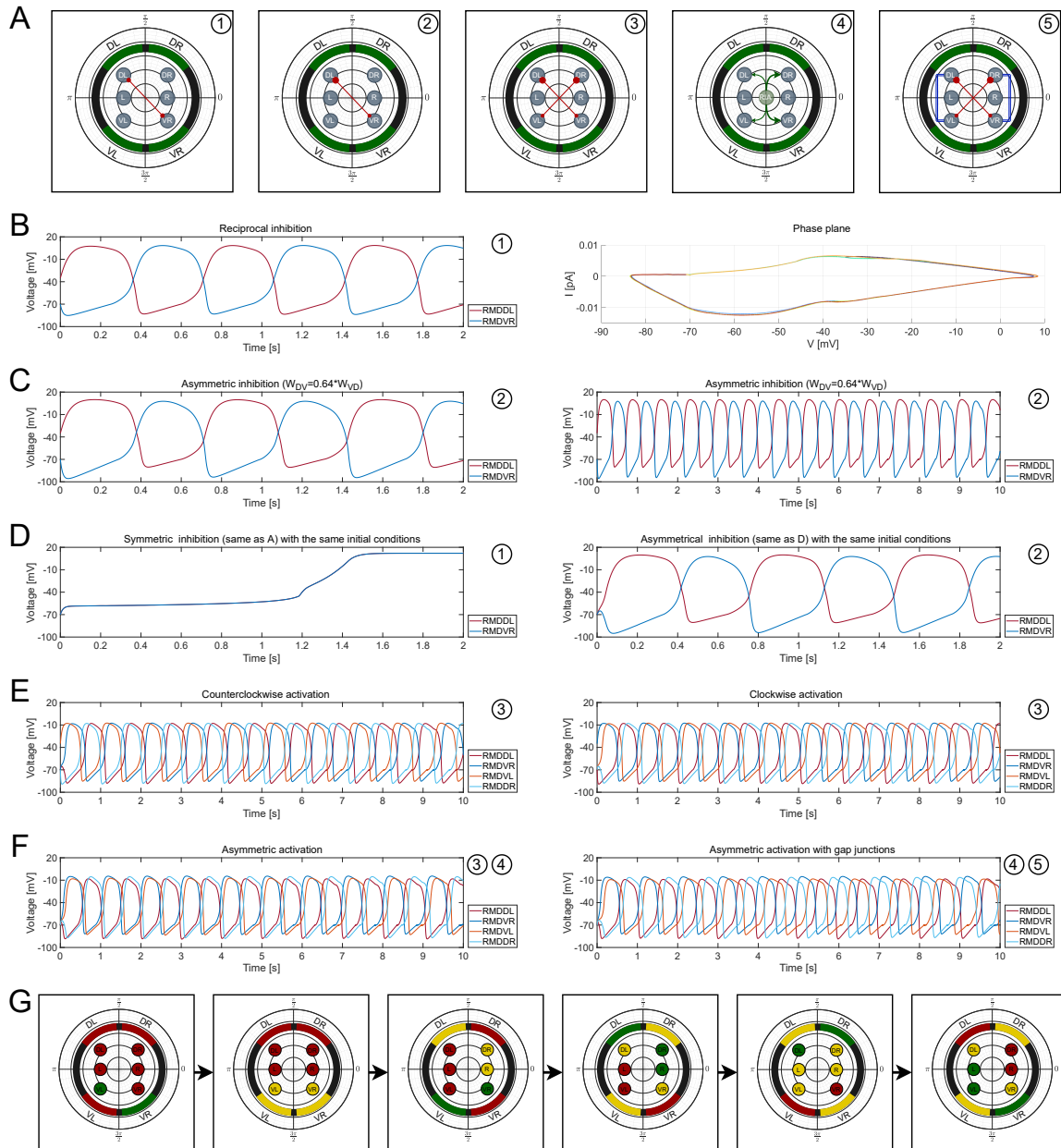


Figure 25. A. Different configurations of the RMD circuit. Green arrows show excitatory connections, and red arrows show inhibitory connections. Arrow head size indicates relative synaptic weight. The circled numbers in B-F correspond to those in A. B. Two RMD neurons connected via symmetric reciprocal inhibition (left) and the corresponding phase plane of one of them. C. Asymmetric inhibition. D. Symmetric (left) and asymmetric (right) inhibition with the initial membrane potential of both neuron set to the resting potential. E. Asymmetric inhibition of two RMD pairs, with the initial membrane potential of one neuron set at the plateau potential. F. Left-right asymmetric activation with the initial membrane potential of all neurons set to the resting potential, without (left) and with (right) gap junctions that couple dorsal-ventral counterparts. G. A schematic of sequential ON/OFF states of the RMD neurons and body wall muscles (corresponding to the right panel in F). ON states (depolarised) are shown in green, OFF states (hyperpolarised) in red, and intermediate activation in yellow. Note that the synaptic weights in B-D are different from those in E-F.

5.2.3 Mechanisms for synchronisation and switching in plateau potential neurons connected via gap junctions and graded inhibitory synapses

The neural dynamics of small neuronal networks (typically up to 10 neurons) has been studied in depth both experimentally and using mathematical modelling. This has proven useful for uncovering fundamental natural mechanisms for pattern generation that underlie animal behaviour, and provides a minimal framework that reduces complexity and redundancy by isolating basic phenomena. However, this reduction often comes at the risk of oversimplification and at the price of detaching the system from its natural environment, and in particular physiological conditions and a physical body. Thus, such reductions are often considered a first step in an incremental process towards the understanding of larger systems in richer contexts.

Synchrony of neural oscillations is important for spatial and temporal coordination of neural programs and motor gaits. Since locomotion in nature involves constantly changing internal and external conditions, pattern generating circuits cannot work in isolation. Different mechanisms have evolved to synchronise oscillatory activity throughout the body and with respect to the environment. Mechanisms such as electrical coupling, inhibition and mechanosensory feedback are used to coordinate animal locomotion via gait selection and modulation [30, 130, 131, 179, 222, 260].

Synchrony and antisynchrony by either electrical coupling or inhibition have been studied extensively both experimentally and in theoretical frameworks [179, 260–264]. Perhaps counterintuitively, it has been shown that there are regimes in which electrical coupling and inhibition work together to promote synchrony, and where either of them alone is not sufficient to induce synchrony [265–269]. The combined role of inhibition and electrical coupling received much less attention and has been addressed almost exclusively in spiking neurons. However, neurons exhibit many other intrinsic dynamics, such as bistability and graded responses [28, 121, 191].

Clockwise (CW) and counterclockwise (CCW) Coiling behaviours (see chapter 4) provide an interesting case study for gait selection mechanisms, as there is no clearly apparent preference to one or the other in terms of the behavioural role that they play, in contrast to, for example, forward and backward locomotion. While it is possible that CW/CCW Coiling and Infinity form a continuum and are all part of the same neural program (with CW and CCW at opposite extremes of the Infinity), the worm clearly must select at any

point in time whether to move in a CW or CCW direction. In the previous section (5.2.2) I demonstrated an intrinsic mechanism for sequential activation in the RMD circuit that may underlie circular muscle activation that gives rise to Coiling behaviours (Fig. 25). However, it is also possible that RMD oscillations are intrinsically dorsoventral-symmetric (i.e., left-right oscillations), and that the mechanism for sequential RMD activation is extrinsic. The connectivity between the RMD and SMD circuits suggests that SMD may act to break RMD's dorsoventral symmetry and promote sequential, out-of-phase activations of four or six RMD neurons. Specifically, gap junctions from the proprioceptive dorsal SMD neurons to dorsal RMD neurons may act to reduce the phase between dorsal RMD neurons, while inhibition may act to destabilise left-right antiphase activity (Fig. 23H).

Since the combined role of electrical coupling and inhibition has been underexplored in both plateau potential and graded transmission regimes, I first use the biologically-grounded RMD model developed in this work to test more general hypotheses regarding basic neural mechanisms for synchronisation and switching. This is motivated by the behavioural and modelling results presented in chapter 4 and this chapter, as well as RMD-SMD connectivity that may underlie an extrinsic mechanism for gait selection and sequential RMD activations. I then take the results of this analysis back to *C. elegans* and propose an extrinsic mechanism for sequential RMD activations and for a spontaneous chirality switch. Since data of the intrinsic dynamics of SMD is not yet available, they are assumed here to be a plateau potential neuron and are modelled the same as RMD.

Stable and unstable in-phase synchrony in a system of four plateau potential neurons

Here I introduce a simple system of two pairs of plateau potential neurons (SMD and RMD), each connected via reciprocal graded inhibitory synapses. The two pairs are connected to one another either via symmetrical gap junctions (Fig. 26A) or via both symmetrical gap junctions and symmetrical inhibitory synapses (Fig. 26B). Since SMD were shown to be proprioceptive, here they are assumed to be entrained by a strong external signal, and are thus not affected by the RMD pair (this is implemented by making all SMD-RMD gap junctions unidirectional).

In what follows, the effect of electrical coupling and inhibition on the dynamics of the RMD pair is tested. All model parameters used here are identical to the ones used in previous sections, apart from synaptic weights

and initial membrane potentials. As before, all neurons receive constant depolarising currents required for their activation, and all synaptic weights are symmetric unless stated otherwise. Also, since the SMDD and SMDV oscillate in antiphase and are not affected by the RMD pair, only SMDD is shown for simplicity (Fig. 26).

I start by testing the effect of the electrical coupling of RMD to SMD (Fig. 26A). When the initial membrane potentials of SMDD and RMDL are set in antiphase to SMDV and RMDR, synchrony is maintained within a range of gap junction conductances (Fig. 26B-C). When an initial lag is applied to SMDD to desynchronise it from RMDL, gap junctions promote in-phase synchrony (Fig. 26E and 26G), whereas in the absence of gap junctions the neurons remain out-of-phase (Fig. 26F) or desynchronise (Fig. 26H). Importantly, whether SMDD is in-phase with RMDL or RMDR depends solely on the initial lag assigned to SMDD (Fig. 26E and 26G). This suggests a neural mechanism for spontaneous pattern selection via symmetric electrical coupling.

Higher gap junction conductances result in the SMDD signal encapsulating both RMDL and RMDR signals such their wavelengths are different and sum up to the wavelength of SMDD (Fig. 26I). Interestingly, in some gap junction conductance regimes, setting the activation on SMD and RMD asymmetrically results in unstable in-phase synchrony, such that SMDD is alternately in-phase with RMDL and RMDR (Fig. 26J). Above some gap junction conductance threshold, oscillations terminate and both RMDs plateau (not shown).

I next tested the combined affect of symmetric electrical coupling and inhibition on the same system (Fig. 26B). While I could not find a regime in which electrical coupling and inhibition work synergistically to promote sustained in-phase synchrony, I found regimes in which they promote unstable synchrony (Fig. 26K and 26M), such that SMDD is transiently and alternately obtained in-phase synchrony with RMDL and RMDR for a few oscillation periods. As a control, I show that inhibition alone resulted in asynchrony (Fig. 26L and 26N) and electrical coupling alone resulted in sustained in-phase synchrony (Fig. 26C). This suggests that the addition of inhibition to electrical coupling provides destabilisation that promotes transient in-phase synchrony. More generally, this may offer a mechanism for periodic alternation between oscillators along an animal's body or between two neural programs that underlie different behavioural gaits.

Figure 26: Pattern switching and unstable synchrony in a system of four plateau potential neurons

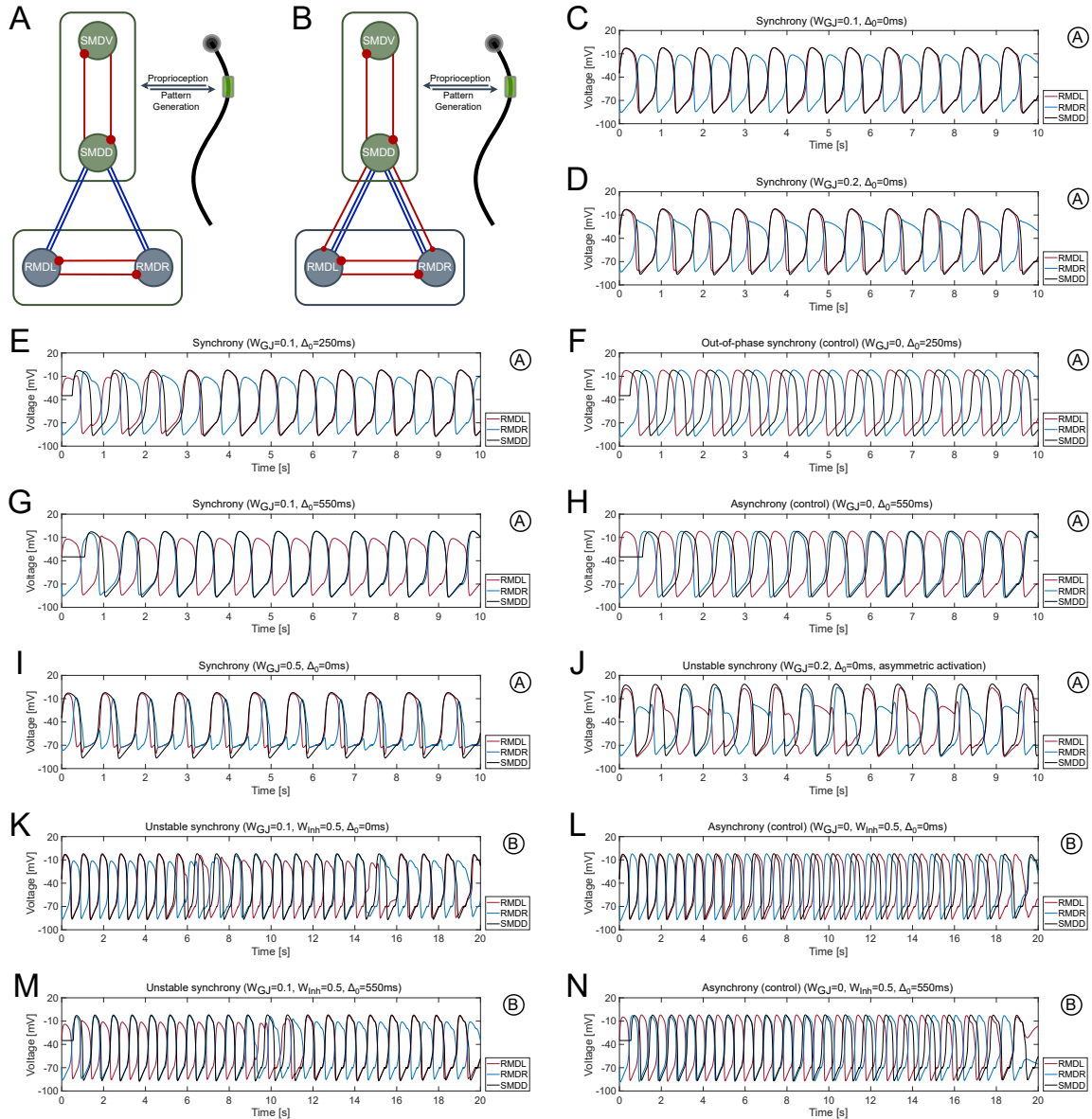


Figure 26. A-B. Two pairs of reciprocally inhibiting plateau potential neurons connected via electrical coupling (A) or via electrical coupling and inhibition (B). The SMD pair is assumed to receive strong external inputs that entrain its oscillations and is thus not affected by the RMD pair. The circled letters in C-N correspond to the models in A-B. In C-N, the trace of SMDV is not shown for simplicity and is always in antiphase to SMDD. C-D. Symmetrical gap junctions from SMDD to RMDL and RMD maintain in-phase synchrony across a range of gap junction conductances when the initial membrane potential of SMDD and RMDL are identical. E-H. SMDD is given an initial lag by setting all its inputs to 0 for 250ms (E-F) or 550ms (G-H). Gap junctions promote in-phase synchrony even when the initial membrane potential of SMDD is out-of-phase relative to both RMDL and RMR, and SMDD can become in-phase with either RMDL (E) or RMDR (G) depending on its their initial relative phases. Removing the gap junctions results in out-of-phase synchrony (F) or asynchrony (H). I. Higher gap junction conductances induce encapsulation of RMDL and RMDR signals by the SMDD signal. J. For some gap junction conductances, when combined with asymmetric activation of SMD and RMD, unstable in-phase synchrony is induced. K-N. Combined electrical coupling and inhibition (model B), promotes unstable in-phase synchrony (K and M). Removal of SMD-RMD gap junctions results in asynchrony (L and N), whereas removal of inhibition results in in-phase synchrony (C).

An extrinsic mechanism for sequential RMD activations and a spontaneous chirality switch

In previous sections in this chapter I showed an intrinsic mechanism for sequential activations of four RMD neurons that give rise to a circular muscle activation (Fig. 26G-H), and then suggested general mechanisms for stable and unstable in-phase synchrony in a system of two pairs of reciprocally inhibiting plateau potential neurons connected via symmetric electrical coupling and inhibition (Fig. 26). Here I test the hypothesis that RMD oscillations are intrinsically dorsal-ventral symmetrical, and that external stimulation from SMD promotes sequential RMD activations. Specifically, I test the role of combined electrical coupling and inhibition from SMD to RMD. The circuit is an extension of the circuit in Fig. 26B as it consists of two more reciprocally inhibiting RMD neurons (Fig. 27A-B). Note that the schematics in Fig. 27A and 27B show two different activation patterns of the same circuit (counterclockwise and clockwise, respectively), rather than two different circuits. As before, SMD are assumed to receive strong external inputs that entrain their oscillations, and thus gap junctions from SMD to RMD are effectively unidirectional.

In this circuit configuration, I found regimes in which symmetric electrical coupling and inhibition from dorsal SMD to dorsal RMDs act synergistically to induce sequential counterclockwise (CCW) and clockwise (CW) RMD activations that give rise to CW and CCW muscle activations, respectively (Fig. 27C-D, see Fig. 23C for neuromuscular anatomy). CW muscle activation arises from CCW RMD activation (Fig. 27C, $\text{RMDDR} \rightarrow \text{RMDDL} \rightarrow \text{RMDVL} \rightarrow \text{RMDVR}$), whereas CCW muscle activation arise from CW RMD activation (Fig. 27D, $\text{RMDDL} \rightarrow \text{RMDDR} \rightarrow \text{RMDVR} \rightarrow \text{RMDVL}$). Importantly, chirality is determined by the order of RMD activations, which only depends on the first RMD neuron to depolarise, thus providing a mechanism for spontaneous chirality selection (Fig. 27E-F). In particular, if the two right RMDs (blue shades) depolarise first, CCW RMD activation is selected (Fig. 27E, same simulation as in C, note the time axes), whereas if the two left RMDs (red shades) depolarise first, CW activation is selected (Fig. 27F, same simulation as in D, note the time axes). Note that in these simulations the initial membrane potential of all neurons are in-phase at the resting potential (-70mV), showing that both oscillatory activity and pattern selection are spontaneous. Asymmetric activation of those neurons was used to break the symmetry between them and allow spontaneous oscillatory activity from an in-phase state (the difference in input current was $\leq 10\%$ of the highest current). To demonstrate CW RMD activation in Fig. 27D and 27F, an initial 10ms lag was given to the two right RMDs by setting all their inputs to zero, whereas no lag resulted in CCW RMD activation (Fig. 27C and 27E).

Finally, I show that in this regime, either electrical coupling or inhibition alone are not sufficient to generate those dynamics (Fig. 27G-H). Electrical coupling alone resulted in in-phase synchrony of left-right RMD counterparts (Fig. 27G), whereas inhibition alone resulted in oscillations with an unstable phase (Fig. 27H).

Figure 27: An extrinsic mechanism for sequential RMD activations and a spontaneous chirality switch

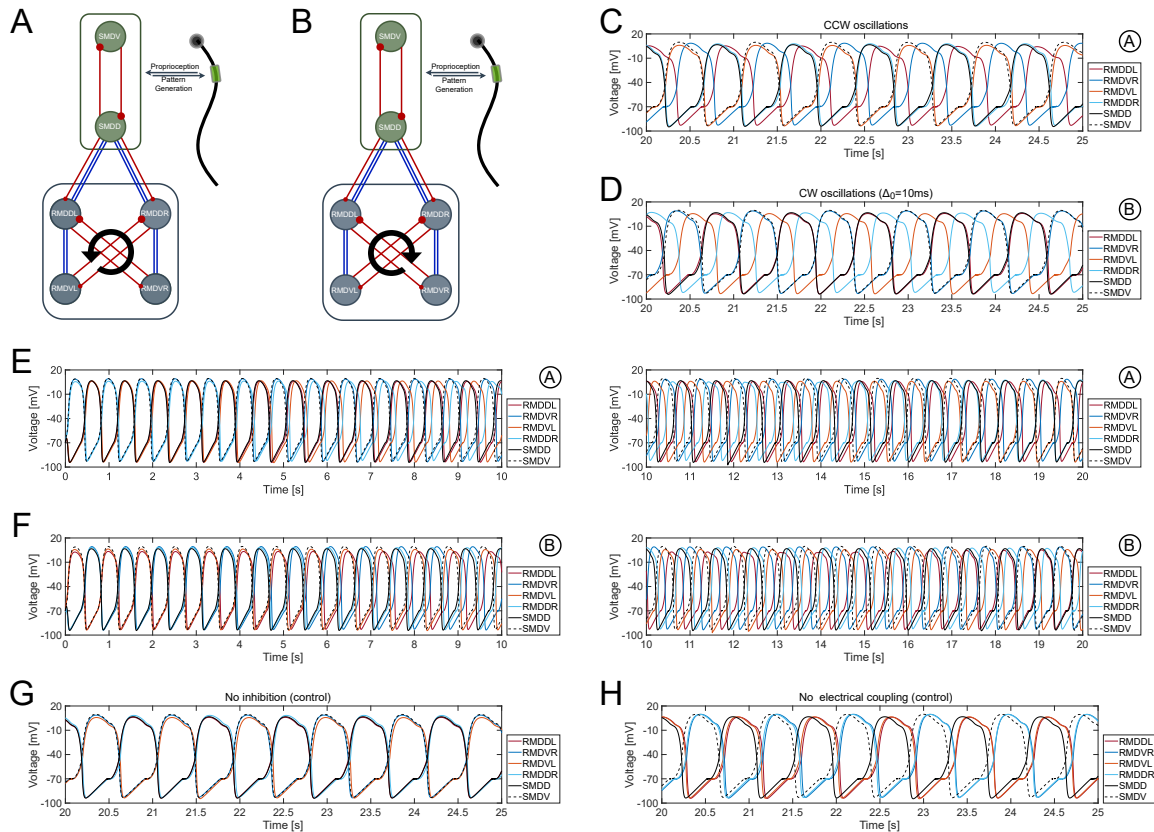


Figure 27. A-B. An extrinsic mechanism for sequential activation of the RMD neurons via symmetric inhibition and electrical coupling from SMD. The schematics show counterclockwise (A) and clockwise (B) modes of the same circuit. C-D. Counterclockwise (C) and clockwise (D) sequential activations of four RMD neurons (showing the last 5s of a 25s simulation). E-F. The first 20s of the simulations in C and D, respectively. The initial membrane potential of all neurons are in-phase at the resting potential (-70mV). In F, an initial 10ms lag was given to the two right RMD neurons. G-H. Controls for C-D showing that electrical coupling alone (G) or inhibition alone (H) from SMD to RMD results in in-phase synchrony of left-right counterparts (G) and out-of-phase oscillations with an unstable phase (H), respectively. Note that in G-H only the last 5s of a 25s simulation are shown. In all simulations, electrical coupling and inhibitory connections were symmetric, while activation was not, in order to allow spontaneous oscillatory activity from an in-phase initial state.

5.3 Methods

Model simulation

All simulations were solved using the Runge-Kutta solver (ode45 in MATLAB R2021a), with a step size of 1ms, using a laptop with an i7 processor (2.8GHz), 16GB RAM and 64-bit Windows 10. The computation time of individual simulations ranged between 0.5-5 minutes.

Single-cell model

The fitting of the model to the experimental data was done manually. First, the fixed points of the system were selected (i.e., the two stable points which correspond to the two resting potentials at -70mV and 35mV, and the unstable point which corresponds to the depolarisation threshold at -45mV). Then, the fixed points were used to split the physiological range of membrane potential into four sub-ranges. Within each sub-range, the current-voltage relationship was approximated as either a linear or a quadratic function (Eq. 5.1 and 5.4, Fig. 24A and Table 5). The parameters of each function were adjusted manually to match experimental data. The expression in the second differential equation was also adjusted manually to account for a desensitisation response on a larger time scale (Eq. 5.2-5.3).

5.4 Discussion

A biologically-grounded single-cell model captures intrinsic RMD dynamics

In this chapter I looked into the neuromuscular control of the motor behaviours introduced in chapter 4 by means of biologically-grounded computational models. My investigation starts with the development of a single-cell model that accurately captures the intrinsic dynamics of the RMD motor neurons as indicated by electrophysiological recordings [70]. The RMD are plateau potential head neurons that I selected as promising candidates for 3D pattern generation in the head of *C. elegans*.

The motivation to accurately capture the intrinsic dynamics of neurons in computational models is two-fold. First, such models provide a fully controlled and reproducible framework for studying single-cell dynamics by arbitrarily perturbing the model cell and by making testable predictions (see Fig. 24). This creates a loop in which the model informs experiments and their results in turn are used to update the

model. Indeed, the model was used to make predictions that may be tested in current-clamp experiments (Fig. 24H-I). Second, since such models can be highly constrained by experimental measurements, they can also be used to put strong constraints on the dynamics neural circuits, for which the size of the parameter space often increases dramatically as a result of including more neurons and their inter-connectivity. This includes electrical and chemical synapses for which experimental data may be missing or incomplete.

The parameter space of such circuit models encompasses many solutions, most do not correspond to physiological conditions or do not match the parameters of the specific modelled system. Nevertheless such solutions may give rise to dynamics that resemble the dynamics of the modelled system, but they lack insight about the underlying mechanisms of such dynamics. Finding the regimes that give rise to specific patterns of oscillatory activity under strong, experimentally-informed constraints helps narrow down the parameter space of the model and gets us closer to uncovering the fundamental principles that govern pattern generation in biological nervous systems.

Other models of the RMD neuron that are based on current-clamp recordings in [70] exist. Nicoletti et al. developed a model based on the Hodgkin-Huxley formulation in order to capture and characterise the role of different calcium and potassium voltage-gated currents. Their model reproduces RMD bistable dynamics as indicated by current-clamp experiments, and is used to make predictions regarding the underlying ionic mechanisms that facilitate this dynamics [259]. Boyle et al. developed a biomechanical framework for modelling *C. elegans* forward locomotion. They modelled the RMD neuron as a bistable, binary switch with hysteresis, such that the threshold for switching between the two states is state-dependent. They used this to model the antiphase activity of dorsal and ventral B-type motor neurons during forward locomotion. The bistability and non-linearity of these model neurons ensures that contralateral muscles do not contract at the same time. Together with stretch-receptors that feed back information from the shape of the body to B-type neuron, this allows the model to generate dorsoventral oscillations across a wide range of neural activation and body undulation frequencies [30].

Here, the RMD model was designed to accurately capture whole-cell dynamics in order to both characterise intrinsic RMD dynamics and constrain circuit dynamics. The first equation of the model captures its fast response using a piecewise function (Eq. 5.1 and 5.4 and Fig. 24A). The second equation captures a slower response and, similar to [30], introduces hysteresis to the model, which makes its depo-

larisation/hyperpolarisation threshold state-dependent (not shown). All model parameters were manually adjusted to fit the model to the experimental data in [70] (Table 5).

The model accurately captures RMD dynamics as indicated by current-clamp recordings, including its dynamics in different extracellular fluids (Fig. 24) [70]. The model does not contain details about sub-cellular components such as ionic current subtypes or dendritic morphology which are beyond its scope. It is also not designed to capture dynamics with a period larger than 1 second, as the period of all oscillatory activity investigated in this work is on the scale of tens or hundreds of milliseconds. However, electrophysiology data is available for larger time scales [70], and depending on the driving hypothesis, future work may generalise this model to account for those too, preferably while maintaining model simplicity and interpretability. Finally, the model does not consider random noise or variability across neurons that are often observed in electrophysiological measurements [70].

Models of neural circuits

To characterise the dynamics of an ensemble of plateau potential neurons, I started from a simple circuit of two neurons connected via symmetric reciprocal inhibition, and gradually increased its complexity by either adding more neurons and synapses (chemical or electrical), or by setting synaptic weights asymmetrically (Fig. 25). In this analysis all model parameters were fixed apart from synaptic weights and initial membrane potentials.

Chemical and electrical synapse models were informed by electrophysiology data available for synaptic channels and neurotransmitters expressed specifically by RMD and SMD, which puts strong constraints on synaptic dynamics [68, 71, 203, 227, 237, 238]. However, data for some aspects of synaptic dynamics is still missing. This includes desensitisation and recovery of inhibitory chemical synapses, as well their reversal potential. These parameters were adjusted manually to allow for rhythmic activity (Table 6).

Both RMD and SMD express the UNC-7b innexin isoform in the adult worm, which makes RMD-RMD and RMD-SMD gap junctions symmetrical (note that UNC-7b is sometimes referred to as UNC-7S, T. Starich, personal communication) [71, 237]. Voltage-clamp recordings were done in *Xenopus* oocytes that express unc-7b. The two cells were first held at -30mV, and then the membrane potential of one of the cells was clamped using 10mV increments between -100mV and +100mV, while current in both cells was recorded.

The results show that the rate of current flow in response to a voltage step depends on the difference in membrane potential between the two cells, and decays exponentially over time, reaching steady-state after approximately 4 seconds. This gives a sigmoid-like current-voltage relationship at steady-state [71]. However, it is not yet known whether this response only depends on the difference in membrane potentials, and in particular whether it is invariant to the absolute membrane potential of the cell that was held at -30mV. Here, I assumed that gap junctions are at steady-state at all times and modelled them as a sigmoid function of the difference in membrane potential between the two coupled cells. This assumption is justified by the fact that in the experiments that measured gap junctional current-voltage relationship over time, the channels were expressed in *Xenopus* eggs and were perturbed after being held at 0V potential for an effectively infinite amount of time. However, in the worm there is always some activity that deviates from 0V potential. For this reason and for simplicity, gap junctions were assumed to have reached steady state prior to any simulated activity and remain at steady-state during the simulation. This assumption can be tested experimentally by carrying out the same voltage-clamp experiment repeatedly at different time intervals, and in particular before and after reaching steady-state [71].

To test the dynamics of cholinergic synapses in *C. elegans* nervous system, Putrenko et al. expressed different combinations of four acetylcholine-gated chloride channels (ACC1-4) in *Xenopus* oocytes and recorded the flow of current in response to acetylcholine (ACh), as well as to the agonist arecoline, while the membrane potential of both cells was held at -80mV. First, they found that all four channels mediate an inhibitory response to ACh. ACC-1 and ACC-2 homomers showed variable responses on different scales of ACh concentration (0.05-1 μ M and 2-100 μ M, respectively). While ACC-2 exhibited desensitisation to ACh, ACC-1 did not (although it did exhibit desensitisation to arecoline at higher concentrations). Further, the heteromeric channel of ACC-1 + ACC-3 did show desensitisation within 2-200 μ M ACh concentrations, with a slower decay rate compared to ACC-2 homomers. The relationship between current and ACh concentration for all channels fitted well to a sigmoid function [227].

The ACC channels were found to be expressed throughout the nervous system of *C. elegans* [68]. ACC-1 was shown to be expressed by the RMD and SMD neurons, and its expression did not overlap with that of ACC-2. ACC-3 expression was very low throughout the animal [68]. Here, I modelled inhibitory chemical synapses as a sigmoid function of the pre-synaptic neuron with desensitisation that was crucial

for obtaining oscillatory activity through the “escape from inhibition” mechanism [179]. Since ACC-1 did not show desensitisation in [227], future experiments may test whether larger ACh concentrations elicit such a response. Alternatively, RMD might express ACC-3 and form ACC-1 + ACC-3 heteromers, or other channels that do desensitise. In addition, in the voltage-clamp recordings of ACC channels, the two cells were clamped at -80mV and their response to a constant ACh concentration was measured. More work is needed to characterise the dependency of these responses on the pre- and post-synaptic membrane potentials. The release of ACh from the pre-synaptic neuron may also have complex, voltage- and time-dependent dynamics.

Similar to electrophysiology data, locomotion data was also used to constrain the circuit model using extracted gait parameters such as undulation frequency. This was done by manually adjusting free parameters in the synapse models (see Section 5.2.2). In future work I plan to test this neural model in a biomechanical framework developed in our group [246]. This will allow to use other locomotion parameters to constrain the mechanics of the worm, such as speed and body twisting and rolling.

The importance of symmetry-breaking for robust pattern generation

I found that symmetry-breaking plays a crucial role in the generation of spontaneous and sustained oscillatory activity. In a circuit made of identical plateau potential neurons with symmetric synaptic connectivity, if the initial membrane potentials of all neurons are set in-phase, oscillatory activity cannot be initiated as all neurons experience the same inputs and will thus follow the same path. While random noise might be useful to break this symmetry, it is possible that natural systems evolved to guarantee symmetry-breaking more robustly, where it is required. In the circuit model described here, symmetry can be broken by means of synaptic weights, including gap junctions and inhibitory and excitatory chemical synapses (see Fig. 25). In particular, I showed how asymmetric inhibition and activation lead to spontaneous oscillatory activity in a system of two or four plateau potential neurons (Fig. 25D and 25F). Future modelling and experimental work may address the importance of hard-wired symmetry-breaking for robust pattern generation in different regimes.

Mechanisms for stable and unstable in-phase synchrony in plateau potential neurons

Mechanisms for synchronisation, modulation and selection of neural gaits have been explored in-depth in spiking neurons that fire all-or-none action potentials [300], while both plateau potential neurons and graded

transmission received much less attention. In particular, some studies focused on the synergistic effects of inhibition and electrical coupling in synchronisation [265–269].

To bridge this gap in knowledge, I performed a preliminary characterisation of the possible dynamics that may arise from a simple system of two pairs of reciprocally inhibiting plateau potential neurons connected via symmetric graded inhibitory and electrical synapses (Fig. 26). While this analysis was aimed at capturing general principles of neural synchronisation, modulation and switching, it was inspired by specific neuroanatomical motifs in *C. elegans* (see Figs. 25A and 27).

Here, the modelled system is a simplified version of the motif described in Fig. 27, and contains only four neurons, left and right RMD (RMDL and RMDR) and dorsal and ventral SMD (SMDD and SMDV), with all four modelled as identical plateau potential neurons (Fig. 26A-B). The RMD pair is linked to the SMD pair only through SMDD, either via electrical coupling (Fig. 26A), or via both inhibition and electrical coupling (Fig. 26B). Since the SMD pair is entrained by a strong proprioceptive input, its activity is assumed to be independent of the RMD pair. This was implemented by making SMD-RMD gap junctions unidirectional.

While keeping all synaptic weights symmetric, I found regimes in which SMD-RMD electrical coupling promotes either stable or unstable in-phase synchrony (Fig. 26A-H). In some regimes, in-phase synchrony was dependent on initial conditions, such that SMDD synchronises with either RMDL or RMDR depending only on their relative initial membrane potentials (Fig. 26E-H). When the activation of SMD and RMD was asymmetric, gap junctions induced unexpected dynamics. This included a case in which the SMDD signal encapsulated the signals of RMDL and RMDR (Fig. 26I), and a case of unstable in-phase synchrony with a significant reduction in amplitude of the antiphase cell (Fig. 26J). In addition, I found regimes in which electrical coupling and inhibition work synergistically to promote unstable synchrony (Fig. 26K-N).

While this was only a preliminary analysis of the potential dynamics of such systems, these results demonstrate their capacity for complex computations. In particular, both stable and unstable in-phase synchrony may hint on general mechanisms for spontaneous gait switching and phase-locking between multiple oscillators. Finally, while different dynamics were obtained by means of changing synaptic weights, they may all appear in a hard-wired circuit in the animal depending on physiological conditions. For example, the properties of the external material may, passively or actively, influence synaptic conductances.

Intrinsic and extrinsic mechanisms for RMD oscillations that may underlie Coiling and Infinity

In this work I discuss multiple hypotheses for pattern generation in RMD that may give rise to 3D motor pattern generation. This includes mechanisms that are intrinsic or extrinsic to the RMD circuit. Here I only consider four of the six RMD neurons (Figs. 25A and 27A-B). Extrinsic mechanisms involve the proprioceptive SMD neurons that were shown to be correlated with head bending during 2D forward locomotion [232], and send both gap junctions and inhibitory synapses onto RMD (Fig. 23H) [37, 86]. Note that RMD dominantly form neuromuscular junctions (NMJ) onto body wall muscles (BWM) in rows 1-2, while SMD dominantly form NMJ onto BWM in rows 3-8 [37, 86]. For both intrinsic and extrinsic mechanisms, I test the circuit capacity to generate sequential RMD activations that will lead to sequential activation of the four BWM quadrants. Note that clockwise (CW) activation of RMD leads to counterclockwise (CCW) activation of BWM, and vice versa (Fig. 23C). Thus, the selection of chirality is determined by the order of RMD activations.

Electrical coupling between dorsal-ventral RMD counterparts suggests that they are synchronised (Fig. 23C). This is in contrast to most *C. elegans* motor circuits that show left-right symmetry, and dorsoventral reciprocal inhibition [37, 86]. While intrinsic sequential RMD activation is possible (Fig. 25F-G), this might not be robust, as dorsal-ventral counterparts might gradually reach in-phase synchrony. If dorsal-ventral counterparts are intrinsically in-phase, sequential RMD activation can be enforced extrinsically. Specifically, symmetric gap junctions from dorsal SMD to both RMDDL and RMDDR (see Fig. 23H) may provide the instability needed to promote sequential RMD activations. Regardless of whether SMD-RMD connectivity promotes sequential RMD activations or not, it may act to synchronise RMD oscillations with dorsoventral oscillations in SMD and the rest of the body.

6 Concluding remarks and future outlook

The primary objective of this work is to advance our understanding of the basic control principles of biological neural networks that underlie animal behaviour. It particularly addresses 3D locomotion of the *C. elegans* nematode, by linking neural dynamics at the single-cell level, to the complex motor patterns that may arise from ensembles of neurons carrying out those dynamics.

Organisms across the animal kingdom show great behavioural diversity, as well as diversity in the biomechanical and neural mechanisms that give rise to those behaviours. In particular, motor behaviour arises from coordinated muscle contraction and relaxation, which results in body deformation and in force applied on an external material. Motor behaviours, as well as the neuromuscular mechanisms that control them, have developed under geometrical and mechanical constraints from both the body and its environment. Expectedly, greater anatomical and behavioural complexities require more complex neuromuscular mechanisms to control them. In addition, biological systems have developed redundancies for robustness, which make it harder to isolate basic phenomenon and study their part in the whole.

To address the problem of complexity in biological systems, I chose to work on one of the simplest multicellular model organisms that possesses a nervous system, the 1mm long *C. elegans* nematode. Its cylindrical body is controlled by only 302 neurons and 95 body wall muscle cells [45, 54, 75], yet it is capable of complex and robust behaviours within a wide range of environmental conditions [60, 73]. Its anatomical compactness and minimal redundancy allow us to study neural dynamics at the single-cell level in the context of the whole-animal, and in particular while considering the geometry and mechanics of its body and environment [22, 33, 62, 64, 65].

I addressed this topic using an integrated approach, combining (1) 3D imaging, computer vision, deep learning and optimisation techniques to acquire locomotion data of freely-moving *C. elegans* worms in a volume and extract meaningful features, (2) quantitative analysis of 3D locomotion data to identify rhythmic locomotion patterns in a volume, and (3) mathematical modelling of head neural circuits, selected as candidates for the neural control of the identified locomotion patterns.

In planar settings, the worm's locomotion has been characterised in-depth, as well as the neurons that

control it. Specifically, the worm moves forward and backward via sinusoidal-like body undulations, carried out by a wave of antiphase dorsoventral body bends that propagate from head to tail (in forward locomotion) or from tail to head (in backward locomotion) [33, 37, 62, 75]. These gaits have been shown to be controlled by a set of motor neurons that span from the neck of the worm to its tail. Their arrangement consists of a repeating motif of a pair of excitatory neurons and a pair of inhibitory neurons, both connect to muscles in a left-right symmetrical manner (Fig. 23A) [37, 68, 75]. This suggests that feedforward body bending posterior to the neck is restricted to the dorsoventral plane.

Despite the worm moving in complex, non-planar environments in its natural habitat, its locomotion in a volume is almost completely unexplored [82, 244, 245]. While the simplification to planar surfaces was crucial to build our understanding incrementally, it is possible that in a volume, where the planarity constraint is removed, the worm can execute different motor programs that are suppressed in 2D, either passively through the mechanics, or actively through mechanosensory feedback mechanisms. Furthermore, neural programs that are unused or silenced in 2D, may be manifested in 3D, and may lead to the discovery of new neuronal functions. Interestingly, the neuromuscular anatomy along most of its body suggests that *C. elegans* is left-right symmetrical and only capable of generating dorsoventral body bends in a feedforward manner. However, the head is not restricted in the same way (Fig. 23) [37, 75, 86]. The circuitry in the head is more complex and consists of multiple motor circuits in which individual neurons dominantly form neuromuscular junctions onto one of the four muscle quadrants, suggesting more degrees of freedom for head motion compared to the rest of the body (Fig. 23B,C,E).

To study *C. elegans* locomotion in 3D, I recorded freely-moving worms in a volume, within a range of gel viscoelasticity corresponding to gelatin concentrations. Our imaging setup consists of three approximately orthogonal cameras, each attached to a telecentric lens. This setup improves on existing methods for 3D imaging of *C. elegans*, with up to 7X magnification, an acquisition rate up to 40Hz, and a field of view and depth of focus of approximately 1cm^2 and 1cm, respectively (see Section 3.2 and Fig. 3) [244, 245]. This allows to accurately capture the worm's shape while allowing it to move freely across a volume that is approximately 10 times larger than itself, thus avoiding wall effects.

This allowed me to generate a database of high-resolution 3D locomotion data. To extract the worm's shape and its location in the volume, the space must first be calibrated in order to convert from camera pixel

space to 3D lab coordinates. This is necessary to match worm features across all cameras and to accurately reconstruct its 3D shape in real length units. The calibration accounts for intrinsic properties such as camera and lens distortion, as well as extrinsic properties such as the relative position and orientations of the cameras (see Section 3.3). Here, I used the pinhole camera model to account for those properties (see Section 3.3 and Fig. 4A) [288]. The camera model was obtained for each experiment using an asymmetric grid pattern which was recorded in the molten gel from all cameras simultaneously in different orientations (see Section 3.3 and Fig. 4B-C). The grid images were then fed into an algorithm (developed by our group), which uses the grid points to construct a camera model (see Section 3.3 and Eq. 3.1-3.5).

Since the camera model is based on information obtained in the molten gel, but worms are recorded only once it solidifies, structural changes in the material might require changes to the camera model. Indeed, I found a significant increase in the calibration error when measured in the solidified gel, compared to the molten gel. To account for this discrepancy, I added a calibration refinement step to the pipeline, which uses the recorded worm in each clip to minimise the calibration error. This reduced the mean calibration error to ≤ 1 pixels (Section 3.3.2 and Fig. 6B-D).

Next, I developed an algorithm for extracting the worm's 3D shape, represented as a discretised midline in lab coordinates, and its position and orientation in the volume over time. This process was broken into two steps. First, the head and tail were tracked using a convolutional neural network (CNN) trained for 3D point detection. Then, the 3D midline was found using a hill-climbing optimisation approach, while constrained at the end-points. Importantly, time information is used in both steps.

For head and tail tracking, the position of the corresponding point in the previous frame is used as the centre of a small neighbourhood within which the target point is searched for (Fig. 7C). Tracking within a small neighbourhood encodes time information implicitly, makes the method memory-efficient and reduces the probability for ambiguities, as only the relevant portion of the image is used. Furthermore, this allows to track multiple points independently. Here, the CNN was trained on head points, but was used to track both head and tail simultaneously (Fig. 8H-M).

For 3D midline tracking, each midline is found using the midline in the previous frame as the initial state for the optimisation process. This allows to use information about shape, position and orientation,

which is crucial for resolving ambiguities (Fig. 9). Combining this methods with the method for head and tail tracking, allows to constrain the midline at the end-points, which dramatically reduces its degrees of freedom and guarantees convergence. Here too, a minimal bounding box around the worm is used to find its midline. This makes the method memory-efficient, helps exclude potentially-misleading information (e.g., other worms in the field of view), and allows to track multiple worms simultaneously (Section 3.4.2).

Nevertheless, some postures cannot be resolved using this method. This includes cases in which the worm's body is too convoluted to resolve its full shape from a single frame image. In some of these cases, using pixel information from adjacent frames might help. Here, such cases were corrected manually. In other cases, all projections appear as a uniform blob and the shape cannot even be resolved, and thus the frame must be discarded. To resolve the posture in such cases, a different imaging approach may be considered, such as using fluorescent markers that can indicate body position along the worm's longitudinal axis.

To make the full pipeline widely available and accessible, I developed a tool with a user-interface that contains all the above functionalities. The tool, as well as the different modules it contains, are designed in a general manner which is scale-free, supports any number of cameras, can be adjusted to other calibration grid patterns, and can be used to study other animals. While the midline finding algorithm is restricted to tubular/slender bodies, the 3D point tracking CNN can be trained to detect any feature that can be localised to a single point, and can be used to track multiple points simultaneously (Section 3.7).

All head and tail points were validated frame-by-frame by generating a video showing the three camera views and the projected head and tail points. Manual correction was required in less than 5% of the frames, mostly where head and tail were close to each other. This was done using a custom 3D annotation tool that I developed (Section 3.7). Then, the midline was found while head and tail were fixed. This was then again validated frame-by-frame in the same manner. Since the midline was highly constrained, both at the end-points and by the shape and position of the midline in the previous frame, it rarely required correction ($\leq 1\%$ of the frames). Cases that required correction mostly included highly convoluted shapes.

Once a database of *C. elegans* locomotion in a volume has been established, I annotated it by assigning tags to sub-clips in order to qualitatively describe the worm's behaviour. I identified multiple patterns of

locomotion that have not been described in *C. elegans*. This includes chiral forward and backward locomotion gaits, as well as non-planar manoeuvres. In this work I chose to focus on forward locomotion gaits, and found that in high viscoelasticity environments (typically 2% – 4% gelatin, corresponding to $100 \leq G' \leq 600$ Pa, see Table 4), the worm moves forward by propagating a wave of dorsoventral body bends from head to tail. While this motion resembles crawling in 2D, in 3D it was highly non-planar. This may be due to the lack of a near-solid substrate, and due to frequent, but not periodic head bending outside the plane of body undulation. In low viscoelasticity environments (typically 1% – 1.5% gelatin, corresponding to $4 \leq G' \leq 13$ Pa, see Table 4), I identified a motion pattern in which the worm forms chiral trajectories that emerge from posture with opposite chirality (Figs. 11-12 and 15-16). During this motion, the worm also rolls around its longitudinal axis at half the rotation rate of the trajectory (Figs. 18B, 20 and 22A). This behaviour was observed in both clockwise (CW) and counterclockwise (CCW) modes. In the same environments, I identified another forward locomotion gait, Infinity, in which the worm forms figure-eight trajectories by alternating CW and CCW rotation. In this behaviour rolling alternated between clockwise and counterclockwise (Figs. 13, 17, 18B, 21 and 22B). Interestingly, I found that individual worms are capable of both CW and CCW Coiling, as well as Infinity.

Since our 3D imaging setup does not provide sufficient information to identify the worm’s intrinsic coordinate system (i.e., dorsal-ventral and left-right axes), I used fluorescence imaging of worms in a volume that express a GFP marker in body wall muscles (Figs. 20-21). Using this method I was able to identify the rolling of the worm (i.e., rotation about its longitudinal axis). Furthermore, despite the chiral motion along the entire body, maximum body curvature posterior to the neck was associated with the dorsoventral axis. This suggests that chiral gaits are an extension of 2D forward locomotion, where feedforward control along most of the body generates dorsoventral body bends, while the head generates chiral motion that passively propagates posteriorly. Taking all this into consideration, I proposed a model that links postures and trajectories to the worm’s intrinsic coordinate system (Fig. 22). In Coiling, during a dorsoventral body curvature period (2π), the worm completes a full rotation about its longitudinal axis (2π), and forms two circle-like trajectory loops (4π). Rolling and the trajectory have the same chirality, while postures have the opposite chirality (Fig. 22A). In Infinity, during a dorsoventral body curvature period, the worm rolls $\frac{\pi}{2}$ CW and $\frac{\pi}{2}$ CCW, and forms and eight-shaped trajectory (Fig. 22B).

The behavioural description of the identified chiral gaits includes a geometrical characterisation of 3D postures and trajectories and their link to the animal's intrinsic coordinate system. This information can be used to study the underlying neuromuscular control of those behaviours. I selected two head motor circuits, RMD and SMD, as candidates for the control of chiral head motions. This is supported by their physiology and neuroanatomy. First, both the RMD and SMD circuits contain extensive cross-inhibitory connections, which suggests that they play a role in pattern generation (Fig. 23B-C) [37, 68, 86]. Second, their pattern of neuromuscular junctions onto body wall muscles suggests that some of these neurons dominantly control individual muscle quadrants, in contrast to the left-right symmetry in the motor circuit posterior to the neck (Fig. 23A-C). While SMD have been shown to control head bending amplitude during 2D forward locomotion, RMD is unnecessary for normal 2D forward locomotion [62]. However, the RMD neurons are necessary for the high frequency nose undulations during foraging, as well as for the head-withdrawal reflex [62, 210, 297, 299]. SMD were shown to be proprioceptive, meaning that their activity is modulated by the shape of the body through stretch-sensitive ion channels. Specifically their expression of the TRP-1 and TRP-2 mechanosensory channels is necessary for SMD-body bending synchrony, and genetic ablation of both channels specifically in SMD causes a ventral bias, resulting in worms moving in circles [232].

To test the role of RMD and SMD in chiral head motion, I developed a biologically-grounded mathematical model constrained by experimental data available in the literature. Nervous systems across the animal kingdom show great complexity and diversity even at the level of individual neurons. While most characterised neurons show all-or-none activity and fire action potentials, electrophysiological recordings have shown that RMD are bistable and respond to input current in a graded manner [70]. I developed a neuron model that captures the intrinsic dynamics of individual RMD neurons, as indicated by current-clamp recordings [70]. The model builds on and improves previous modelling work in RMD in that it captures its dynamics more accurately and using simpler formulation [70, 259]. The model captures RMD dynamics at the whole-cell level and does not consider the underlying ionic currents. Here, constraining the model and accurately capturing the current-voltage relationship of the biological neuron, is motivated by the importance of constraining network dynamics to biologically-relevant pattern generation mechanisms. Free parameters in the models of individual neurons lead to an exponential increase in the degrees of freedom as network complexity increases. In addition, the chemical and electrical synapses which couple neurons, have their own intrinsic dynamics, which increase even more the computational complexity of biological nervous systems.

To further constrain network dynamics, I developed biologically-grounded models for chemical and electrical synapses, based on available data relevant to the specific synapses that couple the RMD and SMD neurons (Eq. 5.5- 5.9) [68, 71, 203, 227, 237, 238].

Voltage-clamp simulations using the single-cell model match in-vivo measurements in both normal and abnormal extracellular fluid conditions (Fig. 24B-G) [70]. Furthermore, the model is used to make predictions to further characterise the neuron's intrinsic dynamics. These may be tested in-vivo using the same setup used for previous measurements [69, 70].

Once the single-cell and synapse models have been developed and tested, their parameters were fixed and they were used to examine the dynamics of ensembles of bistable neurons. This was done incrementally, by gradually increasing circuit complexity, both in terms of the number of neurons involved, as well as by breaking circuit symmetries by modifying the conductances of synaptic connections.

In the simplest case, I looked at pattern generation in pairs of bistable neurons connected via symmetrical reciprocal inhibition. I found that this system is capable of generating rhythmic activity if the initial membrane potentials are set in antiphase (Fig. 25B). Setting the weights of the inhibitory synapses asymmetrically allowed for spontaneous rhythmic activity from an in-phase initial state (Fig. 25C). This suggests that hard-wired asymmetry in synaptic weights is crucial for robust rhythmic activity in circuits of bistable neurons. Next, I looked at ensembles of four model neurons and implicitly included mechanosensory feedback in the model, corresponding to SMD's entrainment by stretch receptors (Fig. 26A-B) [232]. In this system, I found regimes that promote spontaneous pattern selection, which may underlie a spontaneous chirality switch in *C. elegans* motor behaviour (Fig. 26C-H). Furthermore, I identified regimes that support unstable synchrony with fixed alternation frequency, which may offer a link to previous findings about frequency-doubling in SMD (Fig. 26J-N) [65]. Finally, I looked at a circuit of six model neurons while also considering connectivity to muscles. This was used to propose a model in which the RMD circuit underlies 3D chiral pattern generation, whereas the SMD circuit underlies spontaneous chirality selection (Fig. 27).

Overall, I have identified novel neural control mechanisms and complex dynamics that may arise from ensembles of apparently simple bistable neurons, connected via inhibitory and electrical synapses. The models developed here provide a formal and reproducible framework for hypothesis testing, and I used them

to make quantitative hypotheses that can be tested in-vivo. These findings extend beyond the scope of *C. elegans* and expand our knowledge of the computational complexity of neural networks, by bridging the gap from single-cell dynamics to whole-animal behaviour.

To test whether RMD and SMD are necessary for chiral head motion, future work may use optogenetics to target individual head motor neurons. According to the models presented here, deactivation of one or more RMD neurons during a Coiling sequence will terminate chiral head motion and result in planar dorsoventral undulations. Since SMD are predicted to be involved in chirality selection, ablation of these neurons is predicted to result in frequent, but not periodic, switching between CW and CCW head undulations.

To identify the muscle activation pattern used by the worm to induce chiral posture sequences as observed in Coiling, the models developed here may be integrated into a biomechanical framework that models the geometry and mechanics of the worm's body and its environment. More specifically, since the neuromuscular anatomy of RMD is known (Fig. 23C), the neural models developed here can be used to generate muscle activation patterns, that can then be used to control body curvature in a mechanical framework [246].

7 References

- [1] Giovanni Alfonso Borelli and Jean Bernoulli. *De motu animalium*. Apud Petrum Gosse, 1743.
- [2] Philip Howard Gray. “The Early Animal Behaviorists: Prolegomenon to Ethology”. In: *Isis* (1968). ISSN: 0021-1753. DOI: 10.1086/350423.
- [3] Robert J Richards. *Darwin and the emergence of evolutionary theories of mind and behavior*. University of Chicago Press, 1987.
- [4] Charles Gross. *Alfred russell wallace and the evolution of the human mind*. 2010. DOI: 10.1177/1073858410377236.
- [5] Alfred R. Wallace. *The intelligence and perfectibility of animals*. 1871. DOI: 10.1038/003182a0.
- [6] Iva B. Zovkic, Mikael C. Guzman-Karlsson, and J. David Sweatt. *Epigenetic regulation of memory formation and maintenance*. 2013. DOI: 10.1101/lm.026575.112.
- [7] Donald Olding Hebb. *The organization of behavior: A neuropsychological theory*. Psychology Press, 2005.
- [8] Ronald M. Harris-Warrick and Eve Marder. *Modulation of neural networks for behavior*. 1991. DOI: 10.1146/annurev.ne.14.030191.000351.
- [9] Karen E. Adolph and John M. Franchak. *The development of motor behavior*. 2017. DOI: 10.1002/wcs.1430.
- [10] Paul S G Stein, Douglas G Stuart, Sten Grillner, and Allen I Selverston. *Neurons, networks, and motor behavior*. MIT press, 1999.
- [11] Mark Bear, Barry Connors, and Michael A Paradiso. *Neuroscience: Exploring the brain*. Jones & Bartlett Learning, LLC, 2020.
- [12] Auke Jan Ijspeert. “Central pattern generators for locomotion control in animals and robots: A review”. In: *Neural Networks* (2008). ISSN: 08936080. DOI: 10.1016/j.neunet.2008.03.014.
- [13] Andrew Biewener and Sheila Patek. *Animal locomotion*. Oxford University Press, 2018.
- [14] Michael M. Francis, Jerry E. Mellem, and Andres Villu Maricq. *Bridging the gap between genes and behavior: Recent advances in the electrophysiological analysis of neural function in *Caenorhabditis elegans**. 2003. DOI: 10.1016/S0166-2236(02)00041-3.

- [15] Cornelia I. Bargmann. *Neurobiology of the Caenorhabditis elegans genome*. 1998. DOI: 10.1126/science.282.5396.2028.
- [16] Ephraim L. Tsalik and Oliver Hobert. “Functional mapping of neurons that control locomotory behavior in *Caenorhabditis elegans*”. In: *Journal of Neurobiology* (2003). ISSN: 00223034. DOI: 10.1002/neu.10245.
- [17] Steven Vogel. *Life in Moving Fluids: The Physical Biology of Flow-Revised and Expanded Second Edition*. Princeton University Press, 2020.
- [18] Netta Cohen and Jack E. Denham. *Whole animal modeling: piecing together nematode locomotion*. 2019. DOI: 10.1016/j.coisb.2018.12.002.
- [19] Deborah M. Thurtle-Schmidt and Te Wen Lo. *Molecular biology at the cutting edge: A review on CRISPR/CAS9 gene editing for undergraduates*. 2018. DOI: 10.1002/bmb.21108.
- [20] W. Clay Spencer, Georg Zeller, Joseph D. Watson, Stefan R. Henz, Kathie L. Watkins, Rebecca D. McWhirter, Sarah Petersen, Vipin T. Sreedharan, Christian Widmer, Jeanyoung Jo, Valerie Reinke, Lisa Petrella, Susan Strome, Stephen E. Von Stetina, Menachem Katz, Shai Shaham, Gunnar Rättsch, and David M. Miller. “A spatial and temporal map of *C. elegans* gene expression”. In: *Genome Research* (2011). ISSN: 10889051. DOI: 10.1101/gr.114595.110.
- [21] Katie S. Kindt, Veena Viswanath, Lindsey Macpherson, Kathleen Quast, Hongzhen Hu, Ardem Patapoutian, and William R. Schafer. “*Caenorhabditis elegans* TRPA-1 functions in mechanosensation”. In: *Nature Neuroscience* (2007). ISSN: 10976256. DOI: 10.1038/nn1886.
- [22] Saul Kato, Harris S. Kaplan, Tina Schrödel, Susanne Skora, Theodore H. Lindsay, Eviatar Yemini, Shawn Lockery, and Manuel Zimmer. “Global Brain Dynamics Embed the Motor Command Sequence of *Caenorhabditis elegans*”. In: *Cell* (2015). ISSN: 10974172. DOI: 10.1016/j.cell.2015.09.034.
- [23] Brian A. Wilt, Laurie D. Burns, Eric Tattwei Ho, Kunal K. Ghosh, Eran A. Mukamel, and Mark J. Schnitzer. *Advances in light microscopy for neuroscience*. 2009. DOI: 10.1146/annurev.neuro.051508.135540.
- [24] Jeffrey P. Nguyen, Frederick B. Shipley, Ashley N. Linder, George S. Plummer, Mochi Liu, Sagar U. Setru, Joshua W. Shaevitz, and Andrew M. Leifer. “Whole-brain calcium imaging with cellular

- resolution in freely behaving *Caenorhabditis elegans*". In: *Proceedings of the National Academy of Sciences of the United States of America* (2016). ISSN: 10916490. DOI: 10.1073/pnas.1507110112.
- [25] Robert Prevedel, Young Gyu Yoon, Maximilian Hoffmann, Nikita Pak, Gordon Wetzstein, Saul Kato, Tina Schrödel, Ramesh Raskar, Manuel Zimmer, Edward S. Boyden, and Alipasha Vaziri. "Simultaneous whole-animal 3D imaging of neuronal activity using light-field microscopy". In: *Nature Methods* (2014). ISSN: 15487105. DOI: 10.1038/nmeth.2964. arXiv: 1401.5333.
- [26] Eviatar Yemini, Albert Lin, Amin Nejatbakhsh, Erdem Varol, Ruoxi Sun, Gonzalo E. Mena, Aravinthan D.T. Samuel, Liam Paninski, Vivek Venkatachalam, and Oliver Hobert. "NeuroPAL: A Multicolor Atlas for Whole-Brain Neuronal Identification in *C. elegans*". In: *Cell* (2021). ISSN: 10974172. DOI: 10.1016/j.cell.2020.12.012.
- [27] Ernst Niebur and Paul Erdős. "Theory of the locomotion of nematodes: Dynamics of undulatory progression on a surface". In: *Biophysical Journal* (1991). ISSN: 00063495. DOI: 10.1016/S0006-3495(91)82149-X.
- [28] Frances K. Skinner, Nancy Kopell, and Eve Marder. "Mechanisms for oscillation and frequency control in reciprocally inhibitory model neural networks". In: *Journal of Computational Neuroscience* (1994). ISSN: 09295313. DOI: 10.1007/BF00962719.
- [29] Eve Marder and Adam L. Taylor. "Multiple models to capture the variability in biological neurons and networks". In: *Nature Neuroscience*. 2011. DOI: 10.1038/nn.2735.
- [30] Jordan H. Boyle, Stefano Berri, and Netta Cohen. "Gait modulation in *C. elegans*: An integrated neuromechanical model". In: *Frontiers in Computational Neuroscience* (2012). ISSN: 16625188. DOI: 10.3389/fncom.2012.00010.
- [31] Jack E. Denham, Thomas Ranner, and Netta Cohen. "Signatures of proprioceptive control in *Caenorhabditis elegans* locomotion". In: *Philosophical Transactions of the Royal Society B: Biological Sciences* (2018). ISSN: 14712970. DOI: 10.1098/rstb.2018.0208.
- [32] Tingyu Ming, Bowen Jin, Jialei Song, Haoxiang Luo, Ruxu Du, and Yang Ding. "3D computational models explain muscle activation patterns and energetic functions of internal structures in fish swimming". In: *PLoS Computational Biology* (2019). ISSN: 15537358. DOI: 10.1371/journal.pcbi.1006883.

- [33] S Brenner. “The genetics of *Caenorhabditis elegans*.” In: *Genetics* (1974). ISSN: 0016-6731. DOI: 10.1016/S0047-2484(78)80101-8. arXiv: arXiv:1408.1149.
- [34] Cynthia Kenyon. “The nematode *Caenorhabditis elegans*”. In: *Science* (1988). ISSN: 00368075. DOI: 10.1126/science.3287621.
- [35] J. E. Sulston, E. Schierenberg, J. G. White, and J. N. Thomson. *The embryonic cell lineage of the nematode Caenorhabditis elegans*. 1983. DOI: 10.1016/0012-1606(83)90201-4.
- [36] J. Sulston and J. Hodgkin. “Methods in the nematode *C. elegans*”. In: *Cold Spring Harbor Laboratory Press*. 1988. ISBN: 087969307X.
- [37] J. G White, E. Southgate, J. N. Thomson, and S. Brenner. “The structure of the nervous system of the nematode *Caenorhabditis elegans* (the mind of a worm)”. In: *Philosophical Transactions of the Royal Society of London. Series B, Biological Sciences* (1986).
- [38] Catharine H. Rankin. *From gene to identified neuron to behaviour in Caenorhabditis elegans*. 2002. DOI: 10.1038/nrg864.
- [39] Oliver Hobert. *Behavioral plasticity in C. elegans: Paradigms, circuits, genes*. 2003. DOI: 10.1002/neu.10168.
- [40] *Genome sequence of the nematode C. elegans: A platform for investigating biology*. 1998. DOI: 10.1126/science.282.5396.2012.
- [41] La Deana W. Hillier, Alan Coulson, John I. Murray, Zhirong Bao, John E. Sulston, and Robert H. Waterston. *Genomics in C. elegans: So many genes, such a little worm*. 2005. DOI: 10.1101/gr.3729105.
- [42] John White Martin Chalfie. “The Nervous System”. In: *Cold Spring Harbor Monograph Archive*. 1988. Chap. 11.
- [43] Scott W. Emmons. *Male development*. 2005. DOI: 10.1895/wormbook.1.33.1.
- [44] Maureen M. Barr and L. Rene Garcia. *Male mating behavior*. 2006. DOI: 10.1895/wormbook.1.78.1.
- [45] Z.F. Altun and D.H Hall. “Introduction to *C. elegans* Anatomy”. In: *Control* (2009). ISSN: 0717-6163. arXiv: arXiv:1011.1669v3.

- [46] Titus Kaletta and Michael O. Hengartner. *Finding function in novel targets: C. elegans as a model organism*. 2006. DOI: 10.1038/nrd2031.
- [47] William G. Kelly. *Transgenerational epigenetics in the germline cycle of Caenorhabditis elegans*. 2014. DOI: 10.1186/1756-8935-7-6.
- [48] Norbert Perrimon, Jian Quan Ni, and Lizabeth Perkins. *In vivo RNAi: today and tomorrow*. 2010. DOI: 10.1101/cshperspect.a003640.
- [49] Catharine H. Rankin. *A review of transgenerational epigenetics for RNAi, longevity, germline maintenance and olfactory imprinting in Caenorhabditis elegans*. 2015. DOI: 10.1242/jeb.108340.
- [50] Gino Poulin, Ramkumar Nandakumar, and Julie Ahringer. *Genome-wide RNAi screens in Caenorhabditis elegans: Impact on cancer research*. 2004. DOI: 10.1038/sj.onc.1208010.
- [51] Morris F. Maduro. *Cell fate specification in the C. elegans embryo*. 2010. DOI: 10.1002/dvdy.22233.
- [52] Coleen T. Murphy and Patrick J. Hu. *Insulin/insulin-like growth factor signaling in C. elegans*. 2013. DOI: 10.1895/wormbook.1.164.1.
- [53] Heidi A. Tissenbaum. *Using C. elegans for aging research*. 2015. DOI: 10.1080/07924259.2014.940470.
- [54] John G. White. “The Anatomy”. In: *The nematode Caenorhabditis elegans*. Cold Spring Harbor Laboratory, New York, 1988. Chap. 4, pp. 81–122.
- [55] Antony P. Page and Iain L. Johnstone. *The cuticle*. 2007. DOI: 10.1895/wormbook.1.138.1.
- [56] Michel Labouesse. *Epithelial junctions and attachments*. 2006. DOI: 10.1895/wormbook.1.56.1.
- [57] Z F Altun and D H Hall. “Muscle system, somatic muscle”. In: *WormAtlas. Edited for the web by Laura A. Herndon. Last revision: May 31 (2009), p. 2013*.
- [58] Kathrin Gieseler. “Development, structure, and maintenance of C. elegans body wall muscle”. In: *WormBook* (2017). ISSN: 1551-8507. DOI: 10.1895/wormbook.1.81.2.
- [59] Laura A. Herndon, Peter J. Schmeissner, Justyna M. Dudaronek, Paula A. Brown, Kristin M. Listner, Yuko Sakano, Marie C. Paupard, David H. Hall, and Monica Driscoll. “Stochastic and genetic factors influence tissue-specific decline in ageing C. Elegans”. In: *Nature* (2002). ISSN: 00280836. DOI: 10.1038/nature01135.

- [60] J. Gray and H. W. Lissmann. “The locomotion of nematodes”. In: *The Journal of experimental biology* (1964). ISSN: 00220949. DOI: 10.1242/jeb.41.1.135.
- [61] Jonathan T. Pierce-Shimomura, Thomas M. Morse, and Shawn R. Lockery. “The fundamental role of pirouettes in *Caenorhabditis elegans* chemotaxis”. In: *Journal of Neuroscience* (1999). ISSN: 02706474. DOI: 10.1523/jneurosci.19-21-09557.1999.
- [62] Jesse M. Gray, Joseph J. Hill, and Cornelia I. Bargmann. “A circuit for navigation in *Caenorhabditis elegans*”. In: *Proceedings of the National Academy of Sciences of the United States of America* (2005). ISSN: 00278424. DOI: 10.1073/pnas.0409009101.
- [63] Jonathan T. Pierce-Shimomura, Michael Does, and Shawn R. Lockery. “Analysis of the effects of turning bias on chemotaxis in *C. elegans*”. In: *Journal of Experimental Biology* (2005). ISSN: 00220949. DOI: 10.1242/jeb.01933.
- [64] Elpiniki Kalogeropoulou. “Role of the SAA and SMB neurons in locomotion in the nematode *Caenorhabditis elegans*, with a focus on steering”. PhD thesis. University of Leeds, 2018.
- [65] Harris S. Kaplan, Oriana Salazar Thula, Niklas Khoss, and Manuel Zimmer. “Nested Neuronal Dynamics Orchestrate a Behavioral Hierarchy across Timescales”. In: *Neuron* (2020). ISSN: 10974199. DOI: 10.1016/j.neuron.2019.10.037.
- [66] Shai Shaham. “Methods in cell biology”. In: *WormBook* (2006). ISSN: 1551-8507. DOI: 10.1895/wormbook.1.49.1.
- [67] Kara Dolinski and David Botstein. *Orthology and functional conservation in eukaryotes*. 2007. DOI: 10.1146/annurev.genet.40.110405.090439.
- [68] Laura Pereira, Paschalis Kratsios, Esther Serrano-Saiz, Hila Sheftel, Avi E. Mayo, David H. Hall, John G. White, Brigitte LeBoeuf, L. Rene Garcia, Uri Alon, and Oliver Hobert. “A cellular and regulatory map of the cholinergic nervous system of *C. Elegans*”. In: *eLife* (2015). ISSN: 2050084X. DOI: 10.7554/eLife.12432.
- [69] Michael M. Francis and Andres Villu Maricq. *Electrophysiological analysis of neuronal and muscle function in C. elegans*. 2006. DOI: 10.1385/1-59745-151-7:175.

- [70] Jerry E. Mellem, Penelope J. Brockie, David M. Madsen, and Andres V. Maricq. “Action potentials contribute to neuronal signaling in *C. elegans*”. In: *Nature Neuroscience* (2008). ISSN: 10976256. DOI: 10.1038/nn.2131.
- [71] Todd A. Starich, Ji Xu, I. Martha Skerrett, Bruce J. Nicholson, and Jocelyn E. Shaw. “Interactions between innexins UNC-7 and UNC-9 mediate electrical synapse specificity in the *Caenorhabditis elegans* locomotory nervous system”. In: *Neural Development* (2009). ISSN: 17498104. DOI: 10.1186/1749-8104-4-16.
- [72] Julijana Gjorgjieva, David Biron, and Gal Haspel. *Neurobiology of caenorhabditis elegans locomotion: Where do we stand?* 2014. DOI: 10.1093/biosci/biu058.
- [73] Stefano Berri, Jordan H. Boyle, Manlio Tassieri, Ian A. Hope, and Netta Cohen. “Forward locomotion of the nematode *C. elegans* is achieved through modulation of a single gait”. In: *HFSP Journal* (2009). ISSN: 1955205X. DOI: 10.2976/1.3082260.
- [74] Christopher Fang-Yen, Matthieu Wyart, Julie Xie, Risa Kawai, Tom Kodger, Sway Chen, Quan Wen, and Aravinthan D.T. Samuel. “Biomechanical analysis of gait adaptation in the nematode *Caenorhabditis elegans*”. In: *Proceedings of the National Academy of Sciences of the United States of America* (2010). ISSN: 10916490. DOI: 10.1073/pnas.1003016107.
- [75] Martin Chalfie, John E. Sulston, John G. White, Eileen Southgate, J. Nichol Thomson, and Sydney Brenner. “The neural circuit for touch sensitivity in *Caenorhabditis elegans*”. In: *Journal of Neuroscience* (1985). ISSN: 02706474. DOI: 10.1523/jneurosci.05-04-00956.1985.
- [76] Gal Haspel, Michael J. O’Donovan, and Anne C. Hart. “Motoneurons dedicated to either forward or backward locomotion in the nematode *Caenorhabditis elegans*”. In: *Journal of Neuroscience* (2010). ISSN: 02706474. DOI: 10.1523/JNEUROSCI.2244-10.2010.
- [77] Jordan H. Boyle, Stefano Berri, Manlio Tassieri, Ian A. Hope, and Netta Cohen. “Gait modulation in *C. Elegans*: It’s not a choice, it’s a reflex!” In: *Frontiers in Behavioral Neuroscience* (2011). ISSN: 16625153. DOI: 10.3389/fnbeh.2011.00010.
- [78] Quan Wen, Shangbang Gao, and Mei Zhen. “*Caenorhabditis elegans* excitatory ventral cord motor neurons derive rhythm for body undulation”. In: *Philosophical Transactions of the Royal Society B: Biological Sciences* (2018). ISSN: 14712970. DOI: 10.1098/rstb.2017.0370.

- [79] Tianqi Xu, Jing Huo, Shuai Shao, Michelle Po, Taizo Kawano, Yangning Lu, Min Wu, Mei Zhen, and Quan Wen. “Descending pathway facilitates undulatory wave propagation in *Caenorhabditis elegans* through gap junctions”. In: *Proceedings of the National Academy of Sciences of the United States of America* (2018). ISSN: 10916490. DOI: 10.1073/pnas.1717022115.
- [80] Neil A. Croll. “Components and patterns in the behaviour of the nematode *Caenorhabditis elegans*”. In: *Journal of Zoology* (1975). ISSN: 14697998. DOI: 10.1111/j.1469-7998.1975.tb03191.x.
- [81] Harksun Lee, Myung Kyu Choi, Daehan Lee, Hye Sung Kim, Hyejin Hwang, Heekyeong Kim, Sungsu Park, Young Ki Paik, and Junho Lee. “Nictation, a dispersal behavior of the nematode *Caenorhabditis elegans*, is regulated by IL2 neurons”. In: *Nature Neuroscience* (2012). ISSN: 10976256. DOI: 10.1038/nn.2975.
- [82] Alejandro Bilbao, Amar K. Patel, Mizanur Rahman, Siva A. Vanapalli, and Jerzy Blawdziewicz. “Roll maneuvers are essential for active reorientation of *Caenorhabditis elegans* in 3D media”. In: *Proceedings of the National Academy of Sciences of the United States of America* (2018). ISSN: 10916490. DOI: 10.1073/pnas.1706754115.
- [83] Becky J. Higgins and David Hirsh. “Roller mutants of the nematode *Caenorhabditis elegans*”. In: *MGG Molecular & General Genetics* (1977). ISSN: 00268925. DOI: 10.1007/BF02425326.
- [84] George N Cox, John S Laufer, Meredith Kusch, and Robert S Edgar. “GENETIC AND PHENOTYPIC CHARACTERIZATION OF ROLLER MUTANTS OF CAENORHABDITIS ELEGANS”. In: *Genetics* (1980). ISSN: 0016-6731. DOI: 10.1093/genetics/95.2.317.
- [85] Lise Frézal and Marie Anne Félix. “The Natural History of Model Organisms: *C. elegans* outside the Petri dish”. In: *eLife* (2015). ISSN: 2050084X.
- [86] S Cook, C Brittin, D Hall, and S Emmons. *The Worm Wiring Project*. 2012.
- [87] Gal Haspel and Michael J. O’Donovan. “A perimotor framework reveals functional segmentation in the motoneuronal network controlling locomotion in *Caenorhabditis elegans*”. In: *Journal of Neuroscience* (2011). ISSN: 02706474. DOI: 10.1523/JNEUROSCI.2186-11.2011.
- [88] Taizo Kawano, Michelle D. Po, Shangbang Gao, George Leung, William S. Ryu, and Mei Zhen. “An imbalancing act: Gap junctions reduce the backward motor circuit activity to bias *C. elegans* for forward locomotion”. In: *Neuron* (2011). ISSN: 10974199. DOI: 10.1016/j.neuron.2011.09.005.

- [89] George E P Box and George C Tiao. *Bayesian inference in statistical analysis*. Vol. 40. John Wiley & Sons, 2011.
- [90] Salem Hamed Abdurrahim, Salina Abdul Samad, and Aqilah Baseri Huddin. *Review on the effects of age, gender, and race demographics on automatic face recognition*. 2018. DOI: 10.1007/s00371-017-1428-z.
- [91] Albert Einstein. “Motion of suspended particles in stationary liquids required from the molecular kinetic theory of heat”. In: *Annalen der Physik* (1905). ISSN: 16159861.
- [92] J. Elgeti, R. G. Winkler, and G. Gompper. “Physics of microswimmers - Single particle motion and collective behavior: A review”. In: *Reports on Progress in Physics* (2015). ISSN: 00344885. DOI: 10.1088/0034-4885/78/5/056601.
- [93] Peter E. Smouse, Stefano Focardi, Paul R. Moorcroft, John G. Kie, James D. Forester, and Juan M. Morales. *Stochastic modelling of animal movement*. 2010. DOI: 10.1098/rstb.2010.0078.
- [94] Howard C. Berg and Robert A. Anderson. “Bacteria swim by rotating their flagellar filaments”. In: *Nature* (1973). ISSN: 00280836. DOI: 10.1038/245380a0.
- [95] E. M. Purcell. “Life at low Reynolds number”. In: *American Journal of Physics* (1977). ISSN: 0002-9505. DOI: 10.1119/1.10903.
- [96] Netta Cohen and Jordan H. Boyle. “Swimming at low Reynolds number: A beginners guide to undulatory locomotion”. In: *Contemporary Physics* (2010). ISSN: 00107514. DOI: 10.1080/00107510903268381.
- [97] Ildefonso M. De la Fuente, Carlos Bringas, Iker Malaina, María Fedetz, Jose Carrasco-Pujante, Miguel Morales, Shira Knafo, Luis Martínez, Alberto Pérez-Samartín, José I. López, Gorka Pérez-Yarza, and María Dolores Boyano. “Evidence of conditioned behavior in amoebae”. In: *Nature Communications* (2019). ISSN: 20411723. DOI: 10.1038/s41467-019-11677-w.
- [98] Walter R. Frontera and Julien Ochala. *Skeletal Muscle: A Brief Review of Structure and Function*. 2015. DOI: 10.1007/s00223-014-9915-y.
- [99] Philip M. Hopkins. “Skeletal muscle physiology”. In: *Continuing Education in Anaesthesia, Critical Care and Pain* (2006). ISSN: 17431824. DOI: 10.1093/bjaceaccp/mki062.
- [100] Manlio Tassieri. *Introduction to Linear Rheology*. CRC Press, 2016.

- [101] Maria Salta, Julian A. Wharton, Paul Stoodley, Simon P. Dennington, Liam R. Goodes, Stéphane Werwinski, Ugar Mart, Robert J.K. Wood, and Keith R. Stokes. *Designing biomimetic antifouling surfaces*. 2010. DOI: 10.1098/rsta.2010.0195.
- [102] Eric D. Tytell. “The hydrodynamics of eel swimming II. Effect of swimming speed”. In: *Journal of Experimental Biology* (2004). ISSN: 00220949. DOI: 10.1242/jeb.01139.
- [103] Eric D. Tytell, Iman Borazjani, Fotis Sotiropoulos, T. Vernon Baker, Erik J. Anderson, and George V. Lauder. “Disentangling the functional roles of morphology and motion in the swimming of fish”. In: *Integrative and Comparative Biology*. 2010. DOI: 10.1093/icb/icq057.
- [104] Rafael D. Schulman, Matilda Backholm, William S. Ryu, and Kari Dalnoki-Veress. “Dynamic force patterns of an undulatory microswimmer”. In: *Physical Review E - Statistical, Nonlinear, and Soft Matter Physics* (2014). ISSN: 15502376. DOI: 10.1103/PhysRevE.89.050701.
- [105] Eric Lauga. *Life around the scallop theorem*. 2011. DOI: 10.1039/c0sm00953a. arXiv: 1011.3051.
- [106] J Gray. “Undulatory propulsion”. In: *Journal of Cell Science* 3.28 (1953), pp. 551–578.
- [107] G. J. Hancock. “The self-propulsion of microscopic organisms through liquids”. In: *Proceedings of the Royal Society of London. Series A. Mathematical and Physical Sciences* (1953). ISSN: 0080-4630. DOI: 10.1098/rspa.1953.0048.
- [108] Geoffrey Ingram Taylor. “Analysis of the swimming of long and narrow animals”. In: *Proceedings of the Royal Society of London. Series A. Mathematical and Physical Sciences* 214.1117 (1952), pp. 158–183.
- [109] J. Gray and G. J. Hancock. “The Propulsion of Sea-Urchin Spermatozoa”. In: *Journal of Experimental Biology* (1955). ISSN: 0022-0949. DOI: 10.1242/jeb.32.4.802.
- [110] R. E. Johnson and C. J. Brokaw. “Flagellar hydrodynamics. A comparison between resistive-force theory and slender-body theory”. In: *Biophysical Journal* (1979). ISSN: 00063495. DOI: 10.1016/S0006-3495(79)85281-9.
- [111] Tingnan Zhang and Daniel I. Goldman. “The effectiveness of resistive force theory in granular locomotion”. In: *Physics of Fluids* (2014). ISSN: 10897666. DOI: 10.1063/1.4898629.
- [112] R G Cox. “The motion of long slender bodies in a viscous fluid Part 1. General theory”. In: *Journal of Fluid mechanics* 44.4 (1970), pp. 791–810.

- [113] James Lighthill. “Flagellar Hydrodynamics”. In: *SIAM Review* (1976). ISSN: 0036-1445. DOI: 10.1137/1018040.
- [114] Ryan Maladen, Yang Ding, Chen Li, and Daniel I. Goldman. “Undulatory swimming in sand: Subsurface locomotion of the sandfish lizard”. In: *Science* (2009). ISSN: 00368075. DOI: 10.1126/science.1172490.
- [115] Benjamin W. Hughes, Linda L. Kusner, and Henry J. Kaminski. *Molecular architecture of the neuromuscular junction*. 2006. DOI: 10.1002/mus.20440.
- [116] Lei Li, Wen Cheng Xiong, and Lin Mei. *Neuromuscular Junction Formation, Aging, and Disorders*. 2018. DOI: 10.1146/annurev-physiol-022516-034255.
- [117] Vincent C.K. Cheung, Andrea D’Avella, Matthew C. Tresch, and Emilio Bizzi. “Central and sensory contributions to the activation and organization of muscle synergies during natural motor behaviors”. In: *Journal of Neuroscience* (2005). ISSN: 02706474. DOI: 10.1523/JNEUROSCI.4904-04.2005.
- [118] Daniel B Forger. “Biological clocks, rhythms, and oscillations: the theory of biological timekeeping”. In: (2017).
- [119] Andrew W. Murray. *Creative blocks: Cell-cycle checkpoints and feedback controls*. 1992. DOI: 10.1038/359599a0.
- [120] Joseph R. Pomerening, Eduardo D. Sontag, and James E. Ferrell. “Building a cell cycle oscillator: Hysteresis and bistability in the activation of Cdc2”. In: *Nature Cell Biology* (2003). ISSN: 14657392. DOI: 10.1038/ncb954.
- [121] Eve Marder and Ronald L. Calabrese. *Principles of rhythmic motor pattern generation*. 1996. DOI: 10.1152/physrev.1996.76.3.687.
- [122] E. Marder. “Motor pattern generation”. In: *Current Opinion in Neurobiology* (2000). ISSN: 09594388. DOI: 10.1016/S0959-4388(00)00157-4.
- [123] Lawrence C. Rome, Douglas Swank, and David Corda. “How fish power swimming”. In: *Science* (1993). ISSN: 00368075. DOI: 10.1126/science.8332898.
- [124] Wardle, Videler, and Altringham. “Tuning in to fish swimming waves: body form, swimming mode and muscle function”. In: *The Journal of experimental biology* (1995). ISSN: 1477-9145.

- [125] Gary B. Gillis. “Neuromuscular control of anguilliform locomotion: Patterns of red and white muscle activity during swimming in the American eel *Anguilla rostrata*”. In: *Journal of Experimental Biology* (1998). ISSN: 00220949.
- [126] W. Otto Friesen and Jianhua Cang. *Sensory and central mechanisms control intersegmental coordination*. 2001. DOI: 10.1016/S0959-4388(01)00268-9.
- [127] Sten Grillner. “The motor infrastructure: From ion channels to neuronal networks”. In: *Nature Reviews Neuroscience* (2003). ISSN: 14710048. DOI: 10.1038/nrn1137.
- [128] Sten Grillner and S Kashin. “On the generation and performance of swimming in fish”. In: *Neural control of locomotion*. Springer, 1976, pp. 181–201.
- [129] Salma S. Islam, Pavel V. Zelenin, Grigori N. Orlovsky, Sten Grillner, and Tatiana G. Deliagina. “Pattern of motor coordination underlying backward swimming in the lamprey”. In: *Journal of Neurophysiology* (2006). ISSN: 00223077. DOI: 10.1152/jn.01277.2005.
- [130] Andrew D. McClellan and André Hagevik. “Coordination of spinal locomotor activity in the lamprey: Long-distance coupling of spinal oscillators”. In: *Experimental Brain Research* (1999). ISSN: 00144819. DOI: 10.1007/s002210050719.
- [131] P. Wallén and T. L. Williams. “Fictive locomotion in the lamprey spinal cord in vitro compared with swimming in the intact and spinal animal.” In: *The Journal of Physiology* (1984). ISSN: 14697793. DOI: 10.1113/jphysiol.1984.sp015063.
- [132] A. D. McClellan. “Locomotor recovery in spinal-transected lamprey: Regenerated spinal coordinating neurons and mechanosensory inputs couple locomotor activity across a spinal lesion”. In: *Neuroscience* (1990). ISSN: 03064522. DOI: 10.1016/0306-4522(90)90338-5.
- [133] Robert A. Pearce and W. Otto Friesen. “Intersegmental coordination of leech swimming: comparison of in situ and isolated nerve cord activity with body wall movement”. In: *Brain Research* (1984). ISSN: 00068993. DOI: 10.1016/0006-8993(84)90720-0.
- [134] Xintian Yu, Binh Nguyen, and W. Otto Friesen. “Sensory feedback can coordinate the swimming activity of the leech”. In: *Journal of Neuroscience* (1999). ISSN: 02706474. DOI: 10.1523/jneurosci.19-11-04634.1999.

- [135] Lorenzo Cangiano and Sten Grillner. “Fast and slow locomotor burst generation in the hemispinal cord of the lamprey”. In: *Journal of Neurophysiology* (2003). ISSN: 00223077. DOI: 10.1152/jn.01100.2002.
- [136] G. Viana Di Prisco, P. Wallén, and S. Grillner. “Synaptic effects of intraspinal stretch receptor neurons mediating movement-related feedback during locomotion”. In: *Brain Research* (1990). ISSN: 00068993. DOI: 10.1016/0006-8993(90)90675-2.
- [137] A. D. McClellan and W. Jang. “Mechanosensory inputs to the central pattern generators for locomotion in the lamprey spinal cord: Resetting, entrainment, and computer modeling”. In: *Journal of Neurophysiology* (1993). ISSN: 00223077. DOI: 10.1152/jn.1993.70.6.2442.
- [138] S. E. Blackshaw and S. W. Thompson. “Hyperpolarizing responses to stretch in sensory neurones innervating leech body wall muscle.” In: *The Journal of Physiology* (1988). ISSN: 14697793. DOI: 10.1113/jphysiol.1988.sp016954.
- [139] J. Cang and W. O. Friesen. “Sensory modification of leech swimming: Rhythmic activity of ventral stretch receptors can change intersegmental phase relationships”. In: *Journal of Neuroscience* (2000). ISSN: 02706474. DOI: 10.1523/jneurosci.20-20-07822.2000.
- [140] Jianhua Cang, Xintian Yu, and Otto W. Friesen. “Sensory modification of leech swimming: Interactions between ventral stretch receptors and swim-related neurons”. In: *Journal of Comparative Physiology - A Sensory, Neural, and Behavioral Physiology* (2001). ISSN: 03407594. DOI: 10.1007/s003590100229.
- [141] J. Chen, W. O. Friesen, and T. Iwasaki. “Mechanisms underlying rhythmic locomotion: Body-fluid interaction in undulatory swimming”. In: *Journal of Experimental Biology* (2011). ISSN: 00220949. DOI: 10.1242/jeb.048751.
- [142] Roy E. Ritzmann and Ansgar Büschges. *Adaptive motor behavior in insects*. 2007. DOI: 10.1016/j.conb.2008.01.001.
- [143] Matthias Gruhn, Géraldine Von Uckermann, Sandra Westmark, Anne Wosnitza, Ansgar Büschges, and Anke Borgmann. “Control of stepping velocity in the stick insect *Carausius morosus*”. In: *Journal of Neurophysiology* (2009). ISSN: 00223077. DOI: 10.1152/jn.00257.2009.

- [144] Anke Borgmann, Scott L. Hooper, and Ansgar Büschges. “Sensory feedback induced by front-leg stepping entrains the activity of central pattern generators in caudal segments of the stick insect walking system”. In: *Journal of Neuroscience* (2009). ISSN: 02706474. DOI: 10.1523/JNEUROSCI.3155-08.2009.
- [145] Einat Fuchs, Philip Holmes, Izhak David, and Amir Ayali. “Proprioceptive feedback reinforces centrally generated stepping patterns in the cockroach”. In: *Journal of Experimental Biology* (2012). ISSN: 00220949. DOI: 10.1242/jeb.067488.
- [146] C. C. Canavier, D. A. Baxter, J. W. Clark, and J. H. Byrne. “Multiple modes of activity in a model neuron suggest a novel mechanism for the effects of neuromodulators”. In: *Journal of Neurophysiology* (1994). ISSN: 00223077. DOI: 10.1152/jn.1994.72.2.872.
- [147] Julie L. Lefebvre, Joshua R. Sanes, and Jeremy N. Kay. “Development of Dendritic Form and Function”. In: *Annual Review of Cell and Developmental Biology* (2015). ISSN: 15308995. DOI: 10.1146/annurev-cellbio-100913-013020.
- [148] Alberto E. Pereda. *Electrical synapses and their functional interactions with chemical synapses*. 2014. DOI: 10.1038/nrn3708.
- [149] Cecilia Conde and Alfredo Cáceres. *Microtubule assembly, organization and dynamics in axons and dendrites*. 2009. DOI: 10.1038/nrn2631.
- [150] David Vandael, Yuji Okamoto, and Peter Jonas. “Transsynaptic modulation of presynaptic short-term plasticity in hippocampal mossy fiber synapses”. In: *Nature Communications* (2021). ISSN: 2041-1723.
- [151] Anthony P. Barnes and Franck Polleux. *Establishment of axon-dendrite polarity in developing neurons*. 2009. DOI: 10.1146/annurev.neuro.31.060407.125536.
- [152] Nariko Arimura and Kozo Kaibuchi. *Neuronal polarity: From extracellular signals to intracellular mechanisms*. 2007. DOI: 10.1038/nrn2056.
- [153] Yishi Jin and Yingchuan B. Qi. *Building stereotypic connectivity: mechanistic insights into structural plasticity from C. elegans*. 2018. DOI: 10.1016/j.conb.2017.11.005.
- [154] Susana Gomis-Rüth, Corette J. Wierenga, and Frank Bradke. “Plasticity of Polarization: Changing Dendrites into Axons in Neurons Integrated in Neuronal Circuits”. In: *Current Biology* (2008). ISSN: 09609822. DOI: 10.1016/j.cub.2008.06.026.

- [155] Z. F. Mainen and T. J. Sejnowski. “Influence of dendritic structure on firing pattern in model neocortical neurons”. In: *Nature* (1996). ISSN: 00280836. DOI: 10.1038/382363a0.
- [156] Ray W. Turner, Neal Lemon, Brent Doiron, Asim J. Rashid, Ezequiel Morales, Andre Longtin, Leonard Maler, and Robert J. Dunn. “Oscillatory burst discharge generated through conditional backpropagation of dendritic spikes”. In: *Journal of Physiology Paris* (2002). ISSN: 09284257. DOI: 10.1016/S0928-4257(03)00007-X.
- [157] Meital Oren-Suissa, David H. Hall, Millet Treinin, Gidi Shemer, and Benjamin Podbilewicz. “The fusogen EFF-I controls sculpting of mechanosensory dendrites”. In: *Science* 328.5983 (2010), pp. 1285–1288. ISSN: 00368075. DOI: 10.1126/science.1189095.
- [158] Adi Albeg, Cody J. Smith, Marios Chatzigeorgiou, Dror G. Feitelson, David H. Hall, William R. Schafer, David M. Miller, and Millet Treinin. “C. elegans multi-dendritic sensory neurons: Morphology and function”. In: *Molecular and Cellular Neuroscience* (2011). ISSN: 10447431. DOI: 10.1016/j.mcn.2010.10.001.
- [159] Omer Yuval, Yael Iosilevskii, Anna Meledin, Benjamin Podbilewicz, and Tom Shemesh. “Neuron tracing and quantitative analyses of dendritic architecture reveal symmetrical three-way-junctions and phenotypes of git-1 in C. elegans”. In: *PLoS Computational Biology* (2021). ISSN: 15537358. DOI: 10.1371/journal.pcbi.1009185.
- [160] Li Tao, Daniel Porto, Zhaoyu Li, Sylvia Fechner, Sol Ah Lee, Miriam B. Goodman, X. Z. Shawn Xu, Hang Lu, and Kang Shen. “Parallel Processing of Two Mechanosensory Modalities by a Single Neuron in C. elegans”. In: *Developmental Cell* (2019). ISSN: 18781551. DOI: 10.1016/j.devcel.2019.10.008.
- [161] Constance Hammond. “Tonic gradients, membrane potential and ionic currents”. In: *Cellular and Molecular Neurophysiology: Fourth Edition* (2015). DOI: 10.1016/B978-0-12-397032-9.00003-0.
- [162] David E. Goldman. “Potential, impedance, and rectification in membranes”. In: *Journal of General Physiology* (1943). ISSN: 15407748. DOI: 10.1085/jgp.27.1.37.
- [163] A. L. Hodgkin and B. Katz. “The effect of sodium ions on the electrical activity of the giant axon of the squid”. In: *The Journal of Physiology* (1949). ISSN: 14697793. DOI: 10.1113/jphysiol.1949.sp004310.

- [164] Jens Christian Skou. “Overview: The Na,K-Pump”. In: *Methods in Enzymology* (1988). ISSN: 15577988. DOI: 10.1016/0076-6879(88)56004-4.
- [165] A. L. Hodgkin and R. D. Keynes. “Active transport of cations in giant axons from *Sepia* and *Loligo*”. In: *The Journal of Physiology* (1955). ISSN: 14697793. DOI: 10.1113/jphysiol.1955.sp005290.
- [166] Alex G. Therien and Rhoda Blostein. *Mechanisms of sodium pump regulation*. 2000. DOI: 10.1152/ajpcell.2000.279.3.c541.
- [167] Yu Shen, Quan Wen, He Liu, Connie Zhong, Yuqi Qin, Gareth Harris, Taizo Kawano, Min Wu, Tianqi Xu, Aravinthan D.T. Samuel, and Yun Zhang. “An extrasynaptic GABAergic signal modulates a pattern of forward movement in *Caenorhabditis elegans*”. In: *eLife* (2016). ISSN: 2050084X. DOI: 10.7554/eLife.14197.
- [168] Mark W. Barnett and Philip M. Larkman. “The action potential”. In: *Practical Neurology* (2007). ISSN: 14747758. DOI: 10.1016/b978-0-12-800883-6.00024-0.
- [169] A. L. Hodgkin and A. F. Huxley. *Action potentials recorded from inside a nerve fibre*. 1939. DOI: 10.1038/144710a0.
- [170] Erwin Neher and Bert Sakmann. “Single-channel currents recorded from membrane of denervated frog muscle fibres”. In: *Nature* (1976). ISSN: 00280836. DOI: 10.1038/260799a0.
- [171] Eric J. Heyer, Robert L. Macdonald, Gregory K. Bergey, and Phillip G. Nelson. “Calcium-dependent action potentials in mouse spinal cord neurons in cell culture”. In: *Brain Research* (1981). ISSN: 00068993. DOI: 10.1016/0006-8993(81)91234-8.
- [172] J. D. Angstadt and R. L. Calabrese. “Calcium currents and graded synaptic transmission between heart interneurons of the leech”. In: *Journal of Neuroscience* (1991). ISSN: 02706474. DOI: 10.1523/jneurosci.11-03-00746.1991.
- [173] David F. Clayton. “The genomic action potential”. In: *Neurobiology of Learning and Memory* (2000). ISSN: 10747427. DOI: 10.1006/nlme.2000.3967.
- [174] Mikko Juusola, Andrew S. French, Raima O. Uusitalo, and Matti Weckström. *Information processing by graded-potential transmission through tonically active synapses*. 1996. DOI: 10.1016/S0166-2236(96)10028-X.

- [175] R L Calabrese and E A Arbas. “Central and peripheral oscillators generating heartbeat in the leech *Hirudo medicinalis*”. In: *Neuronal and cellular oscillators*. Marcel Dekker, New York (1989), pp. 237–267.
- [176] W. Otto Friesen. “Neuronal control of leech swimming movements - II. Motor neuron feedback to oscillator cells 115 and 28”. In: *Journal of Comparative Physiology A* (1989). ISSN: 03407594. DOI: 10.1007/BF00193465.
- [177] Sten Grillner, Peter Wallén, Lennart Brodin, and Anders Lansner. *Neuronal network generating locomotor behavior in lamprey: Circuitry, transmitters, membrane properties, and simulation*. 1991. DOI: 10.1146/annurev.ne.14.030191.001125.
- [178] Allen I Selverston and Maurice Moulins. *The crustacean stomatogastric system: a model for the study of central nervous systems*. Springer Science & Business Media, 2012.
- [179] Xiao-Jing Wang and John Rinzel. “Alternating and Synchronous Rhythms in Reciprocally Inhibitory Model Neurons”. In: *Neural Computation* (1992). ISSN: 0899-7667. DOI: 10.1162/neco.1992.4.1.84.
- [180] Thomas Graham Brown. “The intrinsic factors in the act of progression in the mammal”. In: *Proceedings of the Royal Society of London. Series B, Containing Papers of a Biological Character* (1911). ISSN: 0950-1193. DOI: 10.1098/rspb.1911.0077.
- [181] W Otto Friesen. “Reciprocal Inhibition: A Mechanism Underlying Oscillatory Animal Movements”. In: *Neuroscience and Biobehavioral Reviews* (1994).
- [182] Balth. van der Pol. “On “relaxation-oscillations””. In: *The London, Edinburgh, and Dublin Philosophical Magazine and Journal of Science* (1926). ISSN: 1941-5982. DOI: 10.1080/14786442608564127.
- [183] M. J. Brennan, B. Tang, and J. C. Carranza. “Insight into the dynamic behaviour of the Van der Pol/Raleigh oscillator using the internal stiffness and damping forces”. In: *Journal of Physics: Conference Series*. 2016. DOI: 10.1088/1742-6596/744/1/012122.
- [184] A. N. Burkitt. “A review of the integrate-and-fire neuron model: I. Homogeneous synaptic input”. In: *Biological Cybernetics* (2006). ISSN: 03401200. DOI: 10.1007/s00422-006-0068-6.
- [185] A. L. Hodgkin and A. F. Huxley. “A quantitative description of membrane current and its application to conduction and excitation in nerve”. In: *The Journal of Physiology* (1952). ISSN: 14697793. DOI: 10.1113/jphysiol.1952.sp004764.

- [186] Richard FitzHugh. “Impulses and Physiological States in Theoretical Models of Nerve Membrane”. In: *Biophysical Journal* (1961). ISSN: 00063495. DOI: 10.1016/S0006-3495(61)86902-6.
- [187] J. Nagumo, S. Arimoto, and S. Yoshizawa. “An Active Pulse Transmission Line Simulating Nerve Axon*”. In: *Proceedings of the IRE* (1962). ISSN: 00968390. DOI: 10.1109/JRPROC.1962.288235.
- [188] Rose T. Faghieh, Ketan Savla, Munther A. Dahleh, and Emery N. Brown. “The FitzHugh-Nagumo model: Firing modes with time-varying parameters & parameter estimation”. In: *2010 Annual International Conference of the IEEE Engineering in Medicine and Biology Society, EMBC’10*. 2010. ISBN: 9781424441235. DOI: 10.1109/IEMBS.2010.5627326.
- [189] C. Morris and H. Lecar. “Voltage oscillations in the barnacle giant muscle fiber”. In: *Biophysical Journal* (1981). ISSN: 00063495. DOI: 10.1016/S0006-3495(81)84782-0.
- [190] P. F. Rowat and A. I. Selverston. “Modeling the gastric mill central pattern generator of the lobster with a relaxation-oscillator network”. In: *Journal of Neurophysiology* (1993). ISSN: 00223077. DOI: 10.1152/jn.1993.70.3.1030.
- [191] Peter F. Rowat and Allen I. Selverston. “Oscillatory mechanisms in pairs of neurons connected with fast inhibitory synapses”. In: *Journal of Computational Neuroscience* (1997). ISSN: 09295313. DOI: 10.1023/A:1008869411135.
- [192] Rex A. Kerr. *Imaging the activity of neurons and muscles*. 2006. DOI: 10.1895/wormbook.1.113.1.
- [193] Francesco Randi and Andrew M. Leifer. *Measuring and modeling whole-brain neural dynamics in *Caenorhabditis elegans**. 2020. DOI: 10.1016/j.conb.2020.11.001.
- [194] Sung Jin Park, Miriam B. Goodman, and Beth L. Pruitt. “Analysis of nematode mechanics by piezoresistive displacement clamp”. In: *Proceedings of the National Academy of Sciences of the United States of America* (2007). ISSN: 00278424. DOI: 10.1073/pnas.0702138104.
- [195] J. Sznitman, Prashant K. Purohit, P. Krajacic, T. Lamitina, and P. E. Arratia. “Material properties of *Caenorhabditis elegans* swimming at low reynolds number”. In: *Biophysical Journal* (2010). ISSN: 15420086. DOI: 10.1016/j.bpj.2009.11.010. arXiv: 0911.1731.
- [196] J. Sznitman, X. Shen, R. Sznitman, and P. E. Arratia. “Propulsive force measurements and flow behavior of undulatory swimmers at low Reynolds number”. In: *Physics of Fluids* (2010). ISSN: 10706631. DOI: 10.1063/1.3529236.

- [197] X. N. Shen, J. Sznitman, P. Krajacic, T. Lamitina, and P. E. Arratia. “Undulatory locomotion of *Caenorhabditis elegans* on wet surfaces”. In: *Biophysical Journal* (2012). ISSN: 00063495. DOI: 10.1016/j.bpj.2012.05.012.
- [198] Matilda Backholm, William S. Ryu, and Kari Dalnoki-Veress. “Viscoelastic properties of the nematode *Caenorhabditis elegans*, a self-similar, shear-thinning worm”. In: *Proceedings of the National Academy of Sciences of the United States of America* (2013). ISSN: 00278424. DOI: 10.1073/pnas.1219965110.
- [199] M. Backholm, A. K.S. Kasper, R. D. Schulman, W. S. Ryu, and K. Dalnoki-Veress. “The effects of viscosity on the undulatory swimming dynamics of *C. elegans*”. In: *Physics of Fluids* (2015). ISSN: 10897666. DOI: 10.1063/1.4931795.
- [200] G. Ross Frances and Robert H. Waterston. “Muscle organization in *Caenorhabditis elegans*: Localization of proteins implicated in thin filament attachment and i-band Organization”. In: *Journal of Cell Biology* (1985). ISSN: 15408140. DOI: 10.1083/jcb.101.4.1532.
- [201] Alan F Bird and Jean Bird. *The structure of nematodes*. Academic Press, 2012.
- [202] A. H.Jay Burr and Carl Gans. “Mechanical significance of obliquely striated architecture in nematode muscle”. In: *Biological Bulletin* (1998). ISSN: 00063185. DOI: 10.2307/1542507.
- [203] Qiang Liu, Gunther Hollopeter, and Erik M. Jorgensen. “Graded synaptic transmission at the *Caenorhabditis elegans* neuromuscular junction”. In: *Proceedings of the National Academy of Sciences of the United States of America* (2009). ISSN: 00278424. DOI: 10.1073/pnas.0903570106.
- [204] Shangbang Gao and Mei Zhen. “Action potentials drive body wall muscle contractions in *Caenorhabditis elegans*”. In: *Proceedings of the National Academy of Sciences of the United States of America* (2011). ISSN: 00278424. DOI: 10.1073/pnas.1012346108.
- [205] Miriam B. Goodman, David H. Hall, Leon Avery, and Shawn R. Lockery. “Active currents regulate sensitivity and dynamic range in *C. elegans* Neurons”. In: *Neuron* (1998). ISSN: 08966273. DOI: 10.1016/S0896-6273(00)81014-4.
- [206] R Lee, L Lobel, M Hengartner, H Horvitz, and L Avery. “Mutations in the alpha subunit of an L-type voltage-activated Ca²⁺ channel cause myotonia in *Caenorhabditis elegans*.” In: *The EMBO Journal* (1997). ISSN: 0261-4189. DOI: 10.5167/uzh-1018.

- [207] Jospin M, Jacquemond V, Mariol MC, Segalat L, and Allard B. “The L-type voltage-dependent Ca²⁺ channel EGL-19 controls body wall muscle function in *Caenorhabditis elegans*.” In: *Journal of Cell Biology* (2002).
- [208] J. G. White, E. Southgate, J. N. Thomson, and S. Brenner. “The structure of the ventral nerve cord of *Caenorhabditis elegans*.” In: *Philosophical transactions of the Royal Society of London. Series B, Biological sciences* (1976). ISSN: 09628436. DOI: 10.1098/rstb.1976.0086.
- [209] Lan Deng, Jack Denham, Charu Arya, Omer Yuval, Netta Cohen, and Gal Haspel. “Inhibition underlies fast undulatory locomotion in *C. elegans*”. In: *eneuro* (2020). DOI: 10.1523/eneuro.0241-20.2020.
- [210] Anne C. Hart, Shannon Sims, and Joshua M. Kaplan. “Synaptic code for sensory modalities revealed by *C. Elegans* GLR-1 glutamate receptor”. In: *Nature* (1995). ISSN: 00280836. DOI: 10.1038/378082a0.
- [211] Kuang Man Huang, Pamela Cosman, and William R. Schafer. “Automated detection and analysis of foraging behavior in *Caenorhabditis elegans*”. In: *Journal of Neuroscience Methods* (2008). ISSN: 01650270. DOI: 10.1016/j.jneumeth.2008.01.027.
- [212] Andrés G. Vidal-Gadea, Scott Davis, Lindsay Becker, and Jonathan T. Pierce-Shimomura. “Coordination of behavioral hierarchies during environmental transitions in *Caenorhabditis elegans*”. In: *Worm* (2012). ISSN: 2162-4046. DOI: 10.4161/worm.19148.
- [213] Shawn R. Lockery. *The computational worm: Spatial orientation and its neuronal basis in C. elegans*. 2011. DOI: 10.1016/j.conb.2011.06.009.
- [214] Jonathan T. Pierce-Shimomura, Beth L. Chen, James J. Mun, Raymond Ho, Raman Sarkis, and Steven L. McIntire. “Genetic analysis of crawling and swimming locomotory patterns in *C. elegans*”. In: *Proceedings of the National Academy of Sciences of the United States of America* (2008). ISSN: 00278424. DOI: 10.1073/pnas.0810359105.
- [215] Z F Altun and D H Hall. “Nervous system, general description”. In: *WormAtlas. doi 10* (2011), pp. 103–116.
- [216] Steven L. McIntire, Erik Jorgensen, Joshua Kaplan, and H. Robert Horvitz. “The GABAergic nervous system of *Caenorhabditis elegans*”. In: *Nature* (1993). ISSN: 00280836. DOI: 10.1038/364337a0.

- [217] Janet S. Duerr, He Ping Han, Stephen D. Fields, and James B. Rand. “Identification of major classes of cholinergic neurons in the nematode *Caenorhabditis elegans*”. In: *Journal of Comparative Neurology* (2008). ISSN: 00219967. DOI: 10.1002/cne.21551.
- [218] Mei Zhen and Aravinthan D.T. Samuel. *C. elegans locomotion: Small circuits, complex functions*. 2015. DOI: 10.1016/j.conb.2015.03.009.
- [219] Shangbang Gao, Sihui Asuka Guan, Anthony D. Fouad, Jun Meng, Taizo Kawano, Yung Chi Huang, Yi Li, Salvador Alcaire, Wesley Hung, Yangning Lu, Yingchuan Billy Qi, Yishi Jin, Mark Alkema, Christopher Fang-Yen, and Mei Zhen. “Excitatory motor neurons are local oscillators for backward locomotion”. In: *eLife* (2018). ISSN: 2050084X. DOI: 10.7554/eLife.29915.
- [220] Nektarios Tavernarakis, Wayne Shreffler, Shiliang Wang, and Monica Driscoll. “unc-8, a DEG/ENaC family member, encodes a subunit of a candidate mechanically gated channel that modulates *C. elegans* locomotion”. In: *Neuron* (1997). ISSN: 08966273. DOI: 10.1016/S0896-6273(01)80050-7.
- [221] William R. Schafer. *Mechanosensory molecules and circuits in C. elegans*. 2015. DOI: 10.1007/s00424-014-1574-3.
- [222] Anthony D. Fouad, Shelly Teng, Julian R. Mark, Alice Liu, Pilar Alvarez-Illera, Hongfei Ji, Angelica Du, Priya D. Bhirgoo, Eli Cornblath, Sihui Asuka Guan, and Christopher Fang-Yen. “Distributed rhythm generators underlie *Caenorhabditis elegans* forward locomotion”. In: *eLife* (2018). ISSN: 2050084X. DOI: 10.7554/eLife.29913.
- [223] Iring Koch, Miriam Gade, Stefanie Schuch, and Andrea M. Philipp. “The role of inhibition in task switching: A review”. In: *Psychonomic Bulletin and Review* (2010). ISSN: 10699384. DOI: 10.3758/PBR.17.1.1.
- [224] Tija C. Jacob, Stephen J. Moss, and Rachel Jurd. *GABAA receptor trafficking and its role in the dynamic modulation of neuronal inhibition*. 2008. DOI: 10.1038/nrn2370.
- [225] David F. Owens and Arnold R. Kriegstein. *Is there more to GABA than synaptic inhibition?* 2002. DOI: 10.1038/nrn919.
- [226] Marie Gendrel, Emily G. Atlas, and Oliver Hobert. “A cellular and regulatory map of the GABAergic nervous system of *C. elegans*”. In: *eLife* (2016). ISSN: 2050084X. DOI: 10.7554/eLife.17686.

- [227] Igor Putrenko, Mahvash Zakikhani, and Joseph A. Dent. “A family of acetylcholine-gated chloride channel subunits in *Caenorhabditis elegans*”. In: *Journal of Biological Chemistry* (2005). ISSN: 00219258. DOI: 10.1074/jbc.M412644200.
- [228] Jinmahn Kim, Jihye Yeon, Seong Kyoon Choi, Yang Hoon Huh, Zi Fang, Seo Jin Park, Myoung Ok Kim, Zae Young Ryoo, Kyeongjin Kang, Hee Seok Kweon, Won Bae Jeon, Chris Li, and Kyuhyung Kim. “The Evolutionarily Conserved LIM Homeodomain Protein LIM-4/LHX6 Specifies the Terminal Identity of a Cholinergic and Peptidergic *C. elegans* Sensory/Inter/Motor Neuron-Type”. In: *PLoS Genetics* (2015). ISSN: 15537404. DOI: 10.1371/journal.pgen.1005480.
- [229] Shawn R. Lockery and Miriam B. Goodman. *The quest for action potentials in C. elegans neurons hits a plateau*. 2009. DOI: 10.1038/nn0409-377.
- [230] Qiang Liu, Philip B. Kidd, May Dobosiewicz, and Cornelia I. Bargmann. “*C. elegans* AWA Olfactory Neurons Fire Calcium-Mediated All-or-None Action Potentials”. In: *Cell* (2018). ISSN: 10974172. DOI: 10.1016/j.cell.2018.08.018.
- [231] Harris S. Kaplan, Annika L.A. Nichols, and Manuel Zimmer. “Sensorimotor integration in *Caenorhabditis elegans*: A reappraisal towards dynamic and distributed computations”. In: *Philosophical Transactions of the Royal Society B: Biological Sciences* (2018). ISSN: 14712970. DOI: 10.1098/rstb.2017.0371.
- [232] Jihye Yeon, Jinmahn Kim, Do Young Kim, Hyunmin Kim, Jungha Kim, Eun Jo Du, Kyeong Jin Kang, Hyun Ho Lim, Daewon Moon, and Kyuhyung Kim. “A sensory-motor neuron type mediates proprioceptive coordination of steering in *C. elegans* via two TRPC channels”. In: *PLoS Biology* (2018). ISSN: 15457885. DOI: 10.1371/journal.pbio.2004929.
- [233] D. Dipon Ghosh, Tom Sanders, Soonwook Hong, Li Yan McCurdy, Daniel L. Chase, Netta Cohen, Michael R. Koelle, and Michael N. Nitabach. “Neural Architecture of Hunger-Dependent Multisensory Decision Making in *C. elegans*”. In: *Neuron* (2016). ISSN: 10974199. DOI: 10.1016/j.neuron.2016.10.030.
- [234] Chiou Fen Chuang, Miri K. VanHoven, Richard D. Fetter, Vytas K. Verselis, and Cornelia I. Bargmann. “An Innexin-Dependent Cell Network Establishes Left-Right Neuronal Asymmetry in *C. elegans*”. In: *Cell* (2007). ISSN: 00928674. DOI: 10.1016/j.cell.2007.02.052.

- [235] David H. Hall. *Gap junctions in C. elegans: Their roles in behavior and development*. 2017. DOI: 10.1002/dneu.22408.
- [236] Kazumichi Shimizu and Mark Stopfer. *Gap junctions*. 2013. DOI: 10.1016/j.cub.2013.10.067.
- [237] Zeynep F. Altun, Bojun Chen, Zhao Weng Wang, and David H. Hall. “High resolution map of *Caenorhabditis elegans* gap junction proteins”. In: *Developmental Dynamics* (2008). ISSN: 10588388. DOI: 10.1002/dvdy.22025.
- [238] Qiang Liu, Bojun Chen, Eric Gaier, Jaya Joshi, and Zhao Wen Wang. “Low conductance gap junctions mediate specific electrical coupling in body-wall muscle cells of *Caenorhabditis elegans*”. In: *Journal of Biological Chemistry* (2006). ISSN: 00219258. DOI: 10.1074/jbc.M512382200.
- [239] Eduardo J. Izquierdo and Randall D. Beer. “From head to tail: A neuromechanical model of forward locomotion in *Caenorhabditis elegans*”. In: *Philosophical Transactions of the Royal Society B: Biological Sciences* (2018). ISSN: 14712970. DOI: 10.1098/rstb.2017.0374.
- [240] John Bryden and Netta Cohen. “Neural control of *Caenorhabditis elegans* forward locomotion: The role of sensory feedback”. In: *Biological Cybernetics* (2008). ISSN: 03401200. DOI: 10.1007/s00422-008-0212-6.
- [241] Beth L. Chen, David H. Hall, and Dmitri B. Chklovskii. “Wiring optimization can relate neuronal structure and function”. In: *Proceedings of the National Academy of Sciences of the United States of America* (2006). ISSN: 00278424. DOI: 10.1073/pnas.0506806103.
- [242] Quan Wen, Michelle D. Po, Elizabeth Hulme, Sway Chen, Xinyu Liu, Sen Wai Kwok, Marc Gershon, Andrew M. Leifer, Victoria Butler, Christopher Fang-Yen, Taizo Kawano, William R. Schafer, George Whitesides, Matthieu Wyart, Dmitri B. Chklovskii, Mei Zhen, and Aravinthan D.T. Samuel. “Proprioceptive Coupling within Motor Neurons Drives *C. elegans* Forward Locomotion”. In: *Neuron* (2012). ISSN: 08966273. DOI: 10.1016/j.neuron.2012.08.039.
- [243] Namseop Kwon, Jaeyeon Pyo, Seung Jae Lee, and Jung Ho Je. “3-D Worm Tracker for Freely Moving *C. elegans*”. In: *PLoS ONE* (2013). ISSN: 19326203. DOI: 10.1371/journal.pone.0057484.
- [244] Namseop Kwon, Ara B. Hwang, Young Jai You, Seung Jae V. Lee, and Jung Ho Je. “Dissection of *C. elegans* behavioral genetics in 3-D environments”. In: *Scientific Reports* (2015). ISSN: 20452322. DOI: 10.1038/srep09564.

- [245] Michael Shaw, Haoyun Zhan, Muna Elmi, Vijay Pawar, Clara Essmann, and Mandayam A. Srinivasan. “Three-dimensional behavioural phenotyping of freely moving *C. Elegans* using quantitative light field microscopy”. In: *PLoS ONE* (2018). ISSN: 19326203. DOI: 10.1371/journal.pone.0200108.
- [246] Thomas Ranner. “A stable finite element method for low inertia undulatory locomotion in three dimensions”. In: *Applied Numerical Mathematics* 156 (2020). ISSN: 01689274. DOI: 10.1016/j.apnum.2020.05.009.
- [247] Greg J. Stephens, Bethany Johnson-Kerner, William Bialek, and William S. Ryu. “Dimensionality and dynamics in the behavior of *C. elegans*”. In: *PLoS Computational Biology* (2008). ISSN: 1553734X. DOI: 10.1371/journal.pcbi.1000028. arXiv: 0705.1548.
- [248] Shuichi Nakamura and Tohru Minamino. “Flagella-driven motility of bacteria”. In: *Biomolecules* (2019). ISSN: 2218273X. DOI: 10.3390/biom9070279.
- [249] Martin Sim, Santosh Koirala, David Picton, Henrik Strahl, Paul A. Hoskisson, Christopher V. Rao, Colin S. Gillespie, and Phillip D. Aldridge. “Growth rate control of flagellar assembly in *Escherichia coli* strain RP437”. In: *Scientific Reports* (2017). ISSN: 20452322. DOI: 10.1038/srep41189.
- [250] Navish Wadhwa and Howard C. Berg. *Bacterial motility: machinery and mechanisms*. 2021. DOI: 10.1038/s41579-021-00626-4.
- [251] D. M. Woolley. “Motility of spermatozoa at surfaces”. In: *Reproduction* (2003). ISSN: 14701626. DOI: 10.1530/rep.0.1260259.
- [252] Luis Alvarez, Benjamin M. Friedrich, Gerhard Gompper, and U. Benjamin Kaupp. *The computational sperm cell*. 2014. DOI: 10.1016/j.tcb.2013.10.004.
- [253] Ting Wei Su, Liang Xue, and Aydogan Ozcan. “High-throughput lensfree 3D tracking of human sperms reveals rare statistics of helical trajectories”. In: *Proceedings of the National Academy of Sciences of the United States of America* (2012). ISSN: 00278424. DOI: 10.1073/pnas.1212506109.
- [254] Jens Elgeti, U. Benjamin Kaupp, and Gerhard Gompper. “Hydrodynamics of sperm cells near surfaces”. In: *Biophysical Journal* (2010). ISSN: 15420086. DOI: 10.1016/j.bpj.2010.05.015.
- [255] Lucia Carichino and Sarah D. Olson. “Emergent three-dimensional sperm motility: coupling calcium dynamics and preferred curvature in a Kirchhoff rod model”. In: *Mathematical medicine and biology : a journal of the IMA* (2019). ISSN: 14778602. DOI: 10.1093/imammb/dqy015. arXiv: 1804.04712.

- [256] Ting Wei Su, Inkyum Choi, Jiawen Feng, Kalvin Huang, Euan McLeod, and Aydogan Ozcan. “Sperm trajectories form chiral ribbons”. In: *Scientific Reports* (2013). ISSN: 20452322. DOI: 10.1038/srep01664.
- [257] Jan F. Jikeli, Luis Alvarez, Benjamin M. Friedrich, Laurence G. Wilson, René Pascal, Remy Colin, Magdalena Pichlo, Andreas Rennhack, Christoph Brenker, and U. Benjamin Kaupp. “Sperm navigation along helical paths in 3D chemoattractant landscapes”. In: *Nature Communications* (2015). ISSN: 20411723. DOI: 10.1038/ncomms8985.
- [258] Richard A. Satterlie. “Reciprocal inhibition and postinhibitory rebound produce reverberation in a locomotor pattern generator”. In: *Science* (1985). ISSN: 00368075. DOI: 10.1126/science.229.4711.402.
- [259] Martina Nicoletti, Alessandro Loppini, Letizia Chiodo, Viola Folli, Giancarlo Ruocco, and Simonetta Filippi. “Biophysical modeling of *C. Elegans* neurons: Single ion currents and whole-cell dynamics of AWCon and RMD”. In: *PLoS ONE* (2019). ISSN: 19326203. DOI: 10.1371/journal.pone.0218738.
- [260] Jaime G. Mancilla, Timothy J. Lewis, David J. Pinto, John Rinzel, and Barry W. Connors. “Synchronization of electrically coupled pairs of inhibitory interneurons in neocortex”. In: *Journal of Neuroscience* (2007). ISSN: 02706474. DOI: 10.1523/JNEUROSCI.2715-06.2007.
- [261] Netta Cohen. *The development of spontaneous beating activity in cultured heart cells: From cells to networks*. Technion-Israel Institute of Technology, Department of Physics, 2000.
- [262] Paul F. Pinsky and John Rinzel. “Intrinsic and network rhythmogenesis in a reduced traub model for CA3 neurons”. In: *Journal of Computational Neuroscience* (1994). ISSN: 09295313. DOI: 10.1007/BF00962717.
- [263] Michael V.L. Bennett and R. Suzanne Zukin. *Electrical Coupling and Neuronal Synchronization in the Mammalian Brain*. 2004. DOI: 10.1016/S0896-6273(04)00043-1.
- [264] Michael Beierlein, Jay R. Gibson, and Barry W. Connors. “A network of electrically coupled interneurons drives synchronized inhibition in neocortex”. In: *Nature Neuroscience* (2000). ISSN: 10976256. DOI: 10.1038/78809.

- [265] Timothy J. Lewis and John Rinzel. “Dynamics of spiking neurons connected by both inhibitory and electrical coupling”. In: *Journal of Computational Neuroscience* (2003). ISSN: 09295313. DOI: 10.1023/A:1023265027714.
- [266] Nancy Kopell and Bard Ermentrout. “Chemical and electrical synapses perform complementary roles in the synchronization of interneuronal networks”. In: *Proceedings of the National Academy of Sciences of the United States of America* (2004). ISSN: 00278424. DOI: 10.1073/pnas.0406343101.
- [267] Benjamin Pfeuty, German Mato, David Golomb, and David Hansel. “The combined effects of inhibitory and electrical synapses in synchrony”. In: *Neural Computation* (2005). ISSN: 08997667. DOI: 10.1162/0899766053019917.
- [268] Adam L. Weaver, Rebecca C. Roffman, Brian J. Norris, and Ronald L. Calabrese. “A role for compromise: Synaptic inhibition and electrical coupling interact to control phasing in the leech heartbeat CPG”. In: *Frontiers in Behavioral Neuroscience* (2010). ISSN: 16625153. DOI: 10.3389/fnbeh.2010.00038.
- [269] Reimbay Reimbayev, Kevin Daley, and Igor Belykh. “When two wrongs make a right: Synchronized neuronal bursting from combined electrical and inhibitory coupling”. In: *Philosophical Transactions of the Royal Society A: Mathematical, Physical and Engineering Sciences* (2017). ISSN: 1364503X. DOI: 10.1098/rsta.2016.0282.
- [270] Benjamin Risse, Nils Otto, Dimitri Berh, Xiaoyi Jiang, and Christian Klämbt. “FIM imaging and FIMtrack: Two new tools allowing high-throughput and cost effective locomotion analysis”. In: *Journal of Visualized Experiments* (2014). ISSN: 1940087X. DOI: 10.3791/52207.
- [271] George V. Lauder. “Fish locomotion: Recent advances and new directions”. In: *Annual Review of Marine Science* (2015). ISSN: 19410611. DOI: 10.1146/annurev-marine-010814-015614.
- [272] Tsevi Beatus, John M. Guckenheimer, and Itai Cohen. “Controlling roll perturbations in fruit flies”. In: *Journal of the Royal Society Interface* (2015). ISSN: 17425662. DOI: 10.1098/rsif.2015.0075.
- [273] Eviatar Yemini, Tadas Jucikas, Laura J. Grundy, André E.X. Brown, and William R. Schafer. “A database of *Caenorhabditis elegans* behavioral phenotypes”. In: *Nature Methods* (2013). ISSN: 15487091. DOI: 10.1038/nmeth.2560.

- [274] Alexander Borst, Juergen Haag, and Dierk F. Reiff. *Fly motion vision*. 2010. DOI: 10.1146/annurev-neuro-060909-153155.
- [275] Stefan R. Pulver, Timothy G. Bayley, Adam L. Taylor, Jimena Berni, Michael Bate, and Berthold Hedwig. “Imaging fictive locomotor patterns in larval *Drosophila*”. In: *Journal of Neurophysiology* (2015). ISSN: 15221598. DOI: 10.1152/jn.00731.2015.
- [276] John Oreopoulos, Richard Berman, and Mark Browne. “Spinning-disk confocal microscopy: present technology and future trends”. In: *Methods in cell biology* 123 (2014), pp. 153–175.
- [277] Philipp J. Keller, Annette D. Schmidt, Joachim Wittbrodt, and Ernst H.K. Stelzer. “Reconstruction of zebrafish early embryonic development by scanned light sheet microscopy”. In: *Science* (2008). ISSN: 00368075. DOI: 10.1126/science.1162493.
- [278] Oliver Bimber and David Schedl. “Light-Field Microscopy: A Review”. In: *Journal of Neurology & Neuromedicine* (2019). DOI: 10.29245/2572.942x/2019/1.1237.
- [279] O. D. Therrien, B. Aubé, S. Pagès, P. De Koninck, and D. Côté. “Wide-field multiphoton imaging of cellular dynamics in thick tissue by temporal focusing and patterned illumination”. In: *Biomedical Optics Express* (2011). ISSN: 2156-7085. DOI: 10.1364/boe.2.000696.
- [280] Yann Lecun, Yoshua Bengio, and Geoffrey Hinton. *Deep learning*. 2015. DOI: 10.1038/nature14539.
- [281] Vijay Badrinarayanan, Alex Kendall, and Roberto Cipolla. “SegNet: A Deep Convolutional Encoder-Decoder Architecture for Image Segmentation”. In: *IEEE Transactions on Pattern Analysis and Machine Intelligence* (2017). ISSN: 01628828. DOI: 10.1109/TPAMI.2016.2644615. arXiv: 1511.00561.
- [282] Jacob M. Graving, Daniel Chae, Hemal Naik, Liang Li, Benjamin Koger, Blair R. Costelloe, and Iain D. Couzin. “Deepposekit, a software toolkit for fast and robust animal pose estimation using deep learning”. In: *eLife* (2019). ISSN: 2050084X. DOI: 10.7554/eLife.47994.
- [283] Mackenzie Weygandt Mathis and Alexander Mathis. *Deep learning tools for the measurement of animal behavior in neuroscience*. 2020. DOI: 10.1016/j.conb.2019.10.008. arXiv: 1909.13868.
- [284] Vivek Venkatachalam, Ni Ji, Xian Wang, Christopher Clark, James Kameron Mitchell, Mason Klein, Christopher J. Tabone, Jeremy Florman, Hongfei Ji, Joel Greenwood, Andrew D. Chisholm, Jagan Srinivasan, Mark Alkema, Mei Zhen, and Aravinthan D.T. Samuel. “Pan-neuronal imaging in roaming

- Caenorhabditis elegans”. In: *Proceedings of the National Academy of Sciences of the United States of America* (2016). ISSN: 10916490. DOI: 10.1073/pnas.1507109113.
- [285] C. Beron, A. G. Vidal-Gadea, J. Cohn, A. Parikh, G. Hwang, and J. T. Pierce-Shimomura. “The burrowing behavior of the nematode *Caenorhabditis elegans*: A new assay for the study of neuromuscular disorders”. In: *Genes, Brain and Behavior* (2015). ISSN: 1601183X. DOI: 10.1111/gbb.12217.
- [286] Leila Lesanpezeski, Jennifer E. Hewitt, Ricardo Laranjeiro, Adam Antebi, Monica Driscoll, Nathaniel J. Szewczyk, Jerzy Blawdziewicz, Carla M.R. Lacerda, and Siva A. Vanapalli. “Pluronic gel-based burrowing assay for rapid assessment of neuromuscular health in *C. elegans*”. In: *Scientific Reports* (2019). ISSN: 20452322. DOI: 10.1038/s41598-019-51608-9.
- [287] John White. “Clues to basis of exploratory behavior of the *C. Elegans* snout from head somatotropy”. In: *Philosophical Transactions of the Royal Society B: Biological Sciences* (2018). ISSN: 14712970. DOI: 10.1098/rstb.2017.0367.
- [288] Richard Hartley and Andrew Zisserman. “Multiple View Geometry in Computer Vision”. In: *Robotica* 19.2 (2001), pp. 233–236.
- [289] G Bradski. “The OpenCV Library”. In: *Dr. Dobb’s Journal of Software Tools* (2000).
- [290] Himadri B. Bohidar and Sidhartha S. Jena. “Study of sol-state properties of aqueous gelatin solutions”. In: *The Journal of Chemical Physics* (1994). ISSN: 00219606. DOI: 10.1063/1.467004.
- [291] Diane H. Theriault, Nathan W. Fuller, Brandon E. Jackson, Evan Bluhm, Dennis Evangelista, Zheng Wu, Margrit Betke, and Tyson L. Hedrick. “A protocol and calibration method for accurate multi-camera field videography”. In: *Journal of Experimental Biology* (2014). ISSN: 00220949. DOI: 10.1242/jeb.100529.
- [292] Johannes Schneider, Falko Schindler, Thomas Läbe, and Wolfgang Förstner. “Bundle adjustment for multi-camera systems with points at infinity”. In: *ISPRS Annals of Photogrammetry, Remote Sensing and Spatial Information Sciences* 3 (2012), pp. 75–80.
- [293] R. G. Coyle. “Simulation by repeated optimisation”. In: *Journal of the Operational Research Society* (1999). ISSN: 14769360. DOI: 10.1057/palgrave.jors.2600713.

- [294] Felix Salfelder, Omer Yuval, Thomas P Ilett, David C Hogg, Thomas Ranner, and Netta Cohen. “Markerless 3D spatio-temporal reconstruction of microscopic swimmers from video”. In: *Visual observation and analysis of Vertebrate And Insect Behavior 2020*. Leeds. 2021.
- [295] Damien Garcia. “Robust smoothing of gridded data in one and higher dimensions with missing values”. In: *Computational Statistics and Data Analysis* (2010). ISSN: 01679473. DOI: 10.1016/j.csda.2009.09.020.
- [296] D. H. Hall and R. L. Russell. “The posterior nervous system of the nematode *Caenorhabditis elegans*: Serial reconstruction of identified neurons and complete pattern of synaptic interactions”. In: *Journal of Neuroscience* (1991). ISSN: 02706474. DOI: 10.1523/jneurosci.11-01-00001.1991.
- [297] Donald L Riddle, Thomas Blumenthal, Barbara J Meyer, and James R Priess. *Mechanosensory control of locomotion*. 1997.
- [298] Noriyuki Ohnishi, Atsushi Kuhara, Fumiya Nakamura, Yoshifumi Okochi, and Ikue Mori. “Bidirectional regulation of thermotaxis by glutamate transmissions in *Caenorhabditis elegans*”. In: *EMBO Journal* (2011). ISSN: 02614189. DOI: 10.1038/emboj.2011.13.
- [299] Miriam B Goodman. “Mechanosensation”. In: *WormBook: The Online Review of C. elegans Biology [Internet]* (2006).
- [300] Eugene M Izhikevich. “Chapter 10: Synchronization”. In: *Dynamical Systems in Neuroscience: the Geometry of Excitability and Bursting*. Chambridge, MA: The MIT Press (2007), p. 441.